

Transactions of the ASME®

Journal of Turbomachinery

Published Quarterly by The American Society of Mechanical Engineers

VOLUME 111 • NUMBER 1 • JANUARY 1989

Technical Editor
G. K. SEROVY
Associate Technical Editors
Advanced Energy Systems
M. J. MORAN
Environmental Control
H. E. HESKETH
Fuels and Combustion Technologies
R. E. BARRETT
Gas Turbine
T. H. OKIISHI
Internal Combustion Engine
J. A. CATON
Nuclear Engineering
S. M. CHO
Power
R. W. PORTER

**BOARD ON
COMMUNICATIONS**
Chairman and Vice-President
R. NICKELL

Members-at-Large
J. LLOYD
R. REDER
F. SCHMIDT
M. FRANKE
M. KUTZ
T. MIN
F. LANDIS
R. ROCKE
W. WINER
R. GENTILE
B. ZIELS
R. MATES

President, **E. L. DAMAN**
Executive Director,
D. L. BELDEN
Treasurer, **ROBERT A. BENNETT**

PUBLISHING STAFF
Mng. Dir., Publ., **JOS. SANSONE**
Managing Editor,
CORNELIA MONAHAN
Sr. Production Editor,
VALERIE WINTERS
Editorial Prod. Asst.,
MARISOL ANDINO

Transactions of the ASME, Journal of Turbomachinery (ISSN 0889-504X) is published quarterly (Jan., Apr., July, Oct.) for \$100 per year by The American Society of Mechanical Engineers, 345 East 47th Street, New York, NY 10017. Second-class postage paid at New York, NY and additional mailing offices. POSTMASTER: Send address change to The Journal of Turbomachinery, c/o The AMERICAN SOCIETY OF MECHANICAL ENGINEERS, 22 Law Drive, Box 2300, Fairfield, NJ 07007-2300.

CHANGES OF ADDRESS must be received at Society headquarters seven weeks before they are to be effective. Please send old label and new address.

PRICES: To members, \$29.00, annually; to nonmembers, \$100.00.

Add \$15.00 for postage to countries outside the United States and Canada.

STATEMENT from By-Laws. The Society shall not be responsible for statements or opinions advanced in papers or ... printed in its publications (B 7.1, para. 3).

COPYRIGHT © 1989 by the American Society of Mechanical Engineers. Reprints from this publication may be made on condition that full credit be given the

TRANSACTIONS OF THE ASME—JOURNAL OF TURBOMACHINERY, and the author, and date of publication be stated.

INDEXED by Applied Mechanics Reviews and Engineering Information, Inc.

TECHNICAL PAPERS

- 1 Fully Scaled Transonic Turbine Rotor Heat Transfer Measurements (88-GT-171)
G. R. Guenette, A. H. Epstein, M. B. Giles, R. Haimes, and R. J. G. Norton
- 8 Phase-Resolved Heat-Flux Measurements on the Blade of a Full-Scale Rotating Turbine (88-GT-173)
M. G. Dunn, P. J. Seymour, S. H. Woodward, W. K. George, and R. E. Chupp
- 20 Developments in Instrumentation and Processing for Transient Heat Transfer Measurement in a Full-Stage Model Turbine (88-GT-11)
R. W. Ainsworth, J. L. Allen, M. R. D. Davies, J. E. Doorly, C. J. P. Forth, M. A. Hilditch, M. L. G. Oldfield, and A. G. Sheard
- 28 Stagnation Point and Surface Heat Transfer for a Turbine Stage: Prediction and Comparison With Data (88-GT-30)
D. B. Taulbee, L. Tran, and M. G. Dunn
- 36 Aerodynamic and Heat Transfer Measurements on a Transonic Nozzle Guide Vane (88-GT-10)
E. T. Wedlake, A. J. Brooks, and S. P. Harasgama
- 43 Study of the Convective Heat Transfer in a Rotating Coolant Channel (88-GT-35)
J. Guidez
- 51 Heat Transfer Visualization and Measurement in Unstable Concave-Wall Laminar Boundary Layers (88-GT-36)
R. I. Crane and J. Sabzvari
- 57 The Use of Foreign Gas to Simulate the Effects of Density Ratios in Film Cooling (88-GT-37)
A. J. H. Teekaram, C. J. P. Forth, and T. V. Jones
- 63 An Experimental and Numerical Investigation of Near Cooling Hole Heat Fluxes on a Film-Cooled Turbine Blade (88-GT-9)
C. Camci
- 71 Effects of Embedded Vortices on Film-Cooled Turbulent Boundary Layers (88-GT-170)
P. M. Ligrani, A. Ortiz, S. L. Joseph, and D. L. Evans
- 78 Free-Stream Turbulence From a Circular Wall Jet on a Flat Plate Heat Transfer and Boundary Layer Flow (88-GT-183)
R. MacMullin, W. Elrod, and R. Rivir
- 87 The Effects of Turbulence and Stator/Rotor Interactions on Turbine Heat Transfer: Part I—Design Operating Conditions (88-GT-125)
M. F. Blair, R. P. Dring, and H. D. Joslyn
- 97 The Effects of Turbulence and Stator/Rotor Interactions on Turbine Heat Transfer: Part II—Effects of Reynolds Number and Incidence (88-GT-5)
M. F. Blair, R. P. Dring, and H. D. Joslyn

ANNOUNCEMENTS

- 62 Change of address form for subscribers
- 104 Information for authors

G. R. Guenette

A. H. Epstein

M. B. Giles

R. Haimes

Gas Turbine Laboratory,
Massachusetts Institute of Technology,
Cambridge, MA 02139

R. J. G. Norton

Rolls-Royce Inc.,
Atlanta, GA 30349

Fully Scaled Transonic Turbine Rotor Heat Transfer Measurements

The heat transfer to an uncooled transonic singlestage turbine has been measured in a short-duration facility, which fully simulates all the nondimensional quantities of interest for fluid flow and heat transfer (Reynolds number, Prandtl number, Rossby number, temperature ratios, and corrected speed and weight flow). Data from heat flux gages about the midspan of the rotor profile, measured from d-c to more than 10 times blade passing frequency (60 kHz), are presented in both time-resolved and mean heat transfer form. These rotating blade data are compared to previously published heat transfer measurements taken at Oxford University on the same profile in a two-dimensional cascade with bar passing to simulate blade row interaction effects. The results are qualitatively quite similar at midspan. The data are also compared to a two-dimensional Navier-Stokes calculation of the blade mean section and the implications for turbine design are discussed.

Introduction

The accurate prediction of heat transfer in high-pressure turbine stages has long been recognized as a key to improved gas turbine performance and engine life. To that end, a vast amount of engineering effort has been extended over the last forty years to provide accurate experimental measurements of the heat transfer distribution and to improve the accuracy by which that distribution can be predicted. This work has included the measurement of two-dimensional airfoil heat transfer in both steady-state (Turner et al., 1985) and transient cascades (Shultz et al., 1977) as well as stage measurements in short-duration test rigs (Dunn et al., 1986). Recently, bars rotating ahead of a two-dimensional transonic cascade have been used to simulate the unsteady effects of blade row interactions on rotor blade heat transfer, in particular those of nozzle guide vane (NGV) wake passing and shock impingement (Doorly and Oldfield, 1985).

Of major intellectual and practical concern are the pronounced differences between two-dimensional cascade heat transfer measurements and actual engine experience. These discrepancies (usually treated empirically in engine design) have been attributed to such factors as turbulence differences, blade row interactions and unsteady effects, three-dimensional flows, and combustor exit profiles. Knowledge of the flow physics and the quantitative contribution of these phenomena is an important factor in improving turbine performance and life.

Described herein are experimental measurements and numerical calculations of the heat transfer to a transonic turbine stage operated in a short duration test facility, which fully simulates all the nondimensional fluid parameters known to be important to turbine heat transfer. The goal of the effort is

to measure unsteady heat transfer to rotors in an environment that simulates that of a full-scale engine in as many ways as possible. A two-dimensional version of the turbine rotor profile studied here was used by Ashworth et al. (1985) in bar passing experiments in a short duration cascade tunnel. Thus, we can use the comparison between the two-dimensional cascade and the three-dimensional rotor measurements to learn something about the relative importance of the combined effects of three-dimensional flow and blade row interaction on turbine heat transfer.

Experimental Apparatus

The experiments were performed in the MIT Blowdown Turbine Tunnel (Epstein et al., 1984). This facility consists of a supply tank separated by a large-diameter, fast-acting valve from the test section, which, in turn, discharges to a dump tank. The test section contains a 0.55 m (22 in.) diameter test turbine stage and rotating assembly, including an eddy brake power absorber and 10 kW drive motor, (Figs. 1 and 2). The flow path upstream of the stage includes a boundary layer bleed and a combustorlike contraction. In the configuration studied, the total temperature and pressure into the turbine are uniform.

The entire facility is initially evacuated and the supply tank and valve heated by circulating oil. The valve is then closed and the supply tank filled with an argon/Freon-12 mixture (used to reproduce the ratio of specific heats of combustor exit air). The turbine rotor is now brought up to operating speed in vacuum. To start the test, the main valve is opened and the eddy brake energized simultaneously. After a 250 ms startup transient, the corrected parameters are constant to better than 1 percent for 300 ms. (The corrected weight flow is held constant so long as the nozzle guide vanes are choked. The corrected speed is held constant by the eddy current brake.) The blades and tunnel walls have sufficient thermal inertia to re-

Contributed by the International Gas Turbine Institute and presented at the 33rd International Gas Turbine and Aeroengine Congress and Exhibition, Amsterdam, The Netherlands, June 5-9, 1988. Manuscript received by the International Gas Turbine Institute November 18, 1987. Paper No. 88-GT-171.

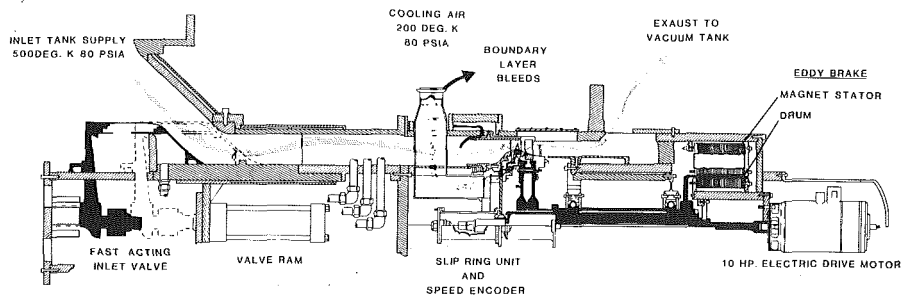


Fig. 1 The MIT Blowdown Turbine flowpath arrangement

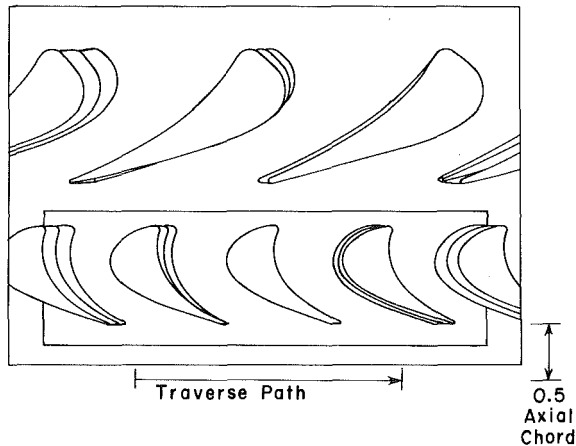


Fig. 2 Turbine stage geometry

Table 1 MIT blowdown turbine scaling

	Full Scale	MIT Blowdown
Fluid	Air	Ar-R12
Ratio Specific Heats	1.28	1.28
Mean Metal Temp.	1118°K (1550°F)	295°K (72°F)
Metal/Gas Temp. Ratio	0.63	0.63
Inlet Total Temp.	1780°K (2750°F)	478°K (400°F)
Cooling Air Temp.	790°K (960°F)	212°K (-77°F)
Airfoil Cooling Air	12.5%	12.5%
True NGV Chord	8.0 cm	5.9 cm
Reynolds Number*	2.7×10^6	2.7×10^6
Inlet Press., atm	19.6	4.3
Outlet Press., atm	4.5	1.0
Outlet Total Temp.	1280°K (1844°F)	343°K (160°F)
Prandtl Number	0.752	0.755
Eckert Number†	1.0	1.0
Rotor Speed, RPM	12,734	6,190
Mass Flow, kg/sec	49.00	16.55
Power, watts	24,880,000	1,078,000
Test Time	Continuous	0.3 sec.

* Based on NGV chord and isentropic exit conditions.

† $(\gamma-1)M^2T/\Delta T$

Table 2 Turbine design parameters

Turbine Loading, $\Delta H/u^2$	-2.3
Total Pressure Ratio	4.5
Velocity Ratio, C_x/U	0.63
Rotor Aspect Ratio	1.5
NGV Exit Mach No.	1.18

main at approximately constant temperature during the test time.

The facility has been designed to simulate closely all the nondimensional parameters important to turbine fluid mechanics and heat transfer: Reynolds number, Mach number, Prandtl number, Rossby number, ratio of specific heats, corrected speed and weight flow, and gas-to-metal temperature ratios. The principal scaling is to reduce the initial turbine metal temperature to room temperature, while keeping the gas-to-metal temperature ratio constant.

The design conditions of the tunnel are summarized in Table 1. (Note that the working fluid is an argon/Freon-12 mixture selected so that the ratio of specific heats (γ) is that of vitiated air (1.28).) The design parameters for the turbine are presented in Table 2. Solid (uncooled) blading was used for these tests. Turbulent intensity was measured with a hot wire in the inlet duct just after the boundary layer bleeds (but before the contraction) where the axial Mach number is 0.07. The level was 0.5 percent and the spectrum was essentially flat to 5 kHz.

Fairly conventional temperature, pressure, and rpm transducers are used to measure the "steady-state" operating conditions of the tunnel. The primary instrumentation is thin film heat flux gages distributed about the rotor blade profile. These transducers measure both the d-c and a-c components of heat flux. The heat flux gages consist of two thin film (140 nm thick) nickel temperature transducers mounted on either side of a 25- μ m-thick polyimide insulator. The sensing area is rectangular (1.0 \times 1.3 mm), oriented such that the longer dimension is in the chordwise direction. The insulator is adhesively bonded to, and completely covers, the blade profile (preventing thermal discontinuities). At low frequencies, the temperature drop across the insulator is a direct measure of the heat flux to the wall (the device is essentially a thermal shunt). This direct proportionality between heat flux and temperature difference extends from d-c to about 20 Hz, at which point the thermal waves within the insulator begin to

damp. Above 1 kHz, however, the 25- μ m-thick insulator appears infinitely thick to the top surface. Thus, above this frequency, a quasi-one-dimensional assumption can be used to infer the heat flux from the top surface temperature history (blade passing frequency is 6 kHz). Using a numerical data reduction technique, the entire frequency domain from d-c to 100 kHz is reconstructed. The gages were calibrated using a pulsed laser. The relative gauge calibrations are accurate to better than 5 percent. Absolute calibration accuracy is about 10 percent. Details of the gage theory, data reduction, and calibration may be found in Epstein et al. (1986).

The rotor heat flux gage signals are transmitted through uncooled slip rings, amplified and filtered, and then recorded on a 12 bit A/D system at 200,000 Hz sampling rate per channel. All signals are sampled simultaneously. Up to 20 million samples can be taken during a test.

This was the first test series with rotor mounted heat transfer gages in this facility. Gages were mounted about the chord at the midspan position only due to scheduling constraints.

Numerical Procedure

The numerical predictions were done with a program (ANSI-2D) that calculates a solution for the two-dimensional Reynolds-averaged Navier-Stokes equations. The beginning and end of transition is set by the user, and the turbulence is

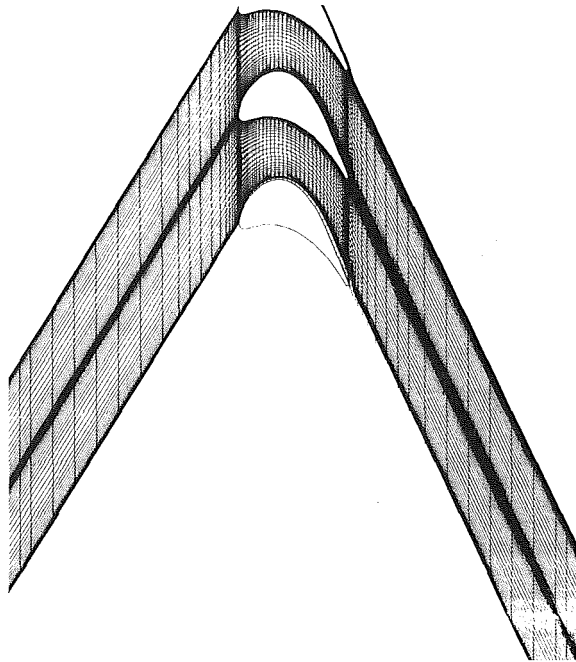


Fig. 3 Grid used for the two-dimensional calculation. Note the O-type grid about the blade is omitted from the lowest blade for clarity.

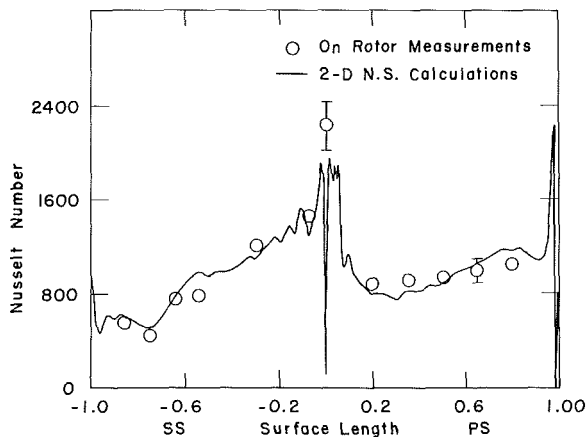


Fig. 4 Design point time-averaged rotor heat flux measurements and two-dimensional Navier-Stokes calculation

modeled as the additional turbulent viscosity given by the Cebeci-Smith model (Cebeci, 1970). At the inflow, the stagnation enthalpy, stagnation pressure, and flow angle are specified, and at the outflow, the static pressure is specified. On the blade surface one can specify either the wall temperature (used here) or zero heat flux for adiabatic conditions.

The numerical procedure is to integrate in time the unsteady Navier-Stokes equations using a finite-volume, explicit, multistep method, similar to that used by Jameson et al. (1981) (for calculating inviscid flows) and Swanson and Turkel (1985) (for calculating viscous flows). A blend of second-order and fourth-order smoothing is used to suppress numerical oscillations. In time-accurate calculations, the maximum stable time step is severely limited by the fine grid resolution in the boundary layer, so for steady-state calculations performed here, convergence is accelerated through the use of varying, local time steps, and implicit residual smoothing.

The grid (Fig. 3) used was of the type described by Norton et al. (1984) and employed an O-type grid about the blade for ready calculation of the eddy viscosity in the boundary layer (since the mesh is normal to the blade surface). The O grid is

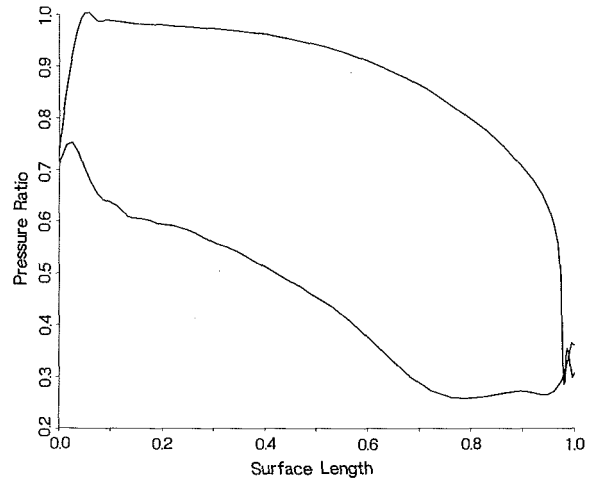


Fig. 5 Profile pressure distribution calculated with two-dimensional Navier-Stokes code

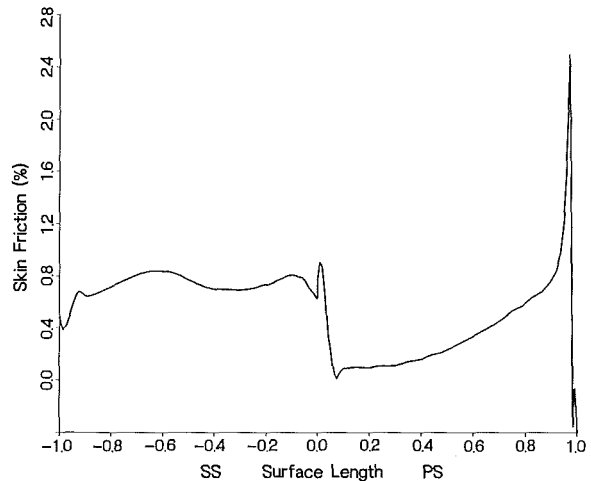


Fig. 6 Profile wall shear distribution calculated with two-dimensional Navier-Stokes code

embedded in a C-type grid used to enhance resolution in the blade wake. The C grid is in turn embedded in an H grid used for the through flow calculation. Near the leading edge, the O grid resolution is low in the streamwise direction resulting in elongated cells in the boundary layer near the stagnation point. The grid resolution normal to the blade surface for the O, C, and H grids is 5, 11, and 16 nodes, respectively. A total of 5100 cells was used.

For the calculations presented here, the inflow conditions and wall temperature were matched to those of the experiment. The code has no empirical, adjustable "knobs" other than the transition location. Transition was specified as a point near the leading edge of the airfoil ($x/s=0.01$).

Time-Averaged Results

The time-averaged heat transfer distribution measured about the midspan profile is shown in Fig. 4 along with the results of the two-dimensional calculation. The heat transfer coefficient is presented as Nusselt number, defined in terms of the rotor blade axial chord, inlet relative total minus local profile temperature, and thermal conductivity based on local temperature. The local profile temperatures used were those measured by the top sensors on the heat flux gages. Unless explicitly indicated, the uncertainties in the measurements are less than the size of the symbols. Surface length (x) is defined with the geometric axial leading edge as the zero reference. The calculated pressure distribution and wall shear are

Table 3 Comparison of rotating stage and cascade test conditions

	Rotor	Cascade*
Axial Chord	25.7 mm	34.8 mm
Tangential Chord	30.4 mm	41.2 mm
Ratio of Specific Heats	1.29	1.4
Molecular Weight	60.6	29.0
Blade Relative Total Pressure	1.77 atm	2.45 atm
Blade Relative Inlet Temp.	404°K	432°K
$[T_{TOT}/T_{BLADE}]_{relative}$	1.3	1.5
Wake Passing Frequency	3.3 kHz	4.2 kHz

* Ashworth et al. (1985)

presented in Figs. 5 and 6, which show the stagnation point (zero skin friction) to be at approximately 5 percent of surface length on the pressure surface. There is a small overspeed evident on the suction surface.

As can be seen, except for near the leading edge, the rotor measurements agree quite well with the fully turbulent two-dimensional prediction. A dip in heat transfer at about 80 percent surface distance on the suction surface, evident in both the measurements and calculations, is seen in the calculation as due to the impingement of the oblique expansion wave from the trailing edge of the adjacent blade. The large spike in the calculated heat flux at the trailing edge is an artifact of the lightly damped steady solution of what is physically an unsteady flowfield. Time-accurate solutions of this airfoil show vortex shedding at the trailing edge. The pronounced downspike near the leading edge in the calculation results from the greatly elongated cells used in this region of the boundary layer and the spatial first-order accuracy of the boundary conditions at the wall combining to limit accuracy in this area.

These results are replotted in Fig. 7 with data taken from cascade tests at the University of Oxford (Fig. 10b of Ashworth et al., 1985) on the same profile shape (at larger physical scale) at similar conditions (Table 3). The cascade data plotted are those with low free-stream turbulence (0.8 percent) and bar passing generated disturbances (shock waves and wakes) upstream of the blade row. All Nusselt numbers in this paper are presented with reference to the blade axial chord length and thermal conductivity based on local surface temperature. Because the Reynolds number of the rotor test was about 15 percent lower than that for the cascade, the cascade data are plotted both as presented in Ashworth et al. (1985) and scaled by the Reynolds number ratio to the 0.8 power. (This scaling is shown without necessarily endorsing a 0.8 power relation.) Overall, the agreement between an ab initio two-dimensional calculation, two-dimensional cascade tests, and full-stage tests is quite close.

Near the stagnation point, the cascade results are higher than those for the rotor. This may be simply due to the larger chordwise extent of the MIT heat flux gages (5 percent of axial chord compared to the Oxford gages' 2 percent) averaging the stagnation peak down. Also, the level here will be quite sensitive to the actual gage placement and stagnation point position relative to the nose of the blade. Along the pressure surface, the Reynolds number corrected cascade data closely agree with the rotor data and calculations for the first 2/3 of the chord with the cascade data 10–15 percent higher near the trailing edge. Similarly, the suction surface measurements agree over the first 2/3 of the blade but the cascade data are 50 percent higher near the trailing edge. It is near the trailing edge that we might expect the non-two-dimensional effects to be the most pronounced (although the calculation is two-dimensional and agrees with the rotor measurements). Note that the rotor, cascade, and calculation all show the dip near the suction surface trailing edge due to expansion wave impingement.

The rotor data, calculation, and cascade data are replotted

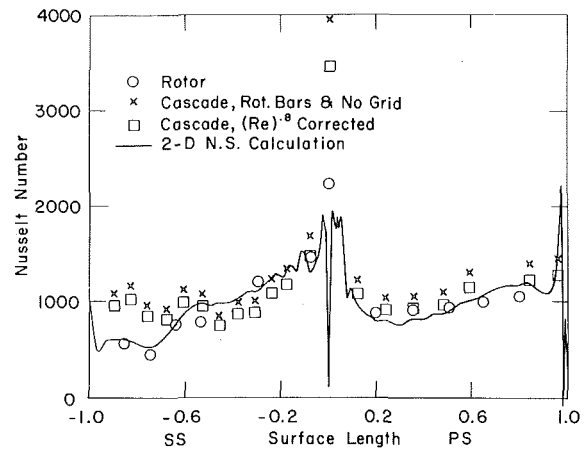


Fig. 7 Comparison of time-averaged heat flux (a) calculated with two-dimensional Navier-Stokes code, (b) measured on a turbine rotor, (c) measured on the same profile in a two-dimensional cascade with bar passing and low turbulence (Ashworth et al., 1985), and (d) the cascade measurements corrected for Reynolds number variation

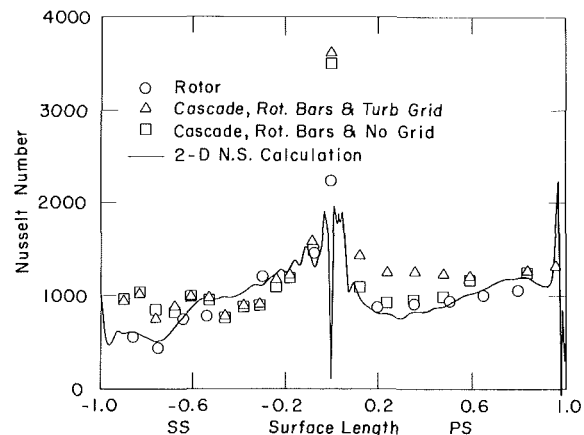


Fig. 8 Comparison of time-averaged heat flux calculated with two-dimensional Navier-Stokes code, measured on a turbine rotor, and measured on a cascade with bar passing at two free-stream turbulence levels—no grid (0.8 percent) and turb grid (4 percent). The cascade data have been corrected to the same Reynolds number as the rotor measurements.

in Fig. 8 with bar passing data from the same cascade but at higher (4 percent) free-stream turbulence (Ashworth et al., 1985, Fig. 10a). Both sets of cascade data have been Reynolds number corrected. There is little difference on the suction surface, but the initial region of the pressure surface has 30 percent higher heat transfer with higher turbulence. This will be discussed later.

Time-Resolved Measurements

Time-resolved measurements of the Nusselt number distribution measured about the rotor profile are shown in Fig. 9. These are ensemble averages of 360 consecutive blade passings. (Thus, all blade passages appear as identical in the figures.) The time jitter in the averaging is less than 1/28 of blade passing. A comparison of the ensemble-averaged and instantaneous temperatures measured by the top sensors at two heat flux gage locations on the suction surface is shown in Fig. 10 (gage 7 at $x/s = 0.10$ and gage 9 at $x/s = 0.31$, where s is surface length). The small fluctuations (0.2 deg) are a combination of slip ring noise, electrical noise, and flow fluctuation. These are effectively filtered by the ensemble technique. Since this procedure can also obliterate aperiodic data, the "raw" temperature traces were examined in detail before generating any conclusions about the averages. For the most part, little

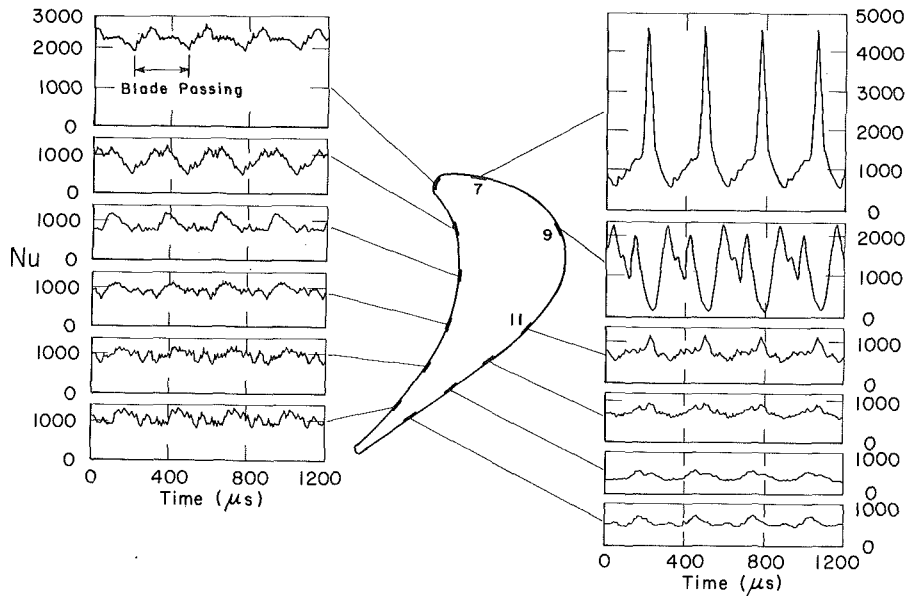


Fig. 9 Ensemble average of time-resolved heat flux measurements about the rotor blade midspan

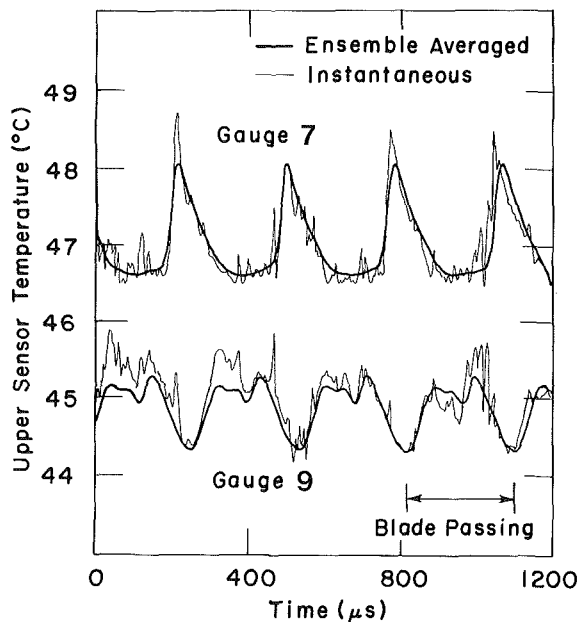


Fig. 10 Comparison of measured instantaneous and ensemble-averaged wall temperature at two suction surface locations

was lost in the ensemble procedure implying that the flow is quite periodic with blade passing and that the tunnel operating conditions are stable.

With reference to Fig. 9, the heat flux at the nose of the blade shows about 20 percent modulation at blade passing frequency. A broad, coherent disturbance can be seen propagating down the pressure surface of the blade, suggestive of wake convection down the passage. There is no evidence of a sharp rise characteristic of a shock wave interaction. This is to be expected in this geometry since the leading edge of the blade shadows the pressure surface from the NGV trailing edge shock wave (see Fig. 2 of Doorly and Oldfield, 1985 for example).

The time-resolved heat flux measured on the suction surface shows very large blade passing modulation ranging from 70–90 percent near the leading edge to 30–40 percent at the trailing edge. As on the pressure surface, the time histories are quite similar to those reported from bar passing in cascade ex-

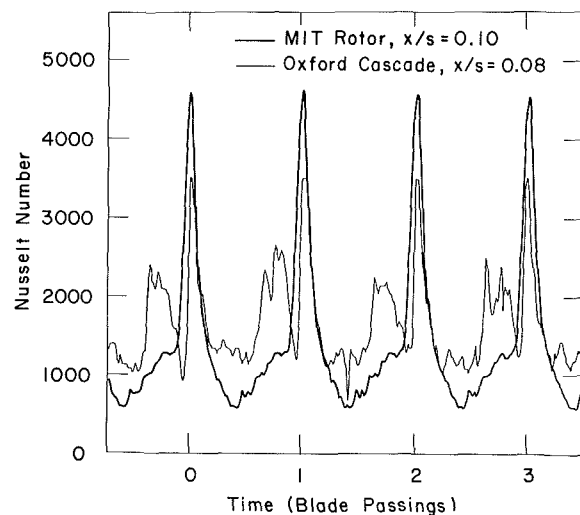


Fig. 11 Comparison on suction surface of MIT rotor measurement ($0.08 \leq x/s \leq 0.12$) with that from two-dimensional bar passing cascade test ($x/x = 0.08$) at 4 percent free-stream turbulence (Ashworth et al., 1985, Fig. 15)

periments previously referenced. In particular, the rotor data would seem to fit quite well the model from Doorly and Oldfield (1985) in which the shock wave from the NGV (in this case) trailing edge impinges near the crown of the suction surface (between gages 9 and 11), generating a shock-induced, transient separation, which causes the very low heat transfer level (the down spikes on gage 9). The shock wave then sweeps forward toward the leading edge, inducing the very large up spike evident at $x/s=0.1$ (gage 7). The disturbance is convected down the suction surface, resulting in a fluctuation of 40 percent of the mean level at the trailing edge.

Time-resolved rotor data on the suction surface are replotted with two-dimensional bar passage cascade data at 4 percent turbulence in Fig. 11 (rotor $0.08 \leq x/s \leq 0.12$, cascade $x/s=0.08$, Ashworth et al., 1985, Fig. 15b) and in Fig. 12 at $x/s=0.31$ (Oldfield, 1987). At $x/s=0.08$ (Fig. 11), distinct “wake” and “shock” spikes are evident in the cascade but not in the rotor, where only the larger “shock” (presumably) spike can be seen. This may be consistent with the observation in the cascade that the magnitude of the wake disturbance

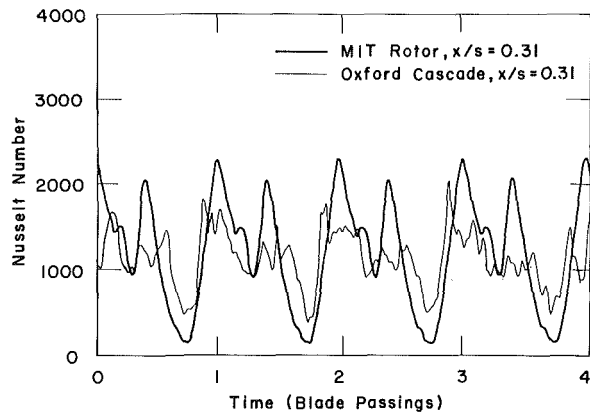


Fig. 12 Comparison at $x/s=0.31$ on suction surface of MIT rotor measurements and two-dimensional bar passing cascade test at 4 percent free-stream turbulence

decreases with decreasing freestream turbulence. At $x/s=0.31$ (Fig. 12), the rotor shows a pronounced double spike, which the cascade does not. (Work in progress on a time-accurate multiblade row calculation leads us to suspect that one peak results from the direct impingement of the NGV shock on the blade while the second results from a secondary reflection of the shock back from the NGV.) It is interesting to note that, at both locations, the degree of modulation is considerably (30–40 percent) larger for the rotor than for the cascade, even though the rotor data presented are a 360-blade average and therefore presumably softened. The implication is that the unsteady interactions are stronger on the rotor than in the two-dimensional cascade, although similar in nature.

Discussion

Overall, both the mean level of heat transfer and the detailed time histories in a fully scaled turbine stage (i.e., rotating, three-dimensional) and in a two-dimensional cascade with bar passing are remarkably similar. We infer from this that (with uniform flow at the stage inlet) the heat transfer processes at midspan on this transonic rotor are largely two-dimensional. The time-resolved measurements in particular indicate that the bar passing technique can accurately model the unsteady heat transfer processes in a high-speed turbine rotor and is thus a powerful tool for research in this area.

It is important to note that there is not complete agreement between the mean levels measured in the rotating rig and two-dimensional cascade. Along the pressure surface, the time-averaged heat transfer in the rotating rig test with a very low level of turbulence inlet to the NGV are quite similar to those in the two-dimensional cascade with low levels of turbulence. However, the rotor data do not clearly show the abrupt rise in heat transfer at the midblade position seen in the low-turbulence cascade data, which is suggestive of transition. Thus, we find it difficult to infer much about pressure side transition from comparison among the three data sets in Fig. 8. The data do suggest that blade row interactions (NGV shock motion due to potential interactions, vortex shedding, etc.) are not necessarily inherent sources of high levels of velocity fluctuations (turbulence). We do not at this time offer an explanation for the differences near the suction surface trailing edge.

The agreement between the time-averaged measurements and the fully turbulent calculation should not be construed as implying that a rotor is always turbulent (the converse can clearly be seen in the time-resolved data). Rather, it indicates that ab initio Reynolds-averaged Navier–Stokes calculations can give quite reasonable results (while the difficulties at the leading and trailing edge imply that work remains to be done

in this area). Prediction of the effective transition point certainly remains a principal concern. It is important to note that the measurements along the beginning of the suction surface show very high levels of modulation (90 percent) while agreeing in the mean with a fully turbulent prediction. This implies that much of the heat flux is at levels greater than that for a turbulent boundary layer. In fact, the peak heat transfer rates near the suction surface leading edge (gage 7) are three times the turbulent mean level. Thus, the heat transfer processes in this region (and their control) may continue to be an active research area, even if the influence on the integrated heat transfer is small.

The data reported herein may be of most interest for what they do not show. No large discrepancy is apparent between two-dimensional cascade data, two-dimensional predictions, and the fully rotating environment, especially on the pressure surface. Thus, the significant difference between cascade data and engine experience may not be simply explained in terms of blade row interactions and three-dimensional effects. The only phenomena identified as not being accurately modeled in the current experiment are the very high levels of turbulent intensity (both velocity and temperature) characteristic of engine turbine inlet (combustor exit) flows and the large temperature and pressure profiles (both radial and circumferential) at the turbine inlet common to full scale engines. The radial temperature profile looks particularly interesting in this respect (Butler et al., 1986).

Conclusions

The primary conclusions of this study of midspan heat transfer in a transonic turbine stage with uniform inflow are the following:

- 1 Mean heat transfer levels with rotation are generally well predicted by two-dimensional cascade bar passing tests, excepting the last part of the suction surface where the rotor results are 40 percent lower.
- 2 The heat transfer levels on the rotor are consistent with cascade measurements with low levels of inlet turbulence.
- 3 The time unsteady heat transfer histories are similar in both the rotating stage and two-dimensional bar passing cascade tests.
- 4 A two-dimensional Navier–Stokes prediction does a creditable job in predicting mean rotor heat transfer levels.
- 5 Rotating, three-dimensional, and blade row interactions do not in themselves explain the difference between cascade results and full-scale engine heat transfer levels.

Further work in this area is certainly suggested. Heat transfer in the regions near the endwalls (hub and tip) where two-dimensional results would not be expected to apply and the effects of nonuniformities at the turbine inlet are particularly of interest.

Acknowledgments

The authors would like to thank Dr. M. L. G. Oldfield and M. Rigby for providing copies of the Oxford data. This work was supported by Rolls-Royce Inc. and the Office of Naval Research, Dr. Richard Miller, technical monitor.

References

- Ashworth, D. A., LaGraff, J. E., Schultz, D. L., and Grindrod, K. J., 1985, "Unsteady Aerodynamic and Heat Transfer Processes in a Transonic Turbine Stage," *ASME Journal of Engineering for Gas Turbines and Power*, Vol. 107, pp. 1022–1030.

Butler, T. L., Sharma, O. P., Joslyn, H. D., and Dring, R. P., 1986, "Redistribution of an Inlet Temperature Distortion in an Axial Flow Turbine Stage," AIAA Paper No. 86-1468.

Cebeci, T., 1970, "Calculation of Compressible Turbulent Boundary Layers With Heat and Mass Transfer," AIAA Paper No. 70-741.

Doorly, D. J., and Oldfield, M. L. G., 1985, "Simulation of the Effects of Shock Wave Passing on a Turbine Rotor Blade," ASME *Journal of Engineering for Gas Turbines and Power*, Vol. 107, pp. 998-1006.

Dunn, M. G., Martin, H. L., and Stanek, M. J., 1986, "Heat-Flux and Pressure Measurements and Comparison With Prediction for a Low-Aspect-Ratio Turbine Stage," ASME *JOURNAL OF TURBOMACHINERY*, Vol. 108, pp. 108-115.

Epstein, A. H., Guenette, G. R., and Norton, R. J. G., 1984, "The MIT Blowdown Turbine Facility," ASME Paper No. 84-GT-116.

Epstein, A. H., Guenette, G. R., Norton, R. J. G., and Yuzhang, C., 1986,

"High Frequency Response Heat Flux Gauge," *Review of Scientific Instruments*, Vol. 57, No. 4, pp. 639-649.

Jameson, A., Schmidt, W., and Turkel, E., 1981, "Numerical Solutions of the Euler Equations by Finite Volume Methods Using Runge-Kutta Time-Stepping Schemes," AIAA Paper No. 81-1259.

Norton, R. J. G., Thompkins, W. T., Jr., and Haimes, R., 1984, "Implicit Finite Difference Schemes With Non-simply Connected Grids—A Novel Approach," AIAA Paper No. 84-0003.

Oldfield, M. L. G., 1987, Private Communication.

Schultz, D. L., 1977, "A New Transient Cascade Facility for the Measurement of Heat Transfer Rates," AGARD CP-227.

Swanson, R. C., and Turkel, E., 1985, "A Multistage Time-Stepping Scheme for the Navier-Stokes Equations," AIAA Paper No. 85-0035.

Turner, E. R., Wilson, M. D., Hylton, L. D., and Kaufman, R. M., 1985, "Turbine Vane External Heat Transfer," NASA CR-174827.

M. G. Dunn

P. J. Seymour

Calspan Advanced Technology Center,
Buffalo, NY 14225

S. H. Woodward

W. K. George

State University of New York at Buffalo,
Buffalo, NY 14225

R. E. Chupp

Teledyne CAE
Toledo, OH 43612

Phase-Resolved Heat-Flux Measurements on the Blade of a Full-Scale Rotating Turbine

This paper presents detailed phase-resolved heat-flux data obtained on the blade of a Teledyne 702 HP full-stage rotating turbine. A shock tube is used as a short-duration source of heated air and platinum thin-film gages are used to obtain the heat-flux measurements. Results are presented along the midspan at several locations on the blade suction and pressure surfaces from the stagnation point to near the trailing edge. For these measurements, the turbine was operating at the design flow function and at 100 percent corrected speed. Results are presented for the design vane/blade spacing ($0.19 C_s$) and at a wide spacing ($0.50 C_s$). Data are also presented illustrating the phase-resolved blade heat-flux distribution with upstream cold gas injection from discrete holes on the vane surface. The results illustrate that several successive passages can be superimposed upon each other and that a heat-flux pattern can be determined within the passage. A Fourier analysis of the heat-flux record reveals contributions from the fundamental and first harmonic of the passage cutting frequency. Time-resolved surface pressure data obtained on the blade pressure surface are compared with heat-flux data.

1 Introduction

Turbomachinery flow fields are inherently unsteady because of the disturbances generated when rotating blades transit nozzle vane wakes and exit passages. Years of experience has illustrated that these flows can be considered to be quasi-steady and satisfactory flow field predictions can be performed. However, the state of the art has progressed to the point where relevant unsteady calculations can now be performed and supporting measurements of the unsteady flow field can be made. Significant current research is directed at determining the influence of flow-field unsteadiness on the blade heat-flux and surface-pressure distributions, on the inner blade-row gas-dynamic parameters, on the state of the blade and vane surface boundary layers, and on the stage efficiency. The results reported in this paper will emphasize phase-resolved¹ heat-flux data on the rotating blade and will demonstrate the influence of vane/blade spacing and cold gas injection on these phase-resolved data. Limited time-resolved surface pressure data obtained on the rotating blade will also be presented.

¹The term "phase" is used here to denote the pitchwise angular displacement of a given rotor blade with respect to the stator vanes. It varies across each stator passage, in a sawtooth fashion, between the limits zero and $360 \text{ deg}/B$, where B is the number of stators. The term "phase resolved" denotes time-resolved data that are presented as a function of phase, rather than as a function of time. The term "phase averaged" denotes an ensemble average in which phase-resolved data at a given phase, over a succession of stator passages, are taken to be different realizations of the same event. This averaging is referred to by Adamczyk (1985) as passage-to-passage averaging.

Contributed by the International Gas Turbine Institute and presented at the 33rd International Gas Turbine and Aeroengine Congress and Exhibition, Amsterdam, The Netherlands, June 5-9, 1988. Manuscript received by the International Gas Turbine Institute June 1987. Paper No. 88-GT-173.

Papers relevant to unsteady flow fields in turbomachinery have been present in the literature for at least the past 35 years. Early work by Kemp and Sears (1953, 1955) provided the ground work for much of the research that was to follow. Subsequently, Giesing (1968), Parker (1969), and Kerrebrock and Mikolajczak (1970) made valuable contributions to the understanding of these problems. More recently, Dring et al. (1980, 1981, 1982) have used a large-scale rotating axial turbine stage to obtain valuable experimental data on the nature of the unsteady flow field. Also, Hodson (1984, 1985a, 1985b) has used several different facilities to study wake-generated unsteadiness in vane exit passages and to perform measurements of boundary-layer transition and flow separation. Detailed measurements of the unsteadiness in the rotor incoming flow are presented in Hodson (1985b) that illustrate the change in incidence angle and the change in turbulence associated with the vane wakes.

Another extensive research program concerned with unsteady flow fields was reported by Gorton and Lakshminarayana (1976). They reported the results of several programs designed to measure the boundary-layer and turbulence characteristics inside turbomachinery rotor passages using a large-scale, slowly rotating rig as the test device. Binder et al. (1985, 1987) reported the results of laser velocimeter measurements in the unsteady rotor flow field. These authors demonstrate very high turbulence levels associated with the vane wakes. Sharma et al. (1985) presented the results of an extensive study conducted to obtain low-speed rig data on the unsteady flow environment associated with axial flow turbines. Doorly and Oldfield (1985) used a piston-driven tunnel and a system of rotating bars to simulate

the effects of shock waves and wakes shed from a nozzle on the blade. The Schlieren photographs presented by Doorly and Oldfield (1985) are helpful in interpreting the results presented herein because they illustrate the rather extensive nature of the vane wake, and the manner in which these wakes interact with the blade.

The purpose of this paper is to present a detailed set of phase-resolved heat-flux data obtained on the blade of the Teledyne CAE full-stage rotating turbine. For several blade locations, the predicted heat-flux values are compared here to the measured phase-dependent heat flux. Two previous papers by Dunn and Chupp (1987, 1988) have described in detail the steady-state gas-dynamic parameters and Stanton number distributions for this turbine. In Dunn and Chupp (1988), the distribution of nozzle inlet and rotor exit total pressure and total temperature, the stage static pressures, the turbine operating conditions, the steady-state vane and blade Stanton number distributions, and comparisons of these distributions with various prediction techniques were all presented. In Dunn and Chupp (1987), the influence of vane/blade spacing on the steady-state vane and blade Stanton number distributions at two different spacings ($0.19 C_s$ and $0.50 C_s$), with and without discrete hole injection, was presented. While the measurements noted above were being performed, the time-resolved (or phase-resolved) data reported in this paper were also being obtained. Two earlier papers (Dunn et al., 1986; George et al., 1987) provide a description of the analysis techniques that were previously developed at the Calspan-UB Research Center to obtain instantaneous heat-flux values from the thin-film gages at a sampling frequency consistent with the requirements of this experiment. Several changes have been made to the electronics of the data recording system since the experimental data reported by Dunn et al. (1986) were taken. These changes were incorporated into the data collection system used for this work and they will be described later in this paper. Previous papers by Dunn et al. (1986), Dunn and Hause (1982), Dunn et al. (1984a), and Dunn (1986) have described time-resolved rotor shroud pressure and time-resolved blade heat-flux measurements for a different turbine, the Garrett TFE 731-2 HP.

2 Experimental Apparatus

The experimental apparatus used in this work has previously been described in depth and will not be repeated here. Only those portions of the apparatus important to the clarity of this paper will be included.

The high-pressure turbine stage was taken from a Teledyne J402-CA-702 turbojet engine. The turbine stage of this engine is a highly loaded, moderately high reaction, state-of-the-art design with an aspect ratio near unity. The corrected speed is 19,510 rpm, the corrected weight flow is 3.92 lb/s, and the overall total-to-total pressure ratio is 3.62. There are 23 nozzle guide vanes, which are convectively cooled and have pressure-side and suction-side discrete hole injection. The injection on each side is from a single spanwise row of circular cooling holes. The turbine has 35 uncooled blades, which are highly tapered, highly cambered, and have elliptical leading edges. The model constructed to house the turbine stage was designed so that the vane/blade spacing could be either $0.19 C_s$ (close spacing) or $0.50 C_s$ (wide spacing). The spacing was increased by moving the nozzle forward and inserting a spacer to provide the proper air seal between the vane exit and the rotor entrance.

The thin-film gage instrumentation used to perform the measurements described here consisted of contoured leading-edge inserts and flush-mounted button-type gages. The instrumentation was concentrated on the blade meanline but a few measurements were obtained at other selected locations as described in Dunn and Chupp (1988). Heat-flux

measurements were obtained for 21 locations on the vane and for 45 locations on the blade.

Figure 1 is a photograph of one of two blade-leading-edge inserts. Each insert had 12 gages, with the distribution of gages selected so that one insert provided a close spacing on one surface (on the order of 1 mm or 0.040 in.) and a wider spacing on the other surface. The second insert has a close gage spacing on the side for which the first insert had a wide spacing. Each of these inserts was contoured to the blade leading-edge profile prior to painting the thin-film gages. The particular insert shown in Fig. 1 contains one gage at the geometric stagnation point, eight gages on the suction surface, and three on the pressure surface.

For the rotor speeds used here (27,000 rpm), a blade traverses a vane passage in $97 \mu\text{s}$, which corresponds to a wake-cutting frequency of approximately 10 kHz. However, in order to sample these data properly as described in Dunn et al. (1986), the overall system frequency response must be substantially greater than 10 kHz. The frequency response of the system used here was limited by the bandwidth of the gage follower amplifiers and subsequent low pass filters, which for this experiment were set with the -3 dB point at 100 kHz.

The output from the gage amplifiers was directly recorded on two 10-bit transient recorders, a Data Laboratories 2000 series and a Physical Data 515A. Both of these were eight-channel units with a storage capability of 4K words/channel and could be sampled at a frequency in the 200 kHz to 2 MHz range. The sampling on these devices was controlled by means of a shaft encoder installed on the rotor assembly providing 720 pulses per revolution and one pulse per revolution. At the time of model assembly, the leading edge of one of the inserts was carefully aligned with the trailing edge of a known vane, as will be described in Section 5.1. The shaft encoder was then adjusted so that the one pulse per revolution always occurred at this alignment point. The vane passages are then 15.65 deg or 31.3 pulses apart. The output signal from the shaft encoder was used as an input to the recording equipment in order to sample the blade data at the same angular location within the passage from one revolution to the next, thus phase resolving the data. This technique resulted in an average sampling frequency on the order of 315 kHz, a value well above twice the highest frequency as required by the Nyquist criterion. The recorder used to store these data had capacity for 4000 words/channel. Therefore, it was possible to record two and

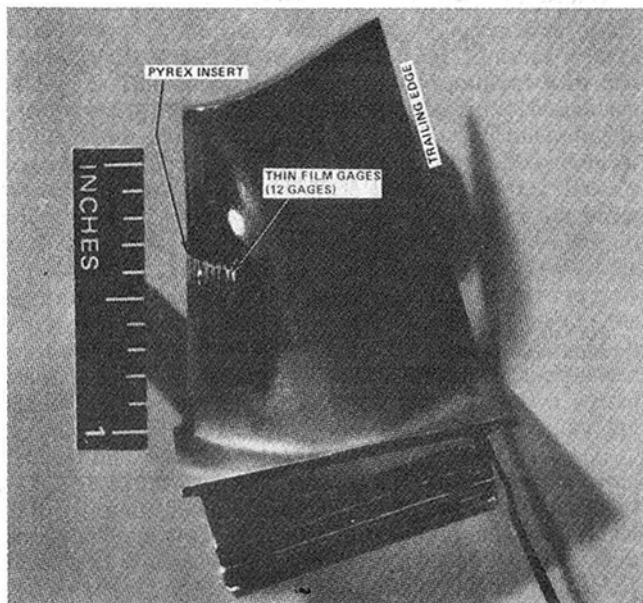


Fig. 1 Photograph of blade suction surface leading edge insert

one half to three rotor revolutions during the test-time duration. One channel of the recorder was used to record a 10 kHz timing pulse in the form of a ramp signal in order to derive the arrival time of each encoder pulse. The absolute time and angular location of each sample is then known.

Dunn et al. (1986) noted that some of the features of the data could not be readily explained by the analysis and that electronic noise combined with frequency splitting due to sampling the slightly accelerating turbine data at constant time intervals made it difficult to recognize the character of the passage heat flux easily. Therefore, prior to obtaining the results reported here, the electronic system and the amplifiers used in the thin-film gage temperature recording circuits were redesigned and rebuilt. These amplifiers were constructed to provide capability of wide band (200 kHz), low noise (less than 3 bits out of 1024 bits), single gain data recording and were powered by d-c voltage (batteries). Great care was taken in providing electrical shielding and adequate grounding for all of the equipment. Where possible, batteries were used as the power supply for the electronic equipment. The noise level on each individual heat-flux gage channel was measured through the entire recording system (including the slip ring) with the turbine rotating. For all channels, the prerun system noise measured at the recording device just prior to recording the data (with the turbine at full speed) was less than 5 bits out of 1024 bits. Throughout the measurement program, an attempt was made to use as large a portion of the 1024 bits as possible for data recording. Figure 2 is a schematic of the data recording system used in this work. For the data presented here, the number of bits utilized on any given channel ranged from 600 to 1000. In several cases, the data range for a particular channel was from 10 to 1000 bits.

3 Data Processing

The technique for recording the unsteady heat-flux values from the phase-sampled gage temperature data was shown schematically in Fig. 2. The digital surface temperature data were converted to unsteady heat flux by utilizing the simple implicit code described by Dunn et al. (1986). No attempt was made to correct the heat-flux data presented here for variable substrate thermal properties. For the purposes of this paper, this correction is estimated to be generally less than 10 percent. The algorithm and a detailed analysis of the simple implicit procedure are presented by George et al. (1987). Briefly, it was concluded that the effective frequency response of the simple

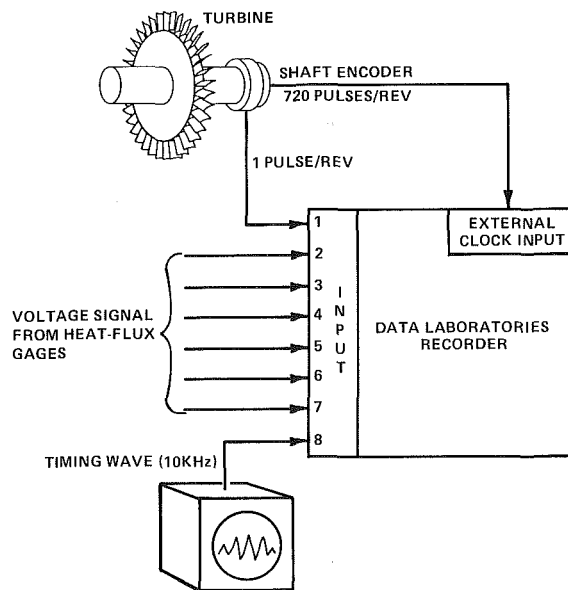


Fig. 2 Schematic of data recording system

implicit code (as determined by the frequency at which the calculated heat flux is 3 dB below the actual value) was one fourth of the rate at which the temperature data were sampled. Thus in the work reported here, the effective bandwidth of the calculated heat flux was approximately 80 kHz, well above the frequency at which quantization and electronic noise would mask the vane-crossing harmonics.

In order further to reduce the effect of the quantization errors and electronic noise on the calculated heat flux, the sampled temperature data were digitally filtered with a simple five-point top-hat filter before utilization in the simple implicit code. This further reduced the effective bandwidth to approximately 65 kHz. This bandwidth was sufficient to capture all of the harmonics present in the original signal as clearly evident from the spectra of the directly recorded data.

4 Experimental Conditions

A table giving the experimental conditions at which the measurements reported here were performed is given in both Dunn and Chupp (1987, 1988) and will not be repeated here. A detailed description of the vane/blade spacing and coolant gas injection parameters was also given. The turbine was operating at nearly the design values of corrected speed, flow function, and total-to-total pressure ratio. The temperature of the injected coolant gas was always 530 R and the total temperature of the free-stream gas was always about 1010 R. The metal surface temperature of the stage components was always nearly equal to 530 R. For this particular turbine, the incoming turbulence intensity was not measured. However, for a comparable experiment, Dunn et al. (1984b) measured the turbulence intensity upstream of the vane row to be about 5 percent. The actual engine values are unknown but estimates in the range of 10 to 20 percent are common.

5 Discussion of Results

A typical thin-film gage temperature history for one revolution at a blade suction-surface location of 14.9 percent wetted distance is given in Fig. 3. For a constant heat-flux input to the gage, the temperature history should have a parabolic shape as illustrated by this figure. The nozzle has 23 vanes, so that for one revolution of the rotor, one observes 23 distinct events, as illustrated in Fig. 3. It can be seen from this thin-film gage temperature history that not all passages produce the identical exit flow. This can be caused by many different factors including turbulence and unsteady flow, as well as the fact that the components used here are actual engine hardware and some manufacturing variation must be expected. Figure 4(a) is the heat-flux history calculated from the temperature history described above using the techniques reported by George et al. (1987). Once again, 23 distinct passages are obvious from the heat-flux history for the single rotor revolution. The experiment is structured so that the rotor completes several revolutions during the useful test time, as has been explained in previous publications. Note that the excursion of the heat flux about an average value is significant, but the heat flux is always positive. Plots for other rotor revolutions within the test time and for different blade locations are similar to those shown here.

Figure 4(b) is an example of the revolution to revolution reproducibility of the heat-flux history. The data shown on this figure were obtained at 10 percent wetted distance on the blade suction surface for the case of close spacing with vane injection (see Fig. 12 for a more detailed description of results obtained at his particular location). Figure 4(b) is presented for one-half revolution so as to illustrate the nature of the flow. Even though the passage-to-passage and revolution-to-revolution details are not reproduced exactly, the overall characteristics of the passage signature are reproduced.

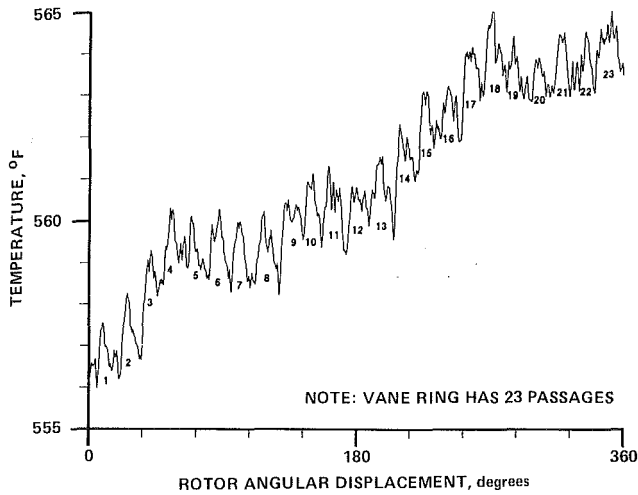


Fig. 3 Thin-film gage temperature history on blade for one revolution of the rotor

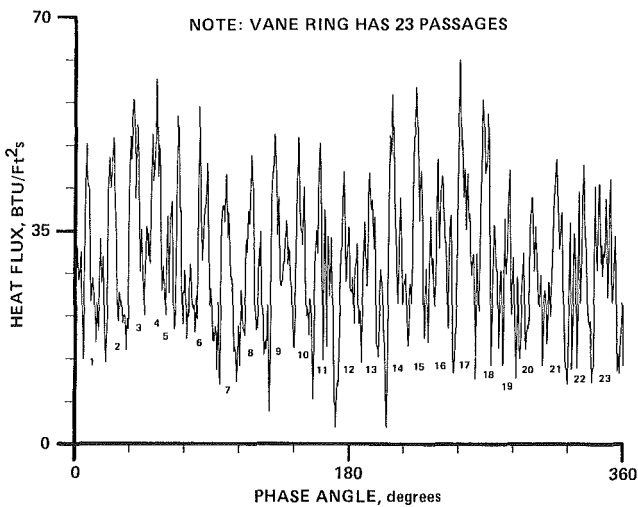


Fig. 4(a) Heat-flux history for one revolution

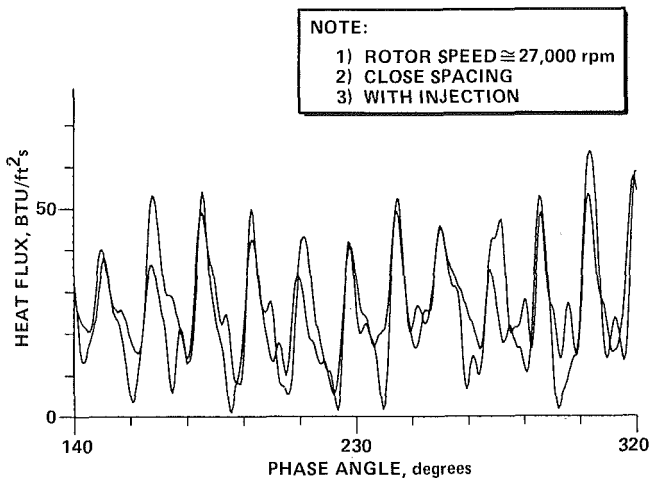


Fig. 4(b) Heat-flux history for two revolutions obtained at 10 percent wetted distance on blade suction surface (see Fig. 12)

Phase-resolved heat-flux data obtained from the instrumented blades will be presented for the cases of: (a) close spacing, no injection, (b) close spacing, with injection, and (c) wide spacing, with injection. An illustration of the time-resolved surface pressure data obtained on the blade pressure surface will also be presented.

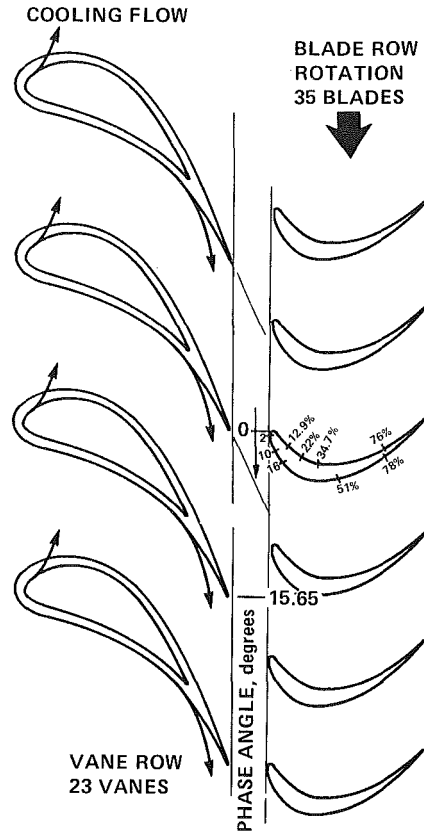


Fig. 5 Sketch of stage and phase angle reference

5.1 Phase-Resolved Heat-Flux Data for Close Spacing in the Absence of Injection. Heat-flux measurements were obtained at several spanwise locations on the blade but the results described herein will be confined to the blade midspan region. As stated previously, the shaft encoder was aligned during model assembly to provide a single pulse each time the blade containing the insert shown to Fig. 1 passed a particular location relative to the vane trailing edge. Thus, by knowing the geometry of the stage, the relative location of the blade with respect to the vane wake can be determined in order to resolve the wake and passage flow. A sketch of the physical arrangement of the vane, blade, and the orientation of the blade at 0 deg and 15.65 deg phase (360 deg/23 vanes) is given in Fig. 5. This alignment procedure is consistent with that used by Dring et al. (1982), thus permitting direct comparison of the results. An extension of the vane mean camber line illustrates that the approximate centerline of the wake would intersect the blade at a phase angle of about 7.6 deg. Exactly where the vane wake is located with respect to the blade phase angle is difficult to predict for this unsteady environment.

It was noted earlier that there are 45 heat-flux gages on the instrumented blades but that space permits discussion of only a few. The specific gages that were utilized to obtain the results presented here were located at the geometric stagnation point, 2.1, 10, 16, 51, and 78 percent wetted distance on the suction surface, and 12.7, 22, 34.7, and 76 percent wetted distance on the pressure surface. These gage locations are denoted on the sketch in Fig. 5.

The heat transfer data presented in this paper will be given in the form of heat-flux (BTU/ft²s) history as a function of phase angle instead of in the form of the nondimensional Stanton or Nusselt number. However, the authors recognize that some may prefer the nondimensional format, so Table 1 is given to provide all of the parameters necessary for the conversion from heat flux to Stanton or Nusselt number.

Table 1 Teledyne 702-HP flow parameters

Vane inlet total temperature	561°K	1010°R
Vane inlet total pressure	6.67×10^2 k Pa	96.8 psia
Vane inlet static pressure	6.60×10^2 k Pa	95.7 psia
Approximate weight flow	8.61 kg/s	19 lb/s
Wall temperature	294°K	530°R
Rotor inlet relative total pressure	3.29×10^2 k Pa	47.8 psia
Rotor inlet relative total temperature	476°K	847°R
Rotor inlet relative velocity	158.6 m/s	520 ft/s

NOTE:

- 1) BLADE ROTATION IS CLOCKWISE LOOKING FROM FRONT
- 2) VANE PASSAGES TRAVERSED 3,6,7,23
- 3) ROTOR SPEED \approx 27,000 rpm
- 4) CLOSE SPACING
- 5) NO INJECTION

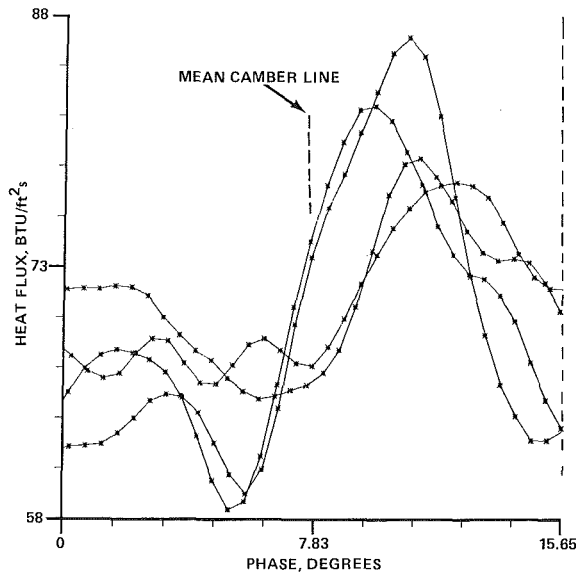


Fig. 6(a) Phase-resolved heat-flux data at geometric stagnation point on blade

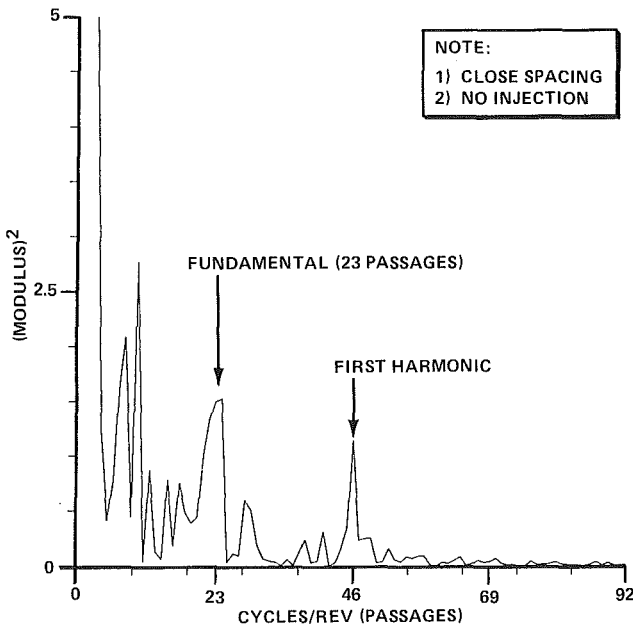


Fig. 6(b) Modulus of Fourier transform of heat-flux data at geometric stagnation point on blade

Figure 6(a) presents the passage phase-resolved heat-flux history for the blade geometric stagnation point. Data from four different passages have been overlaid on this plot to provide an illustration of the passage heat-flux history. As

NOTE:

- 1) BLADE ROTATION IS CLOCKWISE LOOKING FROM FRONT
- 2) VANE PASSAGES TRAVERSED 1, 2, 4, 6, 12
- 3) ROTOR SPEED \approx 27,000 rpm
- 4) CLOSE SPACING
- 5) NO INJECTION

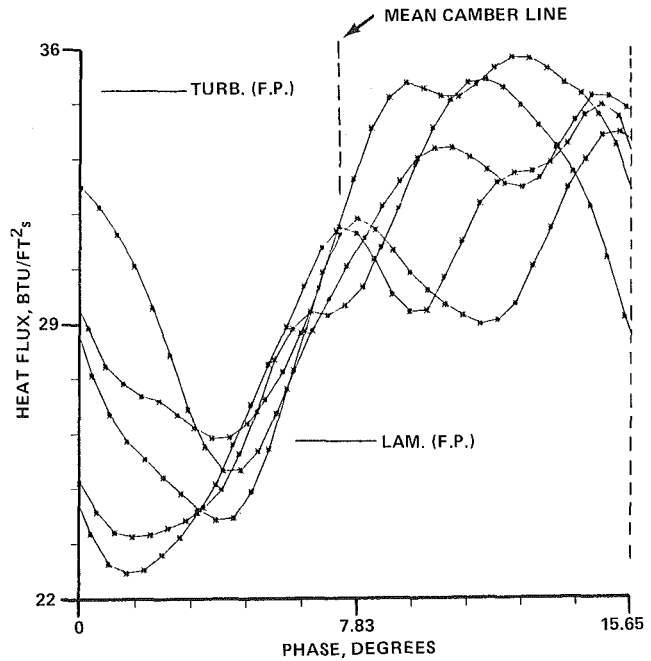


Fig. 7(a) Phase-resolved heat-flux data at 2.07 percent wetted distance on blade suction surface

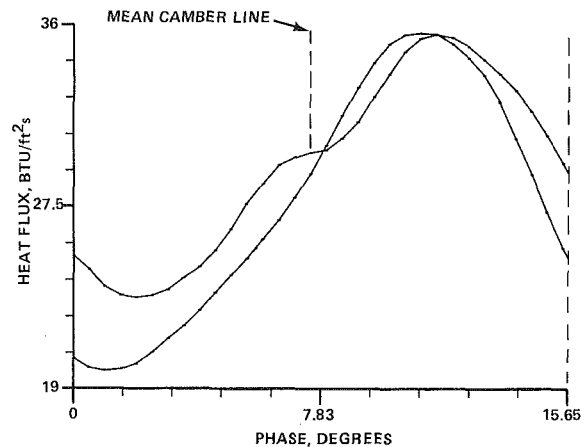


Fig. 7(b) Phase-resolved heat-flux data at 2.07 percent wetted distance on blade suction surface for passage #1 on successive revolutions

previously noted, the passage separation is approximately 15.65 deg, which results in 31.3 data points per passage for an encoder with 720 pulses/rev. The blade is rotating clockwise when viewed from the front at a speed of nearly 27,000 rpm. On all of the plots presented in Fig. 6(a), 7, 8(a), 9(a), 10, 11(a), and 12(a) the phase position 0 deg corresponds to the initial blade/vane alignment illustrated in Fig. 5 and the phase position 15.65 deg corresponds to the arrival of the blade at the next vane. The location of the intersection of the vane mean camber line with the plane of the blade leading edge is noted on Fig. 6(a), 7, 8(a), 12(a), and 13(a). Previous work by Dring et al. (1985) using photographs with smoke in the free-stream flow and the detailed rotating bar measurements of Doorly and Oldfield (1985) have illustrated the nature of the vane trailing edge wake. In addition, there are probably

several interacting vortex flows coming through the passage flow. The extent of these disturbances is not well known for a three-dimensional, compressible turbine flow of the type used here and some definition of their influence on the blade heat-flux distribution is a portion of the intent of this work.

The ordinate on Fig. 6(a) has been expanded to illustrate the variation in heat flux. Note that the scale begins at 58 and goes to 88 Btu/ft²s. The heat-flux level is lowest in the vicinity of 0 deg phase angle, which presumably corresponds to flow outside the vane wake and remains relatively low for the initial 6 deg of the passage and then begins to increase rapidly, reaching a peak in the vicinity of 10.3 deg, and then falls off again. An extension of the vane mean camber line as shown on Fig. 5 would suggest that the blade would intercept this wake

flow at about 7.6 deg. The rapid increase in heat flux near 6 deg is consistent with this interaction. The stagnation-point flow is unsteady as the blade moves from passage to passage. However, the general characteristics of the passage distribution are repeatable showing the peak heat flux occurring in the vicinity of 10 deg and then falling off rapidly. There appears to be a broader region of increased heat flux associated with the flow in the region of the wake location suggesting that the wake region is not a small, well-defined one at this location, consistent with the visual observations of Doorly and Oldfield (1985). This same general pattern will be shown for the initial four locations on the suction surface, but it will change for the pressure surface. Figure 6(b) is the modulus squared of the FFT² of a single record of the stagnation point heat-flux data

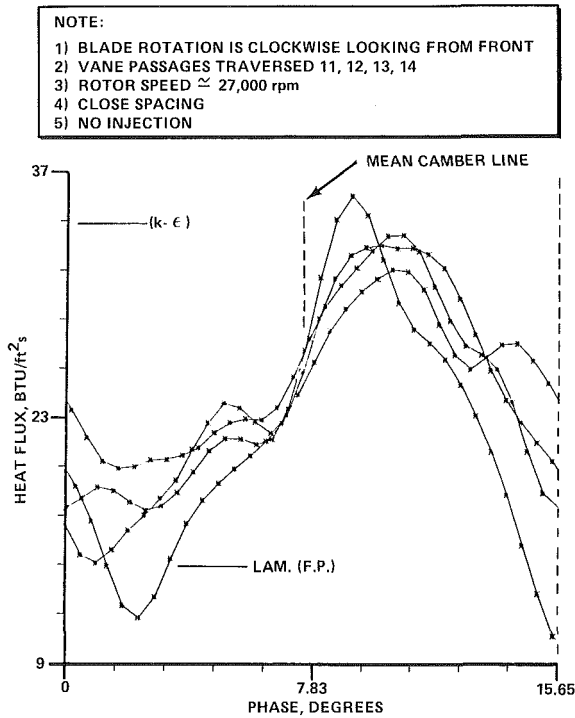


Fig. 8(a) Phase-resolved heat-flux data at 10 percent wetted distance on blade suction surface

²The phrase "modulus of the FFT" is used to refer to the modulus of the Fourier series coefficients obtained by an FFT algorithm. The square of the modulus corresponds to the Fourier line spectrum of the data record.

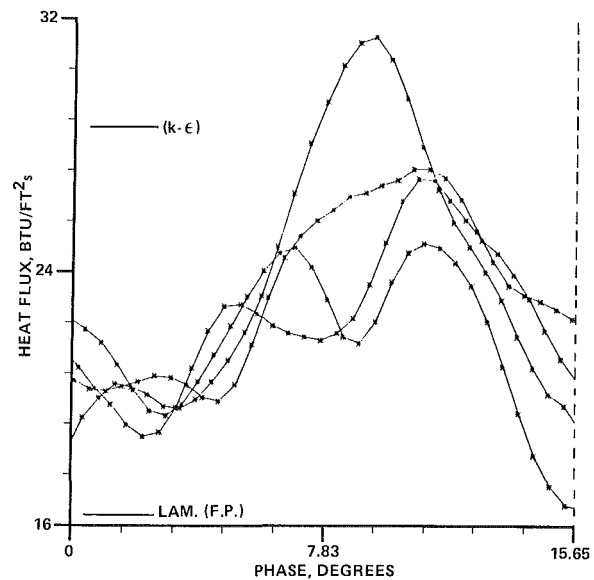


Fig. 9(a) Phase-resolved heat-flux data at 16.1 percent wetted distance on blade suction surface

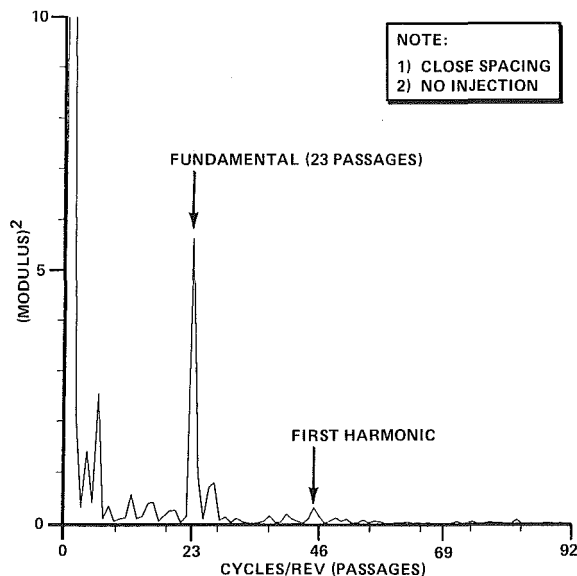


Fig. 8(b) Modulus of Fourier transform of heat-flux data at 10 percent wetted distance on blade suction surface

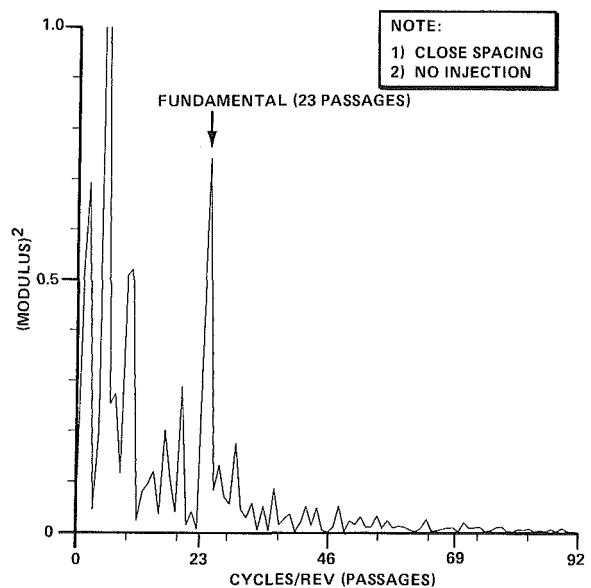


Fig. 9(b) Modulus of Fourier Transform of heat-flux data at 16.1 percent wetted distance on blade suction surface

illustrating a relatively broad peak in the distribution at 23 cycles/rev and the first harmonic at 46 cycles/rev. As noted earlier, there are 23 passages in the nozzle so one would expect to see a significant peak in the modulus at 23 cycles/rev. As discussed in Dunn et al. (1986), the lower frequency peaks are associated with the short-duration nature of the experiment and the unsteady nature of the flow.

Figure 7(a) presents a phase-resolved distribution of heat flux for a location of 2.07 percent wetted distance on the blade suction surface and includes the steady-state predicted heat-flux values taken from Dunn and Chupp (1988) for the flat-plate case. The ordinate on Fig. 7(a) has again been expanded in order to illustrate the heat-flux variation. The general characteristic of the heat-flux history is similar to that seen for the stagnation-point gage. Four of the five passages shown on Fig. 7(a) have a suppressed heat-flux value in that portion of the flow corresponding to the initial 4.6 deg of phase or to the flow that is outside the anticipated vane wake location. At about 5 deg, the heat-flux value increases rapidly reaching a peak in the vicinity of 10 deg as was observed for the stagnation point gage. The fifth passage shown starts out with a heat-flux value at 0 deg that is about 5.5 Btu/ft²s greater than the average of the other four. However, once the blade moves about 5 deg into this passage, the remainder of the profile is very similar. The predicted turbulent flat plate value of heat flux is in reasonable agreement with the peak passage values and the predicted laminar value is in reasonable agreement with the minimum passage values.

It was noted in Section 2 that at the sampling frequency used in this work and because of the necessity to record the early portion of the gage temperature-time history, storage space was available to record two and one half to three rotor revolutions during the useful test time. Figure 7(b) shows the phase-resolved heat-flux history for passage #1 obtained for two successive rotor revolutions. The heat-flux levels for the two revolutions are in very good agreement but there is a displacement of about one degree in phase. Review of the phase-resolved data presented in later figures will indicate that passage-to-passage phase displacements on the order of one degree are not unusual.

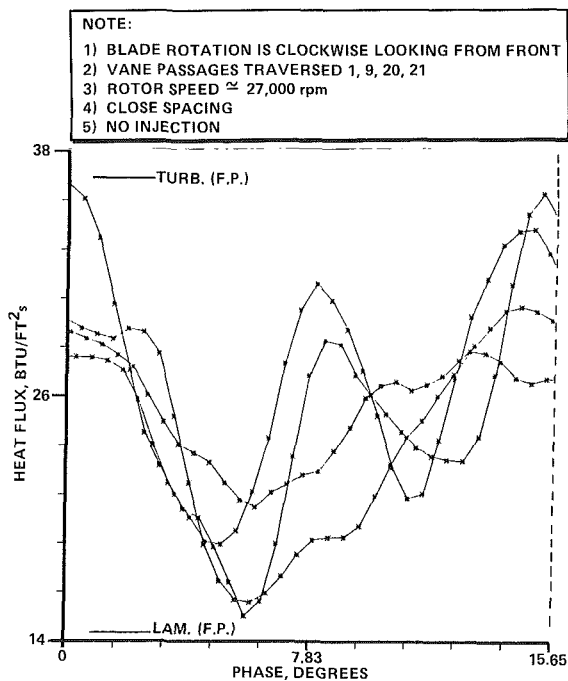


Fig. 10 Phase-resolved heat-flux data at 12.7 percent wetted distance on blade pressure surface

Moving farther along on the suction surface of the blade to 10 percent wetted distance, a heat-flux history very similar to the stagnation-point history was measured and is shown in Fig. 8(a) along with the predicted steady-state heat-flux values. For this comparison, the $k-\epsilon$ and the laminar flat plate values were used because the turbulent flat plate prediction is known to overpredict the blade suction surface heat flux significantly. The general unsteadiness of the flow at this location is somewhat less than that observed at the 2.07 percent location and the profiles nicely overlay. Again, the trend of the results is for the heat flux to be lowest in the region hypothesized to be outside of the wake. The peak heat-flux values occur at a phase angle in the vicinity of 10 deg as noted for the previous locations. Figure 8(b) is the modulus squared

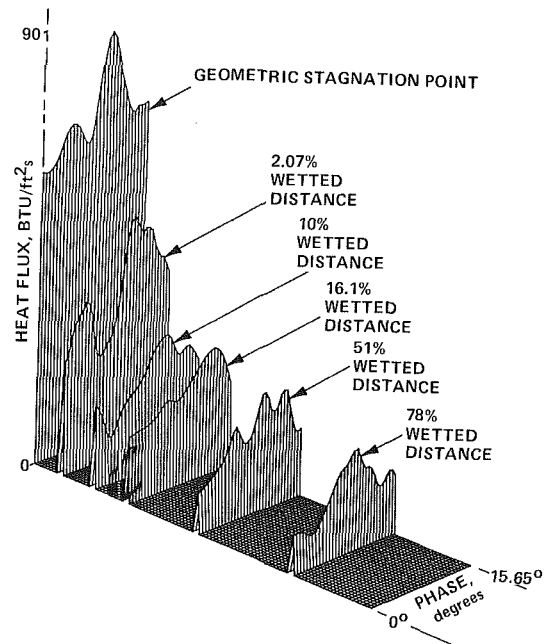


Fig. 11(a) Phase-resolved contour plot of heat-flux distribution on blade suction surface

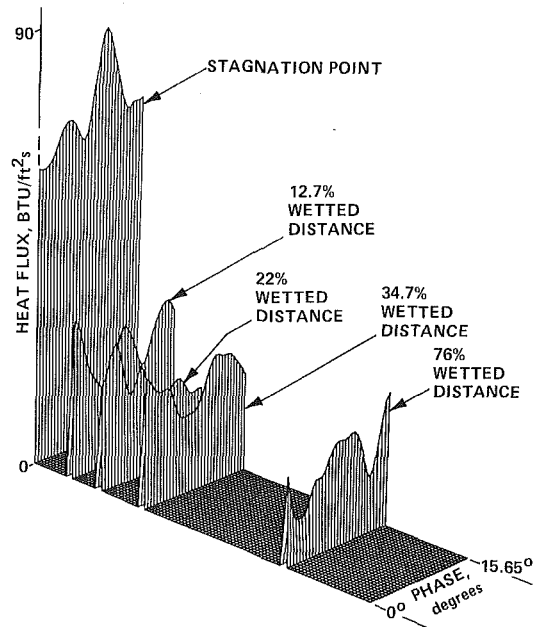


Fig. 11(b) Phase-resolved contour plot of heat-flux distribution on blade pressure surface

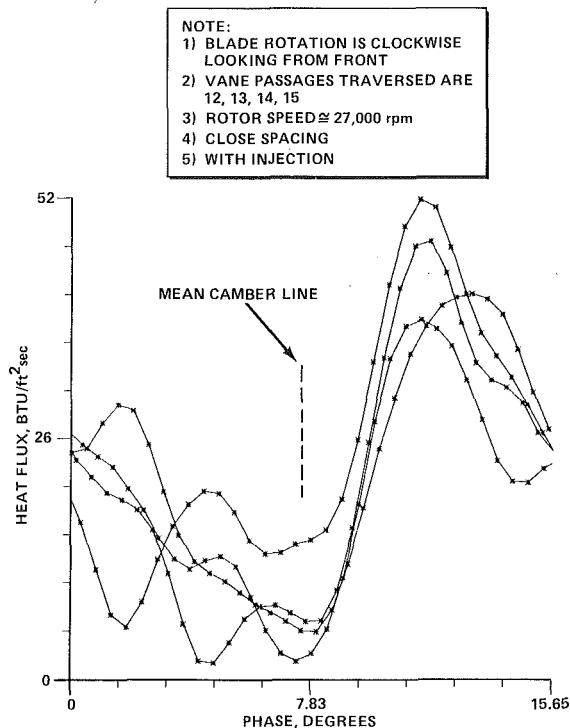


Fig. 12(a) Phase-resolved heat-flux data at 10 percent wetted distance on blade suction surface

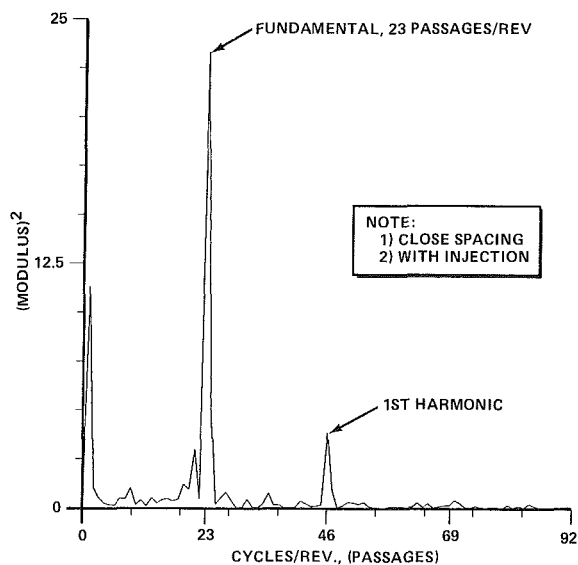


Fig. 12(b) Modulus of Fourier transform of heat-flux data at 10 percent wetted distance on blade suction surface

of the heat-flux data at the 100 percent location and this plot illustrates the strong signal at 23 cycles/rev corresponding to the 23 vanes in the nozzle. The first harmonic is visible, but by this point in the flow its contribution is reduced.

The final location on the suction surface for which detailed results will be presented is at 16.1 percent wetted distance and the phase-resolved heat-flux history is shown in Fig. 9(a). The heat flux starts out low as it did at previous locations, but the increase near 5 deg is more gradual than observed closer to the geometric stagnation point. However, the peak heat-flux value continues to occur in the vicinity of 9 deg. Figure 9(a) also includes the predicted heat-flux values obtained from the $k-\epsilon$ prediction and the laminar flat-plate prediction reported in

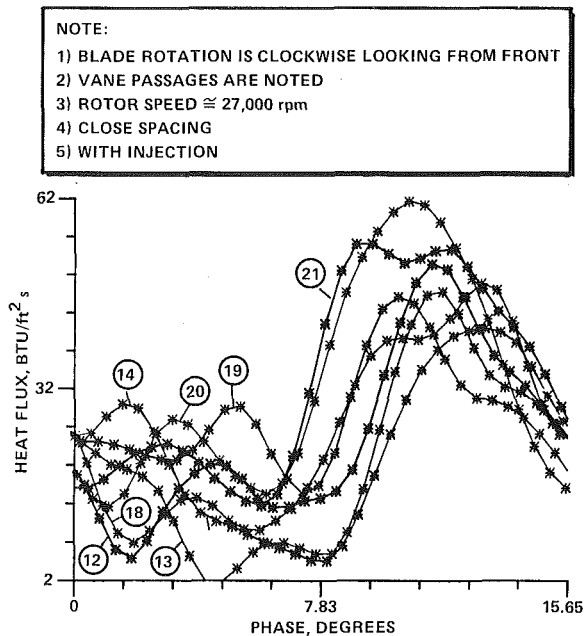


Fig. 12(c) Phase-resolved heat-flux data at 10 percent wetted distance on blade suction surface

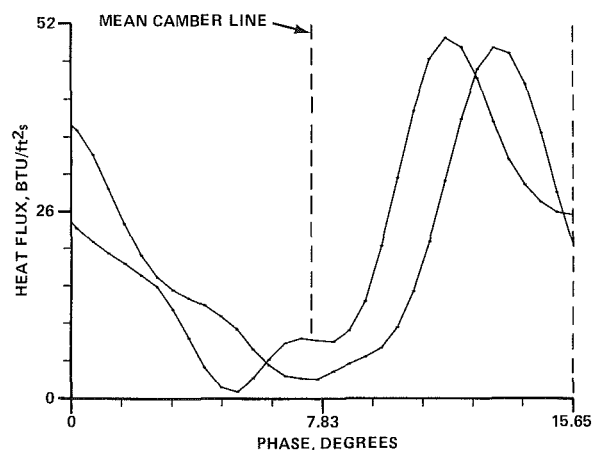


Fig. 12(d) Phase-resolved heat-flux data at 10 percent wetted distance on blade suction surface for passage #13 on successive revolutions

Taulbee et al. (1989). At this particular blade location, the predicted values bound the measured unsteady results. Figure 9(b) is the modulus squared of the phase-resolved data illustrating the fundamental at 23 cycles/rev, but the first harmonic is no longer clearly shown. Its absence is consistent with a wake that is becoming less spatially confined as it moves through the passage.

The results presented in Fig. 6-9 suggest that the gages located between 0 and 16 percent on the suction surface all intercepted the vane wake at about the same relative location and reached the peak heat-flux value at about the same location. This trend is consistent with the observations of Dring et al. (1982, 1985) and Doorly and Oldfield (1985). The thin-film rotor data shown by Dring et al. (1982) illustrate a depressed heat-flux value associated with the passage flow and a much broader and considerably greater heat-flux value associated with the vane wake region. A similar picture was described by Doorly and Oldfield (1985), which also included the complication of a shock wave in the flow. In that regard, it should be noted that the vane exit Mach number for the Teledyne 702 turbine used here was slightly greater than 1.0 but the manner

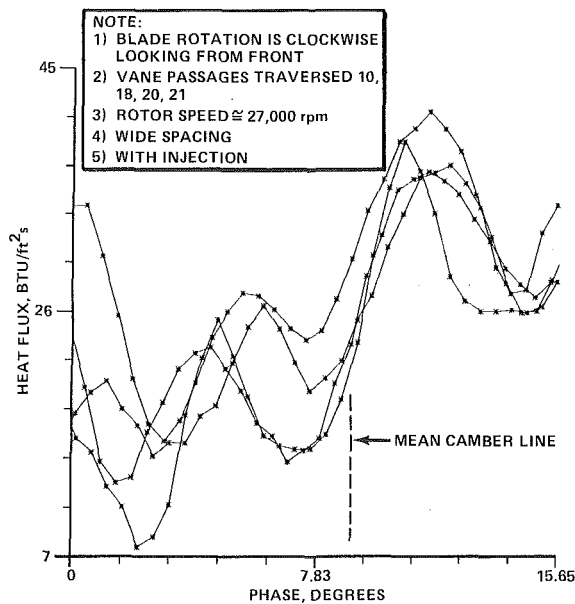


Fig. 13(a) Phase-resolved heat-flux data at 14.9 percent wetted distance on blade suction surface

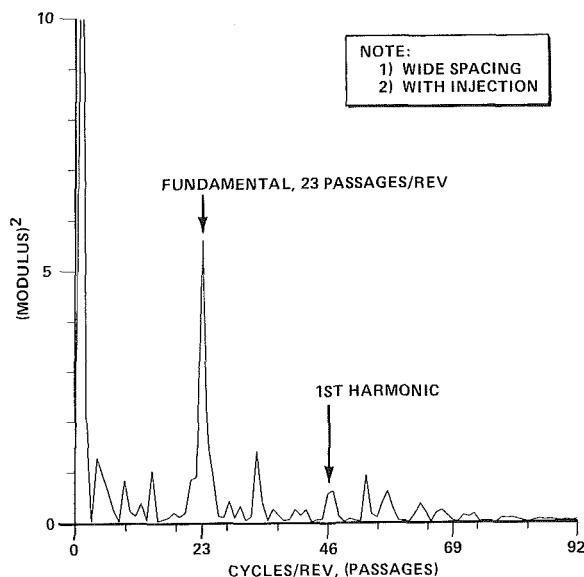


Fig. 13(b) Modulus of Fourier transform of heat-flux data at 14.9 percent wetted distance on blade suction surface

in which potential shock waves interact with the flow field has not been obtained from the data.

The predicted heat-flux values previously reported for this turbine were also noted on Figs. 7-9. Comparison of these predictions with the time-resolved data suggests that the blade boundary layer state was probably fluctuating between laminar and turbulent as the blade interacts with the NGV flow field. This influence of vane rows on the blade boundary layer has previously been described by Evans (1978), Dring et al. (1982), and Doorly and Oldfield (1985).

Figure 10 presents phase-resolved heat-flux data for the blade pressure surface at 12.7 percent wetted distance. All of the gages used to obtain the data reported in Figs. 6(a) to 10 were located on the same blade. The pressure surface heat-flux history for the passage is significantly different from the suction surface histories. The heat-flux value over the initial 2 deg is relatively high, but falls rapidly to a minimum in the vicinity of 5 deg and then peaks again near 8 deg. This peak near 8 deg

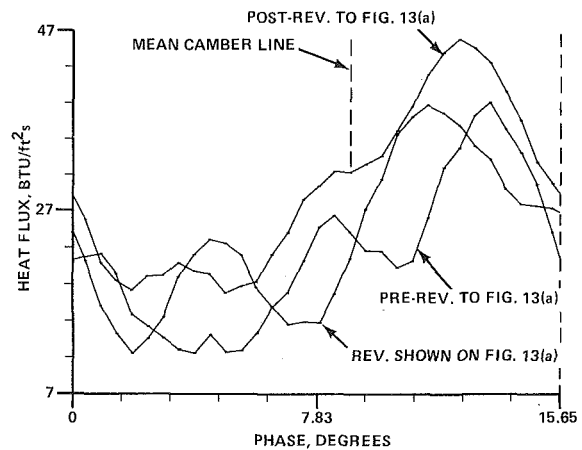


Fig. 13(c) Phase-resolved heat-flux data at 14.9 percent wetted distance on blade suction surface for passage #18 and three successive revolutions

is present on many of the passages but not all of them, as illustrated in Fig. 10, indicating a substantial random component to the flow disturbances at this location.

Contour plots have been constructed from the blade phase-resolved heat-flux distributions. Figure 11(a) presents the blade suction contour plot for the geometric stagnation point, 2.07, 10, 16.1, 51, and 78 percent wetted distance for a given blade passage at a selected time. The blade location relative to the vane trailing edge is again referenced according to Fig. 5. The plot illustrates the magnitude of the phase-varying portion of the heat flux, and shows clearly the high degree of correlation of the disturbances. Also illustrated is the very rapid decrease in heat flux as one moves from the geometric stagnation point to the location at 2.07 percent wetted distance. This rapid decrease can be associated with a broadening of the disturbance, a fact also consistent with the reduction in the first harmonic in the blade crossing rate. Figure 11(b) presents a similar contour plot for the blade pressure surface constructed from measurements performed at the geometric stagnation point, 12.7, 22, 34.7, and 76 percent wetted distance. Once again, the heat flux falls off rapidly between the stagnation point and 12.7 percent wetted distance. Figures 11(a) and 11(b) were constructed from heat-flux data taken from the same rotor revolution on the same test run. Note that the characteristics of the unsteady components for the pressure-surface data are different from the corresponding characteristics on the suction-surface results.

5.2 Phase-Resolved Heat-Flux Data on the Blade With Discrete-Hole Vane Injection.

A description of the influence of discrete hole injection on the blade steady-state Stanton-number distribution and the influence of vane/blade spacing on this distribution was reported by Dunn and Chupp (1987). While obtaining those steady-state data, a limited quantity of phase-resolved data was also obtained. Figure 12(a) presents phase-resolved heat-flux data obtained at 10 percent wetted distance on the blade suction surface at close ($0.19 C_s$) vane/blade spacing with upstream injection. The injection holes were located at 18.4 percent wetted distance on the vane suction surface and at 71.8 percent wetted distance on the pressure surface. Air at a temperature of 530 R was injected at a flow rate of 0.23 lb/s through the suction surface holes and at 0.20 lb/s through the pressure surface holes for a total of 0.43 lb/s. Comparison of Figs. 12(a) and 8(a) suggests that the character of the blade flow in the early portion of the passage (see Fig. 5) has been influenced by the cold gas injection. However, the peak heat-flux value again occurred at that phase angle associated with this wake flow and the standard deviations of the time averaged heat flux with and without in-

jection overlapped. Thus, although the presence of injection resulted in a change in the character of the passage heat-flux history, it did not significantly alter the time-averaged level. Figure 12(b) is the modulus squared of the heat-flux data reported in Fig. 12(a) and this plot clearly shows the fundamental 23 cycles/rev and the first harmonic at 46 cycles/rev. Figure 12(c) has been included to demonstrate the nature of the data if seven passages are overlaid. The particular passages are identified by the numbers in circles. The general characteristic of this plot is consistent with the data obtained at other locations and illustrates that an average phase-resolved heat-flux distribution can be obtained from the data. Figure 12(d) is another example of the passage phase-resolved heat flux for two successive revolutions of the rotor. These particular data were obtained for passage #13 and illustrate reasonable revolution-to-revolution agreement.

A sample of the blade data obtained with cold gas injection for a vane/blade spacing of $0.5 C_s$ at 14.9 percent wetted distance on the suction surface is shown in Fig. 13(a). The details of the time-averaged data for this configuration are given by Dunn and Chupp (1988). Air was the cooling gas, injected at the locations described in the preceding paragraph, and with a flow rate of 0.13 lb/s through the suction surface holes and 0.11 lb/s through the pressure surface holes. The total weight flow of gas injected through the vane for this case was 0.24 lb/s compared to 0.43 lb/s for the data shown in Fig. 12(a). The results shown in Fig. 13(a) suggest that the influence of vane/blade spacing was to diffuse the sharp increase in heat flux previously observed to begin in the vicinity of 5 or 6 deg (see Figs. 8(a), 9(a), and 12(a)). At the wider vane/blade spacing, the heat-flux profile increases from 0 deg more slowly, reaching a peak in the vicinity of 12 deg. These results suggest that the blade intersects the vane wake flow at a larger phase angle as would be expected from the geometry of the configuration. The thin-film gage results reported by Dring et al. (1982) illustrate a similar finding for a gap of $0.65 C_s$. The modulus squared of the blade data are presented in Fig. 13(b) and these results illustrate the fundamental peak at 23 passages/rev. However, because of the diffusing effect of the vane/blade spacing and the greater distance from the stagnation region, the first harmonic is suppressed. The result shown in Fig. 9(b) for 16.1 percent wetted distance and close spacing also illustrated a suppressed first harmonic.

Figure 13(c) presents the phase-resolved heat-flux history for three successive rotor revolutions for a location of 14.9 percent wetted distance on the blade suction surface. The particular passage selected for this presentation was #18. The phase-resolved data are in reasonably good agreement with each other demonstrating the same type of variation in heat-flux and phase angle as demonstrated for the passage-to-passage variation for a particular revolution.

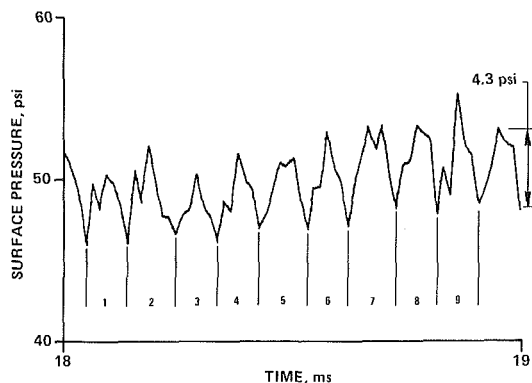


Fig. 14 Blade pressure surface pressure history at 39.3 percent wetted distance

5.3 Time-Resolved Surface Pressure Data on the Blade Pressure Surface. The blade pressure and suction surfaces were instrumented with flush-mounted miniature Kulite pressure transducers. A limited amount of surface pressure data was obtained and a sample of the time-resolved surface pressure history is shown in Fig. 14. The pressure data shown on this figure are for a portion of one revolution (nine passages) obtained from the pressure transducer located at 39.3 percent wetted distance on the blade pressure surface. The pressure data were sampled at a frequency of approximately 70 kHz in constant time intervals. (The one pulse per revolution shaft encoder used to determine the location of the blade relative to the vane trailing edge was not carried on the data system from which the pressure data were obtained.) The steady-state pressure level at this location on the blade surface was approximately 46 psi and the peak-to-peak fluctuation on the time-resolved signal shown on Fig. 14 is on the order of 10 to 15 percent of the time-averaged value. Also it should be noted that the nine passages shown, as defined by the minimum in the pressure data, are not identical in width. This observation is not surprising since the sampling frequency is such that the minimum might have been missed and because the vane is engine hardware and some manufacturing tolerance is to be anticipated. It is planned to obtain significantly more time-resolved and phase-resolved blade pressure data in the near future. These data will be reported as they become available. However, on the basis of the pressure data reported by Dring et al. (1982), and the phase-resolved heat-flux data obtained for this particular blade location in these experiments, the pressure valley is felt to be associated with the vane wake region and the pressure peaks with the passage flow. The magnitude of the fluctuating pressure measured here is of the same order as that reported by Dring et al. (1982).

A heat-flux gage located at 34.7 percent wetted distance on the pressure surface was sufficiently close to the pressure gage location of 39.3 percent to make a meaningful comparison between the general flow characteristics obtained with the two diagnostics. Figure 15 presents the phase resolved heat-flux

NOTE:
 1) BLADE ROTATION IS CLOCKWISE LOOKING FROM FRONT
 2) VANE PASSAGES TRAVERSED 1, 12, 13, 16
 3) ROTOR SPEED $\approx 27,000$ rpm
 4) CLOSE SPACING
 5) NO INJECTION

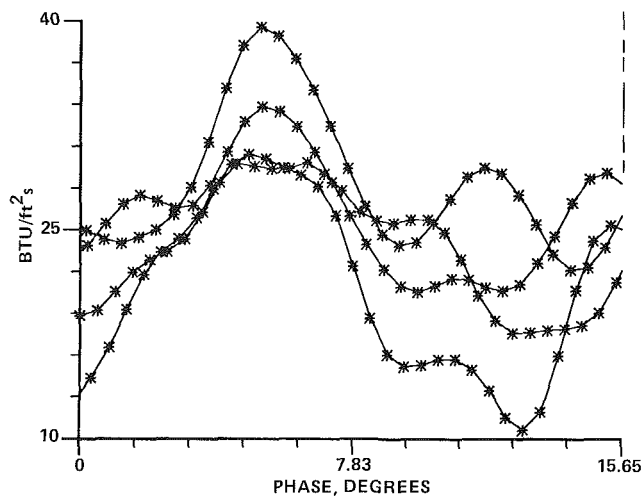


Fig. 15 Phase-resolved heat-flux data at 34.7 percent wetted distance on blade pressure surface

result at 34.7 percent wetted distance. These results were obtained for the same test conditions as the pressure data. The relative location of the vane is again illustrated on Fig. 5. Only a qualitative comparison can be made between Figs. 14 and 15 because the pressure data were not phase resolved as noted above. Comparison of Fig. 15 with Fig. 10 illustrates that farther back on the pressure surface, the general character of this phase-resolved heat-flux history is relatively uniform with peaks occurring at about 6.5 and 12 deg. The minimum again occurs near 0 deg phase angle. However, the general character of the phase-resolved heat-flux history at the farther downstream location appears to be more steady than it was at 12.7 percent wetted distance.

5.4 Consideration of Unsteady Heat-Flux Impact on Blade Durability. The primary purposes of obtaining the unsteady heat-flux and pressure data are to get a better understanding of the flow field around a rotating turbine blade and to obtain validation data for unsteady aerodynamic codes. A separate issue is the impact of the rapidly varying heat flux at the blade surface on blade durability in an engine application. For an uncooled blade such as considered in this experiment, the varying heat flux will be small because the temperature difference between the gas stream and the blade surface is small and durability should not be affected. For a cooled airfoil, the temperature difference can be significant so that the heat flux does vary considerably. Typical heat-flux variation data from this test were corrected to an engine condition with a 1200°F temperature difference between the gas stream and the blade surface. The blade material temperature variation was calculated using an exact solution for a semi-finite solid given by Carslaw and Jaeger (1959). The results show that the surface temperature of a metallic blade would change about 1.5°F in the 21 μ s over which the heat flux varied from minimum to maximum (see Fig. 12(c) for example). This temperature change dampens quickly into the wall away from the surface (within 0.001 in.). If the blade were coated with a thermal barrier coating, the surface temperature change would be of the order of 6°F and would dampen within 0.00015 in. from the surface. Even though these temperature changes are small, the gradient at the surface is large (3,000 to 40,000°F/in.). Gradients of this magnitude, occurring at such high frequencies, may play a role in determining the fatigue life of blading, particularly since the number of repetitions over the life of an engine is large (typically, 23 vanes \times 27,000 rpm \times 60 s/min \times 1000 h lifetime = 1.3×10^{10}). Further studies, including laboratory testing of blade samples, are required in order to bring these heat transfer results to bear on engine durability problems.

6 Conclusions

Time-resolved or phase-resolved heat-flux data have been presented for the blade of the Teledyne 702 HP turbine. Detailed results have been presented at several locations on the blade. Other results have been shown to illustrate the influence of vane cold-gas injection and vane/blade spacing on the time-resolved blade heat-flux history. All of the blade suction surface data presented illustrate that the peak heat-flux value occurs in that portion of the flow which can be associated with the vane wake. The suction surface boundary layer appears to fluctuate between laminar and turbulent as the blade moves from the passage flow into the vane wake and then out again. The blade pressure surface heat-flux history is shown to be somewhat more unsteady than the suction surface history. The effect of injection at close spacing is shown to influence the early portion of the wake flow resulting in an extended period of low heat flux. The effect of increasing the vane/blade spac-

ing is shown to diffuse the character of the passage heat-flux history.

Acknowledgments

The authors would like to thank Mr. Tom Hajek and Ms. Celina Kosier, both formerly of Teledyne CAE, for many helpful discussions during the initial efforts of this research program. The authors would also like to thank Prof. William J. Rae of the State University of New York at Buffalo for many helpful discussions during the course of this work. The research described in this paper was supported by Teledyne CAE Independent Research and Development funds. The phase-resolved data analysis procedure was developed under support from NASA Lewis Research Center, Grant No. NAG3-581 and monitored by Mr. Kas Civinskis.

References

- Adamczyk, J. J., 1985, "Model Equation for Simulating Flows in Multistage Turbomachinery," ASME Paper No. 85-GT-226.
- Anand, A. K., and Lakshminarayana, R., 1978, "An Experimental Study of Three-Dimensional Turbulent Boundary Layer and Turbulence Characteristics Inside a Turbomachinery Passage," *ASME Journal of Engineering for Power*, Vol. 100, pp. 676-690.
- Binder, A., Forster, W., Kruse, H., and Rogge, H., 1985, "An Experimental Investigation Into the Effect of Wakes on the Unsteady Turbine Rotor Flow," *ASME Journal of Engineering for Gas Turbines and Power*, Vol. 107, pp. 458-466.
- Binder, A., Forster, W., Mach, K., and Rogge, H., 1987, "Unsteady Flow Interaction Caused by Stator Secondary Vortices in a Turbine Rotor," *ASME JOURNAL OF TURBOMACHINERY*, Vol. 109, pp. 251-257.
- Carslaw, H. S., and Jaeger, J. C., 1959, *Conduction of Heat in Solids*, 2nd ed., Oxford University Press, New York, p. 72.
- Doorly, D. J., and Oldfield, M. L. G., 1985, "Simulation of the Effects of Shock Wave Passing on a Turbine Rotor Blade," *ASME Journal of Engineering for Gas Turbines and Power*, Vol. 107, pp. 998-1006.
- Dring, R. P., Blair, M. F., and Joslyn, H. D., 1980, "An Experimental Investigation of Film Cooling on a Turbine Rotor Blade," *Journal of Engineering for Power*, Vol. 102, pp. 81-87.
- Dring, R. P., and Joslyn, H. D., 1981, "Measurement of Turbine Rotor Blade Flows," *ASME Journal of Engineering for Power*, Vol. 103, pp. 400-405.
- Dring, R. P., Joslyn, H. D., Hardin, L. W., and Wagner, J. H., 1982, "Turbine Rotor-Stator Interaction," *ASME Journal of Engineering for Power*, Vol. 104, pp. 729-742.
- Dunn, M. G., 1986, "Experimental Measurements of Heat-Flux Distribution in a Turbine Stage With Upstream Disturbances," NASA CP-2436, Vol. 1, pp. 614-636.
- Dunn, M. G., and Chupp, R. E., 1987, "Influence of Vane/Blade Spacing and Cold-Gas Injection on Vane and Blade Heat-Flux Distributions for the Teledyne 702 HP Turbine Stage," Paper No. AIAA 87-1915, 23rd Joint Propulsion Conf., San Diego, CA.
- Dunn, M. G., and Chupp, R. E., 1988, "Time-Averaged Heat-Flux Distributions and Comparison With Prediction for the Teledyne 702 HP Turbine Stage," *ASME JOURNAL OF TURBOMACHINERY*, Vol. 110, pp. 51-56.
- Dunn, M. G., and Hause, A., 1982, "Measurements of Heat Flux and Pressure in a Turbine Stage," *Journal of Engineering for Power*, Vol. 104, pp. 76-82.
- Dunn, M. G., Lukis, G., Urso, M., Hiemenz, R. J., Orszulak, R. L., and Kay, N. J., 1984a, "Instrumentation for Gas Turbine Research in Short-Duration Facilities," Paper No. 841504, Aerospace Congress and Exposition (SAE), Long Beach, CA.
- Dunn, M. G., Rae, W. J., and Holt, J. L., 1984b, "Measurement and Analysis of Heat Flux Data in a Turbine Stage: Part II—Discussion of Results and Comparison With Predictions," *Journal of Engineering for Gas Turbines and Power*, Vol. 106, pp. 234-240.
- Dunn, M. G., George, W. K., Rae, W. J., Woodward, S. H., Moeller, J. C., and Seymour, P. J., 1986, "Heat Flux Measurements for the Rotor of a Full-Stage Turbine: Part II—Technique and Typical Time-Resolved Measurements," *ASME JOURNAL OF TURBOMACHINERY*, Vol. 108, pp. 98-107.
- Evans, R. L., 1978, "Boundary Layer Development on an Axial-Flow Compressor Stator Blade," *ASME Journal of Engineering for Power*, Vol. 100, pp. 287-293.
- George, W. K., Rae, W. J., Seymour, P. J., and Sonnenmeier, J. K., 1987, "An Evaluation of Analog and Numerical Techniques for Unsteady Heat Transfer Measurements With Thin-Film Gauges in Transient Facilities," *Proc. of the 1987 ASME-JSME Thermal Engineering Joint Conf.*, pp. 611-617.
- Giesing, J. P., 1968, "Nonlinear Interaction of Two Lifting Bodies in Arbitrary Unsteady Motion," *ASME Journal of Basic Engineering*, Vol. 90, pp. 387-394.

Gorton, C. A., and Lakshminarayana, B., 1976, "A Method of Measuring the Three-Dimensional Mean Flow and Turbulence Quantities Inside a Rotating Turbomachinery Passage," *ASME Journal of Engineering for Power*, Vol. 98, pp. 137-146.

Hodson, H. P., 1984, "Boundary Layer and Loss Measurements on the Rotor of an Axial-Flow Turbine," *ASME Journal of Engineering for Gas Turbines and Power*, Vol. 106, pp. 391-399.

Hodson, H. P., 1985a, "Boundary-Layer Transition and Separation Near the Leading Edge of a High-Speed Turbine Blade," *ASME Journal of Engineering for Gas Turbines and Power*, Vol. 107, pp. 127-134.

Hodson, H. P., 1985b, "Measurements of Wake-Generated Unsteadiness in the Rotor Passages of Axial Flow Turbine," *ASME Journal of Engineering for Gas Turbines and Power*, Vol. 107, pp. 467-476.

Joslyn, H. D., Caspar, J. R., and Dring, R. P., 1985, "Inviscid Modeling of Turbomachinery Wake Transport," Paper No. AIAA-85-1132.

Kemp, N. H., and Sears, W. R., 1953, "Aerodynamic Interference Between Moving Blade Rows," *J. Aero. Sci.*, Vol. 20, No. 9, pp. 585-597.

Kemp, N. H., and Sears, W. R., 1955, "The Unsteady Forces Due to Viscous Wakes in Turbomachine," *J. Aero. Sci.*, Vol. 22, No. 7, pp. 478-483.

Kerrebrock, J. L., and Mikolajczak, A. A., 1970, "Intra-Stator Transport of Rotor Wakes and Its Effect on Compressor Performance," *ASME Journal of Engineering for Power*, Vol. 92, pp. 359-368.

Lakshminarayana, B., Govindan, T. R., and Reynolds, B., 1982, "Effects of Rotation and Blade Incidence on Properties of Turbomachinery Rotor Wake," *AIAA Journal*, Vol. 20, No. 2, pp. 245-253.

Parker, R., 1969, "Relation Between Blade Row Spacings and Potential Flow Interaction Effects in Turbomechanics," *Proceedings of the Institute of Mechanical Engineering*, Vol. 184, Pt. 3G, No. 11, pp. 1-8.

Sharma, O. P., Butler, T. L., Joslyn, H. D., and Dring, R. P., 1985, "Three-Dimensional Unsteady Flow in an Axial Flow Turbine," *J. of Propulsion*, Vol. 1, No. 1, pp. 28-38.

Taulbee, D. B., Tran, L., and Dunn, M. G., 1989, "Stagnation Point and Surface Heat Transfer for a Turbine Stage: Prediction and Comparison With Data," *ASME JOURNAL OF TURBOMACHINERY*, this issue.

R. W. Ainsworth

J. L. Allen

M. R. D. Davies

J. E. Doorly

C. J. P. Forth

M. A. Hilditch

M. L. G. Oldfield

A. G. Sheard

University of Oxford,
Department of Engineering Science,
Oxford, United Kingdom

Developments in Instrumentation and Processing for Transient Heat Transfer Measurement in a Full-Stage Model Turbine

Transient heat transfer measurement techniques have long been used in two-dimensional stationary cascade tests designed to model turbine conditions used in Oxford. More recently, experiments studying some of the unsteady effects have been carried out using a rotating wake generator upstream of the rotor cascade. Currently work has concentrated on providing a fully three-dimensional rotating turbine stage. In an associated paper, the modifications necessary to accommodate this stage in the Oxford Isentropic Light Piston Tunnel are discussed. In this paper the developments necessary to permit the measurement of transient heat transfer under these rotating conditions are fully described.

Introduction

The use of transient heat transfer measurement techniques in turbomachinery applications has long been one of the foci of research activities in Oxford. Early work involved the use of thin-film platinum resistance thermometers mounted on semi-infinite (thermally) substrates, made of quartz or a Pyrex glass. One of the problems of using discrete heat transfer gages mounted in the model under test was associated with discontinuities in both the surface profile and more especially the thermal boundary layer. Although an approximate analysis of the effect of discontinuities in the thermal boundary layer was made by Kays (1966) and extended by Schultz and Jones (1973), and was experimentally verified (Ainsworth, 1976), no correction could be properly made to the measured heat transfer rate if the boundary layer was transitional. The discovery of a machinable glass (Corning MACOR) removed these difficulties by enabling the model under test to be fabricated completely from a material that could then be instrumented directly. This technique has been used successfully for over a decade.

In moving to a fully three-dimensional rotating geometry, the relatively high stress levels prevented the use of machinable glass. The choice then lay between returning to the use of discrete instrumentation inserts and their associated discontinuity problems, or using the newly developed technology (Doorly, 1985, 1988; Doorly and Oldfield, 1986, 1987) of mounting heat transfer gages onto a thin insulating layer applied directly to a metal surface. This latter technique was chosen for reasons of profile and thermal boundary layer in-

tegrity, and represents an approach that is complimentary to that of both Epstein et al. (1985) and Dunn (1986).

The present investigation has concentrated on:

- (i) developing and testing methods of using the technique on a three-dimensional blade profile;
- (ii) providing the necessary electronics to service the gages and to reduce slip-ring noise, and
- (iii) devising a digital signal processing system that would evaluate measured heat transfer rate as a function of time.

The combination of these aspects of technology should permit the fulfillment of the primary objective of the new Oxford rotor facility, the measurement of unsteady and mean heat transfer rates to a three-dimensional profile under rotating conditions.

Heat Transfer Measurement

Instrumentation System Overview. The specification for the heat transfer instrumentation was obviously related to the performance of the rotor facility, discussed in detail by Ainsworth et al. (1988). In brief, the mode of operation consisted of allowing the turbine disk, placed behind a nozzle guide vane ring, to speed up during the transient run, with design speed being achieved at an appropriate moment during the experiment. Simulation of engine conditions (Reynolds number, Mach number, dimensionless speed, dimensionless mass flow rate, and therefore specific work function) in this facility resulted in a run time of order 200 ms, depending on the gas-to-wall temperature ratio being used.

The rotational speed changed from of order 6000 rpm to 10,000 rpm during the experiment, with a design speed of 8400 rpm. It was considered that meaningful heat transfer results

Contributed by the International Gas Turbine Institute and presented at the 33rd International Gas Turbine and Aeroengine Congress and Exhibition, Amsterdam, The Netherlands, June 5-9, 1988. Manuscript received by the International Gas Turbine Institute September 15, 1987. Paper No. 88-GT-11.

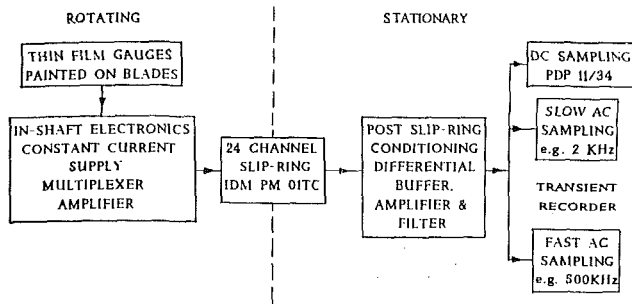


Fig. 1 Data acquisition system

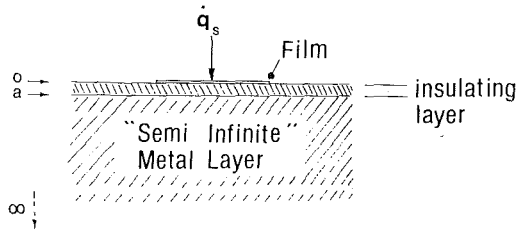


Fig. 2 Thin-film gage on two-layered substrate with semi-infinite metal layer

on the rotor could be obtained within ± 0.5 deg of design incidence.

In practice, given a desire to take fast data at 500 kHz, and a memory usage of 3.5 kbytes per channel, sampling would be over in 7 ms. During this time one rotor blade would be influenced by 35 nozzle guide vane wakes at design speed, with a change of incidence of ± 0.3 deg.

Given a wake-passing frequency of 5 kHz at design speed, the requirement was that the instrumentation should be capable of measurements up to 100 kHz with an ability to measure d-c response (gage temperature) as well as the a-c response. In the first instance the specification called for eight gages on one blade, and given 60 blades in the disk, there should be up to 100 measurement points available in one build. The instrumentation had to withstand accelerations of 32,000g.

A block diagram of the proposed measuring system is given in Fig. 1, and will be discussed in detail below. Multiplexers, current sources, and amplifiers were to be mounted within the hollow turbine shaft, to select the required thin film gages, and amplify the signals to high level for transmission through the slip-rings. Differential post-slip-ring amplifiers would be used to avoid earth loop problems, and to condition the signals for A/D conversion by the computer and transient recorder acquisition systems.

Heat Transfer Gage Design. The theory behind the mounting of a thin-film thermometer on a two-layered substrate consisting of a vitreous enamel coat on a semi-infinite metal layer has been developed by Doorly (1988), and only the bare essentials are given here. Considering the gage mounted as indicated schematically in Fig. 2, the equations governing the one-dimensional heat transfer are as follows:

$$\frac{\partial^2 T_1}{\partial x^2} = \frac{1}{\alpha_1} \frac{\partial T_1}{\partial t} \quad 0 \leq x \leq a \quad (1)$$

$$\frac{\partial^2 T_2}{\partial x^2} = \frac{1}{\alpha_2} \frac{\partial T_2}{\partial t} \quad a \leq x \leq \infty \quad (2)$$

with boundary conditions

$$\dot{q}_s = -k \frac{\partial T_1}{\partial x} \quad x = 0 \quad (3)$$

$$T_1 = T_2 \quad x = a \quad (4)$$

$$k_1 \frac{\partial T_1}{\partial x} = k_2 \frac{\partial T_2}{\partial x} \quad x = a \quad (5)$$

$$T_2 = 0 \quad x = \infty \quad (6)$$

Solution of these equations yields the surface heat transfer rate as a function of surface temperature in the Laplace transform domain

$$\dot{q}_s(s) = (\rho_1 c_1 k_1 s)^{1/2} \frac{(1 - A \exp\{-2a(s/\alpha_1)^{1/2}\}) \bar{T}_s}{(1 + A \exp\{-2a(s/\alpha_1)^{1/2}\})} \quad (7)$$

By transforming to the frequency ($j\omega$) plane it is now possible to examine the inherent sensitivity of the gage/layer combination as a function of the frequency of the perturbation. Defining the modulus of this transfer function in terms of

$$|G(j\omega)| = \frac{1}{\sqrt{\rho_1 c_1 k_1 \omega}} \frac{[1 + 2A \exp\{-b\} \cos b + A^2 \exp\{-2b\}]^{1/2}}{[1 - 2A \exp\{-b\} \cos b + A^2 \exp\{-2b\}]^{1/2}} \quad (8)$$

where

$$A = \frac{\sqrt{\rho_1 c_1 k_1} - \sqrt{\rho_2 c_2 k_2}}{\sqrt{\rho_1 c_1 k_1} + \sqrt{\rho_2 c_2 k_2}}$$

and

$$b = \frac{2\omega a^2}{\alpha_1} = \sqrt{2\omega} \sqrt{\rho_1 c_1 k_1} \left(\frac{a}{k_1}\right)$$

Thus the behavior of the gage depends only on the thermal products $\sqrt{\rho_1 c_1 k_1}$, $\sqrt{\rho_2 c_2 k_2}$ of the insulating layer and metal substrate, respectively, together with the ratio of thickness to thermal conductivity of the insulating layer, a/k . Doorly and Oldfield (1986) show calibration techniques for obtaining these. It is of importance to see how sensitive the response of the gage/layer system is to variations in these parameters. Taking firstly the typical values for:

(i) thermal product of the insulating layer—1460 $\text{Jm}^{-2}\text{K}^{-1}\text{s}^{-1/2}$

(ii) its thermal conductivity—1.36 W/m K

(iii) thermal product of the metal substrate—14190 $\text{Jm}^{-2}\text{K}^{-1}\text{s}^{-1/2}$

the value of the insulating layer thickness was varied over the values of 50 μm , 100 μm , 200 μm , and 400 μm . This is equivalent to varying a/k from 25 to 200 percent of its nominal value. The resulting variation of the modulus of the

Nomenclature

$$A = \frac{\sqrt{\rho_1 c_1 k_1} - \sqrt{\rho_2 c_2 k_2}}{\sqrt{\rho_1 c_1 k_1} + \sqrt{\rho_2 c_2 k_2}}$$

a = insulating layer thickness

$$b = 2\omega a^2 / \alpha_1 = \sqrt{2\omega} \sqrt{\rho_1 c_1 k_1} (a/k_1)$$

C = capacitance values

c = specific heat

k = conductivity

\dot{q} = heat transfer rate

R = resistance values

s = Laplace transform variable

T = temperature

t = time

x = distance

— = Laplace transformed variable

α = thermal diffusivity = $(k/\rho c)$

ρ = density

ω = angular frequency

Subscripts

1 = insulator properties

2 = metal properties

3 = surface

system gain (defined now as \dot{q}/T) is plotted in Fig. 3, where it will be seen that for layer thicknesses greater than 100 μm , the response is virtually invariant above 100 Hz. In practice at these frequencies the insulating layer is behaving as if it were semi-infinite.

Other sensitivity tests carried out included examining the effect of varying the layer thermal product (Fig. 4). In the semi-infinite region, for a given amplitude of heat transfer variation, the variation in temperature is seen to be proportional to the thermal product as expected. Changes in layer conductivity have a marked effect only below 10 Hz.

It will be seen from these plots that the sensitivity of the heat transfer gages at the high-frequency end of the spectrum falls as the square root of the frequency (in line with semi-infinite theory). Since there is particular interest in the high-frequency information, an obvious advantage would follow if a means could be found of improving the signal-to-noise ratio over this range by preferentially amplifying the higher fre-

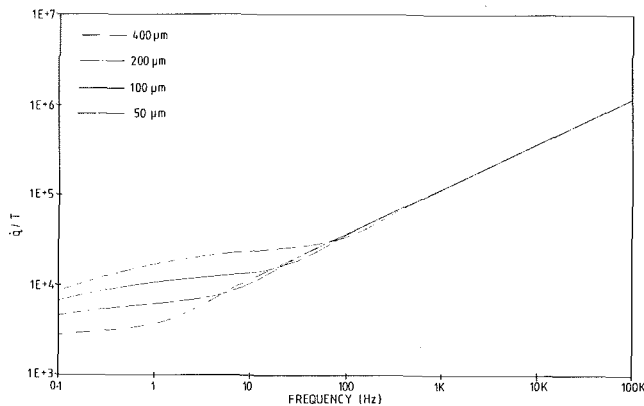


Fig. 3 Frequency response of layered gages of various enamel thicknesses

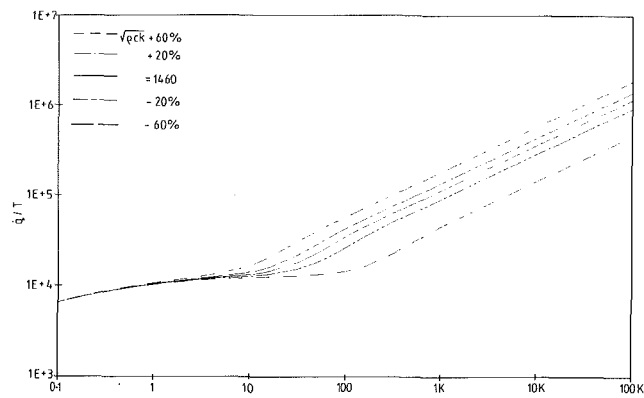


Fig. 4 Frequency response for various values of $\sqrt{\rho ck}$ enamel

quency information before passing the signals through a slip-ring. The sensitivity analysis indicated that a common electronic circuit for providing the gain boosting should suffice for all practical gage/layer combinations. The design objective was now to provide this inside the rotor shaft, together with a suitable means for decoding the signals afterward.

Heat Transfer Gage Construction. The theory outlined above indicates how the surface temperature and the surface heat transfer rate of a two-layered system are related. In the experiment, it is the surface temperature history that is monitored. This is inferred by passing a constant current through the thin-film thermometer, and measuring changes in the voltage across it, a knowledge of the temperature coefficient of resistance yielding the surface temperature.

The standard thin-film thermometers used previously in Oxford on semi-infinite substrates were applied by a process of painting on liquid platinum 05-X (Englehard Industries) and firing at high temperature. In the case of a two-layered system, the same sensors may be used, but the insulating layer has to be carefully chosen so that the coefficient of linear expansion of the metal substrate and the insulating layer are matched over the temperature range of firing.

The insulating layer itself, a vitreous enamel (WB5847 supplied by Ferro G.B. Ltd.), is also applied by a process of spraying and firing. The enamel material is supplied from the manufacturers as a water-based solution, which after spray application is dried to bisque stage, at 125°C. Final firing takes place at 825°C before allowing the substrate to cool naturally. Enameling techniques require stringent cleaning of the substrate materials, followed by a surface roughening using glass bead blasting.

The instrumentation processes can be significant in reducing the strength of the metal blade, depending upon its composition, but the strength can be restored by heat treatment.

In practice, the substrate metal used was Inco 718, and specimens subjected to various representative heat treatments were tested in a tensile testing machine (see Table 1). Taking even the most pessimistic estimate, an acceptable factor of safety was available in the most highly stressed part of the blade.

Gold tags (liquid bright gold KA6) were used to bring contacts away from the thin-film thermometer positions on the blade profile, down to the root region, where copper wires (0.11 mm diameter) were attached directly using a conducting adhesive, Eccobond 58C (Hitek Electronic Materials Ltd.). This led to a shoulder on the turbine disk, where a set of soldered contacts permitted the blades to be interchanged readily. Again, copper wire was used to connect these pads to the servicing electronics inside the rotor shaft. A picture of an instrumented blade is shown in Fig. 5.

For aerodynamic reasons, it was desired to limit the insulating layer thickness to a value of order 125 μm . This was inspected by measuring the profile of a blade after it had been

Table 1 The effect of various heat treatments on the strength of Inco 718

Specimen	Heat Treatment from Fully Annealed State	σ Yield
1	Heat at 825° C for 15 minutes. Air cool. Cycle from 20 - 640° C twice. Air cool.	695.0 N/mm ²
2	None.	352.9 N/mm ²
3	Heat at 825° C for 15 minutes. Air cool. Cycle from 20 - 640° C four times. Air cool.	781.3 N/mm ²
4	Heat at 925° C for 15 minutes. Air cool. Cycle from 20 - 640° C four times. Air cool.	595.2 N/mm ²

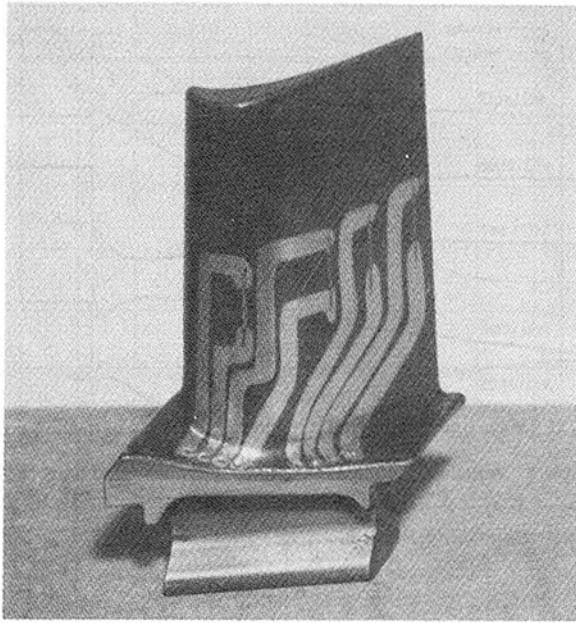


Fig. 5 Photograph of an instrumented rotor blade

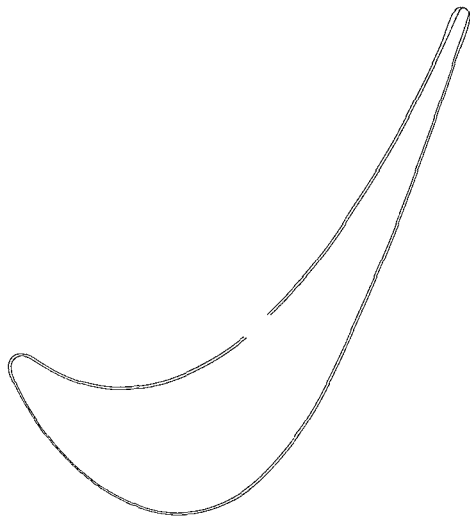


Fig. 6 Measured blade profile before and after enameling

manufactured, and repeating the measurement after the insulating layer had been applied. A typical comparison between the two at a root section on the blade is shown in Fig. 6, where it will be seen that the layer is remarkably uniform, with some slight thickening toward the trailing edge region.

Electronic Circuit Design

The thin-film thermometers were to be energized from a constant current source inside the rotor shaft, and the output signals would also be amplified in the rotating frame, permitting transmission through the slip-ring at a relatively high level. The signal conditioning in-shaft would be somewhat similar to that provided by the present generation of electrical analogues in use in Oxford (Oldfield et al., 1982) though with the advent of digital signal processing, an exact mirroring of the semi-infinite behavior with frequency was not now necessary, reducing the component count to a manageable level. After transmission through the electrical slip-ring, signals would be buffered by differential amplifiers before being sampled by the data acquisition A/D system.

In-Shaft Electronics Conceptual Design. The in-shaft sig-

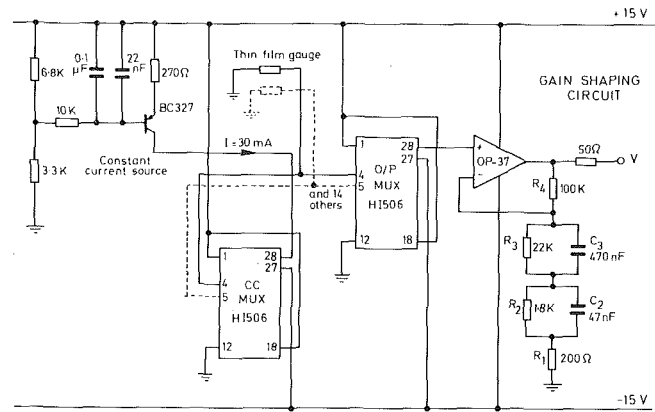


Fig. 7 In-shaft signal conditioning unit

nal conditioning (Fig. 7) was designed around the OP-37 low-noise, fast-response operational amplifier. Configured in non-inverting mode the gain of the amplifier was designed to vary with frequency using a variable impedance in the feedback leg. Given a gain-bandwidth product of 40 MHz for this amplifier, and a desire for an upper frequency response of close to 100 kHz, the two extremes of gain were set at 5 (d-c) and 500 at high frequency. A reasonable component count was achieved using four break points between these frequencies. The break points, at decade values, were set using the nominal gage/layer response for a 200- μ m-thick layer (Fig. 3), at nominal values of 20 Hz, 200 Hz, 2 kHz, and 20 kHz. The gain of the amplifier (in terms of the components R_1 - R_4 , C_2 - C_3 in Fig. 7) was calculated as a function of the frequency to be:

$$\left(R_4 + R_1 + \frac{R_2}{1 + j\omega C_2 R_2} + \frac{R_3}{1 + j\omega C_3 R_3} \right) \left(R_1 + \frac{R_2}{1 + j\omega C_3 R_2} + \frac{R_3}{1 + j\omega C_3 R_3} \right) \quad (9)$$

A superposition of this frequency response on the standard gage/layer combination is shown in Fig. 8, while the overall system gain is given in Fig. 9. Here it can be seen that there is only a variation of expected signal level of order 2-3 over all frequencies, and consequently full use could be made of the resolution of the data-acquisition converters. In practice, standard value resistors and capacitors were used, and these changed the nominal break points slightly to 18.7 Hz, 170.7 Hz, 191.5 Hz, and 20.35 kHz.

Other features of the electronic design (Fig. 7) included a low-noise constant current supply to energize the thin-film thermometers, with a current capability of up to 50 mA, and two sixteen-channel multiplexers (HI-506). Both multiplexers were addressed in parallel, the first being used to supply a particular thin-film sensor with current, and the second to connect the gain-shaping amplifier to that sensor. In this way 16 thin-film sensors could be connected to one electronic module, with one sensor in operation at any one instant. The multiplexers were not switched during the run.

In-Shaft Electronics Design Realization. In practice, the design of the in-shaft electronics was constrained by the dimensions inside the rotor shaft, and the number of slip-ring channels available. There was room inside the shaft for two boards, each 62 mm by 360 mm. A locally available CAD package for printed circuit board development was used to design two double-sided boards carrying eight of the modules shown schematically in Fig. 7. By running the eight modules in parallel inside the shaft, it was possible to monitor eight thin-film gages simultaneously with differential output. Since 16 gages could be connected up to one module, a total of 128 sensors could be accommodated on one build, with gage se-

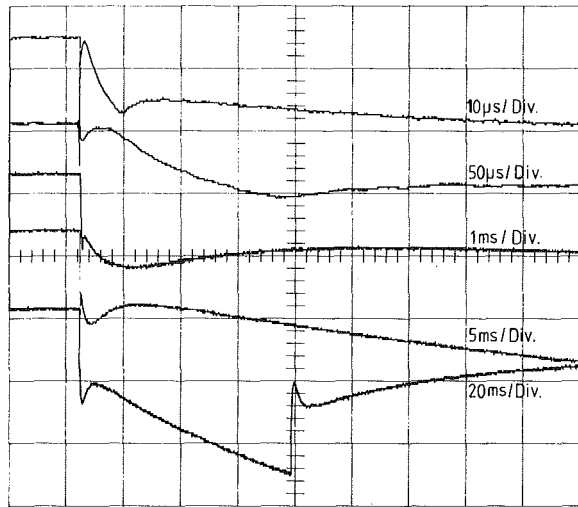


Fig. 12 Response, at various timescales, of thin-film circuit to parabolic input

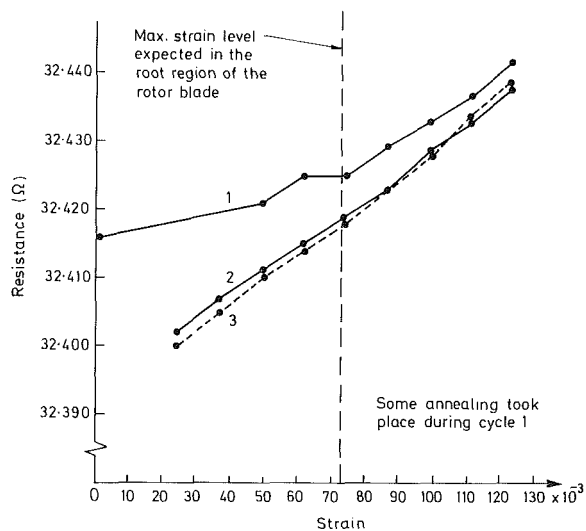


Fig. 13 Variation of thin-film gage resistance with applied strain

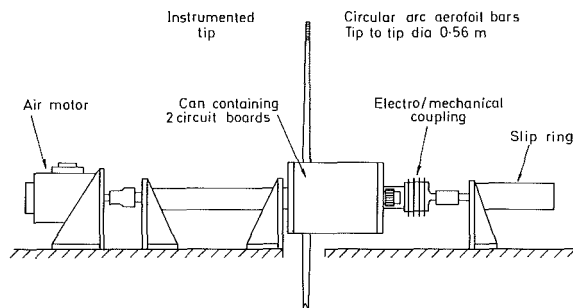


Fig. 14 Schematic of spinning rig

for numerical processing the nominal break points could be used. Measurements of noise indicated values of order 0.5 mV rms at output, with a thin-film gage connected and using a wide-bandwidth voltmeter.

The continued correct functioning of the in-shaft electronics could be tested using an anti-analogue (Carlini, 1984). This was designed to apply a parabolic (with time) voltage input to a conventional heat transfer analogue, which should then produce a step output, simulating the semi-infinite response of a thin-film thermometer to a step in heat transfer.

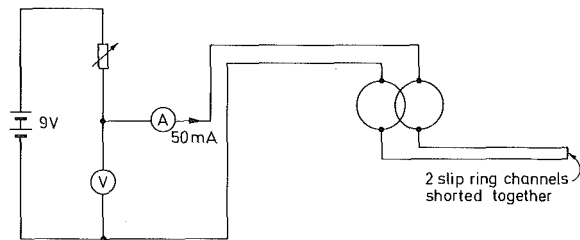


Fig. 15 Measurement of slip-ring noise

In the conventional analogue, the gain varies linearly with the square root of frequency. As noted earlier, the in-shaft electronics used a series of break points to mirror crudely the root frequency response. Depending on position relative to the break points, the gain was either constant or varied in direct proportion to the frequency. In applying the anti-analogue to the in-shaft electronics, and measuring the output voltage at different time scales, rather than seeing a step output, it was possible to see the resulting waveform increasing and decreasing with respect to time, as the various break points came into play. An example of this is given in Fig. 12. This proved to be a reliable method for verifying the continuing functioning of the circuits after the initial frequency response tests. It also provided valuable early data with which to test the digital signal processing system (see below).

Bench tests were also conducted on the thin-film thermometers themselves. Tensile specimens were constructed from the same insulating layer/metal substrate combination that was used on the rotor blades. There was a particular interest in testing the change in thin-film resistance with strain, and a plot of the results in Fig. 13 shows that after some initial annealing (curve 1), the variation was quite repeatable, up to much higher levels of strain than those expected on the rotor blades. This change in resistance corresponds to a temperature change of order 0.5°C.

Rotating Tests. At an early stage in the project it was decided to construct a spinning rig, designed to test the heat transfer instrumentation and the in-shaft electronics at the correct radius and rotational speed. The rig, shown schematically in Fig. 14, consisted of an air motor driving a shaft with a can mounted at one end. The can contained a version of the in-shaft electronics, and the two aerofoil-shaped bars were mounted from it, with thin-film thermometers and semi-conductor pressure transducers held at a radius of 255 mm, representing positions on the rotor blade.

An electrical slip-ring was used to power the electronics, and to extract data from the rig. In addition the system, which was to monitor and control the rotating section on the ILPT, was tested on this rig.

Using some of the slip-ring channels, a frequency response test was carried out on the in-shaft electronics while the rig was rotating. There was no discernable change in the performance of the circuit.

The noise characteristics of the slip-ring were tested using the system shown in Fig. 15. It was possible on occasions to obtain a noise power spectrum showing a peak at the fundamental rotational frequency, with higher harmonics (Fig. 16), though more generally, none was evident (Fig. 17). Measuring the true rms voltage directly yielded a value of less than 0.5 mV.

As well as establishing the mechanical integrity of the thin-film thermometers and the connections to the in-shaft electronics, the rotating tests also provided useful results on the performance of the gages. The spinning rig was mounted in a pressure tank, but the system had never been designed for a high vacuum and the level of vacuum that could be achieved

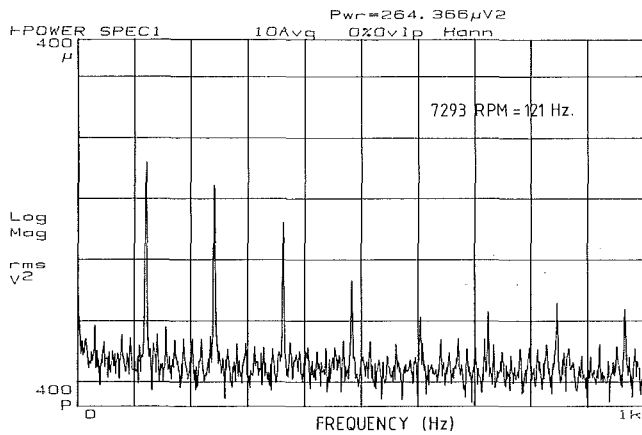


Fig. 16 Noise power spectrum from slip-ring tests, showing peaks at multiples of the rotational speed

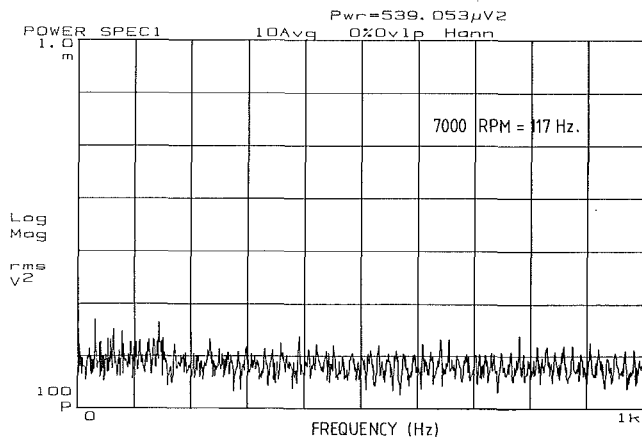


Fig. 17 Noise power spectrum from slip-ring tests

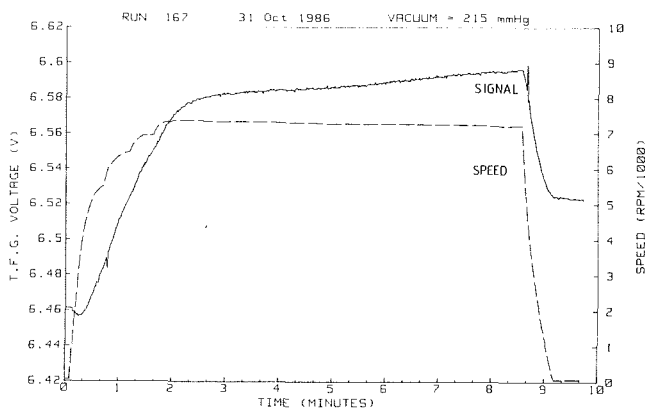


Fig. 18 The d-c shift in signal from thin-film gage

in practice was never better than 15 torr (mm of Hg). This, however, produced some interesting data on the operation of the thermometers.

Referring to Fig. 18, as the speed of the rig was cycled over 7000 rpm and down again in a period of 10 min, the d-c shift in signal from the thin-film gage was monitored, being a measure of the surface temperature. As the bar rotated, a driving temperature difference (ambient to recovery temperature) was created and although the convective heat transfer coefficient was low at these low pressure levels, it was still enough to cause a significant increase in the thin film temperature. With a lower plenum pressure level (18 torr in Fig. 19) the same phenomenon existed, but the lower convective heat transfer coefficient slowed the response. At these pressure

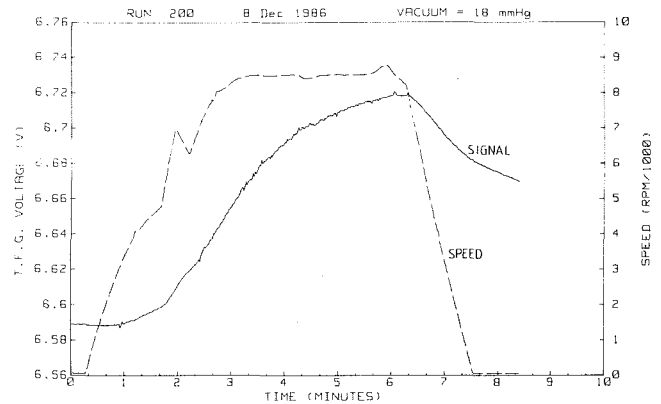


Fig. 19 The d-c shift in signal from thin-film gage

levels, the expected temperature increase due to rotation before a run in the ILPT from these tests would be of order 13°C. This could be reduced by lowering the pressure in the working section still further (target 1–5 torr) and minimizing the time taken for the rotor to spin up to the desired speed before a run.

Further details of these technology developments are given in an internal report (Ainsworth et al., 1987).

Digital Signal Processing

The instrumentation and data processing systems were required to provide accurate measurements of both the mean and unsteady heat flux components. The thin-film gage responds directly to the surface temperature, so that the surface heat flux must be inferred from the temperature, rather than being directly measured.

The amplitude of the Fourier Component of the temperature signal, with frequency f , is proportional to $1/\sqrt{f}$ times the amplitude of the corresponding heat flux signal component. Consequently, if the temperature signal were recorded directly, the high-frequency content of the derived heat flux signal could be swamped by one or both of electronic noise picked up before digital recording and quantization noise resulting from the A/D conversion.

For the gage on the single-layer substrate, the problem may be overcome by using an electrical analogue (Meyer, 1960), which, suitably designed (Oldfield et al., 1982), produces an almost exact \sqrt{f} gain. This improves the signal-to-noise ratio across the entire recording bandwidth and also yields the surface heat flux directly.

In the case of a gage on a multilayered substrate the analogue may again be used to preserve the high-frequency content, but a postrecording digital filter must be applied to the sampled data to yield the heat flux. This corrects the low-frequency part of the spectrum to compensate for the metal base underlying the coating (Doorly, 1985; Doorly and Oldfield, 1986, 1987).

Rather than use an analogue to amplify the high-frequency component of the temperature signal before transmission through the slip ring, the simpler frequency boosting circuit described earlier in this paper was adopted. The analogue would require more electronic components and digital postprocessing of the signal for multilayered gages would also be needed. The principles of converting a frequency-boosted gage signal into the corresponding surface heat flux have been described and illustrated for the analogue (Doorly, 1988). The procedure adopted depends somewhat on the details of the boosting circuit, although there are basically two alternatives. Firstly, a digital filter may be employed to transform the signal directly to heat flux, or secondly, the signal may be deboosted to

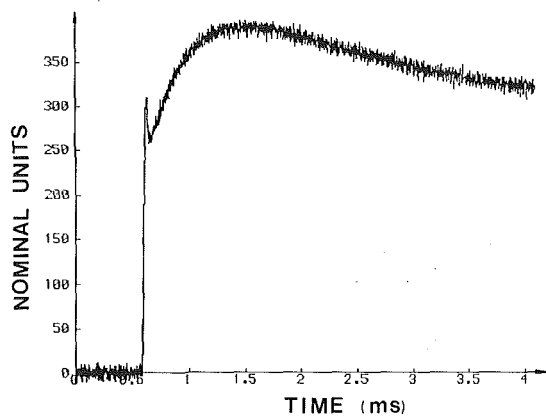


Fig. 20 Response of frequency boosting circuit to parabolic input

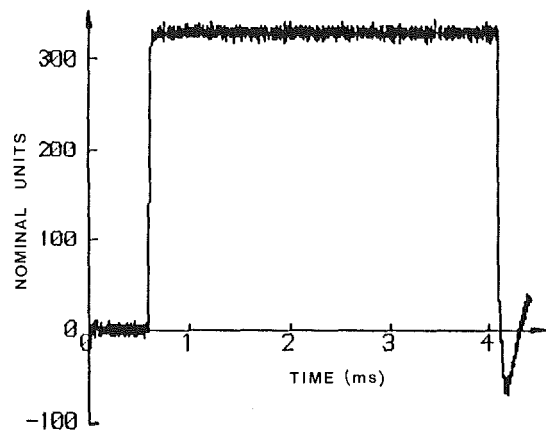


Fig. 21 Reconstructed step in heat transfer

recover a high-fidelity temperature signal, which may subsequently be transformed to heat flux. The advantage of the first procedure is that it is more direct and faster. The second alternative, however, is useful in providing a record of the surface temperature rise, so that a correction for the decrease in driving temperature potential may be made in calculating the Nusselt number. Furthermore, a nonlinear partial differential equation solver may be used, such as the method of lines, in order to check the possibility of errors induced by nonuniform thermal properties or finite model thickness. In using the latter approach, it may also be necessary to counteract numerical damping of the high-frequency signal components.

For a general gage

$$\begin{aligned}\bar{q}(s) &= F(s) \cdot \bar{T}(s) \text{ in Laplace Transforms} \\ &= \sqrt{s} \cdot \bar{T}(s) \cdot C(s) \\ &= V_a(s) \cdot C(s)\end{aligned}$$

where $V_a(s)$ is the output of a perfect analogue and $C(s)$ is the multilayer compensating filter.

Writing the boosted temperature signal as

$$V_B = B(s) \cdot \bar{T}(s)$$

$$\text{gives } \bar{q}(s) = V_B(s) \cdot \frac{\sqrt{s}}{B(s)} C(s).$$

Inverting the Laplace Transform gives the convolution

$$\dot{q}(t) = V_B(t) * g(t) * c(t)$$

where $c(t)$ is given by Doorly (1988) and

$$g(t) = L^{-1} \left(\frac{\sqrt{s}}{B(s)} \right)$$

The accuracy of this approach was tested using the anti-analogue circuit (Carlini, 1984), to provide a parabolic signal corresponding to the response of a single-layer gage to a step in heat flux, which was then passed through the frequency boosting circuit (Fig. 20). The sampled output $V(t)$ was FFT convolved with $g(t)$ (Fig. 21). As is evident, the step in heat flux is successfully recovered.

Further details are given by Doorly (1987) together with illustrations of the recovered temperature signal procedure. Digital processing per se of the output signal from the in-shaft electronics introduces an error of order 0.1 percent in heat transfer level. The major error source in establishing heat flux level arises from the measurement of the enamel thermal product, accurate to ± 5 percent.

Conclusions

The newly developed technology of mounting thin-film thermometers on an insulating layer applied directly to a metal surface has now been extended to a fully three-dimensional turbine blade surface, manufactured from a typical alloy in use for these components. The accompanying signal conditioning electronics have been developed, permitting amplification of signals to a higher level within the rotating frame, before transmission through a slip-ring.

Extensive tests, both on the bench and in a purposely built spinning rig, have taken place, proving the technology that will be applied in the Oxford rotor experiment. In addition, the necessary digital signal processing routines have been developed and tested during the course of this research program.

Acknowledgments

The authors gratefully acknowledge the extensive support of the MoD (Procurement Executive), the SERC and Rolls-Royce plc for the work, and the kind permission of the MoD and Rolls-Royce plc to publish the paper.

References

- Ainsworth, R. W., 1976, D. Phil. Thesis, University of Oxford, United Kingdom.
- Ainsworth, R. W., Allen, J. L., and Hilditch, M. A., 1987, "Instrumentation Developments for the Oxford Rotor," OUEL Report No. 1717/87.
- Ainsworth, R. W., Shultz, D. L., Davies, M. R. D., Forth, C. J. P., Hilditch, M. A., Oldfield, M. L. G., and Sheard, A. G., 1988, "A Transient Flow Facility for the Study of the Thermofluid-Dynamics of a Full Stage Turbine Under Engine Representative Conditions," presented at the 33rd ASME International Gas Turbine Conference, Amsterdam, The Netherlands, Paper No. 88-GT-XX.
- Carlini, A. R., 1984, "To Design and Construct a Calibration Device for Electrical Analogues of the Heat Conduction Process in a Transient Cascade," Third Year Project, Department of Engineering Science, University of Oxford, United Kingdom.
- Doorly, J. E., 1985, D. Phil. Thesis, University of Oxford, United Kingdom.
- Doorly, J. E., and Oldfield, M. L. G., 1986, "New Heat Transfer Gages for Use on Multilayered Substrates," ASME JOURNAL OF TURBOMACHINERY, Vol. 108, No. 1.
- Doorly, J. E., 1987, OUEL Report No. 1697/87.
- Doorly, J. E., and Oldfield, M. L. G., 1987, "The Theory of Advanced Heat Transfer Gauges," *Int. J. Heat and Mass Transfer*, Vol. 30, No. 6, pp. 1159-1168.
- Doorly, J. E., 1988, "Procedures for Determining Surface Heat Flux Using Thin Film Gages on a Coated Metal Model in a Transient Test Facility," ASME JOURNAL OF TURBOMACHINERY, Vol. 110, pp. 242-250.
- Dunn, M. G., 1986, "Heat Flux Measurements for the Rotor of a Full-Stage Turbine, Part I - Time Averaged Results," ASME JOURNAL OF TURBOMACHINERY, Vol. 108, No. 1, pp. 90-97.
- Epstein, A. H., Guenette, G. R., Norton, R. J. G., and Yuzhan, C., 1985, "High Frequency Response Heat Flux Gauge for Metal Blading," AG-CP-390, Paper No. 30.
- Kays, W. M., 1966, *Convective Heat and Mass Transfer*, McGraw-Hill, New York.
- Meyer, R. F., 1960, "A Heat Flux Meter for Use With Thin Film Surface Thermometers," NRC Canada, Aero. Rep. LR-279.
- Oldfield, M. L. G., Burd, H. J., and Doe, N. G., 1982, "Design of Wide Bandwidth Analogue Circuits for Heat Transfer Instrumentation in Transient Tunnels," 16th Symp. of ICHMT, Dubrovnik, Hemisphere Publ., Washington, DC.
- Schultz, D. L., and Jones, T. V., 1973, "Heat Transfer Measurements in Short Duration Hypersonic Facilities," AGARD AG-165.

Stagnation Point and Surface Heat Transfer for a Turbine Stage: Prediction and Comparison With Data

D. B. Taulbee

L. Tran

State University of New York at Buffalo,
Buffalo, NY 14260

M. G. Dunn

Calspan Advanced Technology Center,
Buffalo, NY 14225

Predictions using turbulence models are reported for the time-averaged heat-flux distributions on the vane and blade surfaces of the Garrett TFE 731-2 HP and Teledyne CAE 702 HP turbines. To provide the proper initial conditions for the boundary layer solution, the stagnation point process starting from the far free stream is considered. The mean velocity and temperature and the turbulence variation along the stagnation streamline are predicted with a Reynolds stress model so as to resolve accurately the turbulent normal stresses that govern the production of turbulence in the stagnating flow. Using the results from the stagnation solution as initial conditions, the k - ϵ model equations in boundary layer form are solved at midspan for the pressure and suction sides of the vane and the blade, using a pressure distribution obtained from inviscid codes. The predicted surface heat transfer distributions are compared with measurements from short-duration full-stage rotating turbine measurements.

Introduction

Turbulence in the flow approaching a turbine blade can have a significant effect on the heat transfer at the blade surface. This free-stream turbulence influences not only the turbulent portions of the boundary layer on the blade, but also the quasi-laminar flow at the leading edge and the location of the transition region. Turbulence in the free stream is characterized by an intensity and a length scale that are measures of the energy and size of the eddies. As the flow approaches the blade from the far free-stream location and passes over the blade these quantities change. Thus, in order to simulate properly the occurrences in the boundary layer generated on the blade surface, the local free stream-turbulence environment should be taken into account.

The effects of the free-stream turbulence enter the prediction of the boundary layer on the blade surface in two ways, as illustrated in Fig. 1. First, the boundary-layer calculation is initiated from profiles for the velocity, turbulent kinetic energy, etc., near the stagnation point. Usually these initial velocity and temperature profiles are taken from laminar stagnation-point theory and the turbulence profiles are obtained from ad hoc assumptions. Secondly, quantities (kinetic energy and length scale or dissipation) describing the turbulence need to be specified as boundary conditions in the free stream adjacent to the boundary layer for the boundary-layer calculation. These conditions in the inviscid stream adjacent to the boundary layer are obtained by integrating simplified

versions of the turbulence-model equations in the streamwise direction around the blade surface from the stagnation region utilizing the inviscid flow velocity. Values at the stagnation point used to initiate this calculation are simply scaled from their far-upstream approach values.

There have been several recent attempts to use the two-equation kinetic energy/dissipation (k - ϵ) model to predict the turbine component heat transfer. Consigny and Richards (1982) compared predictions made with the k - ϵ model of Jones and

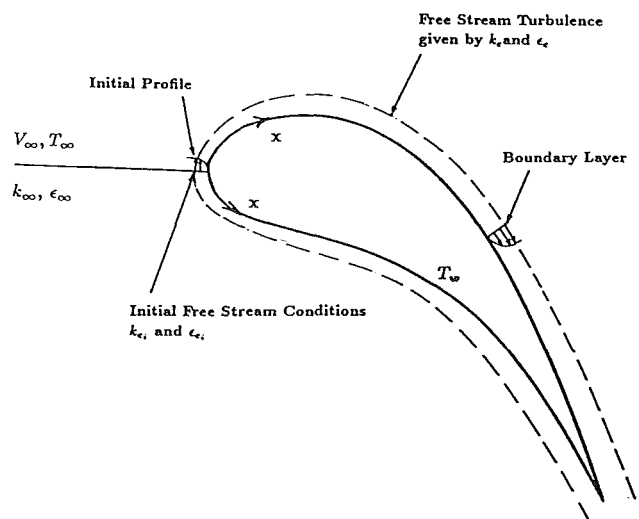


Fig. 1 Turbine flow with free-stream turbulence

Contributed by the International Gas Turbine Institute and presented at the 33rd International Gas Turbine and Aeroengine Congress and Exhibition, Amsterdam, The Netherlands, June 5-9, 1988. Manuscript received by the International Gas Turbine Institute June 18, 1987. Paper No. 88-GT-30.

Lauder (1973) with the experimental heat transfer for a cascade of turbine blades. The heat transfer at the leading edge region was not predicted. Their calculations started at some location away from the stagnation point with the initial velocity profile given by the solution of the Falkner-Skan equation and initial profiles for k and ϵ obtained using the mixing length hypothesis. They found that the predicted beginning of transition was not well located, and in some cases, not predicted at all. Because of the failure to predict the transition there were discrepancies with experimental data on the suction surface where the flow is in a state of transition over a considerable portion of the surface. Wang et al. (1985) also used the Jones and Launder k - ϵ model to predict the heat transfer on two different cascades of turbine vanes. The general trends on both surfaces of the vanes were predicted, although the heat transfer levels were somewhat in error in some cases. They investigated two different methods to generate the stagnation-point profiles, one utilizing the fully laminar flow solutions and the other utilizing the zero-equation model of turbulence. To predict transition on the suction surface correctly they argued that the free-stream turbulence remained constant down the vane surface until a critical free-stream velocity was reached, at which point it was allowed to vary according to the one-dimensional model equations. Rodi and Scheuerer (1985) used the low-Reynolds-number version of the k - ϵ model by Lam and Bremhorst (1981) to predict the turbine vane heat transfer. The calculations were initiated at a location away from the stagnation point, with the laminar velocity profile given by the Pohlhausen formula and the temperature profile related linearly to the velocity profile. The initial profiles of kinetic energy and dissipation were obtained from the empirical formulations. This version of the k - ϵ model, with the above assumptions at the starting location, gave predictions of heat transfer coefficients with reasonably good accuracy. Discrepancies with the measurements occurred only in the transition region, where the method showed a somewhat more rapid transition than was observed in the experiments.

In order to obtain the proper conditions concerning the free-stream turbulence for the boundary-layer prediction, the de-

tails of the stagnation process should be considered. Hence, the turbulence needs to be determined from the far upstream location, where the inlet conditions to the blade row are specified, to the blade surface at the stagnation point. In this paper we use Reynolds stress modeling to calculate the variation of the turbulence quantities along the stagnation streamline, thus determining the stagnation-point heat transfer. This solution also provides the initial conditions for the boundary-layer calculation down the component surfaces. The boundary-layer solution, from which the surface heat transfer is determined, is obtained using the two-equation k - ϵ model of turbulence. Surface heat transfer predictions are compared with data taken with thin-film gages mounted on the vanes and blades of a full-stage rotating turbine with a shock tube used as a short duration source of heated air. Comparisons are made for the Garrett TFE 731-2 HP and the Teledyne CAE 702 HP turbines.

Discussion of Method

Stagnation Streamline Turbulence. The stagnation point process can be viewed as made up of two parts. First, in the outer flow, an order of magnitude analysis shows that the turbulence does not significantly affect the mean flow. The turbulent stresses are negligible in the momentum equations and the flow is essentially inviscid. Turbulence in the outer flow is not directly affected by the surface except through interaction with the mean flow. Turbulence, starting in the flow far upstream of the stagnation point, will tend to decay by dissipation, but also will tend to increase by production due to streamwise velocity gradients as the body is approached. Hence, the turbulence is not constant between the far-upstream approach flow and a location at the outer edge of the stagnation region boundary layer. In the outer flow the turbulence begins to be significantly changed at several leading edge radii upstream by production from the mean flow velocity gradients.

Secondly, the inner flow or near-wall region is directly affected by the wall. The flow is affected by viscosity and the turbulent shear stress is important. A rough estimate shows

Nomenclature

A = nozzle guide vane inlet area
 C_μ, C_1, C_2 = k - ϵ model constants
 f_μ, f_2 = low-Reynolds number functions
 f' = $df/d\eta$ = similarity velocity variable
 g = similarity temperature variable
 H = total enthalpy
 k = turbulent kinetic energy
 l_∞ = free-stream turbulence scale
 p = static pressure
 $Pr = 0.7$ = Prandtl number
 $Pr_t = 0.90$ = turbulent Prandtl number
 q_w = wall heat flux
 $\overline{q^2} = \overline{u^2} + \overline{v^2} + \overline{w^2}$ = mean squared turbulent velocity
 R = leading edge radius
 $Re = 2V_\infty R \rho_\infty / \mu_\infty$ = Reynolds number
 $Re_T = k^2 / \nu \epsilon$ = turbulent Reynolds number
 $St = \frac{q_w}{(w/A)(H_0 - H_w)}$ = inlet Stanton number
 $Tu = u'_\infty / V_\infty$ = free-stream turbulence intensity
 U_i = mean velocity in i direction
 U = mean velocity in x direction
 $u_* = \sqrt{\tau_w / \rho}$ = friction velocity
 V = mean velocity in y direction
 V_∞ = mean free-stream velocity

w = weight flow rate through turbine
 x = coordinate parallel to wall
 y = coordinate perpendicular to wall
 y^+ = yu_* / ν
 $\overline{u_i u_j}$ = turbulent stresses (Reynolds stresses)
 $\overline{u^2}, \overline{v^2}, \overline{w^2}$ = turbulent normal stresses
 \overline{uv} = turbulent shear stress
 $\overline{u_i H'}$ = turbulent heat flux
 δ = boundary layer thickness
 δ_{ij} = Kronecker delta
 ϵ = rate of dissipation of turbulent kinetic energy
 η = similarity variable
 μ, μ_t = molecular and turbulent viscosity
 ρ = fluid density
 σ_ϵ = k - ϵ model constant
 $\tau_w = (\mu \partial u / \partial y)_w$ = shear stress at wall

Superscripts

(*) = refers to similarity variables
 ()' = fluctuating quantity
 () = time average

Subscripts

w = refers to wall surface
 ∞ = refers to free-stream condition
 e = refers to boundary layer edge

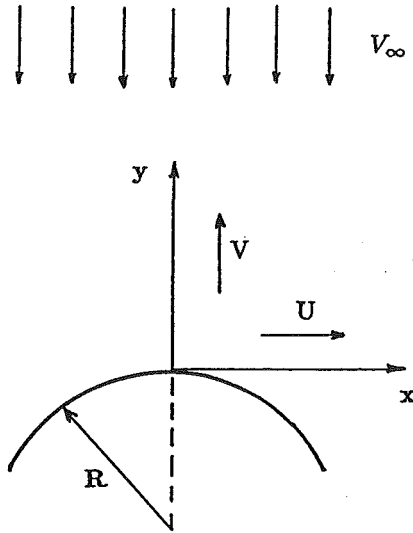


Fig. 2 Stagnation point nomenclature

that, for flow over a circular cylinder, this layer can have a thickness of roughly

$$\delta/R \cong 0.54(\text{Tu } l_\infty/R)^{1/2} \quad (1)$$

where Tu is the intensity and l_∞ is the length scale of the far-upstream turbulence, and R is the radius of the cylinder. This relation was obtained from $\delta/R = 2.4/\text{Re}^{1/2}$ for the laminar stagnation boundary layer, but using a turbulent eddy viscosity $\nu_t = c_\nu k^{1/2} l_\infty$ with $c_\nu = 0.09$ in place of the laminar viscosity and assuming that the turbulence intensity and length scales do not change in the outer flow. This relation shows that the boundary-layer thickness in the stagnation region can be on the order of 0.01 to 0.1 of the leading edge radius, depending on the magnitude of Tu and l_∞ . In this layer the wall directly affects the turbulent diffusion processes.

There have been many theoretical investigations of the effects of turbulence on stagnation-point flow. However, only Traci and Wilcox (1975), Sunden (1979), Strahle (1985), Strahle et al. (1987), and Hijikata et al. (1982) have considered the entire stagnation streamline process. Traci and Wilcox (1975) and Sunden (1979) used the $k-\omega$ two-equation model, where ω is the pseudovorticity. Although the predicted results of Traci and Wilcox (1975) and Sunden (1979) agree with each other, Sunden had to use low-Reynolds-number formulations of the model parameters to obtain agreement with experiment. Strahle (1985) and Strahle et al. (1987) used the $k-\epsilon$ two-equation model of Lam and Bremhorst (1981). They had to adjust a parameter in the outer solution in order to get agreement with experiment. Hijikata et al. (1982) recognized the shortcomings of the $k-\epsilon$ model when applied to the stagnation flow and developed a three-equation model, the third equation in addition to those for k and ϵ being written for the anisotropy between the streamwise and transverse Reynolds stress components. They had to modify the return-to-isotropy expression in that equation to obtain agreement with experimental data.

Two-equation models of turbulence utilize the constitutive relation

$$-\overline{u_i u_j} = \nu_t \left(\frac{\partial U_i}{\partial x_j} + \frac{\partial U_j}{\partial x_i} \right) - \frac{2}{3} k \delta_{ij} \quad (2)$$

for the Reynolds stresses. This equation works well for the shear components; however, it is not accurate for the normal components. The example of a homogeneous shear flow where $U = U(y)$, for which equation (2) gives $\overline{u^2} = \overline{v^2} = \overline{w^2} = 2k/3$, shows that it is not consistent with experimental observations even though $\overline{uv} = -\nu_t dU/dy$ is satisfied. Furthermore, equation (2) shows that if the flow has no mean flow gradients,

the turbulence can only be isotropic, which may not be true. If the flow is shear dominated then turbulent models utilizing equation (2) work well. However, if the shear is zero or weak and the production of turbulence is governed by normal stresses, as in the present problem, then the model prediction may be inaccurate. To avoid these difficulties, the dynamic equations for the Reynolds stresses should be used. Comparisons between predictions from the $k-\epsilon$ model and the Reynolds stress model will be presented later to illustrate the inadequacy of the $k-\epsilon$ model with equation (2).

We consider the stagnation flow on a cylindrical surface as illustrated in Fig. 2. To a first approximation the potential flow field near the stagnation point is given by

$$U = 2V_\infty x/R, \quad V = -2V_\infty y/R \quad (3)$$

which is reasonably valid for $y/R \leq 0.1$. The potential flow velocity field is linear in the region occupied by the boundary-layer region whose thickness is given by equation (1). Hence, similar scaling to that used in the laminar solution can be applied to the turbulent case. Then for the mean flow

$$\begin{aligned} \eta &= \text{Re}^{1/2} \int_0^\eta (\bar{\rho}/\rho_\infty) dy/R \\ U &= 2V_\infty(x/R)f' \\ \rho V &= -2\rho_\infty V_\infty f/\text{Re}^{1/2} \\ \bar{p} &= \bar{p}_0 - 2\rho_\infty V_\infty^2 [x^2/R^2 + F(\eta)] \end{aligned} \quad (4)$$

where $f' = df/d\eta$ and $\text{Re} = 2\rho_\infty V_\infty R/\mu_\infty$, and for the turbulence quantities

$$\begin{aligned} \overline{u^2} &= V_\infty^2 \overline{u^{2*}}(\eta) \\ \overline{v^2} &= V_\infty^2 \overline{v^{2*}}(\eta) \\ \overline{w^2} &= V_\infty^2 \overline{w^{2*}}(\eta) \\ \overline{uv} &= V_\infty^2 (x/R) \overline{uv^*}(\eta) \\ \epsilon &= (V_\infty^3/R)\epsilon^*(\eta) \end{aligned} \quad (5)$$

The momentum equation is

$$\bar{\rho} U_j \frac{\partial U_i}{\partial x_j} = -\frac{\partial \bar{p}}{\partial x_i} + \frac{\partial}{\partial x_j} \left[\mu \left(\frac{\partial U_i}{\partial x_j} + \frac{\partial U_j}{\partial x_i} \right) - \rho \overline{u_i u_j} \right] \quad (6)$$

where the mean quantities are taken to be mass averaged to account conveniently for variations in density, which are taken to be due only to changes in temperature and not compressibility. Changes in density only occur in the boundary layer where the temperature changes. Substituting equations (4) and (5) into (6) and keeping first-order terms gives

$$\begin{aligned} \left[\left(\frac{\bar{\rho}}{\rho_\infty} \frac{\bar{\mu}}{\mu_\infty} f'' - \frac{\text{Re}^{1/2}}{4} \frac{\bar{\rho}}{\rho_\infty} \overline{uv^*} \right) \right]' \\ + ff'' - (f')^2 + \frac{\rho_\infty}{\bar{\rho}} = 0 \end{aligned} \quad (7)$$

This equation determines the velocity profile in the boundary layer portion of the stagnating flow. The boundary condition at the edge of the boundary layer is $f'(\eta_\infty) = 1.0$ where η_∞ is roughly given by equation (1) in the numerical solution. However, care was taken to make η_∞ sufficiently large so the solution to equation (7) was independent of its choice. In the outer portion of the flow the potential flow solution for flow over a circular cylinder gives

$$f = \frac{\text{Re}^{1/2}}{2} \left[1 - \frac{1}{(1 + \eta/\text{Re}^{1/2})^2} \right] \quad (8)$$

It is assumed that the flow within a distance of several leading edge radii R of the turbine component is close to being that of a circular cylinder. Equation (8) is used outside the point where the solution to equation (7) is $f' = 0.995$.

The thermal field is determined from the energy equation

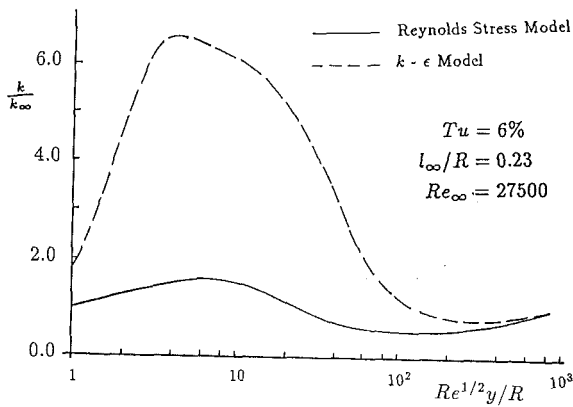


Fig. 3 Comparison of turbulent kinetic energy approaching the stagnation point

$$\bar{\rho} U_j \frac{\partial H}{\partial x_j} = \frac{\partial}{\partial x_j} \left[\left(\frac{\mu}{\text{Pr}} + \frac{\mu_r}{\text{Pr}_r} \right) \frac{\partial H}{\partial x_j} \right] \quad (9)$$

where $H = h + V^2/2 + k$ and the dissipation terms are negligible for relatively low speed stagnation-point flow. Since H significantly changes only in the boundary layer portion of the flow and is mainly influenced by cross-stream transport, a gradient diffusion assumption $\bar{\rho} u_i \bar{H}' = (\mu_r/\text{Pr}_r) \partial H/\partial x_i$ can be used. For the eddy viscosity we use $\mu_r = \rho C_{\mu} f_{\mu} k^2/\epsilon$ where $f_{\mu} = 1 - e^{-0.0115y^+}$ as given by Chien (1982). The turbulent Prandtl number is taken to be $\text{Pr}_r = 0.9$. Introducing the similarity variables given by equation (4) gives

$$\left[\frac{\mu}{\mu_{\infty}} \left(\frac{1}{\text{Pr}} + \frac{\mu_r/\mu}{\text{Pr}_r} \right) g' \right]' + fg' = 0 \quad (10)$$

where $g = (H - H_w)/(H_{\infty} - H_w)$. The temperature profile can be obtained from the stagnation enthalpy profile with the velocity profile from the solution of equation (7) and utilizing perfect gas relations. The density profile is obtained from the perfect gas equation of state $\bar{p} = \bar{\rho}RT$ where the pressure is determined from the last of equations (4) and $F(\eta)$ is determined from the y - momentum equation.

To determine the Reynolds stress components the second-order turbulence model given by Lumley (1978) was used with the formulation for the wall influence on the pressure-strain correlations given by Shih and Lumley (1986). These equations for the Reynolds stress model, when written in component form, are quite lengthy and, consequently, are given in the appendix along with the relevant model parameters. The equations are presented in Cartesian form and only those terms that remain after substituting the stagnation point form of the solution given by equations (4) and (5) are given.

To illustrate the final form of the equations we present the turbulent kinetic energy equation even though in our solution we calculate the component energies and find the energy by $k = (\bar{u}^2 + \bar{v}^2 + \bar{w}^2)/2$. The turbulent kinetic energy equation is

$$\bar{\rho} U_j \frac{\partial k}{\partial x_j} = -\frac{\partial}{\partial x_j} \left(-\mu \frac{\partial k}{\partial x_j} + \bar{\rho} \overline{u_j q^2/2} + \overline{u_j p} \right) + \bar{\rho} (P - \epsilon) \quad (11)$$

where the production is $P = -\overline{u_i u_j} \partial U_i/\partial x_j$. The pressure diffusion is modeled $\overline{u_j p} = -\rho \overline{u_j q^2/5}$ (Lumley, 1978); retaining first-order terms after substituting equations (4) and (5), the turbulent kinetic energy equation for stagnation-point flow becomes

$$\left[\frac{\mu}{\mu_{\infty}} k^{*'} - \frac{3}{5} \frac{\bar{\rho}}{\rho_{\infty}} \sqrt{\text{Re}} \overline{u q^2/2} \right]' + fk^{*'} + \frac{\bar{\rho}}{\rho_{\infty}} (P^* - \epsilon^*)/2 = 0 \quad (12)$$

and the production is

$$P^* = 2[\bar{v}^{2*} \bar{\rho} (f/\bar{\rho})' - \bar{u}^{2*} f'] \quad (13)$$

Note that the production involves the normal stresses \bar{u}^2 and \bar{v}^2 and for constant-density flow the production is proportional to their difference. The anisotropy in the turbulence that governs the production arises from the rapid part of the pressure-strain correlation $\bar{p}(\partial u_i/\partial x_j + \partial u_j/\partial x_i)$, which accounts for the distortion of the turbulence by the mean flow. The turbulent interaction part of the pressure-strain correlation tends to return the turbulence to isotropy. In the k - ϵ model the normal stresses are modeled with a gradient hypothesis that does not properly reflect the nature of the pressure-strain processes. In the present work, the Reynolds stresses are computed from the component equations given in the appendix.

Equations (A1)-(A4), when put into similarity form with equations (4) and (5), determine the Reynolds stress components \bar{u}^{2*} , \bar{v}^{2*} , \bar{w}^{2*} , and $\bar{u}v^*$ along the stagnation streamline. These equations, along with equation (A5) for ϵ^* , are valid along the entire stagnation streamline, although $\bar{u}v^*$ becomes negligibly small in the outer flow. This boundary value problem, consisting of the ordinary differential equations for the Reynolds stresses, is solved by finite differences and a block tridiagonal matrix solver. Zero stress conditions are set at the surface and $\bar{u}^2 = \bar{v}^2 = \bar{w}^2 = 2k_{\infty}/3$, $\bar{u}v = 0$ in the far free stream at a value of η equivalent to many radii. Similarly, the equation for ϵ^* is finite differenced and solved by a tridiagonal solver with $\epsilon = (2\nu \partial k^{1/2}/\partial y)^2$ at the surface as given by Hanjalic and Launder (1976) and $\epsilon_{\infty} = k_{\infty}^{3/2}/l_{\infty}$ where the far free-stream kinetic energy $k_{\infty} = 1.5 (TuV_{\infty})^2$ and length scale l_{∞} are specified. Equations (7) and (10) are solved for the velocity and enthalpy profiles in the boundary-layer portion of the flow. Equation (8) gives the velocity in the outer portion of the flow and the total enthalpy is essentially constant there. The entire set of equations is iterated until satisfactory convergence is achieved.

Figure 3 shows the Reynolds stress model solution (solid line) for the variation of turbulent kinetic energy along the stagnation streamline starting from far upstream values of $Tu = 6$ percent and $l_{\infty}/R \cong 0.23$, which are the conditions for the TFE vane. It is seen, starting from far upstream ($\eta = 2000$ or $y/R = 5$), that the energy first decreases by dissipation before it begins to increase significantly by production at about $\eta = 200$ or $y/R = 0.5$. At about the edge of the boundary layer ($\eta = 10$ or $y/R = 0.025$) the energy decreases toward the surfaces.

Also shown in Fig. 3 is the k - ϵ model (see next section) solution and it is seen that it is considerably different from the Reynolds stress model solution. As pointed out previously, the k - ϵ model does not accurately predict normal stresses and these components govern the production in stagnation flow. The Reynolds stress model predictions were compared with turbulence data given by Hijikata et al. (1982) and heat transfer data from several sources in the literature. Good agreement was found. Details of these results are given by Tran and Taulbee (1988).

Shown in Fig. 4 are the stagnation boundary layer temperature and velocity profiles for the TFE vane ($Tu = 6$ percent and $l_{\infty}/R = 0.23$). It is seen that the turbulent predictions are not too different from the laminar profiles. However, the predicted turbulent kinetic energy (Fig. 3) and dissipation profiles can be significantly different from those obtained from ad hoc assumptions, particularly since it is usually assumed that the turbulence properties are constant in the outer flow in turbine analysis (Consigny and Richard, 1982; Wang et al., 1985; Rodi and Scheuerer, 1985).

Boundary Layer Prediction. The boundary layer is a shear-dominated flow and the k - ϵ model can be used with confidence. The low-Reynolds-number version of the k - ϵ model used is from Chien (1982). This version was chosen because it predicts

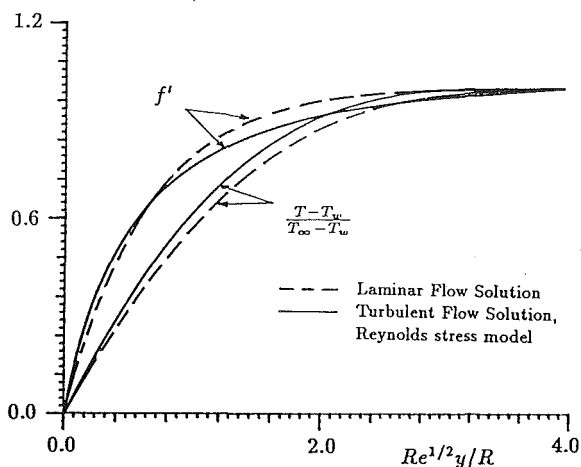


Fig. 4 Velocity and temperature profiles in the stagnation boundary layer

transition and the succeeding turbulent boundary layer on a flat plate with good accuracy, although predicted transitions occurred more abruptly than observed from experiment, as is common with the $k-\epsilon$ model. According to Patel et al. (1985) this version also performed reasonably well when compared with other model versions in predicting boundary layers with pressure gradients.

The continuity, momentum, thermal energy, turbulent energy, and dissipation equations are

$$\frac{\partial \bar{\rho} U}{\partial x} + \frac{\partial \bar{\rho} V}{\partial y} = 0 \quad (14)$$

$$\bar{\rho} U \frac{\partial U}{\partial x} + \bar{\rho} V \frac{\partial U}{\partial y} = - \frac{dP}{dx} + \frac{\partial}{\partial y} \left[(\mu + \mu_t) \frac{\partial U}{\partial y} \right] \quad (15)$$

$$\bar{\rho} U \frac{\partial U}{\partial x} + \bar{\rho} V \frac{\partial H}{\partial y} = \frac{\partial}{\partial y} \left[\left(\frac{\mu}{Pr} + \frac{\mu_t}{Pr_t} \right) \frac{\partial H}{\partial y} \right] + \frac{\partial}{\partial y} \left\{ \left[\mu \left(1 - \frac{1}{Pr} \right) + \mu_t \left(1 - \frac{1}{Pr_t} \right) \right] \frac{\partial}{\partial y} \left(\frac{U^2}{2} \right) \right\} \quad (16)$$

$$\bar{\rho} U \frac{\partial k}{\partial x} + \bar{\rho} V \frac{\partial k}{\partial y} = \frac{\partial}{\partial y} \left[(\mu + \mu_t) \frac{\partial k}{\partial y} \right] + \mu_t \left(\frac{\partial U}{\partial y} \right)^2 - \bar{\rho} \epsilon - \bar{\rho} D \quad (17)$$

$$\bar{\rho} U \frac{\partial \epsilon}{\partial x} + \bar{\rho} V \frac{\partial \epsilon}{\partial y} = \frac{\partial}{\partial y} \left[\left(\mu + \frac{\mu_t}{\sigma_\epsilon} \right) \frac{\partial \epsilon}{\partial y} \right] + C_1 \frac{\epsilon}{k} \mu_t \left(\frac{\partial U}{\partial y} \right)^2 - C_2 f_2 \bar{\rho} \frac{\epsilon^2}{k} + \bar{\rho} E \quad (18)$$

where the turbulent eddy viscosity is $\mu_t = \bar{\rho} C_\mu f_\mu k^2 / \epsilon$. For Chien's version, the model parameters are

$$C_\mu = 0.09 \quad C_1 = 1.35 \quad C_2 = 1.8 \quad \sigma_\epsilon = 1.3$$

$$D = 2\nu k / y^2 \quad E = -2(\nu\epsilon / y^2) e^{-0.5y^+}$$

$$f_\mu = 1 - e^{-0.0115y^+} \quad f_2 = 1 - 0.22 e^{-(Re_T/6)^2} \quad (19)$$

where $y^+ = U_\tau y / \nu$ and $Re_T = k^2 / \nu\epsilon$. The turbulent Prandtl number was taken to be $Pr_t = 0.9$.

Equations (14)–(18) were solved numerically, marching down the surface, to determine the boundary layer and resulting heat transfer on the vane or blade surfaces. The calculation was initiated from the stagnation point solution profiles similar to those illustrated in Fig. 4. The turbulence conditions at the boundary layer edge, which are used as boundary conditions, are determined from a streamwise (one-dimensional version) of the $k-\epsilon$ model

Table 1 Reference and turbulence conditions

	GARRETT TFE 731		Teledyne 702	
	Vane	Blade	Vane	Blade
Re_∞	27500	8190	91600	31000
Tu	6%	6%	6%	6%
l_w/R	0.23	0.22	0.09	0.24
k_e/k_∞	1.56	1.62	0.91	1.84
l_e/l_{m1}	5.89	5.65	0.67	9.66

$$U_e \frac{dk_e}{dx} = -\epsilon_e \quad U_e \frac{d\epsilon_e}{dx} = -C_2 \frac{\epsilon_e^2}{k_e} \quad (20)$$

which are solved numerically starting from initial conditions obtained from the stagnation-point solution at a location just outside the stagnation point boundary layer. The production terms in equations (20) have been neglected, though they can be significant in the highly accelerated flow on the suction surface. However, some difference in the free-stream turbulence level does not have much effect on the surface heat transfer in highly accelerated flow. The free-stream inviscid velocity distribution $U_e(x)$ was obtained from MERID and TSONIC for the Garrett TFE 731-2 as outlined by Rae et al. (1986) and from the three-dimensional Denton code for the Teledyne 702 as outlined in by Dunn and Chupp (1988).

Reference conditions for the two turbines used in the calculation are given in Table 1. The far free-stream turbulence level for the vane was estimated from a heat transfer measurement obtained using a circular rod placed 0.0074 m upstream of the vane for the TFE-731 test (Dunn et al., 1984). The length scale as well as the nature of the turbulence approaching the nozzle guide vane is unknown. In the test facility turbulence is produced by the shock wave standing in front of the model and by disturbances being fed upstream by the rotating turbine. Hence, the turbulence could be characteristic of the boundary layers on the component walls or it could be characteristic of the interaction between the shock wave and the oncoming flow. The length scale ($l_w = 0.3$ mm) used for the vane is characteristic of boundary layer turbulence at a Reynolds number based on the flow length from the inlet to the nozzle guide vane. Length scales estimated from the small-scale variations in the time records from pressure transducers and resistance thermometers indicated length scales an order of magnitude larger. However, these fluctuations could be associated with some other unsteadiness in the flow, since the resolution of the pressure instrument is not sufficient to resolve the turbulence in this flow.

Another problem associated with the upstream conditions is where to start the calculation for the approach flow. With no transport and production the model predicts essentially a decaying grid turbulence, which has a relatively rapid attenuation immediately after its initiation. If the calculation were initiated at the location (0.0074 m) upstream of the vane where the turbulence intensity was inferred to be 6 percent, little turbulence would be present as the fluid reaches the guide vanes. Since the turbulence in the vicinity upstream of the vanes is produced much farther upstream in the test model, the model calculation, corresponding to grid turbulence being initiated 0.0074 mm upstream of the guide vanes, is incorrect. However, the turbulence should probably decay in the midspan region of the channel upstream of the vane since the mean velocity gradient is small and the production is weak. For lack of something better, the calculation along the stagnation streamline was simply initiated at $y/R = 5$. This position allowed the turbulence to decay some before entering the steeper velocity gradients set up by the rounded leading edge of the vane contours where production becomes significant.

The turbulent intensity and length scales for the blade were chosen to be characteristic of those in the trailing edge boundary layer of the vane but allowing for some decay (~ 25 percent)

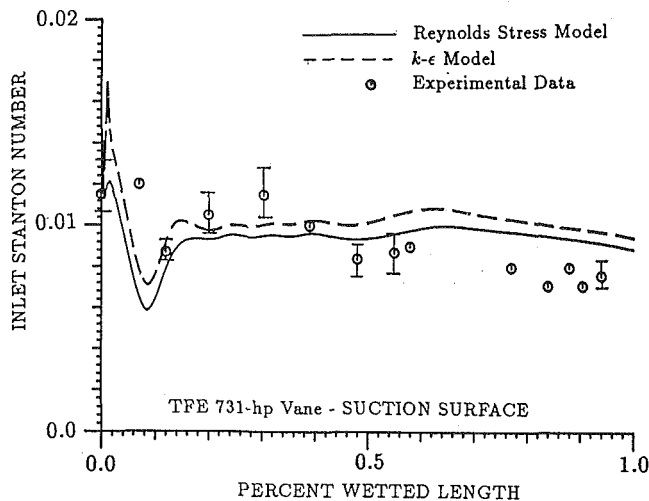


Fig. 5 Predictions of turbine blade heat transfer using different stagnation point initial profiles

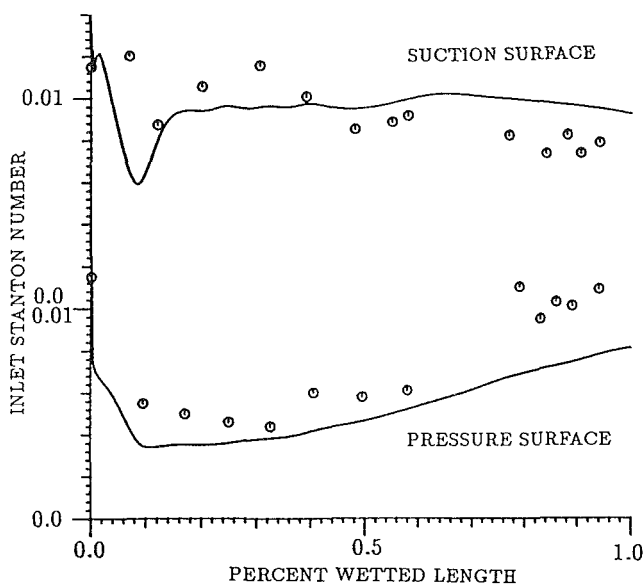


Fig. 6 Comparison of experimental data with prediction for the TFE 731-hp nozzle guide vane midspan

since the blade would see somewhat lower turbulence levels than appear on vane surfaces. Also, given in Table 1 are the predicted conditions just outside the stagnation-point boundary layer.

Discussion of Results

Figure 5 shows the boundary-layer heat transfer predictions on the surface of the TFE-731 vane using stagnation-point conditions from the Reynolds stress model and from the $k-\epsilon$ model. It is seen that the stagnation point predictions from the two turbulence models are not too different. However, immediately after the stagnation point, the boundary layer calculation initiated from the $k-\epsilon$ model stagnation-streamline calculations yields a high heat transfer due to the excessively large amount of turbulent energy in the stagnation profile. The high heat transfer rate rapidly attenuates farther down the surface so that the boundary layer heat transfer prediction from either initial condition is not too different. Away from the stagnation point the surface heat transfer is primarily governed by the high local pressure gradients, which tend to negate the effect of large turbulent kinetic energy in the stagnation region. Except for the region very near the stagnation point, the heat transfer from the boundary layer calculation initiated

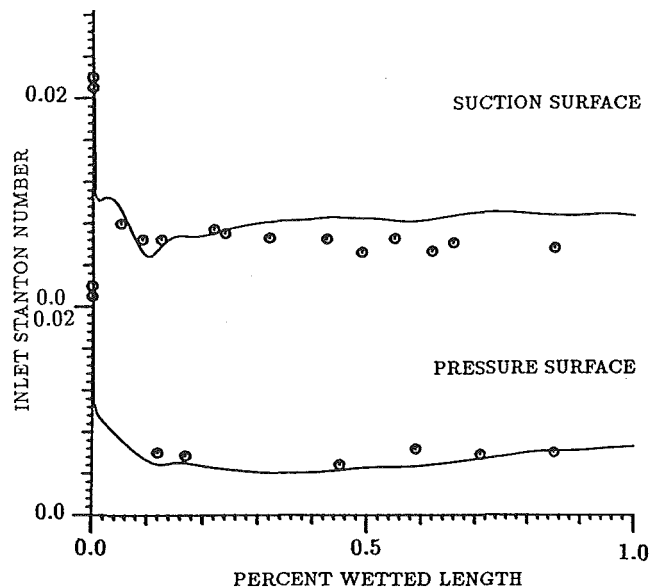


Fig. 7 Comparison of experimental data with prediction for the TFE 731-hp blade midspan

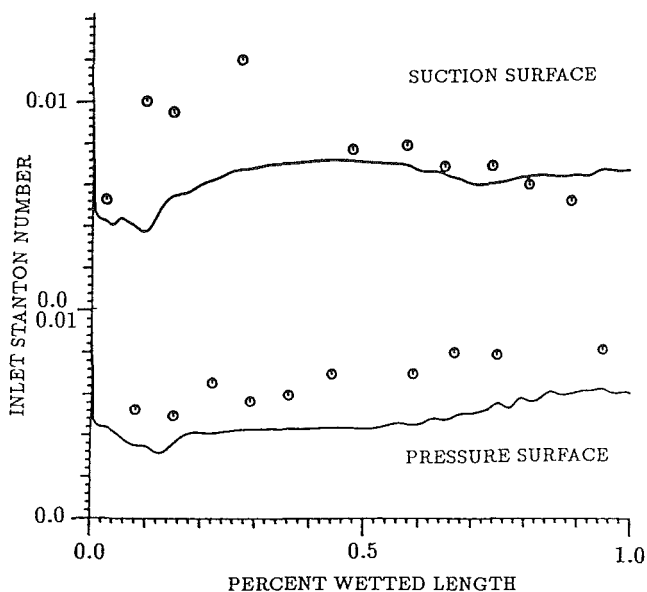


Fig. 8 Comparison of experimental data with prediction for the Teledyne 702 nozzle guide vane midspan

with the $k-\epsilon$ model stagnation-process prediction is 5-10 percent higher than that initiated from the Reynolds-stress model predictions.

The predictions for the TFE-731 turbine surfaces are shown in Figs. 6 and 7 and for the Teledyne turbine in Figs. 8 and 9. In each case the stagnation point Stanton numbers were overpredicted - 24 percent for the TFE vane, 41 percent for the TFE blade, and 15 percent for the Teledyne blade (there are no data at the stagnation point for the Teledyne vane). Part of these differences can be due to specification of the reference length scale and the choice of the point where the stagnation streamline calculation is initiated as discussed previously. Also, the velocity distribution on the stagnation streamline was assumed to be that for a circular cylinder. The measured values at the stagnation points were not too different from laminar stagnation point predictions. However, the leading edge thin-film gage may not have been placed at the actual stagnation point location. Also, predictions farther down the surface required certain amounts of turbulence at the stag-

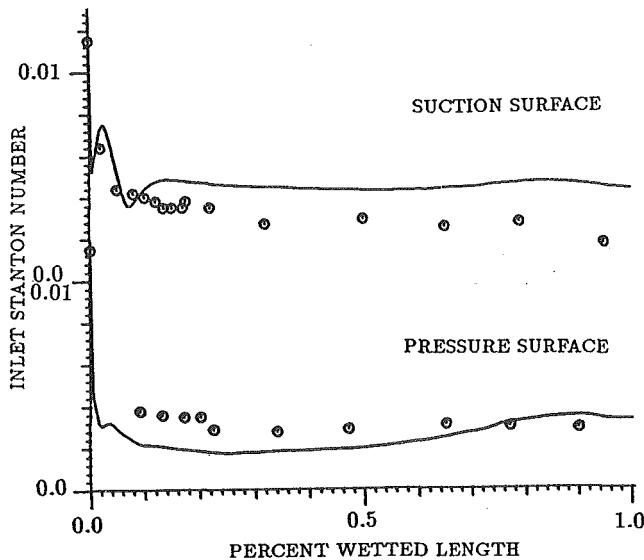


Fig. 9 Comparison of experimental data with prediction for the Teledyne 702 blade midspan

nation point region to prevent large laminar-type regions with low heat transfer rates from occurring on the suction surfaces.

Overall the predicted heat transfer rates are reasonably good. Immediately downstream of the stagnation point the predicted Stanton numbers follow the trends of the experimental data: rapidly decreasing to a lower level. However, in the case of the Teledyne vane suction surface (Fig. 8) the experimental Stanton number increases to higher values between roughly 10 and 40 percent of the wetted surface where the prediction did not increase rapidly. Part of the differences between prediction and experiment near the leading edge can be attributed to the pressure distribution obtained from inviscid codes. The grid spacings in these solutions were relatively coarse and may not have been able to resolve the rapid change in pressure along the surface away from the stagnation point. This is especially critical on the suction surfaces where the pressure decreases very rapidly to a sharp minimum at about 5–10 percent of surface from the stagnation point. The boundary layer calculation required interpolation of the surface pressure distribution from the inviscid solution, which also introduces errors. The lack of accurate definition of the inviscid pressure distribution is felt to be responsible for some of the discrepancies observed in the predictions near the leading edge on the suction surfaces.

Differences between the predictions and the measurements farther down the surface may be due to the use of a two-dimensional boundary layer solution. However, due to secondary flow phenomena in the passage the boundary layer can be highly three dimensional. Also, the inviscid pressure distributions may be in error since they do not reflect vorticity-generated secondary flows such as the horseshoe vortex. Furthermore, the actual average pressure distributions, particularly near the trailing edge of the vanes and the leading edge of the blades, may be different from steady inviscid predictions due to rotor–stator interactions. Finally, it is known that the k - ϵ model does not perform very well in adverse pressure gradients (Rodi and Scheuerer, 1986).

Conclusions

In general, it is concluded that the Reynolds-stress model (Lumley, 1978) without adjusting model constants reasonably predicts the stagnation point process even though assumptions are made concerning the nature of the turbulence and its length scale far upstream of the vanes. With proper initial conditions obtained from the stagnation point solution, the k - ϵ boundary

layer model gives reasonable predictions for the heat transfer rates on the vane and blade surfaces. There are some discrepancies between predictions and experiment that are thought to be due to inadequate definition of the inviscid flow pressure distribution, lack of knowledge concerning the length scale of the free-stream turbulence, and the inadequacy of the k - ϵ model to predict boundary layers in adverse pressure gradients and the effects of free-stream turbulence with relatively large length scale.

References

- Chien, K. Y., 1982, "Predictions of Channel and Boundary Layer Flows With a Low-Reynolds Number Turbulence Model," *AIAA Journal*, Vol. 20, pp. 33–38.
- Consigny, H., and Richards, B. E., 1982, "Short Duration Measurements of Heat Transfer Rate to a Gas Turbine Rotor Blade," *ASME Journal of Engineering for Power*, Vol. 104, pp. 542–551.
- Dunn, M. G., Rae, W. J., and Holt, J. L., 1984, "Measurement and Analyses of Heat Flux Data in a Turbine Stage: Part II – Discussion of Results and Comparison With Predictions," *ASME Journal of Engineering for Gas Turbines and Power*, Vol. 106, pp. 234–240.
- Dunn, M. G., and Chupp, R. E., 1988, "Time-Averaged Heat-Flux Distributions and Comparison With Prediction for the Teledyne 702 HP Turbine Stage," *ASME JOURNAL OF TURBOMACHINERY*, Vol. 110, pp. 51–56.
- Hanjalic, K., and Launder, B. E., 1976, "Contribution Towards a Reynolds-Stress Closure for Low-Reynolds Number Turbulence," *J. of Fluid Mechanics*, Vol. 74, pp. 593–610.
- Hijikata, K., Yoshida, H., and Mori, Y., 1982, "Theoretical and Experimental Study of Turbulence Effects on Heat Transfer Around the Stagnation Point of a Cylinder," *Proceedings of the 7th Int. Conference*, Vol. 3, Hemisphere Publ. Corp., Washington, DC, pp. 165–170.
- Jones, W. P., and Launder, B. E., 1973, "The Calculation of Low-Reynolds Number Phenomena With a Two-Equation Model of Turbulence," *Int. J. Heat Mass Transfer*, Vol. 16, pp. 1119–1130.
- Lam, C. K. G., and Bremhorst, K. A., 1981, "Modified Form of the k - ϵ Model for Predicting Wall Turbulence," *ASME Journal of Fluids Engineering*, Vol. 103, pp. 456–460.
- Lumley, J. L., 1978, "Computational Modeling of Turbulent Flows," *Advances in Applied Mechanics*, Vol. 18, pp. 123–176.
- Patel, V. C., Rodi, W., and Scheuerer, G., 1985, "Turbulence Models for Near-Wall and Low-Reynolds Number Flows: A Review," *AIAA Journal*, Vol. 23, No. 9, pp. 1308–1318.
- Rae, W. J., Taulbee, D. B., Civinskas, K. C., and Dunn, M. G., 1986, "Turbine-Stage Heat Transfer: Comparison of Short-Duration Measurements With State-of-the-Art Prediction," *AIAA Paper No. 86-1465*.
- Rodi, W., and Scheuerer, G., 1985, "Calculation of Heat Transfer to Convection-Cooled Gas Turbine Blades," *ASME Journal of Engineering for Gas Turbines and Power*, Vol. 107, pp. 620–627.
- Rodi, W., and Scheuerer, G., 1986, "Scrutinizing the k - ϵ Turbulence Model Under Adverse Pressure Gradient Conditions," *ASME Journal of Fluids Engineering*, Vol. 108, pp. 174–179.
- Shih, T.-H., and Lumley, J. L., 1986, "Second-Order Modeling of Near Wall Turbulence," *Phys. Fluids*, Vol. 29, pp. 971–975.
- Strahle, W. C., 1985, "Stagnation Point Flow With Freestream Turbulence – The Matching Condition," *AIAA Journal*, Vol. 23, pp. 1822–1824.
- Strahle, W. C., Sigman, R. K., and Meyer, W. L., 1987, "Stagnating Turbulent Flows," *AIAA Journal*, Vol. 25, pp. 1071–1077.
- Sunden, B., 1979, "A Theoretical Investigation of the Effect of Freestream Turbulence on Skin Friction and Heat Transfer for a Bluff Body," *Int. J. Heat Mass Transfer*, Vol. 22, pp. 1125–1135.
- Traci, R. M., and Wilcox, D. C., 1975, "Freestream Turbulence Effects on Stagnation Point Heat Transfer," *AIAA Journal*, Vol. 13, pp. 890–896.
- Tran, L., and Taulbee, D. B., 1988, "Prediction of Stagnation Point Heat Transfer With Free Stream Turbulence," to be submitted.
- Wang, J. H., Jen, H. F., and Hartel, E. O., 1985, "Airfoil Heat Transfer Calculation Using a Low-Reynolds Number Version of a Two-Equation Turbulence Model," *ASME Journal of Engineering for Gas Turbines and Power*, Vol. 107, pp. 60–67.

APPENDIX

Reynolds Stresses

$$\begin{aligned} \bar{\rho} V \frac{\partial \bar{u}^2}{\partial y} = & \frac{\partial}{\partial y} \left[\left(\mu + \frac{5\beta + 8}{3\beta(4\beta + 10)} \frac{\bar{q}^2}{\epsilon} \rho v^2 \right) \frac{\partial \bar{u}^2}{\partial y} \right] \\ & + \frac{\partial}{\partial y} \left[\frac{\bar{q}^2}{\epsilon} \left(\frac{\beta - 2}{3\beta(4\beta + 10)} \rho v^2 \frac{\partial}{\partial y} (\bar{w}^2 + 3\bar{v}^2) \right. \right. \\ & \left. \left. + \frac{2(5\beta + 8)}{3\beta(4\beta + 10)} \rho \bar{u}^2 \frac{\partial \bar{u}v}{\partial x} \right) \right] \end{aligned}$$

$$-2(4C+1)\rho\bar{u}^2 \frac{\partial U}{\partial x} + 4C\rho\bar{v}^2 \frac{\partial V}{\partial y} + 4\left(C + \frac{1}{10}\right)\rho\bar{q}^2 \frac{\partial U}{\partial x} - \beta\epsilon\rho \frac{\bar{u}^2}{\bar{q}^2} + \frac{\beta-2}{3}\rho\epsilon + C_{2w} \left(\frac{\bar{u}^2}{\bar{q}^2} - \frac{1}{3}\right)\rho\epsilon F^{1/2} \frac{l}{y} \quad (\text{A1})$$

$$\begin{aligned} \bar{\rho}V \frac{\partial \bar{v}^2}{\partial y} &= \frac{\partial}{\partial y} \left[\left(\mu + \frac{17\beta+20}{5\beta(4\beta+10)} \frac{\bar{q}^2}{\epsilon} \rho\bar{v}^2 \right) \frac{\partial \bar{v}^2}{\partial y} \right] \\ &+ \frac{\partial}{\partial y} \left[\left(-\frac{\beta+10}{5\beta(4\beta+10)} \frac{\bar{q}^2}{\epsilon} \right) \left(\rho\bar{v}^2 \frac{\partial \bar{u}^2}{\partial y} + \rho\bar{v}^2 \frac{\partial w^2}{\partial y} + 2\rho\bar{u}^2 \frac{\partial \bar{u}\bar{v}}{\partial x} \right) \right] \\ &+ 4C\rho\bar{u}^2 \frac{\partial U}{\partial x} - 2(4C+1)\rho\bar{v}^2 \frac{\partial V}{\partial y} + 4\left(C + \frac{1}{10}\right)\rho\bar{q}^2 \frac{\partial U}{\partial x} \\ &- \beta\epsilon\rho \frac{\bar{v}^2}{\bar{q}^2} + \frac{\beta-2}{\epsilon}\rho\epsilon + C_{2w} \left(\frac{\bar{v}^2}{\bar{q}^2} - \frac{1}{3}\right)\rho\epsilon F^{1/2} \frac{l}{y} \quad (\text{A2}) \end{aligned}$$

$$\begin{aligned} \bar{\rho}V \frac{\partial \bar{w}^2}{\partial y} &= \frac{\partial}{\partial y} \left[\left(\mu + \frac{5\beta+8}{3\beta(4\beta+10)} \frac{\bar{q}^2}{\epsilon} \rho\bar{v}^2 \right) \frac{\partial \bar{w}^2}{\partial y} \right] \\ &+ \frac{\partial}{\partial y} \left[\left(\frac{\beta-2}{3\beta(4\beta+10)} \frac{\bar{q}^2}{\epsilon} \right) \left(\rho\bar{v}^2 \frac{\partial \bar{u}^2}{\partial y} + 3\rho\bar{v}^2 \frac{\partial \bar{v}^2}{\partial y} + 2\rho\bar{u}^2 \frac{\partial \bar{u}\bar{v}}{\partial x} \right) \right] \\ &+ 4C \left(\rho\bar{u}^2 \frac{\partial U}{\partial x} + \rho\bar{v}^2 \frac{\partial V}{\partial y} \right) - \beta\epsilon\rho \frac{\bar{u}^2}{\bar{q}^2} + \frac{\beta-2}{\epsilon}\rho\epsilon \quad (\text{A3}) \end{aligned}$$

$$\begin{aligned} \bar{\rho}U \frac{\partial \bar{u}\bar{v}}{\partial x} + \rho V \frac{\partial \bar{u}\bar{v}}{\partial y} &= \frac{\partial}{\partial y} \left[\left(\mu + \frac{8}{15\beta} \frac{\bar{q}^2}{\epsilon} \rho\bar{v}^2 \right) \frac{\partial \bar{u}\bar{v}}{\partial y} \right] \\ &+ \frac{\partial}{\partial y} \left[\left(\frac{1}{3\beta} \frac{\bar{q}^2}{\epsilon} \rho\bar{u}\bar{v} \right) \left(\frac{\partial}{\partial y} \left(\bar{v}^2 - \frac{2}{5}\bar{u}^2 - \frac{1}{5}\bar{q}^2 \right) + \frac{8}{5} \frac{\partial \bar{u}\bar{v}}{\partial x} \right) \right] \\ &+ \left[-\frac{2C+1}{3} \rho\bar{v}^2 - \frac{2(8C+1)}{3} \rho\bar{u}^2 + 2\left(C + \frac{1}{10}\right)\rho\bar{q}^2 \right] \frac{\partial U}{\partial y} \\ &- \beta\epsilon\rho \frac{\bar{u}\bar{v}}{\bar{q}^2} + \left[2C_{1w} \rho\bar{q}^2 \frac{\partial U}{\partial y} + C_{2w} \frac{\bar{u}\bar{v}}{\bar{q}^2} \rho\epsilon \right] F^{1/2} \frac{l}{y} \quad (\text{A4}) \end{aligned}$$

Dissipation

$$\begin{aligned} \bar{\rho}V \frac{\partial \epsilon}{\partial y} &= \frac{\partial}{\partial y} \left[\left(\mu + \frac{9}{5(4\beta+10)} \rho \frac{\bar{q}^2}{\epsilon} \left(\bar{v}^2 + 2 \frac{(\bar{v}^2)^2}{\bar{q}^2} \right) \right) \frac{\partial \epsilon}{\partial y} \right] \\ &+ \frac{\epsilon}{\bar{q}^2} \psi_1 \text{Prod} - \rho \frac{\epsilon}{\bar{q}^2} \tilde{\epsilon} f_\epsilon \psi_0 \end{aligned}$$

where

$$\begin{aligned} \text{Prod} &= -\rho\bar{u}^2 \frac{\partial U}{\partial x} - \rho\bar{v}^2 \frac{\partial V}{\partial y} \\ \tilde{\epsilon} &= \epsilon - 2\nu \left[\frac{\partial(\bar{q}^2/2)}{\partial y} \right]^2 \\ f_\epsilon &= 1 - \frac{0.4}{1.8} \exp\left(-\left(\frac{\text{Re}_T}{6}\right)^2\right) \quad (\text{A5}) \end{aligned}$$

Model Parameters

$$\beta = 2 + \exp\left(\frac{-7.77}{\sqrt{R_l}}\right) \left(\frac{F}{9}\right)x$$

$$\left\{ \frac{72}{\sqrt{R_l}} + 80.1 \ln[1 + 62.4(-\text{II} + 2.3\text{III})] \right\}$$

$$F = 1 + 9\text{II} + 27\text{III}$$

$$\text{II} = -\frac{b_{ij}b_{ji}}{2}$$

$$\text{III} = \frac{b_{ij}b_{jk}b_{ki}}{3}$$

$$R_l = \frac{(\bar{q}^2)^2}{9\epsilon\nu}$$

$$b_{ij} = \left(\frac{u_i u_j}{\bar{q}^2} - \frac{1}{3} \delta_{ij} \right)$$

$$C = \frac{1}{10} (1 + 0.8\sqrt{F})$$

$$C_{1w} = 0.015$$

$$C_{2w} = 0.25$$

$$\psi_1 = 2.4$$

$$\psi_0 = \frac{14}{5} + 0.98 \left[\exp\left(\frac{-2.83}{\sqrt{R_l}}\right) [1 - 0.33 \ln(1 - 55\text{II})] \right]$$

Aerodynamic and Heat Transfer Measurements on a Transonic Nozzle Guide Vane

E. T. Wedlake

A. J. Brooks

S. P. Harasgama

Procurement Executive, Ministry of Defence,
Royal Aerospace Establishment,
Pyestock, Farnborough,
Hampshire, England

Experimental determination of heat transfer rates to gas turbine blading plays an important part in the improvement of both the validation of existing design methods and the development of improved design codes. This paper describes a series of tests on an annular cascade of nozzle guide vanes designed for a high-work-capacity single-stage transonic turbine. The tests were carried out in the Isentropic Light Piston Cascade at the Royal Aerospace Establishment, Pyestock, and a brief description of this new test facility is included. Measurements of local heat transfer rates and aerodynamic data around the blade surface and on the end walls are described.

Introduction

For many years it has been recognized that the design of an efficient high-pressure turbine with adequate component life is crucial to the success of any gas turbine engine project, military or civil. Inherent in the design process is the need to predict accurately the aerodynamic flow and external heat transfer distributions around the airfoils and endwall surfaces. The increasingly complex three-dimensional geometry of modern high-pressure turbine blading compounds the problems of accurate prediction. The need for high-quality experimental data is still paramount, both to understand the performance of current and proposed designs and as a basis for the development and validation of theoretical prediction methods.

Some major advances in the techniques for measuring heat transfer to turbine blading originated from research at the Department of Engineering Science of Oxford University. Studies of blade cooling using shock tunnels and specialized instrumentation techniques for measurement of heat transfer began in the late 1960s, leading to the development of a novel form of intermittent wind tunnel specifically for this work.

Out of this work came the facility at RAE Pyestock known as the Isentropic Light Piston Cascade (ILPC), which tests an annular cascade of turbine airfoils where secondary flow and endwall heat transfer have been correctly simulated. The facility was fully described by Brooks et al. (1985) but a brief summary of the principles of operation is included below for completeness.

This paper presents the results of the first set of tests carried out in the tunnel on a cascade of nozzle guide vanes.

The Principles

For measurement of heat transfer from the gas to turbine components, it can be shown that it is acceptable to model the

gas-to-metal temperature ratio rather than actual temperatures. Thus, although the gases entering a turbine may be at around 1500 K and the blades at 1000 K, tests with blades at ambient temperature (288 K) only require a test gas temperature of 432 K. By using thin-film resistance thermometers on an insulating substrate of known thermal properties to record local surface temperatures on the blades and by considering the flow of heat into the body of the blade to be one dimensional over short time periods, local heat transfer rates may be deduced. Heat transfer measurements may therefore be made by passing moderately heated gas over test blades for a period just long enough to record the response of surface temperatures to the passage of the hot gas.

A gas total temperature of 432 K can be obtained by an isentropic compression of modest pressure ratio from an initial temperature of 288 K. The test gas was contained within a tube and was compressed isentropically by a piston, which was driven along the tube by a flow of air from a high-pressure reservoir. When the gas had been compressed, and hence heated to the required temperature, a fast-acting valve was opened, which allowed the compressed gas to flow through a cascade of airfoils in the working section (Fig. 1).

The specification for the ILPC required it to be capable of testing a full-size annular cascade of nozzle guide vanes from a large civil engine at correct Reynolds number and Mach number. This demanded a pump tube with a large volume. Considerations of a fine surface finish to permit smooth travel of the free piston limited the dimensions of the pump tube to a bore of 1.2 m with a length of 9 m.

Initial pressures in the pump tube and downstream of the working section were preset to control the Reynolds number and Mach number of the flow through the working section. The area of the throat admitting high-pressure air behind the piston was matched to the throat area of the test cascade so that volumetric flow rates into and out of the tube were equal and thus conditions in the working section were constant over the test period. An idealized pressure-time relationship during a run is shown in Fig. 2.

Contributed by the International Gas Turbine Institute and presented at the 33rd International Gas Turbine and Aeroengine Congress and Exhibition, Amsterdam, The Netherlands, June 5-9, 1988. Manuscript received by the International Gas Turbine Institute November 9, 1987. Paper No. 88-GT-10.

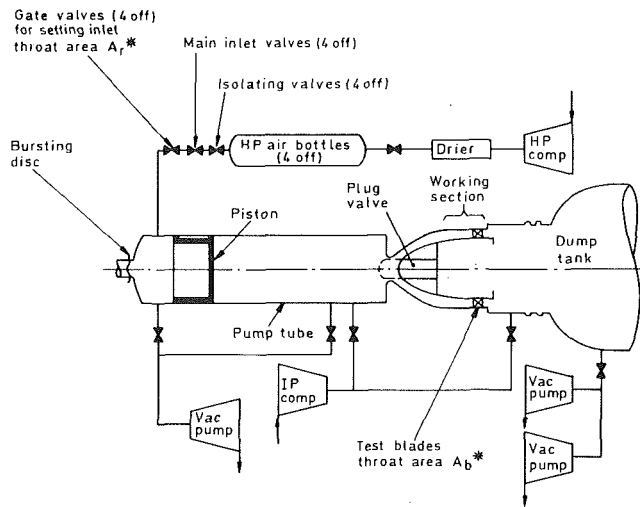


Fig. 1 Configuration of the ILPC facility

Signals from instrumentation in the test cascade were recorded during the run. Even in the short times available (typically 0.5 s) it was practical to record aerodynamic as well as heat transfer data provided that care was taken to minimize transducer tubing lengths and volumes.

The derivation of heat transfer rates from surface temperatures may be done numerically. However, it can be done much more simply and directly by the use of an electrical analogue circuit.

Testing at reduced temperature offers two further benefits. Firstly, at the lower temperatures a design Reynolds number simulation can be achieved at only 20–25 percent of the pressure levels required at typical engine temperatures. This significantly reduced rig stressing problems. Secondly, easily machinable materials can be used for the construction of test blades and other parts.

The use of short-duration test facilities is also advantageous from the point of view of power requirements. To test a full-scale set of nozzle guide vanes for a typical civil engine at maximum operating conditions in a continuous flow rig would require approximately 20 MW. The high-pressure compressor for the ILPC is rated at 43 kW.

Data Acquisition System

The data acquisition system included:

- 96 pressure measuring channels
(Scanivalve ZOC subsystem 25,000 samples/s)
- 64 heat transfer rate channels
- 16 tunnel monitoring channels
- 128 computer A/D channels
(20,000 samples/s, 12 bit)
- DEC PDP 11/24 computer employing the RT11 operating system
- 8 channel, 2 MHz, fast transient recorder (10 bit)
- 12 channel UV recorder

For the large number of pressure channels required, the Scanivalve ZOC (Zero, Operate, Calibrate) system was adopted. This system used multiple silicon pressure sensors that were partially temperature compensated and that had their zero, range drift, and linearity corrected immediately prior to making a measurement. The system had its own microprocessor, which, by controlling pneumatic valves built into the transducer modules, zeroed and calibrated each transducer before the tunnel was run. The system stored the pressure data taken during the run, scaled them according to the calibrations, and later downloaded them to the host PDP 11/24 computer.

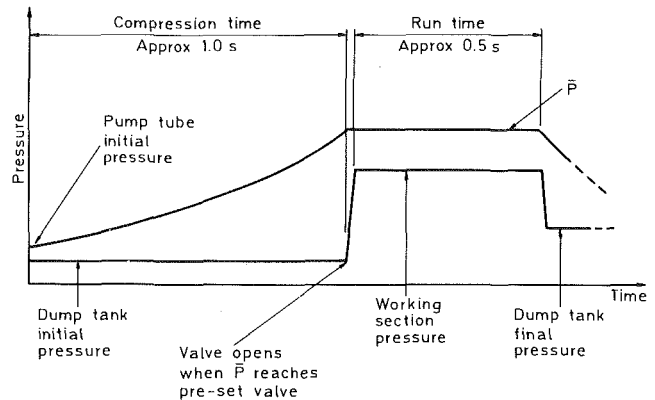


Fig. 2 Idealized pressure-time history

From there, test data were sent directly to a VAX 11/780 computer for more detailed analysis and three-dimensional graphical presentation.

The complete instrumentation system was run and monitored by a tunnel operating system software suite developed at Oxford by Baines (1983). It has been developed as a user-friendly, modular, menu-driven system, which was used to set up the instrumentation before a run, acquire data during the run, and subsequently process, print, and plot the results.

Interlocking, alarms, and operating sequences for the rig's plant and test valve systems were controlled by two Programmable Logic Controllers (PLCs).

The Cascade

The annular cascade of 40 NGVs under test was from a high-work-capacity, single-stage, transonic, HP turbine designed and tested by Bryce et al. (1985) at RAE Pyestock. The NGVs had a design outlet angle of over 74 deg, approximately constant from root to tip, and a design point exit Mach number of around 1.3. A major objective of the design was to control the transonic flow in order to achieve good turbine performance, and to this end the NGVs had convergent-divergent passages with some degree of suction surface concavity. The design gave full recognition to the constraints imposed by a practical coolable engine configuration.

Two-dimensional cascade tests at Oxford by Litchfield and Norton (1982) demonstrated good aerodynamic performance of the midheight section at design conditions. However, in the cold flow turbine testing reported by Bryce et al. (1985) the mass flow was about 1.3 percent less than design, resulting in a significant overexpansion of the flow downstream of the throat followed by a sharp recompression.

In these ILPC tests, the vanes and outer endwall were instrumented with heat transfer gages and static pressure tappings. On the vanes, heat transfer gages were positioned at midspan and at 20 and 80 percent span planes on two vanes, which formed one passage. Pressure tappings were provided at midspan and at 8 and 92 percent span on six separate vanes around the annulus. Outer endwall measurements were taken from 30 static pressure tappings and 29 heat transfer gages positioned in two vane passages. Static pressure tappings and total pressure rakes were installed in the inlet casings at various points around the annulus and were used during initial testing to verify the uniformity of the inlet flow.

The heat transfer instrumentation consisted of platinum thin-film thermometers on the vane surfaces and endwalls, which were manufactured from Corning MACOR machinable glass ceramic, a semi-infinite substrate for heat transfer analysis (Oldfield et al., 1978; Schultz and Jones, 1973). The heat transfer rates to the surfaces were derived from the surface temperature signals by the use of the 100 kHz bandwidth analogue circuits described by Oldfield et al. (1982).

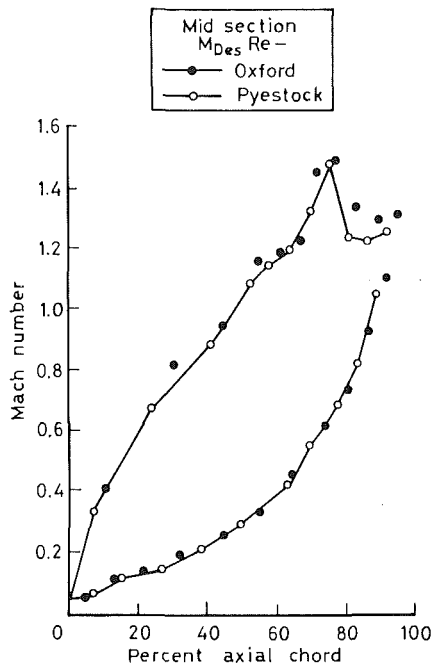


Fig. 3 Comparison of Mach number distributions measured at Pyestock and Oxford

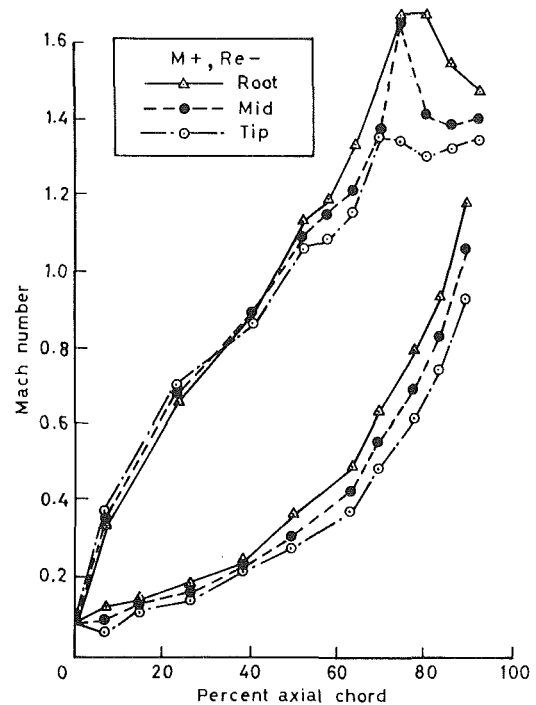


Fig. 5 Variation of Mach number distribution with position on vane

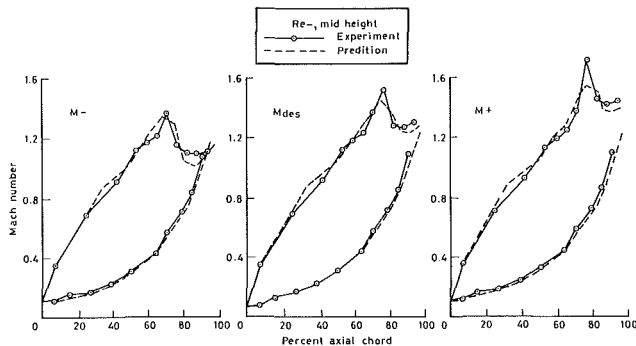


Fig. 4 Comparison of measured and predicted Mach number distribution

Test Conditions

Testing was carried out at three exit Mach numbers (1.1, 1.3, and 1.4 designated M-, M design, and M+, respectively) and at two Reynolds numbers (1.75×10^6 and 3.5×10^6 , designated Re- and Re des). Testing at higher Reynolds numbers, and at lower exit Mach numbers at Re des, was not possible due to mechanical limitations applicable to this initial commissioning build only.

Vane surface heat transfer and pressure results were also compared with work undertaken at OUEL on a two-dimensional cascade of the same vane profile (Litchfield and Norton, 1982). Throughout the build, a grid was installed in the inlet duct to generate isotropic turbulence at the vane leading edge plane sufficient to ensure suction surface boundary layer transition. The turbulence intensity was measured at 6.9 percent using a constant-temperature hot-wire anemometer built into the leading edge of one vane (Appendix 1).

Profile Aerodynamic Measurements

The isentropic Mach number distribution around the midheight section of the airfoil, calculated from measured surface static pressures, is shown in Fig. 3. The smooth acceleration around the suction surface will be noted with no discon-

tinuities due to overexpansion and recompression near the throat. Downstream of the throat a pronounced peak in the characteristic occurred followed by a sharp recompression and some supersonic expansion toward the trailing edge. This discontinuity on the suction surface was caused by the impingement of the cross-passage oblique shock wave system emanating from the trailing edge of the adjacent vane. The figure also compares the results from this annular cascade with those obtained on the two-dimensional cascade at Oxford University using the same midspan profile (Litchfield and Norton, 1982). The distributions are very similar with the exception that the annular cascade experienced a sharper recompression downstream of the shock wave impingement region.

The close agreement between the experimental vane surface Mach number distribution at various vane exit conditions and that computed using a Denton three-dimensional time marching program can be seen in Fig. 4.

Higher experimental velocities near the trailing edge were probably caused by increased flow blockage due to viscous effects which were not modelled in the inviscid calculation procedure. The trailing edge shock interaction remained significant even at low exit Mach numbers on this midspan section and there is evidently some negative lift over the final 10 percent of the surface.

The nozzle was designed to produce the maximum efficiency from its matching turbine stage by concentrating the work in regions of minimum loss, i.e., in the hub and midspan regions, where secondary and tip clearance losses are less severe. This spanwise variation may be seen in Fig. 5, where the Mach number profiles at 8, 50, and 92 percent are superimposed. The tip section of the vane has been successfully off-loaded even at the high exit Mach number test condition shown and did not experience the sharp, shock wave induced expansion and contraction that were features of the midspan and root sections.

Gradual spanwise surface variations were also present, but at all test conditions the pressure surface flow remained stable with no evidence of diffusion.

The vane's aerodynamic performance was largely independent of Reynolds number, and Fig. 6 shows the close agreement

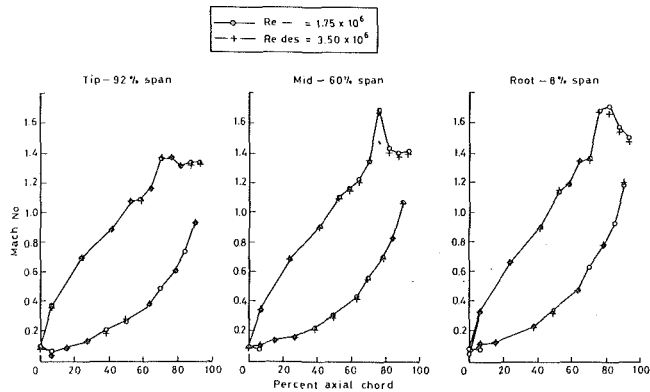


Fig. 6 Effect of Reynolds number on Mach number distribution

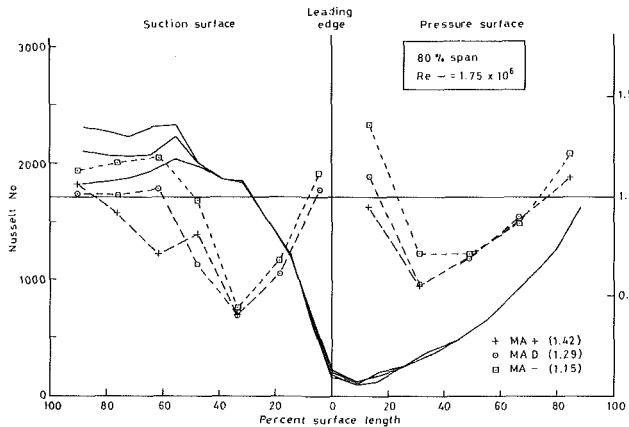


Fig. 7 Effects of exit Mach number on heat transfer: tip

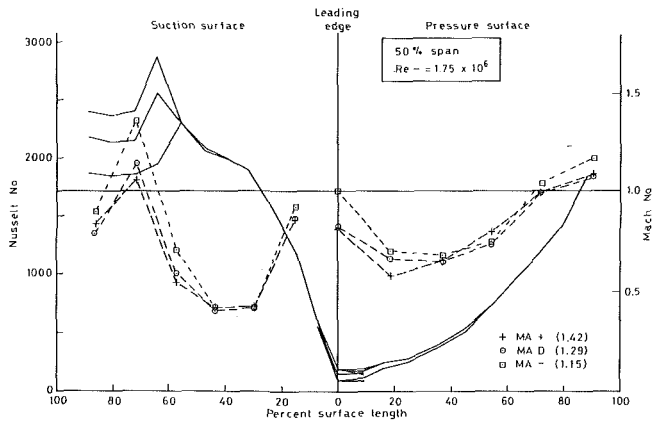


Fig. 8 Effects of exit Mach number on heat transfer: midspan

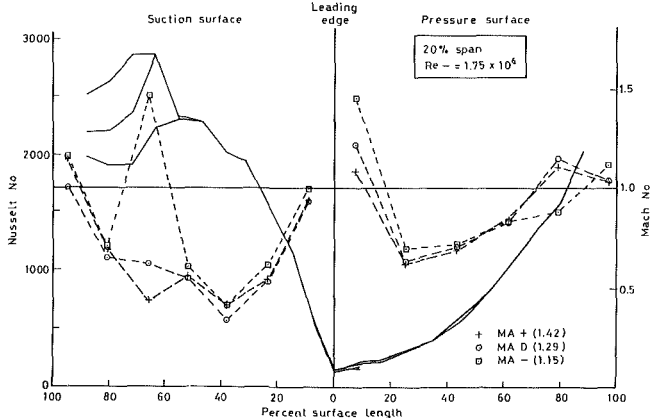


Fig. 9 Effects of exit Mach number on heat transfer: root

ment of the surface Mach numbers at the two Reynolds numbers used for these tests.

The aerodynamic results fully confirmed the repeatability and consistency of the cascade's performance both with previous work and theoretical prediction.

Vane Surface Heat Transfer

Figures 7, 8, and 9 show the variation of heat transfer over the vane surfaces at three spanwise planes and at three exit Mach numbers all at a Reynolds number of 1.75×10^6 . Superimposed on these figures are the corresponding surface Mach number distributions (pressures were measured at 8, 50, and 92 percent span). On the pressure surface, high leading edge stagnation region heat transfer fell to reach a minimum at 30 percent of the surface length before increasing gradually as progressive turbulent boundary layer growth took place over the pressure surface.

The pressure surface heat transfer was virtually unaffected by the exit Mach number variation. This may be expected due to the nozzle being fully choked, with no variation in pressure surface Mach number distribution. At higher exit Mach numbers on the 20 percent span, root section there is evidence of a reduction in heat transfer over the final 20 percent of the surface. Brown and Martin (1979) have shown that pressure surface turbulent heat transfer rates can be determined from flat plate Nusselt/Reynolds number correlations. The heat transfer coefficient is then directly related to free-stream mass flux (or mass flow density) (ρu) and inversely to the length of the fully turbulent surface by the equation

$$h = k \mu^2 (\rho u)^{0.8} / x^{0.2} \quad (1)$$

It follows that heat transfer will fall if the following condition is true:

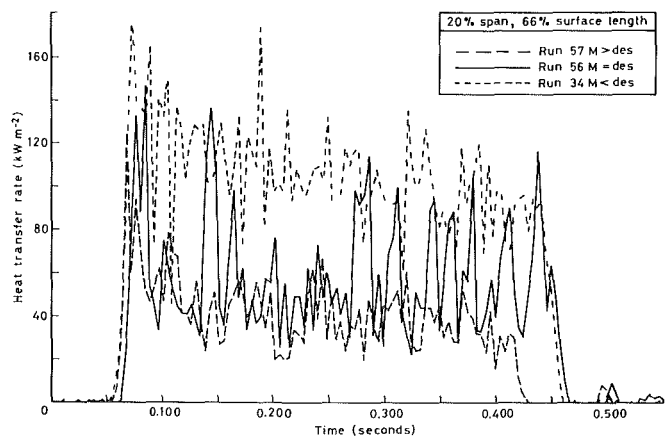


Fig. 10 Sensitivity of suction surface boundary layer to exit Mach number

$$\frac{\partial}{\partial x} \frac{(\rho u)^4}{x} \mu \leq 0 \quad (2)$$

In accelerating supersonic flow, density decreases at a faster rate than the velocity increases, so that the mass flux decreases and hence a reduction in heat transfer coefficient is to be expected. The fall in heat transfer at the rear of the pressure surface was probably due to this effect.

There is some evidence from Figs. 7 to 9 that the leading edge stagnation point was displaced from the geometric stagnation point, at which the heat transfer gage at midspan was positioned, around on to the pressure surface.

The rapid acceleration around the suction surface with its favorable pressure gradient produced the expected fall in heat

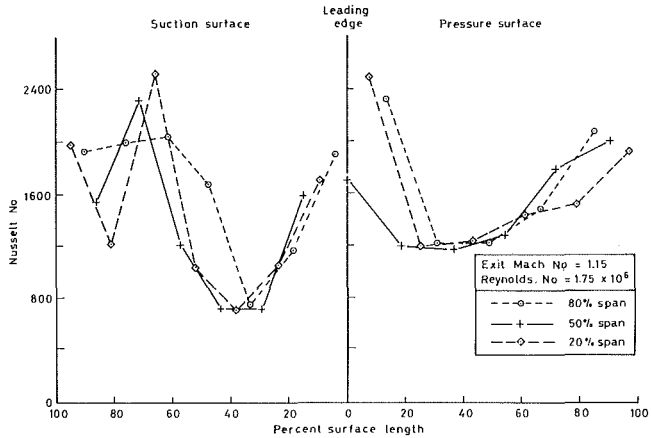


Fig. 11 Spanwise variation of heat transfer: $Re -$, $M -$

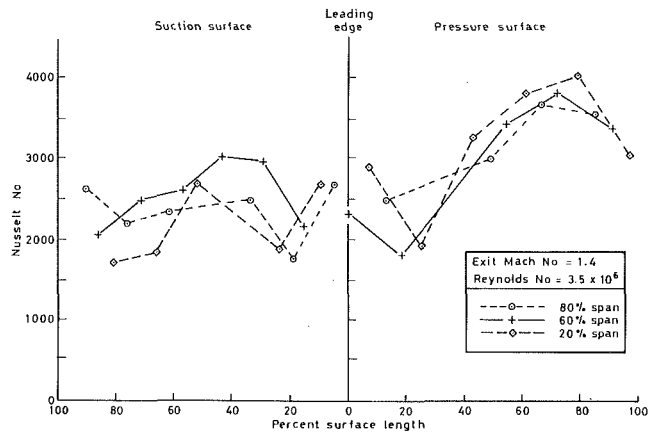


Fig. 14 Spanwise variation of heat transfer: Re_{des} , $M +$

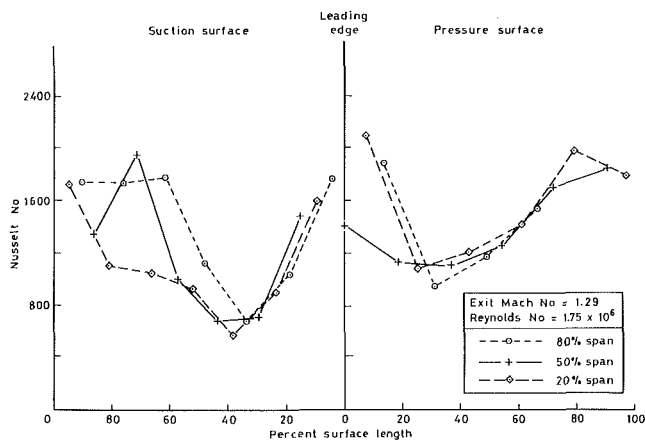


Fig. 12 Spanwise variation of heat transfer: $Re -$, M_{des}

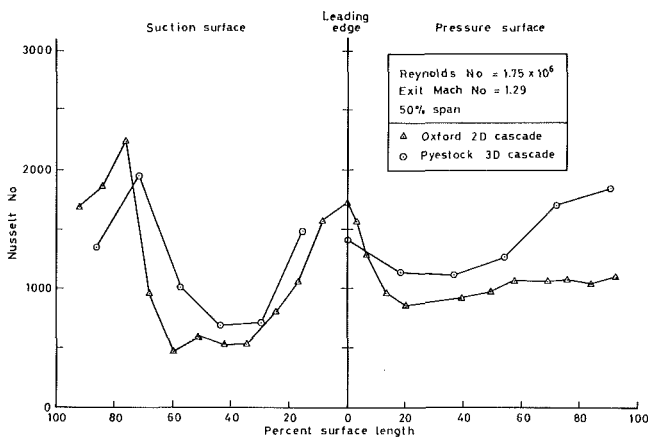


Fig. 15 Comparison of heat transfer measured at Pyestock and Oxford: $Re -$

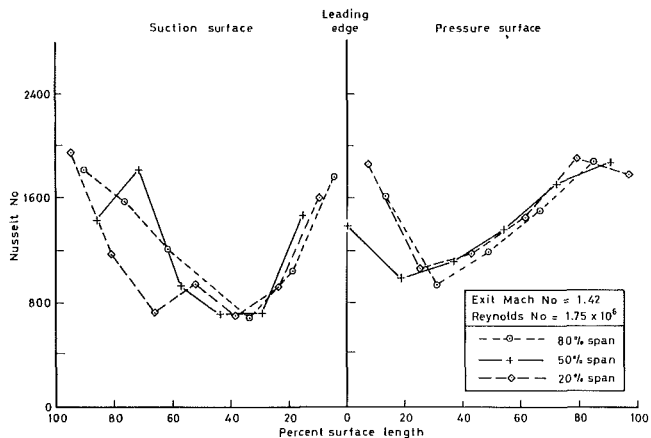


Fig. 13 Spanwise variation of heat transfer: $Re -$, $M +$

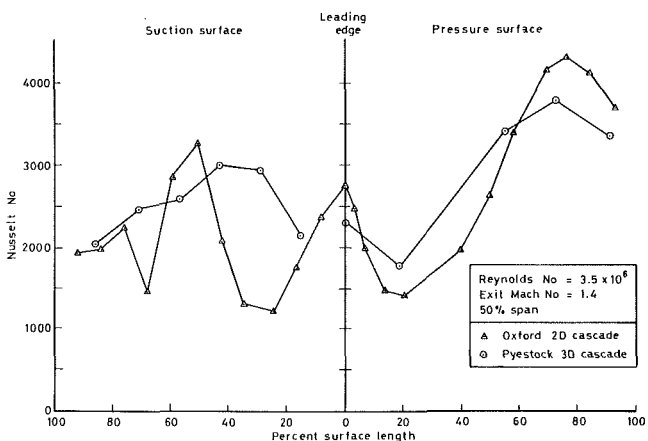


Fig. 16 Comparison of heat transfer measured at Pyestock and Oxford: Re_{des}

transfer through the laminar boundary layer, which reached a minimum at 30 to 40 percent of the surface length. This region was insensitive to exit Mach number variation, as would be expected. Turbulence-induced transition took place over the next 10 percent of the surface with a consequent increase in heat transfer. The boundary layers beyond this point were affected dramatically by shock wave interaction as discussed earlier. As may be seen in Fig. 9, wide variations in heat transfer were found at the same location due to the strength and point of impingement of this shock system. The gages showing reductions in heat transfer in this region were affected by the supersonic acceleration upstream of the impinging compression shock wave and it is possible that some relaminarization of the boundary layer may also have oc-

curred. Following the compression through the shock, a further increase in heat transfer was experienced on some films. The lack of flow visualization results and the wide spacing of the heat transfer gages at each spanwise plane on this critical part of the suction surface did not allow a more detailed study of the shock wave impingement effects during this commissioning build.

Figure 10 is the raw heat transfer signal from one heat transfer gage on the suction surface of the vane. As the exit Mach number was increased, the boundary layer at that point changed from turbulent through transitional to laminar with a consequent reduction in heat transfer. This clearly

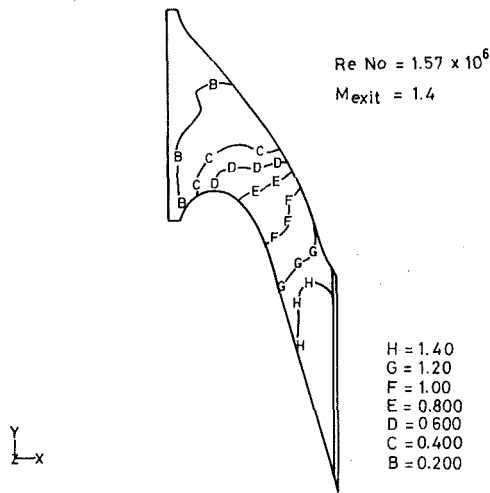


Fig. 17 Outer endwall Mach number contours

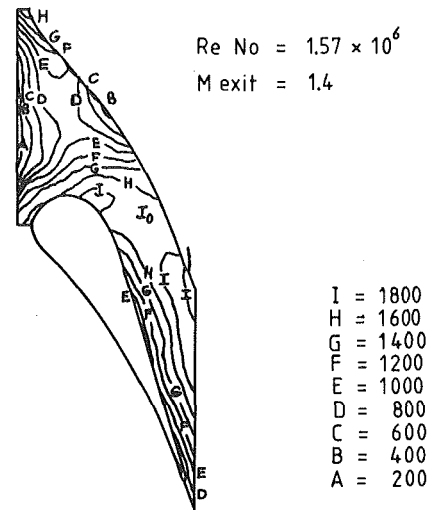
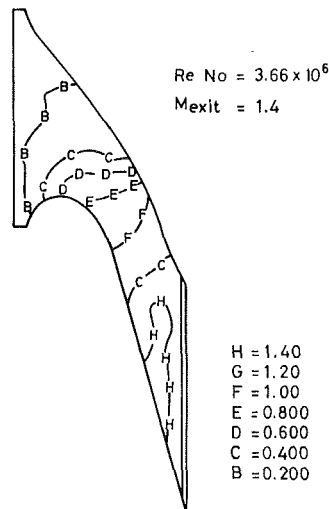
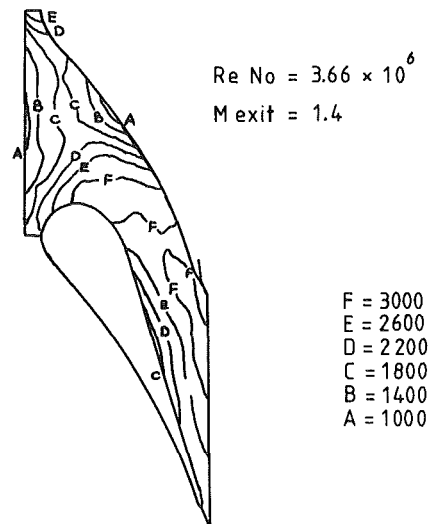


Fig. 18 Outer end wall Nusselt number contours



demonstrates the ability of the measurement technique to identify boundary layer states around turbine vane surfaces.

For completeness, the low Reynolds number spanwise heat transfer distributions are reproduced in Figs. 11, 12, and 13 at the three exit Mach numbers. There was little spanwise variation over the pressure and suction surfaces outside the regions affected by shock wave impingement on the suction surface. The higher exit Mach numbers, and in consequence, increased rate of supersonic acceleration toward the root of the blade, is indicated by the trends at the downstream end of the pressure surface.

Figure 14 is analogous to Fig. 13 but at the design Reynolds number of 3.5×10^6 . Pressure surface behavior was very similar to the low Reynolds number tests but with levels of heat transfer significantly higher than the leading edge stagnation values. The suction surface data were less well ordered but earlier transition would appear to have taken place on the midspan and tip sections.

Limited comparison with the Oxford two-dimensional results was possible and Figs. 15 and 16 compare the midspan heat transfer distributions at two different test conditions. The general shape of the curves is similar and higher heat transfer toward the rear of the pressure surface at low Reynolds number (Fig. 15) on the ILPC tests was probably due to variations in surface finish and turbulence levels between the two test vane installations (Tu (ILPC)=6.9 percent, Tu (OUEL)=4.5 percent). Work at Oxford on surface finish, cleanliness, and the effect of turbulence demonstrated that the

transitional pressure surface boundary layer on this vane was sensitive to changes in these variables.

Endwall Results

This build allowed both pressure and heat transfer measurements to be taken on the outer endwall of a vane passage. Figure 17 shows the Mach number contours for the two Reynolds numbers used. The close similarity and location of the sonic line will be apparent. The flow accelerated uniformly downstream of the throat until a region of overexpansion was encountered toward the rear of the suction surface due to trailing edge shock wave systems.

The heat transfer Nusselt number contours in Fig. 18 show a uniform distribution across the vane inlet at midpassage with high levels concentrated under the leading edge horseshoe vortex regions. A saddle point region of moderate heat transfer is evident early in the passage with its major axis aligned with the anticipated path of the pressure surface leg of the horseshoe vortex as it moved across the passage towards the suction surface. As was seen by Graziani et al. (1979) and Gaugler and Russell (1983), this region has a complex flow pattern and rapid variations in heat transfer are to be expected.

The endwall contours around the suction surface, leading edge, endwall region show a progressive increase in heat transfer having similar curvature to that of the Mach number contours over the same region.

The midpassage region featured a broad plateau of high heat transfer stretching right across the passage. In this region, it is to be expected that endwall boundary layers will be thin and heat transfer consequently high due to the cross-passage pressure gradient sweeping endwall flow toward the suction surface.

Toward the rear of the suction surface the contours are parallel to the vane profile and heat transfer decreased toward the suction surface endwall intersection.

The work of Gaugler and Russell (1983) and York et al. (1984) produced similar contour patterns in the downstream endwall areas and around the suction surface leading edge region to the present work. There was no obvious evidence of the passage vortex itself creating high heat transfer as it passed across the endwall surfaces.

Any meaningful study of the complex influence of passage flows on endwall heat transfer must include the study of temperature ratio, turbulence, contouring, and inlet boundary layer effects. None of these variables were changed in the present tests but the results presented here show that the rig and instrumentation techniques are capable of measuring end-wall heat transfer detail.

Conclusions

The measurements have been shown to be repeatable and consistent with both prediction and previous test results from a two-dimensional cascade. The inlet turbulence level was measured and found to be adequate to ensure that suction surface boundary layer transition occurred.

Endwall heat transfer and pressure measurements have been made and localized effects identified but with no strong evidence of high heat transfer due to cross-passage vortices.

This test facility provides an ideal vehicle for realistic three-dimensional heat transfer and aerodynamic studies on high-pressure turbine nozzle guide vanes and the work will be extended to include flow field traversing, flow visualization, and representative cooling flow.

Acknowledgments

Without the creativity and expertise of the Oxford University Engineering Science Department team led by the late Professor Schultz, this program of work could not have been launched or reached its present state of development. Their advice, encouragement and support have been indispensable and are gratefully acknowledged.

References

- Baines, N. C., 1983, "Laboratory Data Acquisition, Processing and Display System. Users and Programmers Guide," Technical Report 1462/83, Department of Engineering Science, University of Oxford, United Kingdom.
- Batchelor, G. K., and Townsend, A.A., 1948, "Decay of Isotropic Turbulence in the Initial Period," *Proceedings of the Royal Society*, London, Vol. 193, p. 539.
- Brooks, A. J., Colbourne, D. E., Wedlake, E. T., Jones, T. V., Oldfield, M.L.G., Schultz, D. L., and Loftus, P. J., 1985, "The Isentropic Light Piston Cascade Facility at RAE Pyestock," *Proceedings, AGARD Conference No. 390, Heat Transfer and Cooling in Gas Turbines*, Bergen, Norway.
- Brown, A., and Martin, B. W., 1979, "Heat Transfer to Turbine Blades With Special Reference to the Effects of Mainstream Turbulence," ASME Paper No. 79-GT-26.
- Bryce, J. D., Litchfield, M. R., and Leversuch, N. P., 1985, "The Design, Performance and Analysis of a High Work Capacity Transonic Turbine," ASME *Journal of Engineering for Gas Turbines and Power*, Vol. 107, pp. 931-937.
- Consigny, H., and Richards, B. E., 1982, "Short Duration Measurements of Heat Transfer Rate to a Gas Turbine Rotor Blade," *AMSE Journal of Engineering for Power*, Vol. 104, pp. 542-551.
- Gaugler, R. E., and Russell, L. M., 1983, "Comparison of Visualised Turbine Endwall Secondary Flows and Measured Heat Transfer Patterns," NASA TM 83016.

Graziani, R. A., Blair, M. F., Taylor, J. R., and Mayle, R. E., 1979, "An Experimental Study of Endwall and Airfoil Surface Heat Transfer in a Large Scale Turbine Blade Cascade," ASME Paper No. 79-GT-99.

Ligrani, P. M., and Breugelmanns, F. A. E., 1981, "Turbine Blade Cooling Research at the Von Karman Institute for Fluid Dynamics," *Fifth Int. Symp. on Air Breathing Engines*, Bangalore, India.

Litchfield, M. R., and Norton, R. J. G., 1982, "Heat Transfer Measurements on a Transonic Nozzle Guide Vane," ASME Paper No. 82-GT-247.

Oldfield, M. L. G., Jones, T. V., and Schultz, D. L., 1978, "On-line Computer for Transient Turbine Cascade Instrumentation," *IEEE Transactions on Aerospace and Electronic Systems* Vol. AES-14, pp. 738-749.

Oldfield, M. L. G., Burd, H. J., and Doe, N. G., 1982, "Design of Wide-Bandwidth Analogue Circuits for Heat Transfer Instrumentation in Transient Wind Tunnels," *16th Symposium of the International Centre for Heat and Mass Transfer (Heat and Mass Transfer in Rotating Machinery)*, Dubrovnik, D. E. Metzger, ed., Hemisphere Publishing Corp., New York, 1984.

Priddy, W. J., and Bayley, F. J., 1985, "Effects of Free Stream Turbulence on the Distribution of Heat Transfer Around Turbine Blade Sections," *Int. Journal of Heat and Fluid Flow*, Vol. 6, No. 3.

Schultz, D. J., and Jones, T. V., 1973, "Heat Transfer Measurements in Short Duration Hypersonic Facilities," AGARDograph AG-165.

York, R. E., Hylton, L. D., and Mihelc, M. S., 1984, "An Experimental Investigation of Endwall Heat Transfer and Aerodynamics in a Linear Vane Cascade," ASME *Journal of Engineering for Gas Turbines and Power*, Vol. 106, pp. 159-167.

A P P E N D I X

Turbulence Measurements

The influence of free-stream turbulence on turbine blade heat transfer is well catalogued. It has been shown that free-stream turbulence levels in excess of 4 percent lead to a turbulent boundary layer on the blade representative of the boundary layer on the NGV of an aircraft gas turbine (Ligrani and Breugelmanns, 1981; Consigny and Richards, 1982; Priddy and Bayley, 1985). The ILPC is fitted with an annular turbulence grid, the bar diameter being 10.0 mm with 80 bars, situated 200 mm upstream of the NGV row. The calculation of bar diameter and spacing was based on Batchelor and Townsend (1948) to yield turbulence levels of 4-5 percent.

Measurements were made using a single hot-wire probe (DISA 55 P11) with a wire diameter of 5 μm and length of 1 mm. The wire was operated at 10 overheat ratios and the resulting data analyzed using a modified version of the theory presented by Oldfield et al. (1978). The modification to the theory is presented below. Using a wire exponent (n) of 0.48 yields a turbulence intensity level of 6.9 percent, which is deemed to be adequately representative of conditions at entry to an engine NGV.

Following the scheme outlined by Oldfield et al. (1978) but redefining the overheat ratio for the hot wire as

$$X = \frac{R - \bar{R}_0}{\bar{R}_0} \quad (3)$$

yields an equation for the power consumption of the hot wire as

$$P_w = c \frac{R - \bar{R}_0}{\bar{R}_0} \text{Re}_w^n \quad (4)$$

which when processed as described by Oldfield et al. (1978) yields

$$\frac{\overline{\delta P_w^2}}{P_w^2} = n^2 \left(\frac{\overline{\delta \text{Re}_w^2}}{\text{Re}_w^2} \right) - \frac{2n}{X} \left(\frac{\overline{\delta R_0 \delta \text{Re}_w}}{R_0 \text{Re}_w} \right) + \frac{1}{X^2} \left(\frac{\overline{\delta R_0^2}}{R_0^2} \right). \quad (5)$$

This is parabolic in the overheat ratio X , and the first term in equation (5) yields the fluctuation of Reynolds number, which is identical to the turbulence intensity.

Study of the Convective Heat Transfer in a Rotating Coolant Channel

J. Guidez

Office National d'Etudes
et de Recherches Aérospatiales,
BP 72-92322 Châtillon Cedex, France

An experimental and theoretical study of convective heat transfer in a rotating coolant channel was inspired by the potential application to cooled turbine rotor blades. The flow that circulates into the internal cavity of the blade is subjected to Coriolis and centrifugal forces, in addition to pressure and friction forces. In this study, the channel is a rectangular-sectioned duct that rotates around an orthogonal axis. The experimental rig is composed of a vacuum enclosure, which includes an electric furnace, and the test section, heated by radiative flux. The temperatures of the wall test section are measured with thermocouples and the infrared pyrometer technique still under development. The convective heat transfer coefficients are determined with transient or steady-state techniques. It is shown that Coriolis acceleration has a beneficial influence on mean heat transfer. Locally, along the pressure side, the transfer increases strongly and on the contrary along the suction side, it decreases slightly. These effects are analyzed theoretically with a Navier-Stokes three dimensional (with mixing length model of turbulence) and explained by the influence of Coriolis force, which induces a secondary flow and distorts the velocity and temperature profiles. Experimental and theoretical results are presented and discussed.

Introduction

Recent progress in research on turbine blade cooling has led to examination of the influence of rotation on different cooling techniques.

Blade cooling is based on three techniques (Fig. 1): (a) internal convection inside a blade (with or without impingement effect), (b) convective heat transfer inside holes, (c) film cooling.

In this paper, a study of the influence of rotation on the convective heat transfer inside a rotor blade is presented.

The internal cavity of modern blades is very complex. Different types of "turbulators" are managed within the blades; they improve the convective heat transfer. But the simultaneous analysis of these different cooling methods with rotation is difficult. Thus, in a first step, in order to emphasize the main influence factors, this study has been restricted to a simple geometry: a turbulent flow in a rectangular-sectioned duct rotating in the orthogonal mode (Fig. 2). In the future, another geometry without or with "turbulators" will be studied.

The flow and heat transfer in a rotating channel have been extensively reviewed and discussed in papers by Morris et al. (1980, 1987), Spalding et al. (1978), Kheshgi and Scriven (1985), and Siegel (1985) in particular for a channel that is perpendicular to the axis of rotation.

However, these studies cover essentially: for the experiments: circular, square, and triangular ducts; for the computations: laminar flows.

The rectangular duct has been studied, for turbulent flow, theoretically by Spalding with a "parabolic" procedure and experimentally by Moore.

In the present work, two approaches have been explored:

- 1 an experimental one for the direct determination of local heat exchange coefficient by use of heat balance for a volume element of the test section. This aspect is the main part of this paper.
- 2 a numerical one based on the resolution of the Navier-Stokes equations in three dimensions with the classical mixing

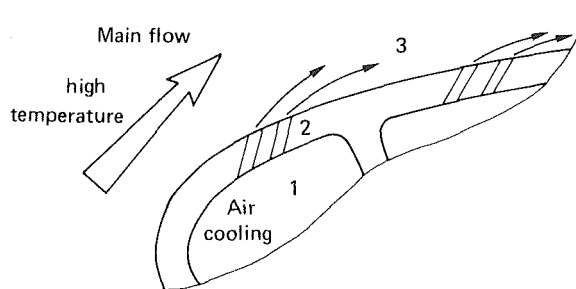


Fig. 1 Cooled blade: (1) internal convection; (2) convective transfer in holes; (3) film cooling

Contributed by the International Gas Turbine Institute and presented at the 33rd International Gas Turbine and Aeroengine Congress and Exhibition, Amsterdam, The Netherlands, June 5-9, 1988. Manuscript received by the International Gas Turbine Institute September 15, 1987. Paper No. 88-GT-35.

length model for the turbulence (boundary layer assumption). This approach will be developed in the theoretical part.

The objective of this work is the validation of the numerical prediction for its extension to the flow and heat transfer in a rotating cavity of rotor blades.

Analysis and Governing Equations of Flow and Heat Transfer in a Rotating Channel

When a channel is rotating around an axis perpendicular to its length (main flow direction), the flow is subjected, in addition to pressure and friction forces, to centrifugal and Coriolis forces. Qualitatively, Coriolis force induces a secondary flow and there are essentially two symmetric vortices. This secondary flow distorts the velocity and temperature profiles; thus the friction factor and heat transfer coefficient are modified. For turbulent flow, the centrifugal force has an effect smaller than the Coriolis force and its influence will be known with precision by comparison between centrifugal (outward flow) and centripetal (inward flow) channels.

The equations governing this problem are continuity, momentum, and energy, where the centrifugal ($\rho\omega^2x$, $\rho\omega^2y$) and Coriolis ($-2\rho\omega u$, $2\rho\omega v$) terms appear (Fig. 3).

In Cartesian coordinates these equations take the form:

Continuity:

$$\frac{\partial(\rho u)}{\partial x} + \frac{\partial(\rho v)}{\partial y} + \frac{\partial(\rho w)}{\partial z} = 0$$

Momentum:

$$\frac{\partial}{\partial x}(\rho u^2) + \frac{\partial}{\partial y}(\rho uv) + \frac{\partial}{\partial z}(\rho uw) = -\frac{\partial P}{\partial x} + \rho\omega^2x + 2\rho\omega v$$

$$+ \frac{\partial}{\partial y}\mu\frac{\partial u}{\partial y} + \frac{\partial}{\partial z}\mu\frac{\partial u}{\partial z}$$

$$\frac{\partial}{\partial x}(\rho uv) + \frac{\partial}{\partial y}(\rho v^2) + \frac{\partial}{\partial z}(\rho vw) =$$

$$-\frac{\partial P}{\partial y} + \rho\omega^2y - 2\rho\omega u + \text{viscous terms}$$

$$\frac{\partial}{\partial x}(\rho uw) + \frac{\partial}{\partial y}(\rho vw) + \frac{\partial}{\partial z}(\rho w^2) = -\frac{\partial P}{\partial z} + \text{viscous terms}$$

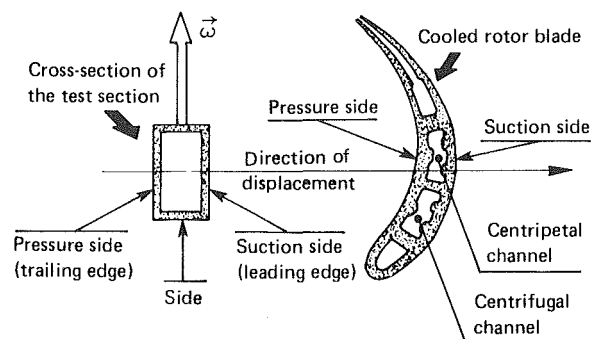


Fig. 2 Schematic representation of rotor blade cooled by internal convection and a channel simulating internal cavity of blade

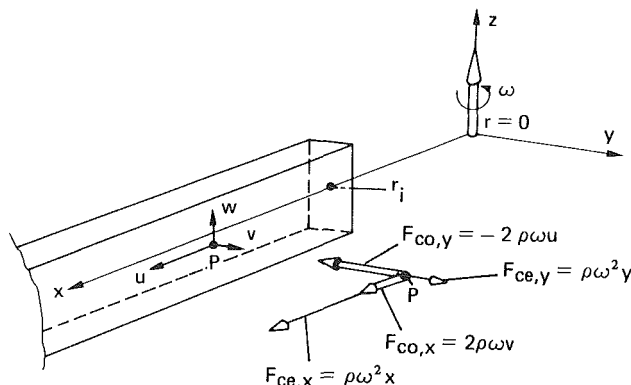


Fig. 3 Representation of a rotating rectangular duct in Cartesian coordinates

Energy:

$$\frac{\partial}{\partial x}(\rho uR) + \frac{\partial}{\partial y}(\rho vR) + \frac{\partial}{\partial z}(\rho wR) = \frac{\partial}{\partial x}\left[\frac{\mu}{Pr_t}\frac{\partial H_i}{\partial x}\right]$$

$$+ \frac{\partial}{\partial y}\left[\frac{\mu}{Pr_t}\frac{\partial H_i}{\partial y}\right] + \frac{\partial}{\partial z}\left[\frac{\mu}{Pr_t}\frac{\partial H_i}{\partial z}\right]$$

where

Nomenclature

C, C_p = specific heat	q_{inc} = incoming radiative flux from the furnace	ΔY = height of surface element
D = diameter	r = radius	β = coefficient of volume expansion
D_H = hydraulic diameter	Ra = Rayleigh number	δ = normal distance to the wall
e = thickness of wall test section	Re = Reynolds number	ϵ = emissivity
F_{ce} = centrifugal force	Ro = Rossby number	λ = wavelength
F_{co} = Coriolis force	\bar{T} = mean temperature	μ = dynamic viscosity
h, h_{PS}, h_{SS} = heat transfer coefficient	T_a = total air temperature	ν = kinematic viscosity
H = eccentricity = $r_i + L/2$	T_F = furnace temperature	ρ = density
k = thermal conductivity	T_w, T_{SS}, T_{PS} = wall temperature	σ = Stefan constant
L = length of the duct	t = time	ω = rotating speed
\dot{m} = mass flow	u, v, w = velocity components	
Nu = Nusselt number	V = velocity	
P = pressure	u_t = friction velocity	
Pr = Prandtl number	x, y, z = coordinates	
Pr_t = turbulent Prandtl number	Y_e = external perimeter of a cross section	Subscripts
q_{cond} = conductive flux	Y_i = internal perimeter of a cross section	0 = static channel
q_{conv} = convective flux	\bar{Y} = mean perimeter of a cross section	c = center of the duct
		i = inlet of the duct
		PS = Pressure Side
		SS = Suction Side

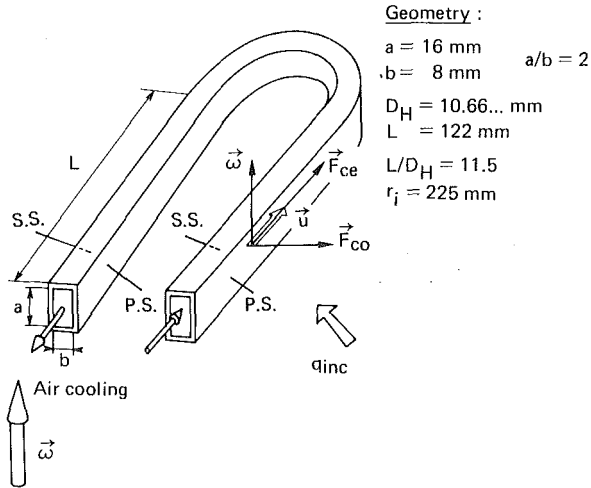


Fig. 4 Test section

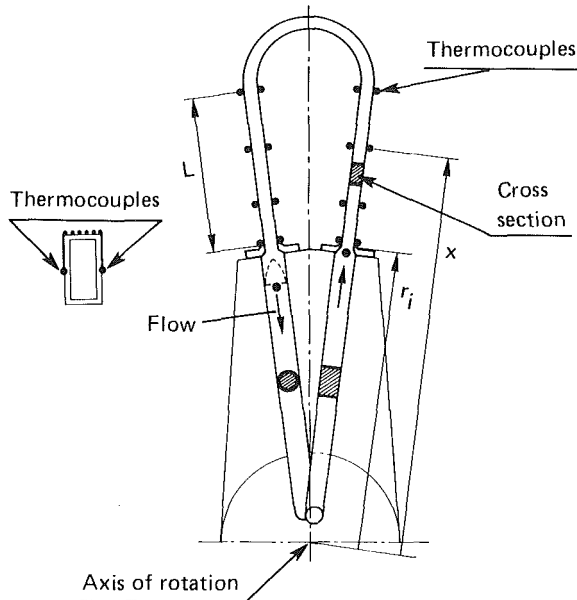


Fig. 5 Position of thermocouples

$$R = H_i - \frac{\omega^2 x^2}{2} - \frac{\omega^2 y^2}{2} \text{ and } H_i = C_p T_a$$

They may be used to identify suitable nondimensional groups that characterize the effect of rotation with dimensional analysis; for example, by use of dimensionless variables, the momentum equation for the x direction is written as

$$\frac{\partial}{\partial \tilde{x}}(\tilde{\rho} \tilde{u}^2) + \frac{\partial}{\partial \tilde{y}}(\tilde{\rho} \tilde{u} \tilde{v}) + \frac{\partial}{\partial \tilde{z}}(\tilde{\rho} \tilde{u} \tilde{w}) = - \frac{\partial \Psi}{\partial \tilde{x}} - \frac{Ra}{Re^2} \tilde{\rho}(\eta - \eta_c) + 2\tilde{\rho} \tilde{v} R_o + \frac{1}{Re} \tilde{\mu} \left(\frac{\partial^2 \tilde{u}}{\partial \tilde{y}^2} + \frac{\partial^2 \tilde{u}}{\partial \tilde{z}^2} \right)$$

where

$$\begin{aligned} \tilde{x} &= x/D_H & \tilde{u} &= u/V_i & \tilde{\rho} &= \rho/\rho_i \\ \tilde{y} &= y/D_H & \tilde{v} &= v/V_i & \tilde{\mu} &= \mu/\mu_i \\ \tilde{z} &= z/D_H & \tilde{w} &= w/V_i \end{aligned}$$

and $\Psi = P'/\rho_i V_i^2$ with $\partial P'/\partial x = \partial P/\partial x - \rho_c \omega^2 x$ and $\eta = Pr \cdot (T_a - T_{a_i})/(T_w - T_{a_i})$.

The nondimensional groups are:

Geometry :

$$\begin{aligned} a &= 16 \text{ mm} & a/b &= 2 \\ b &= 8 \text{ mm} \\ D_H &= 10.66 \dots \text{ mm} \\ L &= 122 \text{ mm} \\ L/D_H &= 11.5 \\ r_i &= 225 \text{ mm} \end{aligned}$$

Table 1

	Re	Ro max	Ra max	ω rd/s	D_{H1} mm	L mm	r_i mm	T_w K	T_{a_i} K	\dot{m} g/s	P_i bar
Rotor blade	$15 \cdot 10^5$									4	13
	to	0.2	$70 \cdot 10^6$							to	
Test section	$50 \cdot 10^5$			500	10.66	122	225	550	350	10	2.2

$$Nu = hD_H/k$$

which characterizes the convective transfer turbulence of the flow

$$Re = \rho V_i D_H / \mu$$

$$Ro = \omega D_H / V_i$$

Coriolis aspect

$$Ra = \rho^2 \omega^2 x D_H^3 \beta (T_w - T_{a_i}) Pr / \mu^2$$

centrifugal aspect

$$Pr = \mu C_p / k$$

The geometry is characterized by the ratio L/D_H (dimensionless length of the duct) and H/D_H (dimensionless eccentricity). In addition, an important factor is the geometry of the inlet, upstream of the channel studied, in the case where the flow is not fully developed.

These nondimensional numbers will be used to scale the effect of rotation and the convective transfer deduced from the experiments.

Experimental Rig and Measuring Techniques

The test section (Fig. 4) is composed of two rectangular ducts: a centrifugal channel one (radially outward flow) and a centripetal channel one (radially inward flow). These two ducts are connected by a curve part. The upstream of the centrifugal channel is also a rectangular duct larger than that of the test section (Fig. 5).

The sizes of the test section are larger than those of the real internal cavity of a blade due to the instrumentation equipment; thus the measurements are easier. In this respect, the experimental conditions have been defined by use of dimensionless parameters. Those similitude conditions have been chosen in order to reduce the wall temperature level and the rotating speed (Table 1).

The general view of the experimental rig is shown in Fig. 6. Two test sections, connected on a support, rotate inside an electric furnace (furnace temperature range: 700 K to 1450 K). One of these test sections contains many instruments, and the other, reserved for infrared measurements, is equipped only for thermal symmetry control. These parts are installed within a vacuum enclosure (pressure ≤ 1 hPa). Thus, these test sections are heated by radiative energy from the furnace, without external convection due to the low pressure into the enclosure. They are cooled inside by air; the air cooling inlet is located at the lower part and the outlet at the higher part of the rotating shaft. Mass flow is measured with a "sonic throat."

Airtightness is secured with four groups of rotating seals. The rotating parts are driven by a controlled electric motor via a toothed pulley. The maximum rotating speed is 550 rd/s (≈ 5000 rpm). This speed is measured with a magnetic sensor installed in front of a metallic toothed wheel (60 teeth).

The test section is built of steel, 1.2 mm thick (cut out in mass by electro-erosion). The temperature of the wall test section is measured by means of two techniques:

1 by Cr/Al thermocouples that equip different cross sections (Fig. 5) at the middle of the larger sides of the rectangular duct. These sides are the most interesting because, according to the rotating direction, they are considered as the pressure side (trailing side) or the suction side (leading side).

There are 20 wall thermocouples (Thermocoax: 0.5 mm di-

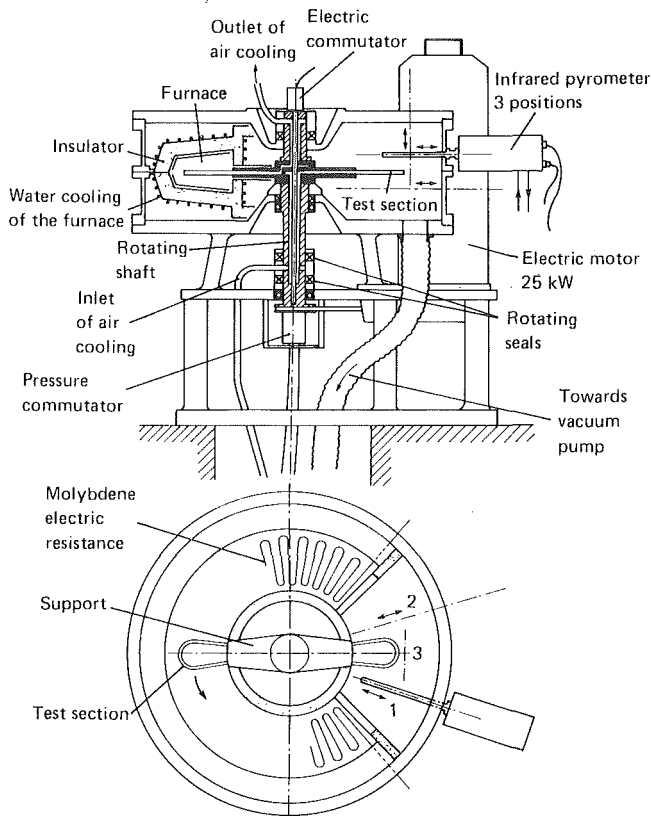


Fig. 6 Experimental rig

ameter). For each test section, the inlet air temperature and the emerging air temperature are also measured by means of thermocouples. All these thermocouples are connected to a rotating electric commutator, and the thermocouple signals are sent to a data acquisition system, of which the main part is a minicomputer HP 9845.

2 by an infrared pyrometer: at ONERA, an infrared pyrometric probe with a high spatial and temporal resolution has been designed to measure the surface temperature field of the mobile blades of a turbine (Charpenel and Wilhelm, 1985). Presently, this technique is in development for the experiments presented in this paper.

With this method, it is possible to obtain a temperature profile when the emissivity and the radiative background are known; generally, an interpretation is necessary. With the thermocouples, only the local temperature is obtained, but directly. In many cases, to achieve thermal analysis, these two complementary techniques should be developed simultaneously.

The infrared pyrometer is shown in Fig. 7(a). The radiative flux coming from the surface element observed (diameter of the target about 1 mm) is collected by a mirror at the end of the mobile probe. The axial displacement of this mobile probe is ensured by pneumatic jack and rotation motion about the probe axis, by a step-by-step motor. This motor allows the probe orientation to scan the test section (angle θ , from -55 to $+55$ deg (Fig. 7b)). The infrared beam is focused on an InSb detector through two fluorine lenses and a diaphragm. The spectral range of the pyrometer is 1 to $5 \mu\text{m}$. The reflex sighting is used for the optical adjustment of the target on the test section. The signal obtained from the detector, via the amplifier, is calibrated with a blackbody source (Fig. 7c) and the lower temperature detectable is 400 K. The zero level is imposed by modulator (chopper), which is in front of the detector. The rotation speed of the modulator is synchronized with the shaft by the spot delivered at each revolution.

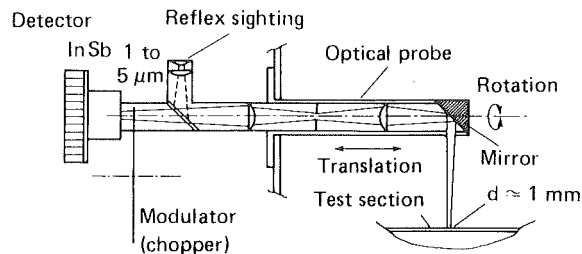


Fig. 7(a) Infrared pyrometer

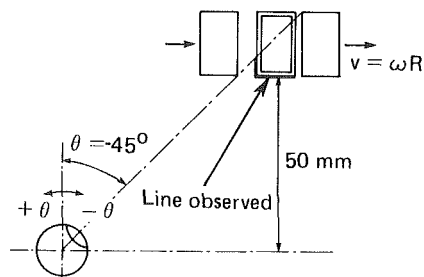


Fig. 7(b) Sketch of the target location

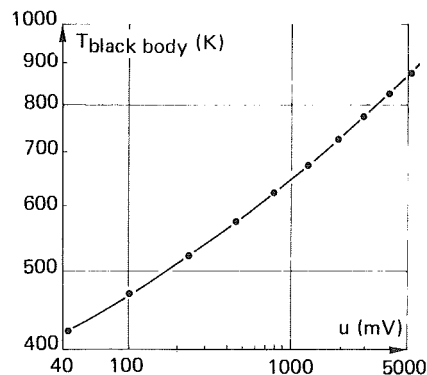


Fig. 7(c) Calibration curve of pyrometer

The pyrometric signal coming from the surface element of the mobile is composed of a directly emitted energy and a reflected energy from the background.

The bulk expression of the signal delivered by the detector with diffuse surface assumption is written as:

$$u = \int_{\Delta\lambda} \underbrace{F_\lambda}_{(*)} \left(\underbrace{\epsilon_\lambda q_{b,\lambda,T}}_{(**)} + \underbrace{(1 - \epsilon_\lambda) q_{inc,\lambda,T}}_{(***)} \right) d\lambda$$

(*) Internal function of the pyrometer; (**) directly emitted energy (where $q_{b,\lambda,T}$ is the radiative flux with blackbody condition); (***) reflection of the background on the target.

In order to minimize this spurious reflection from the background, two techniques have been used:

(a) The external surface of the test section is painted in black with a limitation to a maximum level of 700 K. The emissivity of this paint has been measured for temperature by comparison of the emission of a sample painted in black and a blackbody radiator when those two sources are at the same temperature. The emissivity obtained for the temperature range from 450 to 700 K is $\epsilon \approx 0.9$.

(b) The furnace is cut on a quarter of its circumference (Fig. 6). Narrow windows (with minimum aperture for passage of the test sections) minimize the configuration factor between the test section and the furnace.

The reflected energy amounts to less than 5 percent of the directly emitted energy.

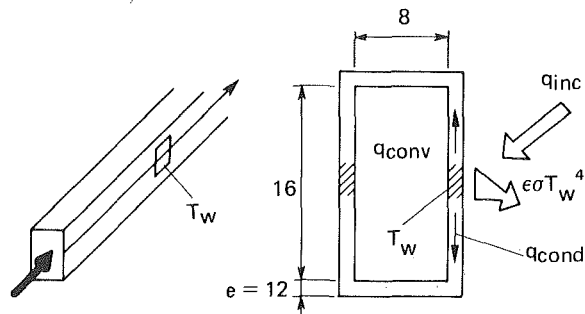


Fig. 8 Heat balance for a volume element near a thermocouple

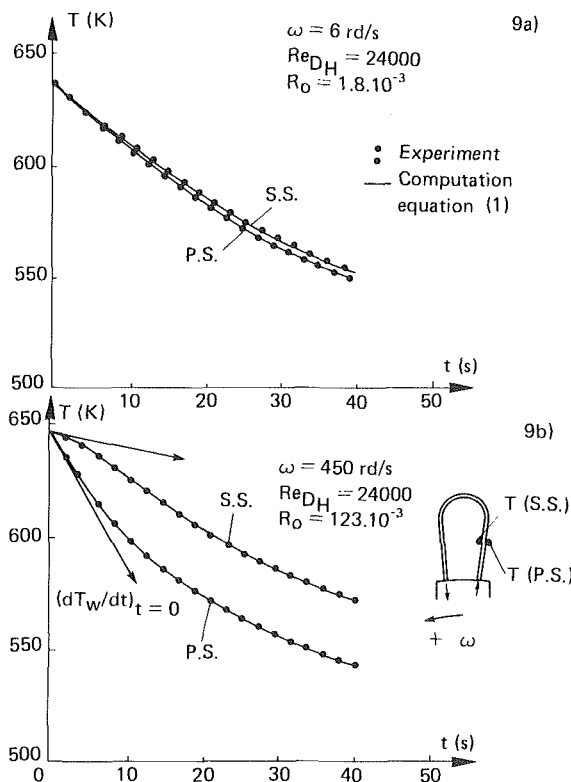


Fig. 9 Example of wall temperature time history (transient technique)

Method of Data Analysis

For each volume element near a thermocouple (Fig. 8), it is possible to make a heat balance as follows:

$$\underbrace{\rho c e \Delta \bar{Y}}_{(*)} \frac{dT_w}{dt} = \underbrace{\epsilon \Delta Y_e (q_{inc} - \sigma T_w^4)}_{(**)} - \underbrace{h \Delta Y_i (T_w - \bar{T}_a)}_{(***)} + \underbrace{q_{cond}}_{(****)}$$

(*) Instationary term; (**) radiative term; (***) convective term, (****) conductive term.

For the determination of the convective heat transfer coefficient the heat balance is carried out at steady state (with $dT_w/dt = 0$) or during a transient period, after the flow is suddenly re-established.

These two methods have been used simultaneously, the latter leading to more precise results.

The influence of rotation on the convective heat transfer, for radially outward flow, is clearly established in Fig. 9, where two examples of wall temperature evolution with time (transient technique) are shown. In Fig. 9(a), the rotation speed is $\omega = 6$ rd/s and in Fig. 9(b), $\omega = 450$ rd/s. For $\omega = 6$ rd/s,

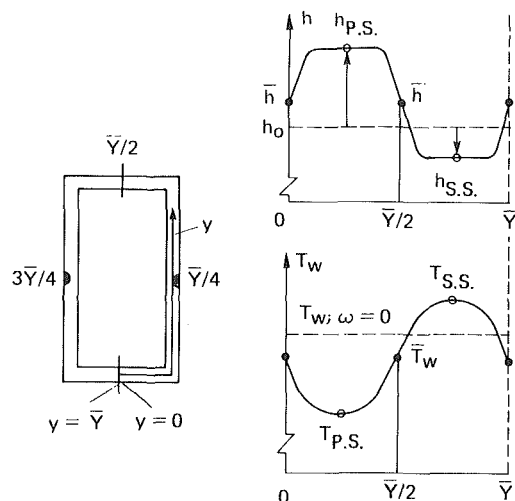


Fig. 10 Wall temperature and heat exchange coefficient profiles

the wall temperature evolution for the pressure side and the suction side are approximately the same, but for $\omega = 450$ rd/s, the convective heat transfer for the pressure side is clearly greater than for the suction side. From the curves of Fig. 9, it is possible to obtain the local heat transfer coefficient by the reconstitution of the wall temperature time history. For that purpose, an iterative method with finite difference is used. This resolution assumes that the expression of the conductive transfer is known. But there are only two thermocouples for each cross section. Thus a hypothesis on the wall temperature profile between the two measured points is necessary: A sinusoidal shape for this profile has been assumed, as shown in Fig. 10, and the temperature and the conductive transfer are written as follows:

$$T_w = \frac{T_{SS} + T_{PS}}{2} - \frac{T_{SS} - T_{PS}}{2} \sin \frac{2\pi y}{\bar{Y}}$$

and

$$q_{cond} = \pm \frac{2\pi^2 k e \Delta \bar{Y}}{\bar{Y}^2} (T_{SS} - T_{PS}) \begin{cases} y = \frac{\bar{Y}}{4} \rightarrow - \\ y = \frac{3\bar{Y}}{4} \rightarrow + \end{cases}$$

This assumption is sustained by the good agreement between the experimental and numerical results. Moreover, the recent infrared pyrometer measurements have confirmed this sinusoidal shape (Fig. 11). In the future the pyrometer results will be systematically used for this thermal analysis, avoiding this previous hypothesis.

Underlying this temperature profile, there is a distribution of the internal heat transfer coefficient. This distribution is constant along 60 percent of the pressure and the suction sides (Fig. 10). This result has been obtained by resolution, with finite difference method, of the heat equation, with a constant radiative flux on the external surface of the channel.

Experimental Results

In the experimental procedure, the temperature of the furnace and the mass flow are kept constant and the rotating speed is regulated (6 rd/s to 550 rd/s). This rotating speed remains constant during data collection.

The previous processing of data is used and a classical representation of the convective transfer is the ratio $N = Nu_w / Nu_0$, where Nu_w is the Nusselt number with rotation and Nu_0

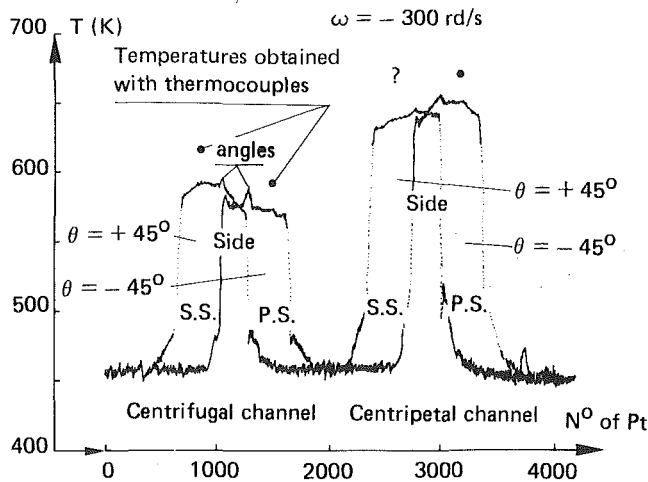


Fig. 11 Wall temperature profile obtained by pyrometer measurement

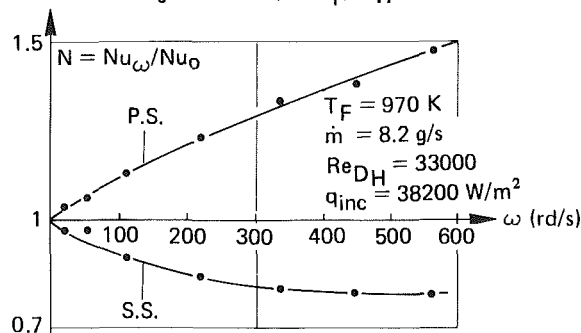
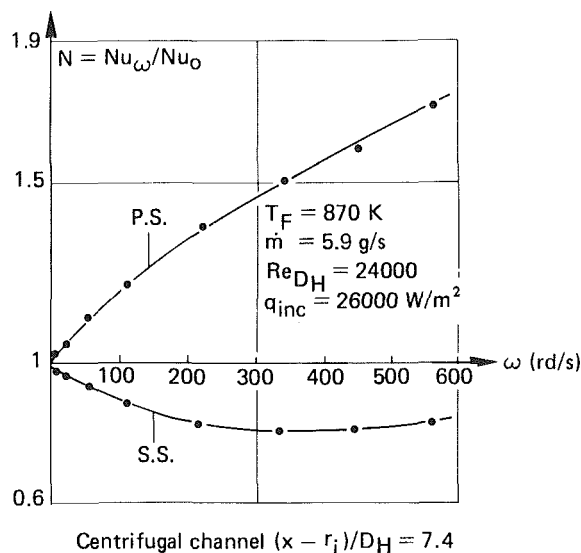


Fig. 12 Ratio, $N = Nu_\omega / Nu_0$ with rotating speed ω , for two Reynolds numbers

is the Nusselt number without rotation. Four Reynolds numbers (based on hydraulic diameter), 17,000, 24,000, 33,000, and 41,000, have been explored (Reynolds number is defined by the mass flow of air cooling). In Fig. 12, the ratio N is plotted versus rotation speed, ω , for two Reynolds numbers and for radially outward flow, pressure and suction sides of cross section located by $(x - r_i) / D_H = 7.4$. For this location, the ratio Nu_ω / Nu_0 , for the pressure side, increases strongly with rotation speed and on the contrary decreases slightly for the suction side. This effect is attenuated when the Reynolds number is higher. For three different cross sections located by $(x - r_i) / D_H = 3.2; 7.4; 11.5$, this phenomenon (increase of

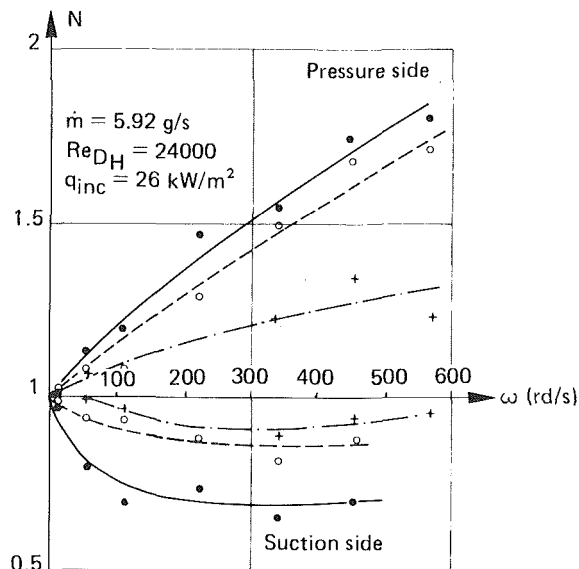


Fig. 13 Ratio $N = Nu_\omega / Nu_0$ with rotating speed ω , for three locations ($x - r_i / D_H = +3.2, 7.4, 11.5$ for the centrifugal channel)

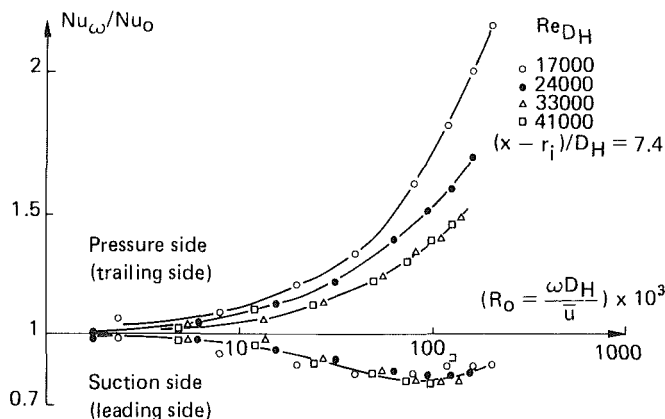


Fig. 14 Variation of ratio N with Rossby number Ro for centrifugal channel

N along the pressure side and decrease along the suction side) continues to evolve; this is explained by the flow, which is still in development (Fig. 13).

The results obtained for the four Reynolds numbers are shown in Fig. 14 with the Rossby number, which characterizes Coriolis aspect. We notice that the data are well correlated with the Rossby number, especially for the suction side.

In Fig. 15, the ratio of the mean Nusselt number $(Nu_\omega (PS) + Nu_\omega (SS)) / 2$ to Nu_0 is shown with Rossby number; this figure compares our results with those from different references. In the same way, a comparison between our results and the prediction of Iskakov and Trushin (1985) with Ra / R_e^2 , which represents the centrifugal aspect, is shown in Fig. 16. The agreement between these results is generally poor. These discrepancies could be explained by the different geometries of the channel itself and the upstream geometry if the flow is in development.

For the centripetal channel, the failure of many thermocouples did not allow us to obtain a complete set of data. In the near future, this channel will be particularly studied with the infrared pyrometer.

Theoretical Analysis

The prediction by a numerical approach of the heat transfer

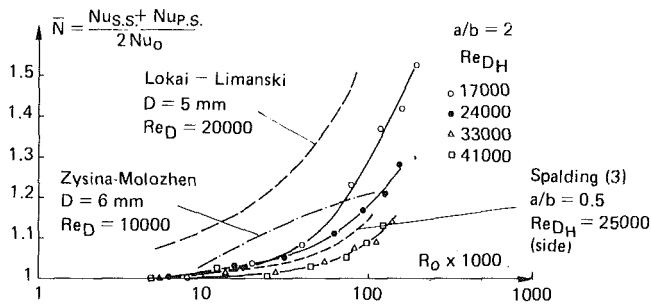


Fig. 15 Variation of ratio N with Rossby number Ro for centrifugal channel and comparison with results of different reference sources

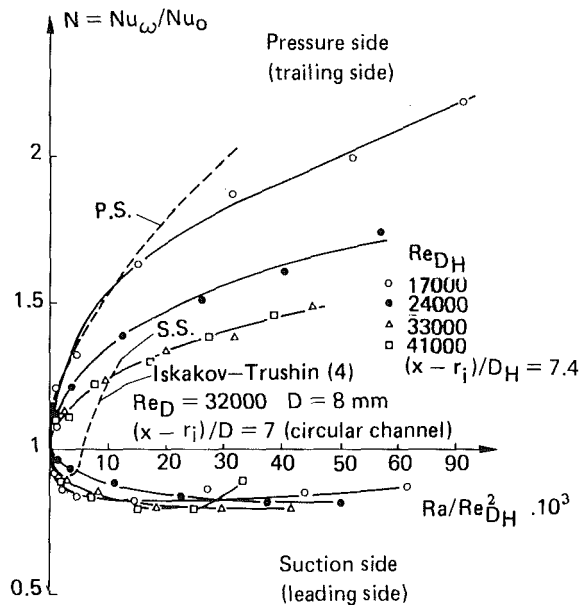


Fig. 16 Variation of ratio N with Rayleigh number for centrifugal channel

coefficient for a rotating coolant channel is in development with the objective of modeling the flow in coolant passages of gas turbine rotor blades.

Only preliminary results of the numerical method will be presented.

In a first step, the flow with heat transfer to the wall (constant heat flux) is modeled for a centrifugal flow in a simple rectangular duct.

The numerical approach consists in solving the Navier-Stokes equations with the mixing length turbulence model. Boundary-layer-type flow is the major assumption. Consequently, near the wall the logarithmic velocity profile has been taken ($u/u_t = 5.50 + 2.5 \ln(\delta u_t/\nu)$). The fluid properties C , k , and μ are constant.

The method chosen to solve the Navier-Stokes equations in three dimensions is the time marching ADI (Alternate Directions Implicit) (Dutoya and Michard, 1979, 1980).

An example of the results obtained for the rectangular duct is shown in Figs. 17 and 18. In Fig. 17, the secondary flow for two locations is shown. As boundary conditions for $x = r_i$, the total pressure and the enthalpy are imposed; for $x = r_i + L$, the static pressure is imposed.

For the secondary flow, we can point out the two vortices developing from the inlet of the channel.

The axial velocity profiles obtained for $(x - r_i)/D_H = 8.7$ without and with rotation are compared (Fig. 18). The distortion of the profiles appears clearly. The flow speeds up for the pressure side and thus the friction factor (and consequently

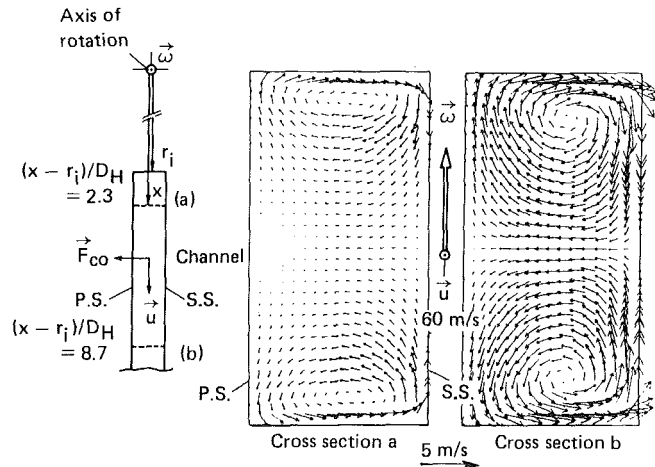


Fig. 17 Secondary flow

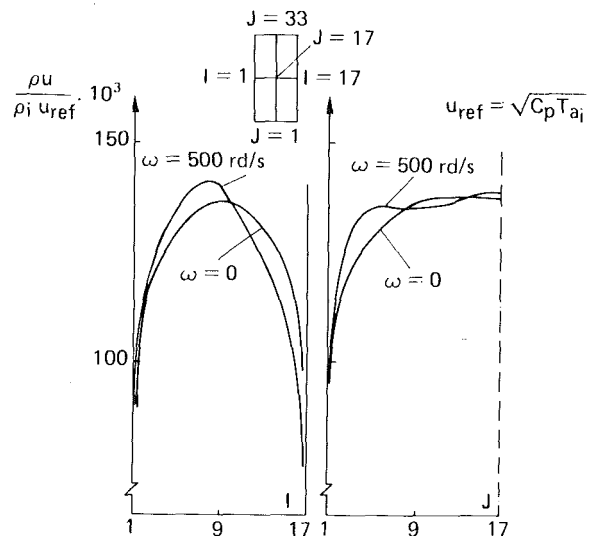


Fig. 18 Axial velocity profiles for $\omega = 0$ and $\omega = 500$ rd/s

the heat transfer coefficient) increases. On the contrary, the flow slows down near the suction side and thus the friction factor (and heat transfer coefficient) decreases.

This qualitative agreement with the experimental results is the first step in the validation of the numerical model.

In a second step, a total representation of the full test section and inlet will be developed.

Concluding Remarks

The results obtained and described in this paper show that the rotation, for a centrifugal channel with turbulent flow, induces a global augmentation of the heat transfer coefficient. The origin of this effect is essentially connected to the Coriolis force. This force gives rise to a secondary flow and the numerical analysis points out two opposing vortices. This secondary flow can greatly distort the velocity and temperature fields and consequently the heat transfer coefficient. Locally, the experimental results show that the transfer coefficient is strongly increased for the pressure side and is slightly depressed for the suction side. This effect is weaker when the Reynolds number is higher. This point could be explained by the natural turbulence of the flow becoming larger than the one induced by rotation. The accuracy of the experimental results is dependent on the transverse wall temperature profile and accordingly depends on the distribution of the heat transfer

coefficient. Thus, another distribution will modify these results. Therefore, the infrared pyrometry measurements will allow us to eliminate all assumptions relative to the conductive term in the heat balance.

The comparison of these experimental results with different reference sources is generally poor. The discrepancies between these results could be explained by the different geometries of the channels. A possible hypothesis is that the development of secondary flow will be different and consequently the distortion of velocity and temperature profiles. In addition, when the flow is not fully developed, the geometry of the inlet before the channel induces an "upstream effect."

Experimental investigations are planned to define precisely the effect of rotation, in particular for the centripetal channel. Also, another test section, a rectangular-sectioned duct with ratio $a/b = 0.5$ instead of $a/b = 2$ for the first test section, will be studied. For that purpose, the infrared pyrometer described here will be used for the thermal analysis.

The theoretical approach will be continued and improved and will allow discussion on these assumptions. Eventual improvement of the numerical modeling could be achieved by a choice of a better turbulence model ($k-\epsilon$, Algebraic Stress Model).

Acknowledgments

The author gratefully acknowledges DRET for permission to publish the studies described.

In addition, the author would like to thank his colleagues

at ONERA, for their support in this work, in particular: Mr. M. Izard, Mr. G. Kergreis, Mr. P. J. Michard, M. P. Nail, Mr. J. Perucchini, and Mr. P. Roux.

References

- Charpenel, M., and Wilhelm, J., 1985, "Pyrometrie I. R. pour la Mesure de Temperatures d'Aubes de Turbine," *Symposium AGARD, Echange Thermique et Refroidissement dans les Moteurs a Turbine*, Norway.
- Dutoya, D., 1979, "A Program for Calculating Boundary Layers and Heat Transfer Along Compressor and Turbine Blades," T. P. ONERA n° 1979-88 and Proceedings of the 1st International Conference held at the University College, *Numerical Methods in Thermal Problems*, Pineridge Press, Swansea, United Kingdom, pp. 501-511.
- Dutoya, D., and Michard, P. J., 1980, "Une Methode de Volumes Finis de type Implicite pour le Calcul des Ecoulements Elliptiques," *La Recherche Aérospatiale*, No. 1980-2, pp. 123-129.
- Harasgama, S. P., and Morris, W. D., 1988, "The Influence of Rotation on the Heat Transfer Characteristics of Circular, Triangular, and Square-Sectioned Coolant Passages of Gas Turbine Rotor Blades," *ASME JOURNAL OF TURBOMACHINERY*, Vol. 110, pp. 44-50.
- Iskakov, K. M., and Trushin, V. A., 1985, "The Effects of Rotation on Heat Transfer in a Radial Cooling Channels of Turbine Blades," *Thermal Engineering*, No. 32 (2), pp. 93-96.
- Kheshgi, H. S., and Scriven, L. E., 1985, "Viscous Flow Through a Rotating Square Channel," *Physics of Fluids*, Vol. 28 (10), pp. 2968-2979.
- Morris, W. D., 1981, "Heat Transfer and Fluid Flow in Rotating Coolant Channels," *Research Studies Press*, Wiley, New York.
- Siegel, R., 1985, "Analysis of Buoyancy Effect on Fully Developed Laminar Heat Transfer in a Rotating Tube," *ASME Journal of Heat Transfer*, Vol. 107, pp. 338-344.
- Spalding, D. B., and Skiadaressis, D., 1978, "Heat Transfer in Ducts Rotating Around a Perpendicular Axis," *6th Int. Heat Transfer Conference*, Toronto, Vol. 2, pp. 91-95.

Heat Transfer Visualization and Measurement in Unstable Concave-Wall Laminar Boundary Layers

R. I. Crane

J. Sabzvari

Department of Mechanical Engineering,
Imperial College of Science & Technology,
London, SW7 2BX, United Kingdom

Using liquid crystal sheet in a hybrid constant-wall-temperature/constant-heat-flux procedure, heat transfer distributions have been measured in concave-wall laminar boundary layers with a natural Görtler vortex system in a near-zero pressure gradient. Stanton numbers at vortex downwash positions across the span exceeded those at upwash positions by factors as high as three. Spanwise-averaged Stanton numbers exceeded analytical flat-plate values only after the appearance of highly inflected upwash velocity profiles and the onset of spanwise meandering of the vortices, where the Görtler number exceeded ten. Levels then reached values comparable with turbulent correlations, at Reynolds numbers and turbulence levels (up to 3 percent) where previous measurements of the intermittency factor indicated that transition had not begun. Boundary layer thinning in downwash zones could account for much of the heat transfer enhancement. The phenomenon could be a contributory factor to the long, apparently transitional regions often reported on blade cascade pressure surfaces, although the Görtler numbers where enhancement occurred are higher than those normally associated with pressure-surface transition.

Introduction

External heat transfer prediction techniques currently in use in the gas turbine industry frequently perform poorly on blade pressure surfaces (e.g., Daniels and Browne, 1981), where cascade experiments often indicate extensive transitional regions in the boundary layer quite unlike those on suction surfaces. There appears to be a delicate balance between the destabilizing effects of free-stream turbulence and concave curvature and the stabilizing influence of a strong favorable pressure gradient. Recently, much progress has been made in two-dimensional prediction codes to model turbulence and pressure gradient effects on transition, for example by computing the entrainment of free-stream turbulent kinetic energy into the boundary layer in order to predict transitional behavior. With higher-order turbulence modeling (e.g., Wang et al., 1985), such codes offer much scope for long-term development, but meanwhile continued use will be made of simpler codes that handle laminar, transitional, and turbulent regions separately and require empirical input to determine the onset and completion of transition.

For concave wall curvature, transition start is typically fixed in these simple models (e.g., Forest, 1977) by monitoring two criteria, one for transition through Tollmein-Schlichting instability using empirical expressions developed for flat surfaces, and the other for Görtler instability; when either of these

reaches the critical value, transition is deemed to have begun and a turbulent diffusivity is gradually switched on in proportion to the intermittency factor, for which yet another empirical expression is used. This approach suffers from three major uncertainties. First, there is as yet no reliable model for transition due to Görtler instability. Second, while Görtler vortices tend to appear naturally under laboratory conditions and in some cascade experiments (Han et al., 1983), there is no direct evidence of their existence under engine conditions although Görtler numbers, representing the ratio of centrifugal to viscous effects in the boundary layer, are in the appropriate range (Brown and Martin, 1982) for amplification of small disturbances with wavelength of the order of 1 mm. Third, if a Görtler vortex structure does exist on a blade, either steadily or intermittently, there is no reason to suppose that its effect on heat transfer would be confined to the position and extent of transition; the magnitude of the heat transfer in the laminar and transitional regions is likely to be affected by the presence of longitudinal vortices.

It is widely felt (e.g., Priddy and Bayley, 1985) that further fundamental work on Görtler vortices is necessary before any significant progress can be made in resolving these uncertainties. Earlier experimental studies of Görtler vortex flows, e.g., Crane and Sabzvari (1982), have concentrated on the fluid dynamics, mainly in laminar flow and more recently examining the phenomena leading to transition (Sabzvari and Crane, 1985; Riley, 1986; Crane et al., 1987). Little, however, has been done to follow up the finding of McCormack et al. (1970) that spanwise-averaged Nusselt numbers Nu (derived from mass

Contributed by the International Gas Turbine Institute and presented at the 33rd International Gas Turbine and Aeroengine Congress and Exhibition, Amsterdam, The Netherlands, June 5-9, 1988. Manuscript received at ASME Headquarters February 11, 1988. Paper No 88-GT-36.

transfer data) in a concave-wall laminar boundary layer with Görtler vortices can exceed those on a flat wall by more than 100 percent. Kan et al. (1971) developed, from mass transfer measurements in a cascade, an empirical relationship whereby Nu is given by multiplying the laminar flat-plate value by $(1 + G_0)^{1/2}$, G_0 being the Görtler number $Re_x(\theta/R)^{1/2}$ where θ is the momentum thickness (calculated) and R the wall radius of curvature. A different viewpoint on the interaction between the vortices and heat transfer was taken by Kamotani et al. (1985), who investigated the effects of heating (from below) on the vortex structure; the strength and nonlinear amplification of the vortices were found to be enhanced. Recently Kottke (1986) has measured spanwise-periodic mass transfer on a concave plate, generating disturbances of varying strength by use of different turbulence grids placed at varying distances from the plate leading edge. He reported mass transfer increases similar to those of McCormack et al. (1970) but found that the magnitude of the increase was strongly dependent on the disturbance wavelength (grid mesh size), being greatest when this coincided with the Görtler vortex wavelength predicted (from a stability diagram) to receive the greatest amplification rate. No fluid dynamic measurements were reported by Kottke so it is not clear whether his results refer to "classical" Görtler vortices (amplified by curvature from small disturbances) or to a periodic structure established upstream of the curved plate; nevertheless, they appear to suggest in addition that spanwise periodicity in mass transfer does not necessarily lead to a significant overall enhancement, and that it is also possible to have no detectable periodicity.

The present paper outlines an experimental study of the thermal effects of Görtler vortices, with the aim of determining spanwise and chordwise variations in heat transfer coefficient in laminar layers whose structure (in the absence of heating) has been established from measurements of the velocity field (Crane and Sabzvari, 1982; Sabzvari, 1984) and intermittency distribution (Crane et al., 1987). It attempts to relate the heat transfer results to the stage of vortex growth.

Experimental Arrangement

Flow Rig and Conditions. The closed-circuit water channel described by Crane and Sabzvari (1982) and Crane et al. (1987) was adapted for the present work. The circuit currently comprises a constant-speed pump with bypass loop, a heat exchanger to maintain constant water temperature, cone-and-float flowmeters, control valves, and an acrylic assembly combining settling chamber and test section. The 90-deg-bend test section has a constant concave-wall radius of 140 mm, and the width between the vertical curved walls is 40 mm. The channel was operated mainly with a water depth of 140 mm and a free surface, giving an effective aspect ratio of 7, which resulted in the most uniform inlet velocity distribution. The settling chamber contains four wire gauze screens of mesh size 1 mm and open area ratio 0.66, followed by a 5:1 area ratio contraction and a 55 mm straight length prior to the bend.

Laminar boundary layers, with a distinct pseudo-potential core flow, were obtained throughout the bend for Reynolds numbers Re_{xc} (based on bulk velocity and streamwise distance from contraction exit to bend exit) below about 55,000. Only for greater Re_{xc} did the hot-film probe measurements of Crane et al. (1987) indicate the onset of transition at any point on the concave wall, in the usual sense of the appearance of bursts of high-frequency turbulence. Core flow fluctuation intensities were at levels that usually have only a small effect on zero-pressure-gradient flat-wall laminar heat transfer. Prior to curvature, the intensity was typically 1 percent, but measured values downstream, up to 2.6 percent, were influenced by interaction between the core flow and a spanwise wandering motion characteristic of Görtler vortices; it could be misleading to regard such values as conventional turbulence intensities.

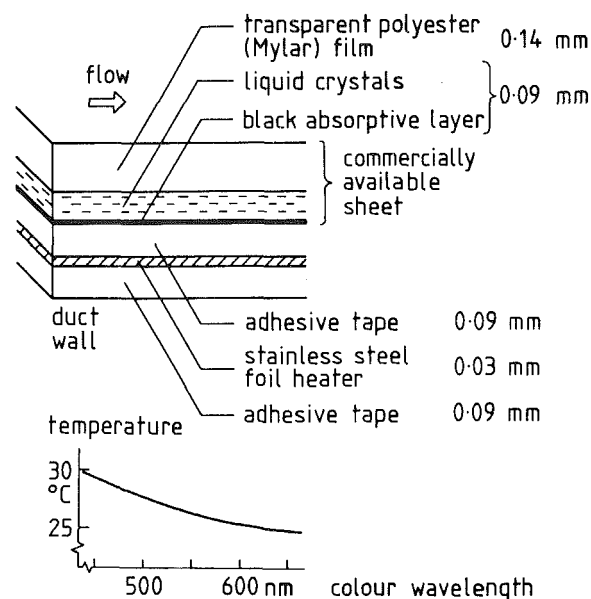


Fig. 1 Liquid crystal plus heater package and typical color-temperature response

More detailed velocity fluctuation results are given later. The ratio of boundary layer thickness δ at the start of curvature to wall radius R was typically 0.05. A short region of adverse pressure gradient at the bend entry was followed over most of the concave wall by a mildly favorable gradient, with velocity gradient parameter $K = (\nu/u_{pw}^2)(du_{pw}/dx)$ averaging 1×10^{-6} at $Re_{xc} = 24,500$. (u_{pw} is the potential wall velocity, obtained in practice by extrapolating to the wall the straight part of the velocity profile in the core). Görtler vortex pairs with a mean spacing (wavelength) of around 17 mm were obtained in that part of the span affected to a negligible extent by endwall secondary flow; vortex strengths and spacing were determined by the final screen (Crane and Sabzvari, 1982).

Heat Transfer Measurement Technique. Liquid crystal thermography has been described in general terms by Simonich and Moffat (1982) and in a form similar to that used here by Goldstein and Timmers (1982). This technique is well suited to the low-conductivity test wall material and has the advantage of mapping wall temperature (hence heat transfer coefficient on a constant-heat-flux wall) over the entire surface, particularly useful since vortex spanwise positions are not always known in advance. Sheets of encapsulated cholesteric liquid crystals (Parker, supplied by Edmund Scientific Corp.) and a stainless steel foil heater were mounted on the test walls as shown in Fig. 1. The heating current was taken from a high-current low-voltage transformer via copper bus bars clamped to the foil on the outside of the test wall, where the foil emerged through sealed slits; care was taken to obtain a uniform current density over the working area of the foil. The chosen event temperature range for the liquid crystals, where the color passes through the complete visible spectrum, was 25–30°C; an example of the color-temperature relationship is also shown in Fig. 2. Any change in this relationship due to water absorption (Simonich and Moffat, 1982) was minimized by carefully sealing the crystal-heater package around all edges and emptying the water channel between experiments.

The measurement procedure consisted of adjusting the current until a chosen color, a calibrated green shade repeatable to a given observer, was obtained at the desired location. Wall-to-core flow temperature ratio was then typically 1.03, sufficiently close to unity that neither the direction of heat flux nor the magnitude of the temperature ratio would cause flat-wall laminar heat transfer to differ substantially from values given

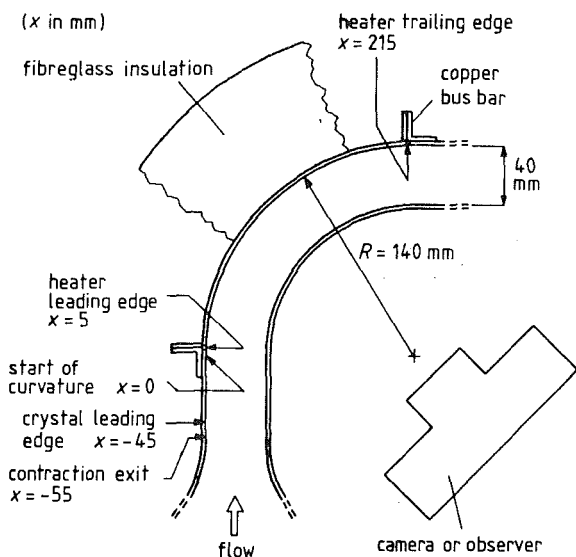
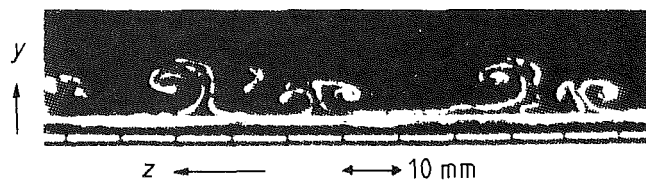


Fig. 2 Water channel test section showing liquid crystal and heater geometry

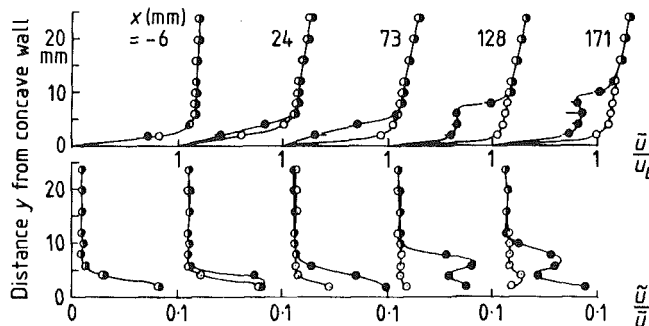
by the standard analytical relationship (given later in equation (2)). Heat loss by conduction through the duct wall was minimized by glass fiber insulation. The ratio Gr/Re^2 was always below the value for which the effect of free convection on forced convection heat transfer should be less than 10 percent (Gebhart, 1971). In practice, losses were estimated by the method suggested by Hippensteele et al. (1981), in which the electrical power required to obtain the same color with no fluid flow was found for each location, before and after the experiment; subtracting this from the flow-on power gives the forced-convection heat flux Q . Knowing this heat flux, the temperature indicated by the chosen color was corrected for conduction through the polyester film covering the crystals to give the actual wall temperature T_w . This hybrid constant-wall-temperature/constant-heat-flux scheme was estimated to give the temperature difference $T_w - T_c$ between wall and core fluid (typically 8°C) to $\pm 0.5^\circ\text{C}$, and the resulting surface heat transfer coefficient h to ± 10 percent, using the uncertainty analysis of Kline and McClintock (1953) with 20:1 odds. (In one or two high-heat-flux locations, where the temperature drop across the polyester film was more significant, the uncertainty rose to ± 15 percent; future measurements in such locations ideally require use of crystals with a different event temperature range, and the uncertainty in all locations could be reduced if the manual procedure were replaced by densitometer analysis of photographs taken with a color filter.) Wall temperature "maps" (uncorrected for the drop across the polyester film) were obtained by photographing the crystal sheet on color transparency film (Kodachrome) having found too wide a variation in color reproduction when using color negative film.

Figure 2 is a diagram of the full-span heater and crystal geometry in the water channel, showing also the observation position, which ensured a viewing angle within the range for which the crystals exhibit no color-angle dependency.

Flow Characterization Techniques. A single-channel fringe-mode laser Doppler anemometer system was used to obtain profiles and spanwise distributions of the streamwise (u) mean velocity with a maximum uncertainty of ± 3 percent and rms fluctuating velocity to ± 4 percent at most. Signal processing was by a Cambridge Consultants CCO8 frequency-tracking demodulator interfaced to an Apple II + microcomputer via a 12-bit fast A/D converter, as described by Crane et al. (1987). Mean velocity u (to ± 3 percent) and rms fluctuating velocity



(a) Hydrogen-bubble visualization of flow cross-section at $x = 186$ mm.



(b) Mean velocity and fluctuation intensity profiles.

○ downwash z -position, ● upwash z -position

Fig. 3 Görtler vortex structure at $Re_{xe} = 24,500$

\bar{u} (to ± 4 percent) were obtained from machine-code programs, with typical sampling times of around 10 s. The surface visualization provided by the liquid crystals was supplemented by hydrogen bubble visualization of cross sections using thin-sheet illumination. It should be noted that all flow field measurements and observations required a transparent concave wall and therefore had to be made before installing the crystal-heater assembly. The validity of comparisons between heat transfer and flow field results relies on the fact that the vortex structure in this rig does not vary from day to day and on the assumptions that (a) the presence of the thin crystal-heater assembly (with a smoothly faired leading edge) and (b) the heat flux do not significantly alter the flow field.

Heat Transfer and Flow Field Results

A typical laminar Görtler vortex structure is illustrated by the cross-section visualization in Fig. 3(a) and the velocity profiles in Fig. 3(b). The mushroom shapes in Fig. 3(a) mark vortex upwash positions, where low-momentum fluid is swept away from the wall; at the intervening and progressively widening downwash zones, core fluid flows toward the wall, resulting in fuller profiles and smaller boundary layer thickness. The temperature distribution on a constant-heat-flux wall, illustrated by the color contours in Fig. 4, reveals the same pattern. Core flow fluctuation intensity \bar{u}'/\bar{u} at $Re_{xe} = 24,500$ was between 0.011 and 0.013 throughout the curved test section and only moderate unsteadiness of the vortex system was seen near the bend exit. At $Re_{xe} = 49,100$, \bar{u}'/\bar{u} rose to 0.026 by $x = 37$ mm, remained close to this level until $x = 110$ mm, and then fell gradually to less than 0.010 by $x = 183$ mm; marked spanwise wandering of vortex pairs at this Re_{xe} is believed to have contributed to the increase in core \bar{u}'/\bar{u} .

In Fig. 5, examples of the streamwise distribution of Stanton number St are plotted for upwash and downwash positions, St being defined here as

$$St = h / (\rho_f U_b c_{p,f}) \quad (1)$$

where $h = \dot{Q} / (T_w - T_c)$; ρ_f = density of fluid at film temperature $T_f = 1/2(T_w + T_c)$; U_b = bulk velocity, used for simplicity in place of u_{pw} (consistent with the uncertainty in

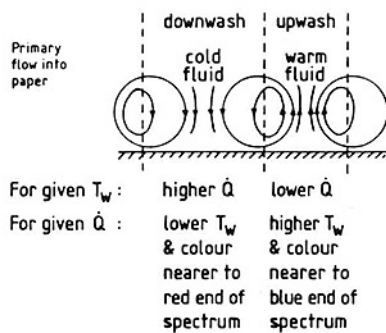
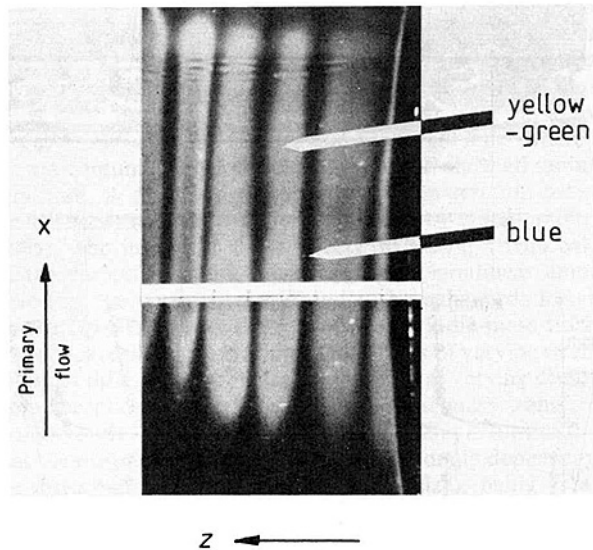


Fig. 4 Wall temperature contours at $Re_{xe} = 40,900$

h); c_{pf} = constant-pressure specific heat of fluid at T_f .

From initially low values near the start of curvature, where the effect of the adverse pressure gradient may still have been felt, St rose rapidly, particularly in the downwash region where it exceeded the upwash value by a factor of 2 to 3 over the downstream half of the bend. Spanwise distributions of St are plotted in Fig. 6. The mean vortex wavelength λ measured from four minima in St agreed to within 4 percent with that measured from five minima in spanwise velocity distributions, although a spanwise shift of the complete vortex system appeared to have occurred, by about 0.2λ . This shift could be explained by the fact that the heat transfer data refer to the wall itself ($y = 0$), whereas the velocity data refer to $y = 4$ mm, in a stage of vortex development where the upwash flows (seen in cross section) are generally not perpendicular to the wall. The distributions show a rapid growth of amplitude with x at $Re_{xe} = 24,500$ but a fall at $Re_{xe} = 49,100$; the fall reflects the increasing effect of spanwise meandering of the vortices (which reduces the time-averaged differences between fixed z positions originally representing upwash and downwash regions). The crystals have a frequency response of around 1 Hz (Simonich and Moffat, 1982) and did not exhibit a significant color fluctuation during the unsteady phase of vortex development (Crane and Sabzvari, 1982) at these Re_{xe} values. However, at still higher flow rates, where the hot-film measurements of Crane et al. (1987) have shown the boundary layer to be transitional (high-frequency fluctuations as well as low-frequency vortex unsteadiness), low-frequency components of the oscillation in vortex positions were detectable as a range of color at a fixed location. Figure 7 illustrates this effect on St at $Re_{xe} = 69,500$ and indicates larger fluctuations in down-

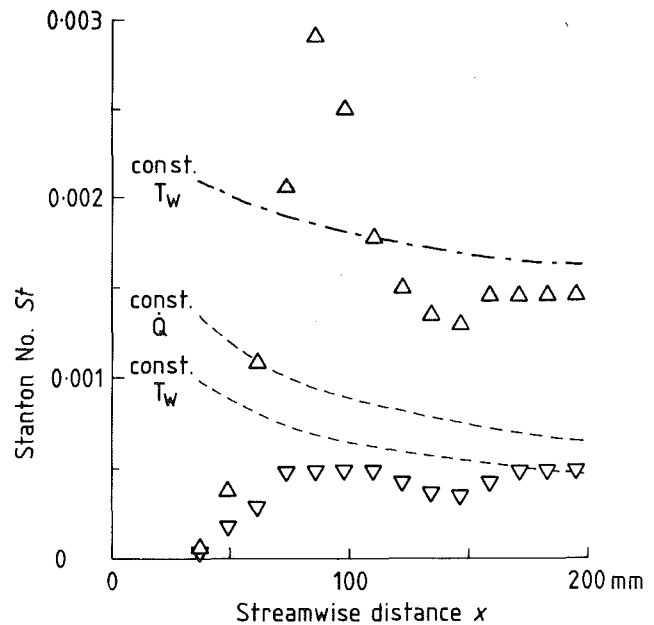


Fig. 5 Streamwise variation of Stanton number at $Re_{xe} = 49,100$: Δ downwash z position, ∇ upwash z position; ---- laminar, - - - - turbulent flat-plate relationships (based on effective x)

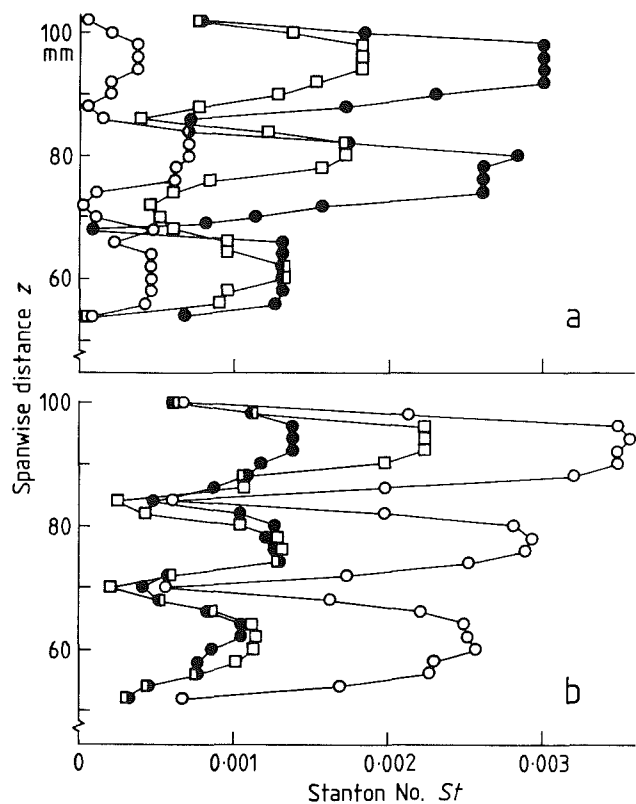


Fig. 6 Spanwise variation of Stanton number at $Re_{xe} = 24,500$ (a) and $49,100$ (b); $x = 86$ mm \circ , 139 mm \square , 186 mm \diamond

wash than in upwash zones. This is consistent with a phenomenon observed by Sabzvari (1984), whereby small secondary vortex pairs appear near the upwash zones of the original vortices, in the inner region ($y/\delta < 0.25$) of the boundary layer; these amplify and migrate to the downwash zones before appearing to merge with the meandering primary vortices.

A comparison of the spanwise-averaged Stanton number (over three vortex wavelengths) with flat-plate analytical results

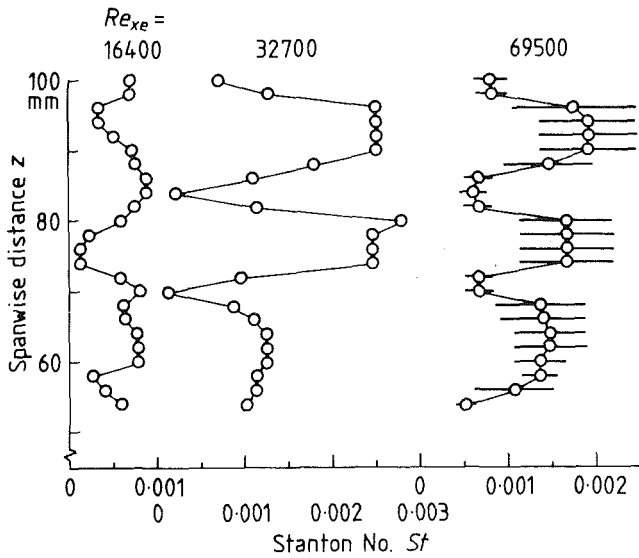


Fig. 7 Effect of flow rate on spanwise distribution of Stanton number at $x = 186$ mm

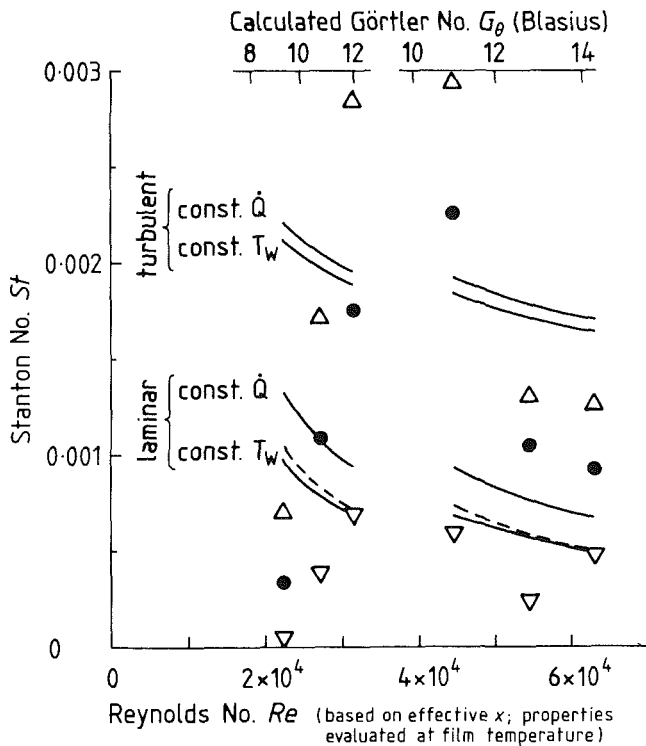


Fig. 8 Comparison of spanwise-averaged Stanton number with flat-plate relationships: \bullet St averaged over three vortex wavelengths; — flat-plate analytical or empirical, using effective x ; --- flat-plate analytical using $x = 0$ at contraction exit; Δ maximum St at downwash near $z = 80$ mm; ∇ minimum St at upwash near $z = 87$ mm

or correlations is shown in Fig. 8, which includes data for $Re_{xe} = 24,500$ and $49,100$. Here Re_x is the effective Reynolds number based on distance from an effective boundary layer origin determined from a measured velocity profile before the start of curvature ($x = -25$ mm) with the assumption of Blasius development up to that point. Since there appears (Crane et al., 1987) to be no true transition at these Re_{xe} , the laminar flat-plate solutions are of more relevance, given by Kays (1966) as

$$St = C Re_x^{-1/2} Pr^{-2/3} [1 - (x_1/x)^{3/4}]^{-1/3} \quad (2)$$

where x_1 is the unheated starting length (and both x and x_1 are

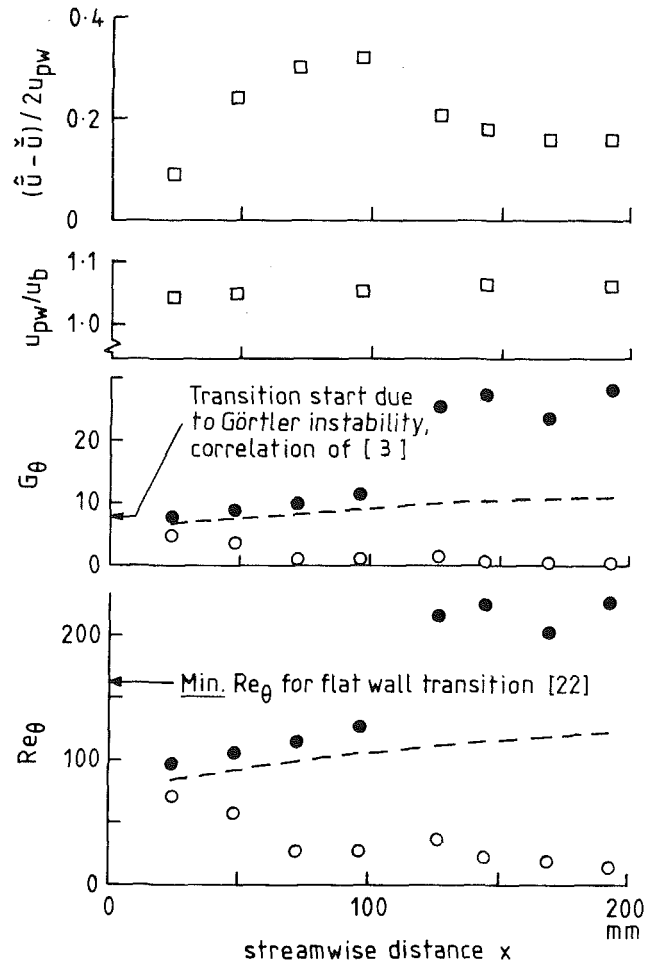


Fig. 9 Amplitude $(\hat{u} - \tilde{u})/(2u_{pw})$ of $\bar{u}(z)$ distribution, potential wall velocity u_{pw}/u_b , Görtler number G_θ , and momentum thickness Reynolds number Re_θ at $Re_{xe} = 24,500$; \circ downwash; \bullet upwash; --- calculated (Blasius, effective x)

now measured from the effective origin) and C has the value 0.332 for a constant T_w (beyond $x = x_1$) or 0.453 for a constant Q . The averaged St (shown by solid circles) is seen to exceed the laminar flat-plate values significantly for $Re_x > 3 \times 10^4$. All the data so far obtained for which this mean heat transfer enhancement occurs correspond to the phase of vortex development following the appearance of a severe inflection in the velocity profile at upwash. This phase, where spanwise meandering occurs, is also identified (Crane and Sabzvari, 1982) with the attainment of Görtler numbers G_θ between 10 and 15 approximately (based on the average of measured θ at an upwash and a downwash position), and with a decrease (with x) in the amplitude of the $u(z)$ distribution after it reaches a peak of $0.3 u_{pw}$ to $0.4 u_{pw}$. This amplitude is plotted, together with other relevant parameters in Fig. 9; $\hat{u} - \tilde{u}$ is the downwash-upwash difference in mean velocity for a given vortex pair at the y position where it peaks. It is interesting to note that G_θ for a Blasius boundary layer (starting at the effective origin) is also in the range 10 to 15 for all the present data where spanwise-averaged St exceeds the laminar analytical flat-plate values. Also, Forest's (1977) correlation for G_θ at transition onset is exceeded by the upwash-downwash averaged G_θ for x greater than a value between 100 and 130 mm, where averaged St first exceeds the laminar flat-plate values. However, flat-plate transition onset, from the correlation of Abu-Ghannam and Shaw (1980), should not occur until $Re_\theta \approx 500$ for $\bar{u}/\bar{u} \approx 1$ percent, or $Re_\theta \approx 163$ for very high turbulence levels. The highest measured spanwise-averaged St are comparable with turbulent flat-plate values, but not quite as high

as suggested by the empirical relationship of Kan et al. (1971).

At $Re_{xc} = 49,100$, upwash-downwash averaged G_θ again exceeded the transition onset value from Forest (1977), while Re_θ at upwash (but not the upwash-downwash averaged value) was greater than the value of ≈ 250 expected (Abu-Ghannam and Shaw, 1980) for start of transition on a flat wall at the measured local \bar{u}/\bar{u} . For this flow rate, upwash-localized transition is therefore less unlikely than at $Re_{xc} = 24,500$ but intermittency factor data (Crane et al., 1987) indicated that the boundary layer was still essentially laminar.

To test the hypothesis that the high transfer coefficients at downwash are simply the result of the reduced boundary layer thickness there (and not, for example, due to crossflow), one can calculate the streamwise distance necessary for a flat-plate boundary layer to achieve a thickness equal to the measured downwash value, and hence find the corresponding flat-plate Stanton number. It was not generally possible to make velocity measurements closer than 2 mm from the wall, so values of δ or θ at downwash locations are subject to considerable uncertainty, as much as 50–100 percent, but their small absolute values allow an upper limit on δ or θ to be found with reasonable confidence. For $Re_{xc} = 24,500$, where the most comprehensive set of velocity data is available, a typical result of such a calculation (at $x = 186$ mm and a downwash zone near $z = 95$ mm) is as follows: The flat-plate St corresponding to the largest conceivable θ derived from the velocity profile is 2.1×10^{-3} ; the flat-plate value corresponding to the effective Re_x is 0.7×10^{-3} ; measured St is 3.0×10^{-3} . These calculations suggest that, once the vortices have developed sufficiently for the downwash heat transfer to exceed expected flat plate values, a substantial part of the increase in St in downwash zones may be attributed to the local thinning of the boundary layer over that part of the span.

In most cascade experiments in the literature, pressure-surface Görtler numbers at the start of transition are reported as being considerably below the value of about 10, which the present data suggest is necessary for any enhancement of laminar heat transfer. However, it may be that the phenomenon regarded as transition by these experimenters was often a heat transfer or skin friction enhancement caused by an unsteady but still laminar vortex system as in the present work, in which case $G_\theta \sim 10$ cannot be regarded as a criterion for such enhancement. (Care must naturally be taken when comparing results with cascade data to exclude cases of bubble transition, unless relaminarization has occurred.) Since genuine transition often follows rapidly after the vortex meandering stage, it may be irrelevant in practice to distinguish between transition onset and the vortex-enhanced heat transfer that precedes it. Further experiments in this area are clearly required; similar heat transfer measurements in air, and in the water channel with strongly favorable pressure gradient and with simulated film cooling, will be reported by the authors in due course.

Conclusions

Liquid crystal sheet used with a hybrid constant-heat-flux/constant-wall-temperature procedure has enabled boundary layer heat transfer coefficients to be mapped in a water flow rig in which velocity and intermittency factor measurements and visualization are also available. In concave-wall laminar boundary layers having a Görtler vortex system, believed to develop from small disturbances originating at a settling chamber screen, Stanton numbers at vortex downwash positions have been found to exceed those at upwash positions by a factor as much as two to three. Spanwise-averaged Stanton numbers over three vortex wavelengths exceeded the analytical flat-plate value only after the mean velocity profile developed a region of negative slope and spanwise meandering set in.

This mean heat transfer enhancement, to levels comparable with turbulent correlations, also corresponded to Görtler numbers (calculated or based on upwash-downwash average measured momentum thickness) exceeding a value of around ten. Local thinning of the boundary layer in the downwash zones, which occupy the greater part of the span in this nonlinear phase of vortex development, could account for a substantial part of the enhancement.

Acknowledgments

This work was carried out with the aid of a Science and Engineering Research Council grant.

References

- Abu-Ghannam, B. J., and Shaw, R., 1980, "Natural Transition of Boundary Layers—the Effects of Turbulence, Pressure Gradient and Flow History," *Journal of Mechanical Engineering Science*, Vol. 22, pp. 213–228.
- Brown, A., and Martin, B. W., 1982, "Flow Transition Phenomena and Heat Transfer Over the Pressure Surfaces of Gas Turbine Blades," *ASME Journal of Engineering for Power*, Vol. 104, pp. 360–367.
- Crane, R. I., Leoutsakos, G., and Sabzvari, J., 1987, "Transition in Pressure-Surface Boundary Layers," *ASME JOURNAL OF TURBOMACHINERY*, Vol. 109, pp. 296–302.
- Crane, R. I., and Sabzvari, J., 1982, "Laser-Doppler Measurements of Görtler Vortices in Laminar and Low-Reynolds-Number Turbulent Boundary Layers," *Proceedings, International Symposium on Applications of Laser Doppler Anemometry to Fluid Mechanics*, Lisbon; also in: *Laser Anemometry in Fluid Mechanics*, R. J. Adrian et al., eds., LADOAN—Instituto Superior Tecnico, Lisbon, 1984.
- Daniels, L. C., and Browne, W. B., 1981, "Calculation of Heat Transfer Rates to Gas Turbine Blades," *International Journal of Heat and Mass Transfer*, Vol. 24, pp. 47–52.
- Forest, A. E., 1977, "Engineering Predictions of Transitional Boundary Layers," AGARD-CP-229, pp. 22.1–22.19.
- Gebhart, B., 1971, *Heat Transfer*, 2nd ed., McGraw-Hill, New York.
- Goldstein, R. J., and Timmers, J. F., 1982, "Visualization of Heat Transfer From Arrays of Impinging Jets," *International Journal of Heat and Mass Transfer*, Vol. 25, pp. 1857–1868.
- Hans, L. S., Chait, A., Boyee, W. F., and Rapp, J. R., 1983, "Heat Transfer on Three Turbine Airfoils," AFWAL-TR-82-2124 (AD-A28762); also Hans, L. S., and Cox, W. R., 1983, "A Visual Study of Turbine Pressure-Side Boundary Layers," *ASME Journal of Engineering for Power*, Vol. 105, pp. 47–52.
- Hippensteele, S. A., Russell, A. M., and Stepka, F. S., 1981, "Evaluation of a Method for Heat Transfer Measurements and Thermal Visualization Using a Composite of a Heater Element and Liquid Crystals," ASME Paper No. 81-GT-93.
- Kamotani, Y., Lin, J. K., and Ostrach, S., 1985, "Effect of Destabilizing Heating on Görtler Vortices," *ASME Journal of Heat Transfer*, Vol. 107, pp. 877–882.
- Kan, S., Miwa, K., Morishita, T., Munakata, Y., and Nomura, M., 1971, "Heat Transfer of a Turbine Blade," *Proceedings, Tokyo Joint International Gas Turbine Conference*, Tokyo, pp. 219–226.
- Kays, W. M., 1966, *Convective Heat and Mass Transfer*, McGraw-Hill, New York.
- Kline, S. J., and McClintock, F. A., 1953, "Describing Uncertainties in Single-Sample Experiments," *Mechanical Engineering*, Vol. 75, pp. 3–8.
- Kottke, V., 1986, "Taylor-Görtler Vortices and Their Effect on Heat and Mass Transfer," *Proceedings, 8th International Heat Transfer Conference*, San Francisco, CA.
- McCormack, P. D., Welker, H., and Kelleher, M., 1970, "Taylor-Görtler Vortices and Their Effect on Heat Transfer," *ASME Journal of Heat Transfer*, Vol. 92, pp. 101–112.
- Priddy, W. J., and Bayley, F. J., 1985, "Effects of Free Stream Turbulence on the Distribution of Heat Transfer Around Turbine Blade Sections," *International Journal of Heat and Fluid Flow*, Vol. 6, pp. 181–192.
- Riley, S., 1986, "Three-Dimensional Boundary Layer Transition," Ph.D. Thesis, Liverpool University, United Kingdom.
- Sabzvari, J., 1984, "Instability in Laminar and Transitional Boundary Layers on Concave Surfaces," Ph.D. Thesis, London University, United Kingdom.
- Sabzvari, J., and Crane, R. I., 1985, "Effect of Görtler Vortices on Transitional Boundary Layers," *International Symposium on Three-Dimensional Flow Phenomena in Fluid Machinery*, ASME FED-Vol. 32, pp. 113–119.
- Simonich, J. C., and Moffat, R. J., 1982, "New Technique for Mapping Heat-Transfer Coefficient Contours," *Review of Scientific Instruments*, Vol. 53, pp. 679–683.
- Wang, J. H., Jen, H. F., and Hartel, E. O., 1985, "Airfoil Heat Transfer Calculation Using a Low Reynolds Number Version of a Two-Equation Turbulence Model," *ASME Journal of Engineering for Gas Turbines and Power*, Vol. 107, pp. 60–67.

The Use of Foreign Gas to Simulate the Effects of Density Ratios in Film Cooling

A. J. H. Teekaram

C. J. P. Forth

T. V. Jones

University of Oxford,
Department of Engineering Science,
Oxford, United Kingdom

This paper provides a unique experimental assessment of the use of a foreign gas to vary the injection-to-mainstream density ratio in film-cooling experiments. It is widely recognized that it is important to scale both the velocity and density field in such tests in order that they will be representative of conditions in the gas turbine. Where it is difficult to achieve the temperature required for the correct injection-to-mainstream density ratio, some experimental techniques resort to the use of a heavier foreign gas to simulate the colder injection flow. In the experiment reported, the Isentropic Light Piston Tunnel has provided an environment in which a desired injection-to-mainstream density ratio can be achieved both by varying the temperature of the two airstreams and by using a heavier injection gas, carbon dioxide. Direct heat transfer measurements, which do not require the use of a mass transfer analogy, are taken. Use of the superposition model of film cooling allows the results to be interpreted easily to yield heat transfer parameters all obtained under isothermal wall boundary conditions. Comparison of results for air and carbon dioxide injection show that with this approach, it is possible to use a foreign injection gas to simulate the required injection-to-freestream density ratio.

Introduction

A great deal of experimental work has been undertaken in the last twenty years in order to provide design data for gas turbine cooling systems that make use of film cooling. These experiments have served to reveal the dependence of the cooling behavior on geometric and fluid mechanic parameters. However, the flow field should simulate as fully as possible that in a gas turbine engine if the measurements are to be used realistically in a design procedure.

The evolution of experimental procedures in film cooling reveals this growing awareness of the need for dimensional similarity. Many early experiments used a slightly heated injection gas, providing a small temperature difference so that gas properties were essentially constant. An adiabatic wall film-cooling efficiency was defined and its dependence on the injection-to-mainstream mass flux ratio investigated. In this constant-density case, the mass flux ratio was varied by varying injection-to-mainstream velocity ratio. Subsequently, it became evident that film-cooling performance depended also on the injection-to-mainstream density ratio, which is far from unity in the engine due to the large temperature differences. This effect was demonstrated by experiments, e.g., Pedersen et al. (1977) for a single row of holes, and Pai and Whitelaw (1968) for tangential slots, which relied on a mass transfer analogy. In these, a foreign, typically heavier gas was injected into the mainstream and measurements of gas concentration at the wall were used to infer the adiabatic wall effec-

tiveness. There is some debate over the accuracy of the analogy, which requires that the turbulent Schmidt and Prandtl numbers should be equal.

Goldstein et al. (1974) obviated the necessity to resort to the mass transfer analogy by measuring adiabatic wall temperature downstream of both air and Freon-12 injection. This again showed significant effects of varying the injection-to-mainstream density ratio on film cooling effectiveness. However, the experiments described all suffer from two drawbacks. Firstly, they only result in the measurement of one cooling parameter, typically the adiabatic wall effectiveness, whereas two parameters are required to quantify the process fully. The effect of the second parameter, for example an adiabatic wall heat transfer coefficient, has been shown to be important, particularly close to the injection location. However, its measurement proved difficult without resorting once again to a mass transfer analogy (Hay et al., 1985). Secondly, the adiabatic thermal boundary condition at the wall is not the best representation of the situation in a gas turbine blade, which more closely approximates an isothermal wall.

The challenge of designing an experiment that would directly measure two film-cooling parameters with the correct thermal boundary condition has been met by the Isentropic Light Piston Tunnel (Jones et al., 1973; Forth et al., 1985). It also enables engine representative Reynolds numbers and Mach numbers to be achieved. In addition, the injection-to-mainstream density ratio can be changed by varying the injection-to-mainstream temperature ratio. The mainstream gas conditions can be varied and the injection gas can either be heated or cooled. Once again, the effect of injection-to-mainstream temperature or density ratio was shown to be

Contributed by the International Gas Turbine Institute and presented at the 33rd International Gas Turbine and Aeroengine Congress and Exhibition, Amsterdam, The Netherlands, June 5-9, 1988. Manuscript received at ASME Headquarters February 11, 1988. Paper No. 88-GT-37.

significant for a single row of holes, a double row, and a slot (Forth et al., 1985; Forth and Jones, 1986).

A superposition model is used to characterize film cooling, which predicts that for an incompressible flow with constant properties, the film-cooled Nusselt number should vary linearly with θ , for a given flow field. This linear relationship can be found from a series of tunnel runs performed at different wall temperatures and fixed mainstream and coolant conditions. The values of the intercept A and slope B of the line are then the two parameters required to characterize the effect of injection on the Nusselt number. This approach has been validated for compressible, variable property flows over a reasonable range of θ (Forth et al., 1985). However, the effect of property variations through the boundary layer, characterized by the gas-to-wall temperature ratio, can be significant and has been quantified (Fitt et al., 1986).

This experimental facility also enables a unique investigation to be performed. A back-to-back comparison can be made between film-cooling experiments in which the injection-to-mainstream density ratio is attained both by varying the injection-to-mainstream temperature ratio and by employing a foreign (heavier) gas as the coolant. In both cases, it is emphasized that heat transfer measurements are taken and invoking a mass transfer analogy is not necessary.

Theoretical Considerations

The objective in injecting a high-molecular-weight foreign gas into an airstream is to produce the same flow field and mixing that take place when cold air of the same density is similarly injected. If turbulent mixing and momentum transport dominate over molecular processes then it would be expected that the governing momentum equation would be independent of the gas species present for incompressible flow. Hence by simulating the velocity and density boundary conditions the flow field would be the same in both cases. The distribution of coolant would also be similar if the above argument was followed. The governing enthalpy equation would, however, differ between the two cases if the specific heat C_p of the foreign gas was not the same as that of air. In the case of carbon dioxide the specific heat is 82 percent of that of air and in the majority of the flow field the local concentration of carbon dioxide will be low; hence the local value of C_p will not be too different from the specific heat for air. It might, therefore, be hoped that the governing enthalpy equation would be approximately the same for the two cases. If this were true then the heat transfer rate to the surface would be the same for identical thermal boundary conditions. However, the similarity in density is produced by using different coolant temperatures for air and carbon dioxide; hence it is necessary to measure parameters that are independent of the thermal boundary conditions. This is done using the quantities A and B in the superposition model of film cooling.

Superposition arises due to the linearity in the energy equa-

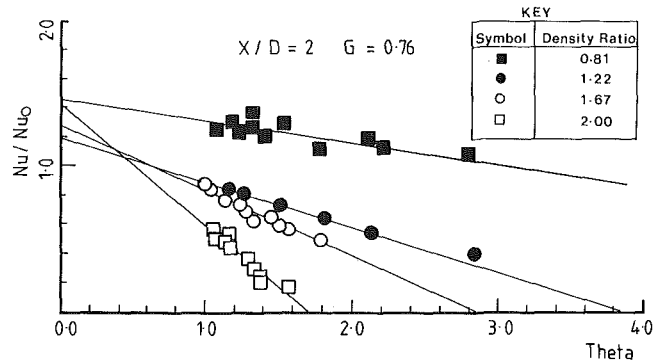


Fig. 1 Single row data: variation of Nusselt number with θ for four injection-to-freestream total density ratios

tion and allows the solution for the temperature field to be given by the sum of scaled solutions due to some reference boundary conditions. Similarly, the surface heat transfer rate is also the sum of scaled heat transfer rates for reference conditions as given below:

$$\dot{q} = \alpha(T_{\infty} - T_w) + \beta(T_{\infty} - T_{ii}) \quad (1)$$

where α is the heat transfer rate when the coolant is at the freestream temperature and there is unit difference between this and the wall temperature. β is similarly defined when the wall is at freestream temperature and the difference between the coolant temperature and the freestream is unity. α and β are thus dependent on the flow field and independent of the thermal boundary conditions. Re-arranging the above equation and dividing by freestream thermal conductivity gives the unit Nusselt number

$$\frac{\dot{q}}{K_{\infty}(T_{\infty} - T_w)} = A + B \left(\frac{T_{\infty} - T_{ii}}{T_{\infty} - T_w} \right) = A + B\theta \quad (2)$$

On dimensional arguments the Nusselt number should be only a function of the Reynolds number and injection-to-freestream density and velocity ratio. Thus in order to find A and B the freestream and coolant conditions are held constant and the wall temperature changed to vary θ . Typical linear plots are shown in Fig. 1. In this figure the mass flux ratio G is held constant and the density ratio is changed. As can be seen at small distances from injection the effect of density ratio is pronounced and it is in this context that it is hoped that variations in C_p would have a smaller effect. The physical reason for such density effects is that the coolant trajectory is significantly different when coolant velocity changes as the density changes at fixed mass flow. It is of interest to note that foreign gas injection through a porous strip was reported in Goldstein et al. (1966) and in this manner the injection mechanism was made similar for the different densities. Even though the variation of C_p was taken into account differences still existed in this case.

Nomenclature

a = speed of sound, m/s
 A, B = constants in the superposition formula:
 $\dot{q}/K_{\infty}(T_{\infty} - T_w) = A + B\theta$
 C_p = specific heat, J kg⁻¹K⁻¹
 d = hole diameter, m
 k = thermal conductivity, W/m K
 \dot{q} = heat transfer rate per unit area, W/m²
 T = temperature, K
 u = velocity, m/s

x = distance downstream from injection, m
 ρ = density, kg/m³

Subscripts

c = incompressible, constant properties
 i = injection
 o = without injection
 t = total conditions
 w = wall

∞ = freestream

Nondimensional Numbers

G = $\rho_i u_i / \rho_{\infty} u_{\infty}$ = mass flux ratio
 M = u_{∞} / a_{∞} = Mach number
 Nu = $\dot{q} x / k t_{\infty} (T_{\infty} - T_w)$ = Nusselt number
 Re = $\rho_{\infty} u_{\infty} x / \mu_{\infty}$ = Reynolds number
 θ = $(T_{\infty} - T_{ii}) / (T_{\infty} - T_w)$

Experimental Facility and Test Conditions

Results were obtained using the Isentropic Light Piston Tunnel, in which the test gas was compressed in a tube by an air-driven piston before flowing through the working section at constant temperature and pressure (Jones et al., 1973; Forth et al., 1985). A schematic of the working section is shown in Fig. 2.

Tests were performed on an instrumented flat plate, which was preheated or precooled by forced convection using air either electrically heated or cooled using a liquid nitrogen heat exchanger. A wall temperature range $280 < T_w < 350$ K was obtainable. Prerun wall temperatures were isothermal to within 1°C , although during the run the wall temperature rose by differing amounts at different locations. Typically a variation of 5°C over the length of the working section was observed in the middle of the run. This variation did not significantly affect the measurements, which could be made at any time during the run, or measurements extrapolated to the start of the run. As mentioned above, the effect of this slight nonisothermal wall temperature distribution was not discernable in the measurements.

The cooling geometry was a single row of circular holes, spacing-to-diameter ratio 2.5, hole length-to-diameter ratio 5, inclined at 30 deg to the flow. Unit Reynolds number and Mach number were $2.7E7/\text{m}$ and 0.55 , respectively.

Carbon dioxide was chosen as the foreign injection gas; it is denser than air, simulating a colder injection gas, is easily available, and has a specific heat of about 82 percent that of air.

Experiments were carried out at two different values of injection-to-mainstream density ratio, both achievable with either air injection or carbon dioxide injection. In all cases, the mainstream was air. The criteria used to determine the most satisfactory mainstream and injection temperatures were:

1 The values and range of θ should be satisfactory for a good comparison between results with air and carbon dioxide injection to be made.

2 The sensitivity of θ to small errors in measurement of temperatures should be small.

3 The value of the wall-to-gas temperature ratio should not be too different in the case of foreign gas injection from that of air injection. This would minimize any effects on heat transfer parameters due to property variations.

Three mass flux ratios of 0.15, 0.40, and 1.00 were investigated, representing mass flux ratios less than, almost equal to, and greater than that causing maximum cooling efficiency, respectively. For each mass flux ratio a number of tunnel runs was performed at the same injection and mainstream total temperature, but varying the wall temperature in order to vary the parameter θ without altering the flow field. Test conditions are summarized in Table 1.

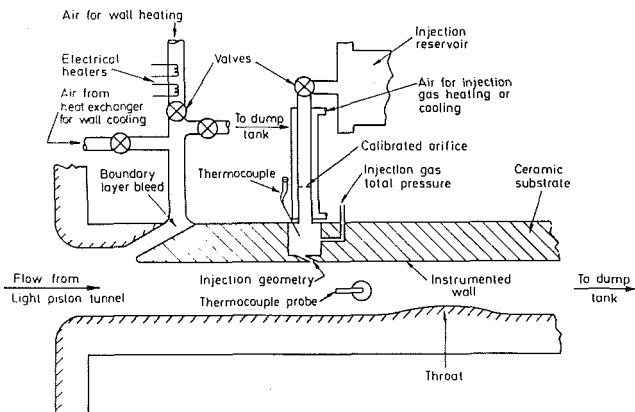


Fig. 2 Schematic of working section

Results were taken in the range $2 < x/d < 56$. Thin film gages were used to obtain spanwise-averaged values of heat transfer rate. Details of the instrumentation and data acquisition system can be found in Schultz and Jones (1973) and Oldfield et al. (1978).

Results and Discussion

A sample of the data taken for each mass flux ratio, for both density ratios, is shown in Figs. 3-8. The data are presented as a film-cooled Nusselt number, nondimensionalized with respect to the constant property unblown Nusselt number at that location, against θ . The lines shown are best fit lines through both air and carbon dioxide data for each x/d position.

General Description. Figures 9 and 10 show the effect of mass flux ratio on the effectiveness for both injection-to-mainstream density ratios. As observed, cooling is best close to the injection for a low mass flux ratio, $G=0.15$, over the tested range of θ . As the mass flux ratio is increased to $G=0.40$ cooling performance is increased at all x/d locations. A maximum value of $-B/A$ (qualitatively similar to an adiabatic wall effectiveness) of approximately 0.59 is obtained

Table 1

Injection Gas	T_{ti} K	$T_{t\infty}$ K	$\rho_{ti}/\rho_{t\infty}$	G
CO ₂	340	280	1.25	0.15 0.40 & 1.00
Air	270	338		
CO ₂	340	373	1.67	
Air	270	450		

KEY FOR FIGURES 3 - 5

SYMBOL	INJECTION GAS	T_{ti} K	$T_{t\infty}$ K
■	Carbon Dioxide	340	280
⊕	Air	270	338

KEY FOR FIGURES 6 - 8

■ ■	Carbon Dioxide	340	373
⊕	Air	270	450

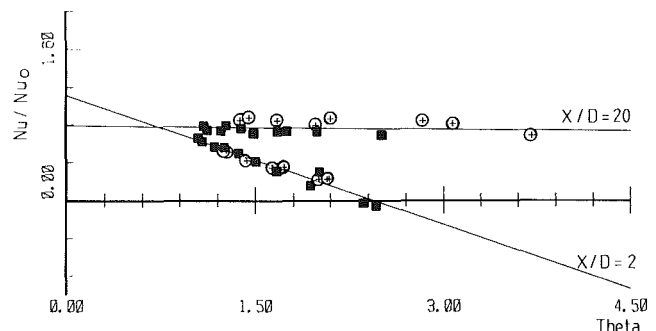


Fig. 3 Variation of Nusselt number with θ for $G=0.15$ at a density ratio = 1.25

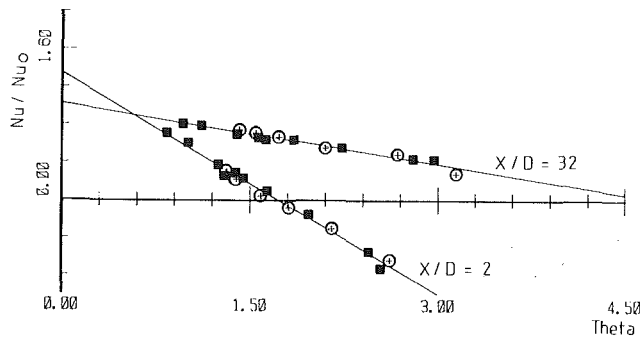


Fig. 4 Variation of Nusselt number with θ for $G=0.40$ at a density ratio = 1.25

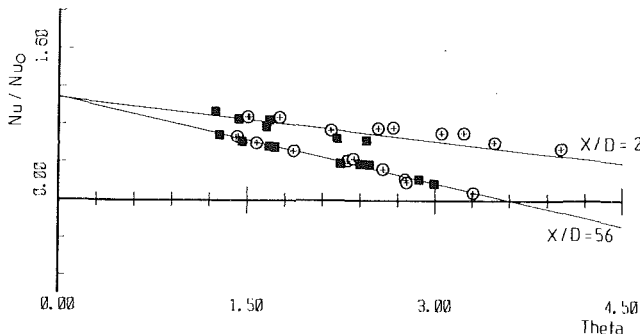


Fig. 5 Variation of Nusselt number with θ for $G=1.0$ at a density ratio = 1.25

at $x/d=2$ for injection-to-mainstream density ratio = 1.25 for both carbon dioxide and air injection. This value decreases monotonically as x/d increases. At $G=1.00$, the cooling performance close to the holes has decreased dramatically, while that farther downstream in the region ($x/d>20$) continues to increase. These trends are in agreement with results previously obtained.

Linearity of Nusselt Number Versus θ Plots. At constant injection temperature, mainstream temperature, and mass flux ratio, the results as shown in Figs. 3–8 indicate that the relationship between the Nusselt number and θ at a given location is linear, for both air and carbon dioxide injection, within the range of θ tested. Thus, values of A and B can be used to quantify the film-cooling performance fully.

Comparison of Air and Carbon Dioxide Injection. For both density ratios, the agreement between results obtained using air injection and those obtained using carbon dioxide injection is remarkably good. This applies to all three mass flux ratios and all x/d locations under investigation as indicated in Figs. 3–8. For the injection-to-mainstream density ratio of 1.25, it was possible to achieve a greater overlap between the two sets of results. This is because in all cases, the wall temperature could be varied approximately between $280 < T_w < 350$ K. This variation results in a smaller range and slightly different values of θ for a density ratio of 1.67.

Figures 9 and 10 show a comparison between values of $-B/A$ resulting from separate linefits through air injection data and carbon dioxide injection data. It is clear that the two methods of achieving the same injection-to-mainstream density ratio yield very similar results over the entire range of test conditions.

Effect of Property Variations. At a given value of θ , the wall-to-mainstream temperature ratio will not be the same for carbon dioxide injection as for air injection. This, and the fact that the injection gages have different thermal properties, would be expected to have an effect on the level of Nusselt number. In choosing the injection and mainstream

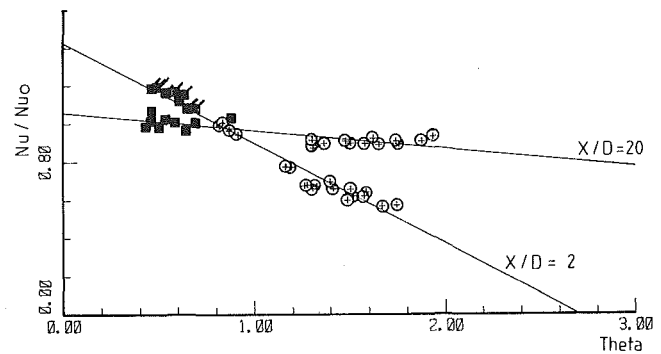


Fig. 6 Variation of Nusselt number with θ for $G=0.15$ at a density ratio = 1.67

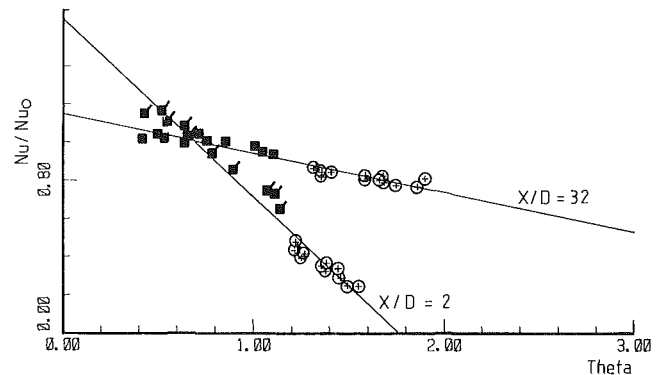


Fig. 7 Variation of Nusselt number with θ for $G=0.40$ at a density ratio = 1.67

temperatures for carbon dioxide and air injection, an attempt was made to minimize the effect of property variations.

The effect of wall-to-mainstream temperature ratio on the Nusselt number in a turbulent boundary layer, with air as the working fluid, has been quantified (Fitt et al., 1986) as

$$\text{Nu}/\text{Nu}_c = (T_w/T_{t\infty})^{-0.25} \quad (3)$$

One would expect to observe an effect of similar magnitude far downstream from film-cooling holes at low mass flux ratios, where the velocity and temperature profiles again resemble a turbulent boundary layer. This effect can be seen, for example, in Fig. 3 at $x/d=20$. The corrected data, shown in Fig. 11, do lie more closely on the same line. It is possible that the data close to injection require a similar type of correction. However, in all cases, the correction is less than 5 percent and is beneficial in terms of bringing the two sets of data closer together.

Comparison of Results With Previous Data. The sole object of the experiments reported here is to compare air and carbon dioxide injection. However, Fig. 12, from Forth et al. (1985), is included in order to show how these present data are consistent with the general variation of the effectiveness with mass flux ratio previously determined from tests at a wider range of density ratios.

Conclusions

1 It has been shown that there is close agreement between film-cooling heat transfer results obtained where the injection-to-mainstream density ratio is achieved either by changing the injection-to-mainstream temperature ratio or by using a foreign injection gas. This comparison has been made on the same test facility, using direct heat transfer measurements, without resorting to a mass transfer analogy. To the authors'

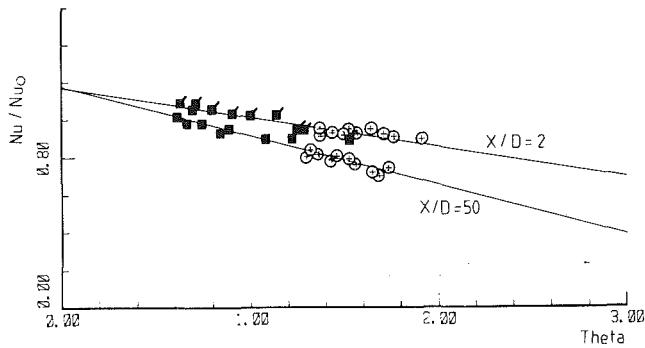


Fig. 8 Variation of Nusselt number with θ for $G=1.0$ at a density ratio = 1.67

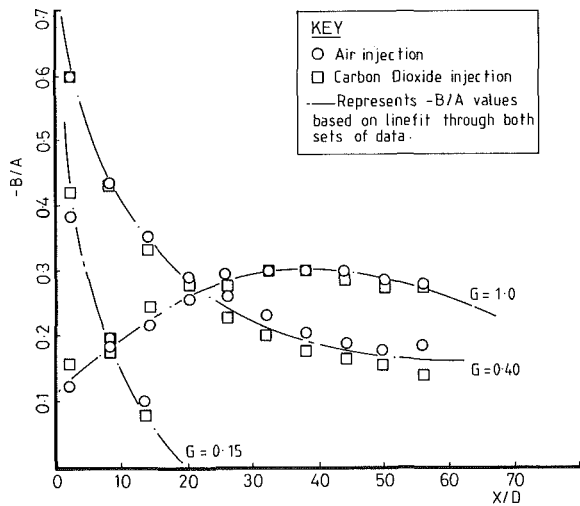


Fig. 9 Variation of the isothermal wall effectiveness with X/D at a density ratio = 1.25

knowledge this is the first such comparison to have been made.

2 This result considerably extends the range of injection-to-mainstream density ratios conveniently attainable in experimental facilities. It is imperative to scale this parameter correctly, since it can have a strong effect on film-cooling performance, particularly close to injection.

3 The results are best interpreted using a superposition model for film cooling. The film-cooling parameters A and B enable the cooling performance to be characterized in a manner independent of the thermal boundary conditions.

4 A slight effect due to the variation in properties with temperature has been observed. However, its quantitative dependence on the wall-to-mainstream temperature ratio, at least for large x/d , appears to be close to that previously reported for a turbulent boundary layer.

Acknowledgments

The authors wish to acknowledge T. Godfrey for his assistance in running the test facility. They also wish gratefully to acknowledge the support of the Ministry of Defence (Procurement Executive) for all of the work and the kind permission of Rolls-Royce plc to publish the paper.

References

Fitt, A. D., Forth, C. J. P., Robertson, B. A., and Jones, T. V., 1986,

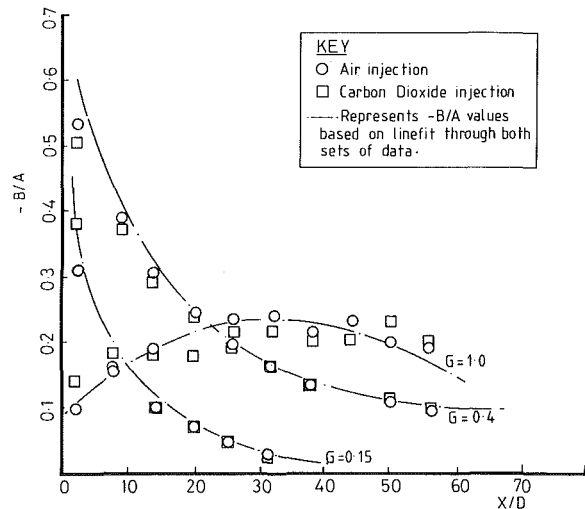


Fig. 10 Variation of the isothermal wall effectiveness with X/D at a density ratio = 1.67

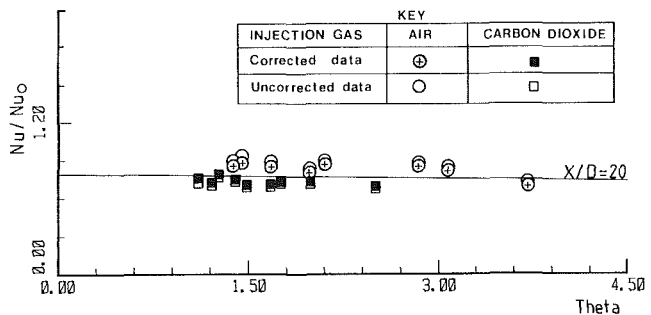


Fig. 11 Comparison between the corrected and uncorrected values of the Nusselt number at varying wall-to-mainstream temperature ratios

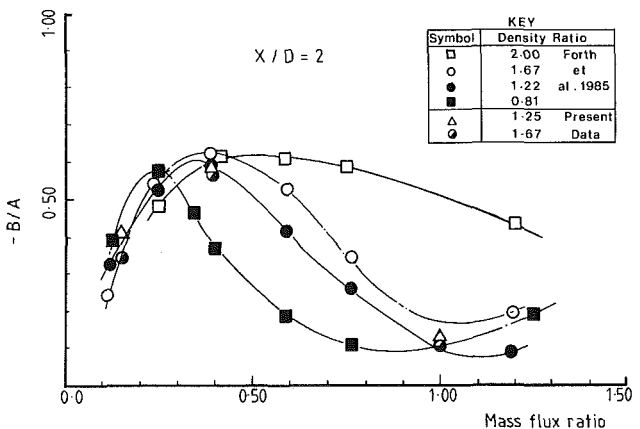


Fig. 12 Variation of the isothermal wall effectiveness with mass flux ratio and injection-to-freestream density ratio

"Temperature Ratio Effects in Compressible Turbulent Boundary Layers," *International Journal of Heat and Mass Transfer*, Vol. 29, No. 1.

Forth, C. J. P., Loftus, P. J., and Jones, T. V., 1985, "The Effect of Density Ratio on the Film-Cooling of a Flat Plate," *AGARD Conference Proceedings* 390.

Forth, C. J. P., and Jones, T. V., 1986, "Scaling Parameters in Film-Cooling," *Proceedings 8th International Heat Transfer Conference*.

Goldstein, R. J., Rask, R. B., and Eckert, E. R. G., 1966, "Film Cooling With Helium Injection into an Incompressible Air Flow," *International Journal of Heat and Mass Transfer*, Vol. 9.

Goldstein, R. J., Eckert, E. R. G., and Burggraf, F., 1974, "Effects of Hole Geometry and Density on Three-Dimensional Film-Cooling," *International Journal of Heat and Mass Transfer*, Vol. 17.

Hay, N., Lampard, D., and Saluja, C. L., 1985, "Effects of Cooling Films on the Heat Transfer Coefficient on a Flat Plate With Zero Mainstream Pressure Gradient," *ASME Journal of Engineering for Gas Turbines and Power*, Vol. 107.

Jones, T. V., Schultz, D. L., and Hendly, A. D., 1973, "On the Flow in an Isentropic Light Piston Tunnel," ARC 34217.

Oldfield, M. L. G., Jones, T. V., and Schultz, D. L., 1978, "On-Line Computer for Transient Turbine Cascade Instrumentation," *IEEE Transactions Aerospace and Electronic Systems*, AES-14, No. 5.

Pai, B. R., and Whitelaw, J. H., 1968, "The Influence of Density Gradients on the Effectiveness of Film-Cooling," *ARC Conference Proceedings 1013*.

Pedersen, D. R., Eckert, E. R. G., and Goldstein, R. J., 1977, "Film-Cooling With Large Density Differences Between the Mainstream and Secondary Fluid Measured by the Heat-Mass Transfer Analogy," *ASME Journal of Heat Transfer*, Vol. 99.

Schultz, D. L., and Jones, T. V., 1973, "Heat Transfer Measurements in Short Duration Hypersonic Facilities," *AGARD Conference Proceedings 165*.

An Experimental and Numerical Investigation of Near Cooling Hole Heat Fluxes on a Film-Cooled Turbine Blade

C. Camci¹

Aerospace Engineering Department,
The Pennsylvania State University,
University Park, PA 16802

Discrete hole film cooling on highly curved surfaces of a gas turbine blade produces very significant wall temperature gradients and wall heat flux variations near downstream and upstream of rows of circular cooling holes. In this study a set of well-defined external heat transfer coefficient distributions in the presence of discrete hole film cooling is presented. Heat transfer coefficients are measured on the suction side of an HP rotor blade profile in a short-duration facility under well-simulated gas turbine flow conditions. The main emphasis of the study is to evaluate the internal heat flux distributions in a detailed way near the cooling holes by using a computational technique. The method uses the measured external heat transfer coefficients as boundary conditions in addition to available internal heat transfer correlations for the internal passages. The study shows the details of the near hole temperature gradients and heat fluxes. The convective heat transfer inside the circular film cooling holes is shown to be very significant even with their relatively small diameter and lengths compared to the chord length. The study also indicates a nonnegligible wall temperature reduction at near upstream of discrete cooling holes. This is explained with the elliptic nature of the internal conduction field of the blade and relatively low coolant temperature levels at the exit of a film cooling hole compared to the mean blade temperature.

Introduction

Gas turbine blades are subject to very high thermal loads in modern high-efficiency engines operating at elevated turbine entry temperatures. An important portion of the thermal load is mainly due to convective heat transfer from the hot mainstream gases to the walls. Discrete hole film cooling is one of the frequently applied wall protection methods on the blade surfaces. Although this method has been used widely, its reduced effectiveness especially very near downstream of the coolant holes is well known because of the limited film cooling coverage in this zone. Reduced film cooling coverage occurs in a very severe manner, especially for higher blowing rate situations, in which coolant jets have more tendency to penetrate into the mainstream. One way of improving the film cooling coverage is to use a number of staggered rows of coolant holes. Shaping the external contour of the coolant hole, and reducing the hole spacing or row spacing, are other alternatives to improve the near hole film cooling coverage. A detailed understanding of the heat transfer mechanisms affecting the zone in the vicinity of the coolant holes is essential

for the improvement of cooling systems. As a fluid dynamics problem, the regions affected by discrete hole film cooling, especially very close to the coolant holes, are characterized by a flow that is viscous, obviously nonadiabatic, and fully three dimensional. However, the three-dimensionality problem reduces to a spanwise periodic three-dimensional problem near the midspan of the turbine blade.

The main objective of this paper is to investigate and understand the near cooling hole heat transfer behavior on a typical turbine rotor blade profile by means of both experiments and analysis. The measurements of the convective heat transfer coefficients with high resolution on the suction surface of the blade are presented. The measurements taken in the VKI short-duration compression tube are reported in a detailed format. In addition to the measurements taken under well-simulated flow conditions, a numerical simulation of the blade internal heat conduction field is presented for a mainstream gas temperature of 1650 K. Heat flux vectors on a sufficiently fine grid for a blade made up of a high-temperature alloy are generated by using a computational procedure using the measured external heat transfer coefficients as prescribed boundary conditions. This method provided the generation of the two-dimensional heat flux map of the metallic blade with a sufficiently high spatial resolution. It is shown that the inclusion of internal heat transfer from film cooling holes affects the

¹Previous address: Von Karman Institute for Fluid Dynamics, Turbomachinery Department, Ch. de Waterloo, 72, Rhode Saint Genese 1640, Belgium. Contributed by the International Gas Turbine Institute and presented at the 33rd International Gas Turbine and Aeroengine Congress and Exhibition, Amsterdam, The Netherlands, June 5-9, 1988. Manuscript received by the International Gas Turbine Institute November 1987. Paper No 88-GT-9.

computed heat flux distribution in a very significant manner. The investigation also indicates that the internal geometric configuration of the blade is an important factor in determining the internal heat flux map of the blade.

Although the heat transfer model used during the measurements of external convective heat transfer was made up of a low-conductivity machinable glass ceramic, the internal heat conduction study was performed on a blade made up of an actual metallic turbine blade material having a relatively high thermal conductivity compared to the ceramic model. The actual blade model consisting of four internal cooling passages in the radial direction did not employ any impingement cooling scheme, in contrast to many present day applications. At this stage, in order to obtain fixed internal thermal boundaries, internal heat transfer was only represented by the flow of coolant from the blade root to the tip and the flow of coolant inside the film cooling holes. The thermal boundary conditions in the radial passages and inside the film cooling holes were obtained from well-established heat transfer correlations existing in the literature. With the help of the fixed internal boundary conditions, the variations in the blade heat flux distribution occurring mainly from the gas side heat transfer (including film cooling) and the film cooling hole internal heat transfer can be visualized clearly.

Experimental Apparatus

Test Facility. A short-duration technique was applied and use was made of the VKI isentropic compression tube facility. The operation principles of this facility were developed by Schultz et al. (1973) about 15 years ago. The VKI CT-2 facility (Richards, 1980), constructed in 1978, consists of a 5-m-long, 1-m-dia cylinder containing a lightweight piston, driven by the air of a high-pressure reservoir. This cylinder is isolated from the test section by a fast opening slide valve. As the piston moves, the gas in front of it is nearly isentropically compressed until it reaches the pressure, and hence temperature levels, defined by the tunnel operator. The fast opening valve is then actuated by means of a detonator, allowing this pressurized air to flow through the test section. Constant free-stream conditions are maintained in the test section until the piston completes its stroke. The maximum test section dimensions are $250 \times 100 \text{ mm}^2$. The free-stream gas conditions can be varied between 300 and 600 K and 0.5 and 7.0 bar. A 5 m^3 dump tank allows downstream pressure adjustments between 0.1 and 4 bar. A typical test duration is about 500 ms. Further details about this facility and its operating principles are described by Jones et al. (1973), Richards (1980), Schultz et al. (1977), Ligrani et al. (1982), and Consigny and Richards (1982).

The Model. All measurements reported in this paper were carried out on the same rotor blade section as tested by Camci and Arts (1985b). The cascade geometry is fully described in

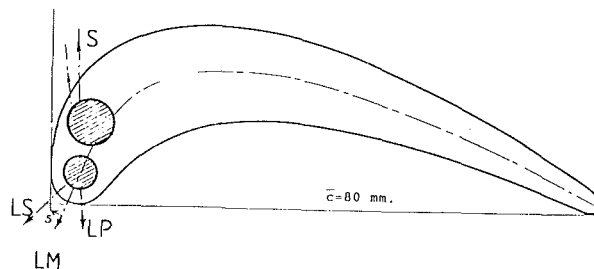
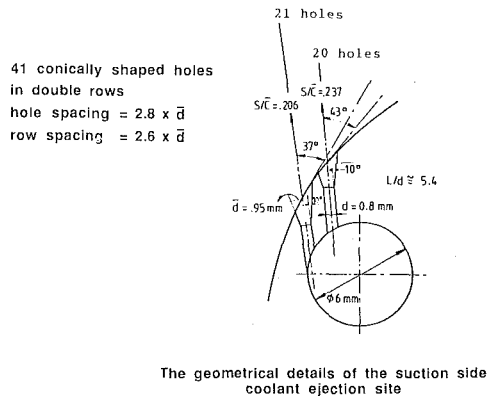


Fig. 1 Film-cooled turbine blade geometry

Consigny and Richards (1982) and the cooling configuration is summarized in Fig. 1. The blade instrumented for heat flux measurements was milled from "Macor" glass ceramic and 45 platinum thin films were painted on its surface. Two staggered rows of shaped holes ($d = 0.80 \text{ mm}$, $s/c = 0.206, 0.237$) are located on the suction side (row S); the row and hole spacing are respectively 2.48 mm and 2.64 mm (Fig. 1). The same model also carries leading edge (LS, LM, LP) cooling arrangements. However, leading edge cooling holes are blocked internally. The coolant flow is supplied by a regenerative-type cryogenic heat exchanger allowing a correct simulation of the coolant-to-free-stream temperature ratio. Pressure tapings and miniature thermocouples continuously provide the coolant characteristics.

Free-Stream Turbulence Generation. The free-stream turbulence was generated by a grid of spanwise oriented bars. The turbulence intensity was varied by displacing the grid upstream of the model; a maximum of 5.2 percent was obtained. The natural turbulence intensity of this facility is about 0.8 percent.

Data Acquisition. All the pressure, temperature, and heat flux measurements were directly acquired by a PDP 11 based high-speed data acquisition system. The details of this system

Nomenclature

\bar{c} = blade chord	m = local blowing rate = $\rho_c U_c / \rho_\infty U_\infty$	U = velocity
C_p = specific heat at constant pressure for air	\dot{m} = mass flow rate	u' = fluctuating velocity
d = coolant hole diameter	\mathbf{n} = unit normal vector	Subscripts
\bar{d} = exit hole diameter of the shaped hole	Nu = Nusselt number $h\bar{c}/k$	c = coolant flow condition
h = convective heat transfer coefficient = $\dot{q}/(T_{0\infty} - T_w)$	P = static pressure	ex = exit
i = incidence angle	Pr = Prandtl number = $\mu C_p/k$	in = inlet
k = thermal conductivity	Re = Reynolds number = $\rho U_\infty \bar{c}/\mu$	is = isentropic
\bar{l}_{max} = augmented mixing length downstream of an ejection site	s = curvilinear coordinate measured from stagnation point	r = recovery
M = Mach number	T = temperature	w = wall
	TU = free-stream turbulence intensity	0 = total condition or without coolant injection
		∞ = free-stream flow condition

Table 1 Detailed experimental parameters of heat transfer experiments

RUN	P _{0∞}	T _{0∞}	T _w /T _{0∞}	T _c /T _{0∞}	P _{oc}	\dot{m}_c/\dot{m}_∞	m
	bar	K	-	-	bar	-	-
092	2.891	408.3	.726	-	-	-	-
098	2.889	407.1	.719	.482	2.80	0.69	0.62
160	2.897	410.0	.711	.496	3.30	0.68	0.61
158	2.890	409.3	.720	.507	3.10	0.41	0.37
161	2.893	409.7	.696	.458	3.82	1.11	0.99
163	2.890	409.3	.711	.586	3.06	0.45	0.40
097	2.884	406.8	.708	.562	2.64	0.49	0.44
164	2.890	409.3	.715	.575	3.19	0.58	0.52
165	2.893	409.7	.704	.552	3.74	1.10	0.97
101	2.889	407.0	.700	.536	3.40	1.16	1.03
091	2.889	407.9	.733	.695	2.87	1.04	0.93
077	2.887	407.8	.725	.722	3.27	0.91	0.81
076	2.891	408.2	.724	.722	2.59	0.77	0.69
075	2.890	407.6	.722	.724	2.59	0.64	0.57
074	2.890	407.6	.720	.727	2.55	0.49	0.44

with a total sampling rate of 500 kHz are given by Camci et al. (1985), Camci (1985), and Camci and Arts (1985a, 1985b).

Measurement Technique. The local wall heat flux is deduced from the corresponding time-dependent surface temperature evolution, provided by the thin films. The wall temperature/wall heat flux conversion is obtained from an electrical analogy, simulating a one-dimensional semi-infinite body configuration. A detailed description of this transient technique is given by Schultz and Jones (1973), and Ligrani et al. (1982). The convective heat transfer coefficient is defined as the ratio of the measured wall heat flux and the difference between the free-stream recovery and the local wall temperatures. A recovery factor equal to 0.896 is used, as if the boundary layer on the blade surface was turbulent elsewhere. The uncertainties on the different quantities measured have been estimated as follows:

$$\begin{aligned}
 h &= 1000 \text{ W/m}^2\text{K} \pm 50 \text{ W/m}^2\text{K} \\
 P &= 2200 \text{ mm Hg} \pm 15 \text{ mm Hg} \\
 T &= 100^\circ\text{C} \pm 0.5^\circ\text{C} \\
 \dot{m}_c &= 0.020 \text{ kg/s} \pm 0.0005 \text{ kg/s} \\
 m &= 0.96 \pm 0.03
 \end{aligned}$$

Experimental Results and Discussion. Figure 2 shows the convective heat transfer behavior on the suction side when there is no coolant ejection. All other heat transfer data sets presented in this paper are nondimensionalized with the data of Fig. 2 (h_0). Details of the experimental conditions related to the heat transfer data sets are given in Table 1. The current film-cooled blade model has also three rows of cooling holes near the leading edge (Fig. 1). However, for this specific study, the leading edge holes are completely blocked internally. Their only influence is apparent on the total length of the transitional zone, as boundary layer roughening elements near the leading edge. Looking at Fig. 2, an early and abrupt laminar-to-turbulent transition is observed compared to the model having an identical external contour but without leading edge holes (smooth blade). A turbulent boundary layer is fully established for $s/\bar{c} > 0.2$. The existence of a transitional or fully turbulent boundary layer is confirmed by examining the timewise variation and the order of magnitude of the heat flux signal traces. As a consequence, the coolant film ejected from the suction side holes always interacts with a fully turbulent boundary layer. The local Nusselt number along the suction side in the absence of coolant has been evaluated as a function of local Reynolds number (Camci and Arts, 1985a). In order to provide a baseline check for heat transfer measurements, the Nusselt

$i = 0^\circ$ $TU_\infty = 5.2\%$ $Re_{c,in} = 8.42 \times 10^5$ $T_w/T_\infty = 0.72$ $T_{0\infty} = 408 \text{ K}$
 $Ma_{in} = 0.25$ $Ma_{ex} = 0.90$

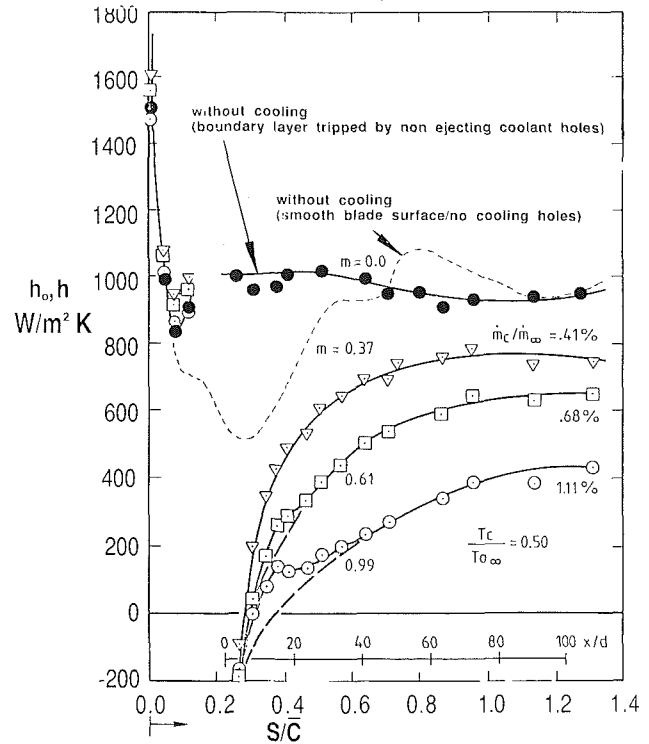


Fig. 2 Measured convective heat transfer coefficients on the suction surface of the blade: baseline tests

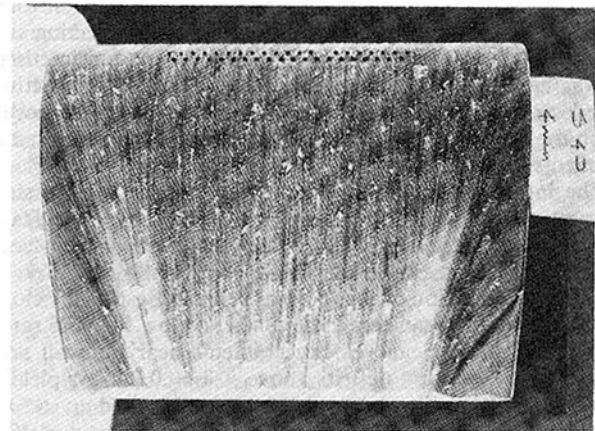


Fig. 3 Oil flow visualization of the coolant field

number data have been compared with the laminar and turbulent flat plate correlations (Camci and Arts 1985a). It is a known fact that the reduction of turbulent shear stress and turbulent kinetic energy levels, especially in the outer layer of a turbulent boundary layer developing on a convex surface, are closely related to wall heating rate reductions (Gillis and Johnston, 1983). The actual data taken by the author indeed show somewhat lower values than the turbulent flat wall correlation (Camci and Arts, 1985a). The largest deviations are observed near the leading edge where the transition is artificially induced by the holes that are not ejecting ($0.05 < s/c < 0.2$). Farther downstream the measured values tend to merge with the flat plate correlation as strong convex curvature dis-

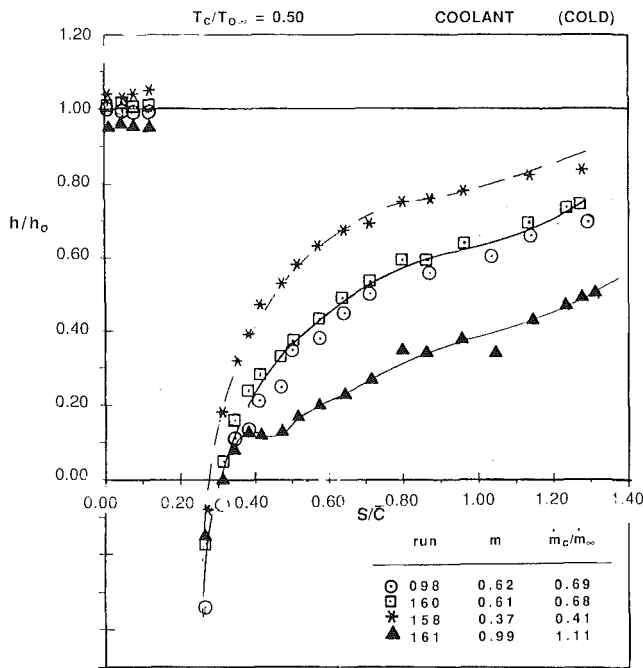


Fig. 4 Nondimensional convective heat transfer coefficients (set I)

appears. A full recovery near the trailing edge is however not expected (Adams and Johnston, 1984).

Qualitative surface oil flow visualizations were performed in order to assess the spanwise uniformity of the coolant flow as well as the film coverage, downstream of the ejection rows (Fig. 3). Visual investigation downstream of the ejection site showed a quite uniform coolant field in the spanwise direction. It was also observed that the separation line of the suction side leg of the leading edge vortex was reasonably far away from the midspan of the blade where the heat transfer measurements were taken.

The influence of the blowing rate m on the suction side convective heat transfer is shown in Fig. 4. The blowing rate was varied from 0.37 to 0.99 for a constant coolant-to-free-stream temperature ratio of $T_c/T_{\infty} = 0.50$. In all cases a significant protection of the wall was achieved, especially close to the ejection holes where $x/d < 40$. For low blowing rates ($m = 0.37$), low mean velocity gradients near the wall and important momentum deficits above $y/\delta = 0.2$ are typically encountered (Camci and Arts, 1985a). If m is raised up to 1.0, a velocity excess region is observed near the wall ($x/d < 40$). Above this zone, the overall mean velocity gradient is very low compared to the low blowing rate case. Since the turbulent kinetic energy production is related to the mean velocity gradient (Yavuzkurt et al., 1980), higher heat flux levels are expected for low blowing rates, whereas, except in the near wall region, a reduction in overall heat flux will be observed for $m = 1.0$. In the near wall region, the heat transfer augmentation observed for $x/d < 40$ may be related to the velocity excesses as suggested by Yavuzkurt et al. (1980). Very steep mean velocity gradients near the wall as well as an eventual jet penetration into the mainstream yield large shear stress and turbulent kinetic energy levels in this region. A numerical simulation of this behavior especially at blowing rates close to unity was performed by the author (Camci and Arts, 1985a) by using a two-dimensional differential boundary layer code Stan-Cool. Meaningful simulations were only achieved when the augmented mixing length parameter was set to a relatively high

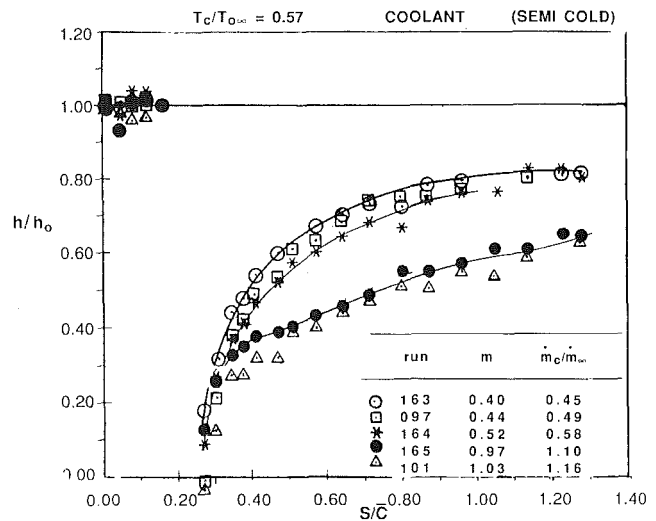


Fig. 5 Nondimensional convective heat transfer coefficients (set II)

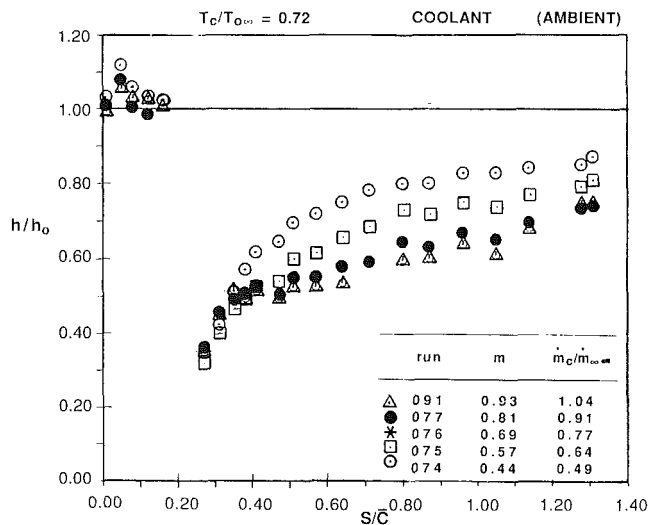


Fig. 6 Nondimensional convective heat transfer coefficients (set III)

value compared to a low blowing rate case (Camci and Arts, 1985a). In the specific simulation study the \bar{t}_{\max} value used was found to be much higher than earlier studies reported by Crawford et al. (1980). For most of the earlier studies the approaching mainstream boundary layer thickness δ has the same order of magnitude as the ejection hole diameter d . The present study uses a well-simulated mainstream flow with actual temperature ratios and a realistic coolant hole diameter. As a result the present boundary layer thickness-to-hole diameter ratio is about 1/5. This ratio suggests that, in a carefully designed film cooling experiment on the suction side, a very strong dominance of the ejected coolant layers is expected to take place. The measured data are indeed consistent with this conclusion as shown in Fig. 4.

Significant coolant temperature effects on convective heat transfer have also been observed. Figures 5 and 6 represent the results obtained for a $T_c/T_{\infty} = 0.57$ and $T_c/T_{\infty} = 0.72$, respectively, in a typical blowing rate range from $m = 0.4$ to 1.0. Important h/h_0 reductions near the ejection site ($x/d < 40$) were achieved when the coolant temperature was changed from wall temperature down to half of the mainstream level. The downstream values of h/h_0 increase smoothly and far

downstream ($x/d = 100$), the heat flux level differences due to coolant temperature variations are not as large as the differences occurring close to the ejection site. Local heat transfer augmentation observed just downstream of the ejection site ($x/d < 40$) appears almost independently from the coolant temperature level. In addition to augmented turbulent shear stress and turbulent kinetic energy levels near the holes, a hot gas/wall interaction due to severe coolant jet penetration into the mainstream is also expected. The penetrating coolant jets were expected to reduce the overall film cooling coverage in this area, mainly because of reduced lateral jet spread. In this area, the wall has more chances to be influenced by the hot mainstream gas. Details of the 15 heat transfer data sets are given in Table 1.

Numerical Computation of Heat Flux Vectors. An accurate thermal analysis of a film-cooled turbine blade is only meaningful by generating the local internal conduction heat flow pattern by using the external and internal surface convective heat transfer information for a specific blade. In order to solve the heat conduction equation for a cooled turbine blade that has a very complex geometry, a computational method based on a variational principle has been implemented.

The steady two-dimensional temperature distribution in a film-cooled gas turbine blade can be calculated by solving

$$\nabla^2 T(x, y) = 0 \quad (1)$$

provided that the convective boundary conditions, free-stream temperature, and thermal conductivity of the blade material are known. The associated boundary condition of the specific heat conduction problem is as follows:

$$-k \left(\frac{\partial T}{\partial x} n_x + \frac{\partial T}{\partial y} n_y \right) = h(T_{\infty} - T(x, y)) \quad (2)$$

The method of solution is based on a variational principle known as Euler's Theorem. The solution of equation (1) satisfying the boundary conditions given in equation (2) is identical to minimizing an integral statement given in equation (3) over the whole domain.

$$I_F = \iint_S \frac{1}{2} k \left[\left(\frac{\partial T}{\partial x} \right)^2 + \left(\frac{\partial T}{\partial y} \right)^2 \right] dx \cdot dy + \int_L \frac{1}{2} h (T - T_{\infty})^2 \cdot dL \quad (3)$$

where dL is an infinitesimal length over the curved boundary of the domain. The two-dimensional domain is discretized using isoparametric finite elements on which the integral statement I_F is minimized. The final result of this minimization procedure is a set of linear algebraic equations and the solution of this set of equations leads to the temperature distribution in the domain of interest. The finite element technique used is a direct minimization technique that does not require any iterations. Therefore, there is no problem like the convergence of the scheme. The finite elements chosen were eight node (quadrilateral) or six node (triangular), second-order isoparametric elements. The advantage of this technique is its exact nature, except for the numerical interpolations and integrations performed in each element. It has also been shown in the past that the second-order polynomials chosen for the geometric description and the scalar temperature field are sufficiently accurate for the solution of steady heat conduction problems. Further details of this analysis are given by Zienkiewicz (1971).

Discretization of the Blade and Boundary Conditions

The finite element discretization of the blade in two dimensions is shown in Fig. 7. The "near film cooling hole" discretization is also shown in the figure. A typical finite element

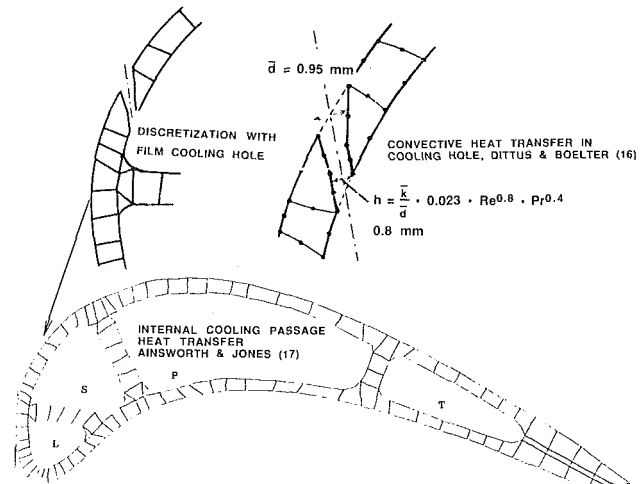


Fig. 7 Discretization of the film cooled blade and cooling hole details

size was about 2 percent of the blade chordlength, when an almost square element was used, in the regions where a high computational resolution was required. The elements chosen were second order, curved, and isoparametric finite elements. Near the sharp corners of the coolant passages and near the trailing edge, triangular elements were employed in addition to the regular rectangular elements.

The element convective heat transfer coefficients in the absence of film cooling were evaluated from the experiments as discussed in experimental results. Figure 2 shows the external heat transfer coefficients used in the analysis both in the absence and presence of film cooling. For the case of film cooling, the coolant to free-stream temperature ratio was 0.50 at a blowing rate of unity. The heat transfer coefficients were acquired from well-simulated cascade tests performed at $T_{\infty} = 408$ K. However, for the calculations in an environment $T_{\infty} = 1650$ K (assuming that Nusselt numbers are similar) the effect of increasing thermal conductivity of the mainstream gas is taken into account. It is a well-known fact that the thermal conductivity of air will approximately increase with the square root of the ambient temperature.

The convective boundary conditions inside the film cooling holes were determined from "fully developed turbulent pipe flow" correlation given by Dittus and Boelter (1930).

$$h = \frac{\bar{k}}{d} \cdot 0.023 \cdot \text{Re}^{0.8} \cdot \text{Pr}^{0.4} \quad (4)$$

The length-to-diameter ratio of the film cooling holes is small for the current problem. Therefore, the assumption of fully developed flow may not be completely realistic since the flow in small diameter cooling holes is still developing and influenced by the hole inlet conditions. This will most likely increase the internal heat transfer coefficient in the holes. The actual cooling geometry used in the computations is somewhat different from a flow in a pipe having a uniform circular cross section in the longitudinal direction of the pipe. There is a conically shaped section near the exit of the cooling hole, as shown in Figs. 1 and 7. This conical shape was taken into account by introducing an average cooling hole diameter of 0.95 mm. The heat transfer coefficients in the internal cooling passages were evaluated from a correlation discussed by Ainsworth and Jones (1979). Reynolds numbers in internal coolant passages were calculated using the hydraulic diameter of each of the passages. The heat transfer correlation is as follows:

$$h = (\rho_c U_c) \cdot C_p \cdot \exp[-3.796 - 0.205 \cdot \text{LnRe} - 0.505 \cdot \text{LnPr} - 0.0225 \cdot (\text{LnPr})^2] \quad (5)$$

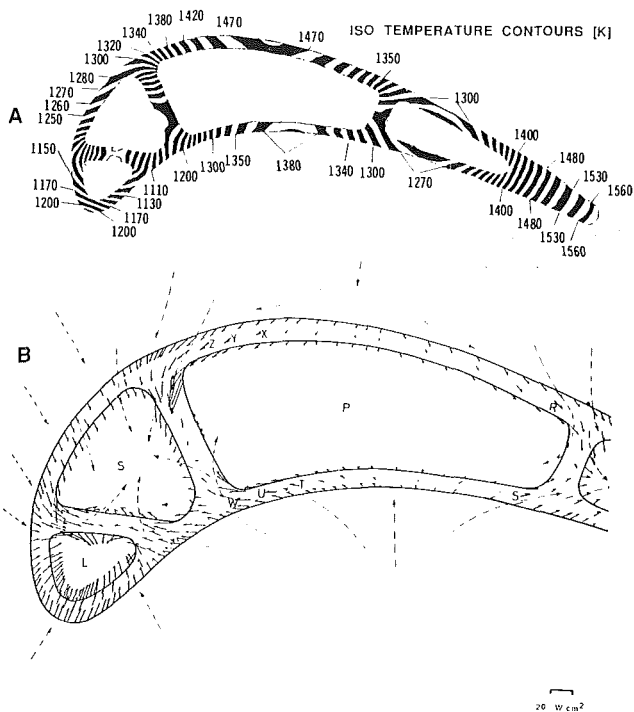


Fig. 8 Case 1: (A) isothermal contours, (B) heat flux vectors; no external film cooling

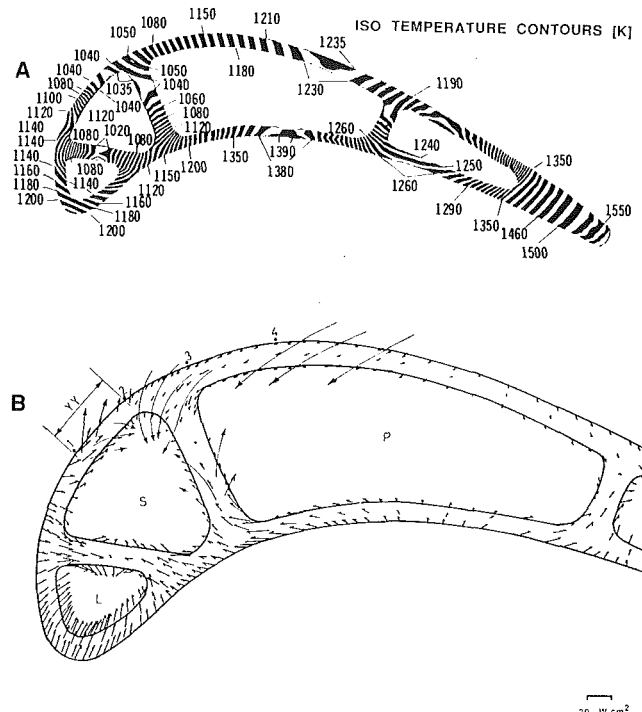


Fig. 9 Case 2: (A) isothermal contours, (B) heat flux vectors; external film cooling; no film cooling hole internal heat transfer effect imposed

Computational Results

Only Internal Convection Cooling. The first computation shown in Fig. 8(A) is simulating an “only internal convection cooling” case. No film cooling is applied on the gas side of the blade. The total coolant to free-stream mass weight ratio is about 3.5 percent. The distribution of the total coolant mass flow rate in the internal coolant passages is prescribed as follows:

Channel	Coolant distribution
L	25 percent
S	25 percent
P	20 percent
T	30 percent

The coolant in each passage is assumed to be entering through the blade root and discharged into the mainstream from the tip. The computational heat conduction analysis resulted in the local temperature map shown in Fig. 8(A). Although this configuration is not the closest case to an actual film-cooled blade, it was considered to be a baseline case to compare the temperature field in the presence and absence of film cooling. The magnitude of the internal heat transfer coefficient in each passage, the interaction of the two neighboring passages, gas side heat transfer coefficient without film cooling, the specific blade geometry, gas total temperature, and the thermal conductivity of the blade material are the determining factors in evaluating the temperature field given in Fig. 8(A).

Although the highest external heat loads are observed near the leading edge zone (Fig. 2), the internal cooling activity of channel “L” and to a less extent the cooling from the neighboring channel “S” provided an average wall to free-stream temperature ratio of $1150/1650 = 0.69$.

The trailing edge of the blade is observed to be the hottest part. In spite of the fact that there is a cooling passage (T) near the trailing edge, the slender geometry and high gas side heat loads resulted in quite high wall temperatures compared to the leading edge area. In practice, more specific trailing edge cooling schemes are used to cool down this region.

The flow of thermal energy by molecular conduction process can be simulated by computing local heat flux vectors. Once the temperature field is known, the temperature gradients and eventually the heat fluxes may be evaluated through equation (3). The resulting heat flux vectors from this analysis are given in Fig. 8(B). Although quite reduced wall temperatures are found, the highest heat flux levels are observed near the leading edge channel. Due to the effective heat removal through channel “L,” the flow of heat is quite induced in the direction from the mainstream to the coolant channel.

The solid walls between the coolant passages are defined as “bridges” in this study. The bridges play a significant role in the conduction process, as shown in Fig. 8(B). A part of the heat flow from the gas side is transferred into the internal channels from both ends of the bridge. The heat flux vectors on bridge 1 are found to meet at the midsection. Relatively reduced heat flux levels and almost minimal bridge temperatures are observed in this area.

The external heat loads evaluated qualitatively from the computed local heat flux pattern are shown as dashed arrows. The heat flux vectors are almost normal to the inner and outer skin of the blade except the bridges, when the heat removal by means of the coolant channel is quite effective (L, S, T). With the help of the heat flux components almost parallel to the external skin of the blade shell, a part of the heat is transferred to the neighboring coolant channels (vectors X, Y, Z, T, U, W, R, S) (Fig. 8B). The curved corners close to the bridges were observed to be highly thermally loaded. Very large temperature gradients and magnitudes of heat flux were found.

Film Cooling Results. When film cooling is applied on the suction side, the computed temperature profiles are shown in Fig. 9(A). The cooling site is located at $s/\bar{c} = 0.235$. In this phase of the analysis, the influence of the convective boundaries surrounding the discrete cooling holes is ignored on the conduction field. The analysis is performed with external film cooling boundary conditions downstream of the ejection site of the suction side. A remarkable influence of film cooling on

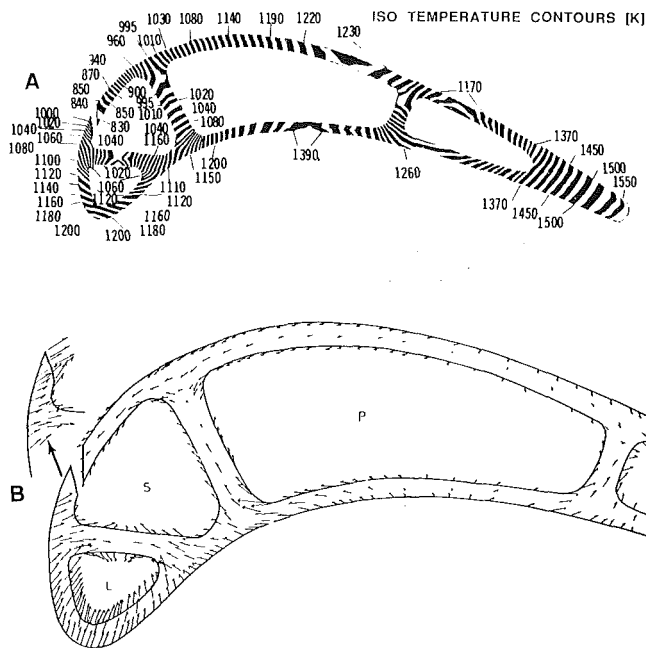


Fig. 10 Case 3: (A) isothermal contours, (B) heat flux vectors; external film cooling; film cooling hole internal heat transfer effect imposed

the downstream temperature evaluation is observed (Fig. 7A). The temperature field in bridge 1 is very similar to the case without film cooling. However, bridge 2 is influenced by film cooling because of the close distance to the film ejection site. The near leading edge temperature pattern is not significantly altered because of the film-cooled boundary conditions.

Because of the very low heat transfer coefficients (Fig. 2 just downstream of the ejection site ($s/\bar{c} = 0.234$)), the heat flux vectors showed a very specific variation compared to the only internal cooling case (Case 1). Heat is transferred from the wall to the free stream (zone YY), within the first six-seven hole diameters. In the vicinity of the wall, the heat may be transferred from the wall to the adjacent coolant layer because of very low coolant temperatures where the film temperature is still very close to the coolant temperature in the plenum chamber. If one follows the wall heat flux component normal to the wall from point 1 to 4 in Fig. 9(B), nonnegligible heat flux levels from the wall to the film (between 1 and 2) are encountered. At about point 2, an almost adiabatic zone is observed. After point 2, the heat flow is from the film to the wall.

The Influence of the Cooling Hole. In Figs. 9(A) and 9(B), the conduction pattern as a result of external film cooling is indicated without taking into account the influence of internal convection in the discrete cooling holes. The result of the computation taking this influence into account is shown in Figs. 10(A) and 10(B). A very strong deviation from the case without cooling hole influence, but with film cooling (Case 2) is observed at near upstream and downstream of the cooling hole. A very steep temperature gradient occurring within the first 10 hole diameters upstream of the hole is found only as a result of the existence of the cooling hole. Downstream of the cooling hole, the wall temperatures are considerably lower than the temperature given for Case 2. The surface temperature variations on the suction side for only internal cooling (Case 1), film cooling without cooling hole influence, (Case 2), and film cooling with the cooling hole effects included, (Case 3), are compared in Fig. 11. A significant contribution of the cooling hole both upstream and downstream of the hole is apparent. This contribution almost disappears at $s/\bar{c} = 0.70$ (bridge 3) in downstream direction. The cooling hole induced

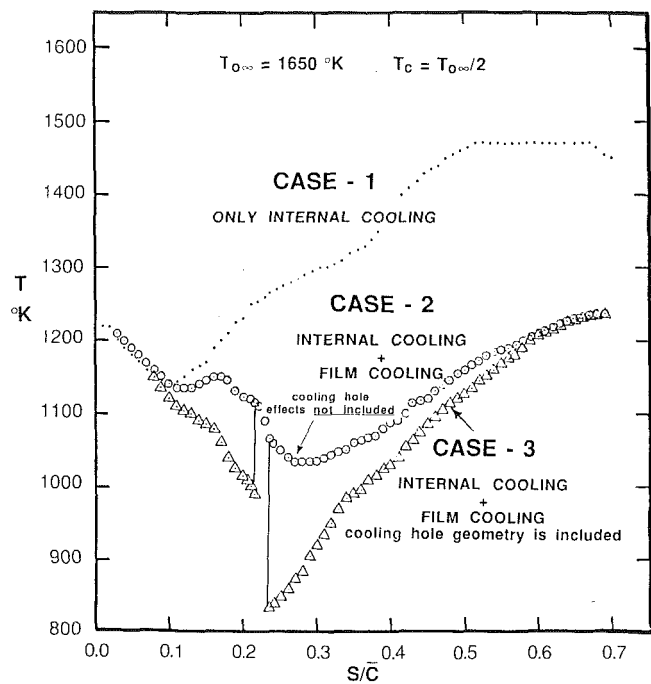


Fig. 11 Computed surface temperature distributions on the suction side, comparison of Cases 1, 2, and 3

conduction does not affect the temperature field near the leading edge, up to $s/\bar{c} = 0.1$ on the suction side. Farther downstream, the significance of the hole continuously increases up to the hole location.

Looking at Fig. 10(B), a very strong heat sink effect of the hole is observed. Most of the heat flux vectors tend to direct themselves through the cooling hole. Very high levels of heat flux exist upstream of the hole. Near downstream of the hole, in accordance with Case 2 (Fig. 9B), first a wall-to-coolant heat transfer zone, an almost adiabatic zone, and a coolant wall heat transfer region are observed. Downstream of the film cooling location, especially between the outer and inner skin of the blade, the main heat conduction tendency is the flow of heat from downstream to upstream in a direction almost parallel to the external contour of the blade. The bridges also slightly modified the heat flux field.

Conclusions

Application of film cooling heat transfer on the suction side ($s/\bar{c} = 0.206$) significantly reduced the near hole wall heat fluxes with a discrete hole configuration having double rows of staggered and shaped holes. High near hole cooling effectivenesses resulted in heat flux vectors in the direction from the wall to the mainstream, within the first few hole diameters distance. Increasing blowing rates improved the overall protection of the wall. However, above $m = 0.61$, a near ejection site augmentation in h occurred because of enhanced turbulent mixing.

Reducing the coolant temperature from wall temperature to half that of the mainstream lowered the heat transfer coefficient at constant m . At high blowing rates ($m = \sim 0.96$), this effect is more pronounced than for $m = 0.40$.

A predictive capability based on a variational method has been developed to investigate the thermal conduction heat transfer behavior of a film cooled gas turbine blade. The blade temperature and local heat flux distributions are obtained with a fine resolution.

When only internal convection cooling is applied without external film cooling, the leading edge is found to be the most

critical area as far as the magnitude of local wall heat fluxes are concerned. However wall temperatures in this region are quite reduced ($T_w/T_{0\infty} = \sim 0.7$) due to the effective cooling from internal channel "L". The results with external film cooling on the suction side show that downstream of a coolant ejection site is far from being either an adiabatic surface or an isothermal wall. The addition of the convective heat transfer contribution from coolant holes to heat conduction analysis indicates that the direction and magnitude of near ejection hole local wall heat fluxes are strongly controlled by the coolant hole convection behavior. Near the ejection site, very significant flow of heat around the film cooling hole both from upstream and downstream direction showed the heat sink influence of the hole. A three-dimensional thermal analysis (conduction/convection) near the cooling hole is under development. More detailed and realistic results from this analysis will be available soon as far as blade heat flux and thermal stress vectors are concerned. The solid walls between the coolant passages were also found to be transmitting significant levels of heat to the internal coolant stream. Large temperature gradients were shown to be accumulated near the corners of internal coolant passages.

Acknowledgments

The experimental part of this study was completed in the Von Karman Institute for Fluid Dynamics. The author acknowledges the continuous support of Professor T. Arts and Professor F. A. E. Breugelmans, during his stay at the V. K. I.

References

Adams, E. W., and Johnston, J. P., 1984, "A Mixing Length Model for the Prediction of Convex Curvature Effects on Turbulent Boundary Layers," *ASME Journal of Engineering for Gas Turbines and Power*, Vol. 106, No. 1, pp. 142-148.

Ainsworth, R. W., and Jones, T. V., 1979, "Measurements of Heat Transfer in Circular, Rectangular and Triangular Ducts, Representing Typical Turbine Blade Internal Cooling Passages, Using Transient Techniques," ASME Paper No. 79-GT-40.

Camci, C., 1985, "Theoretical and Experimental Investigation of Film Cooling Heat Transfer on a Gas Turbine Blade," Ph.D. Thesis, Von Karman Institute for Fluid Dynamics and University of Leuven, Belgium.

Camci, C., and Arts, T., 1985a, "Short Duration Measurements and Numerical Simulation of Heat Transfer Along the Suction Side of a Gas Turbine Blade," *ASME Journal of Engineering for Gas Turbines and Power*, Vol. 107, No. 4, pp. 991-997.

Camci, C., and Arts, T., 1985b, "Experimental Heat Transfer Investigation Around the Film Cooled Leading Edge of a High Pressure Gas Turbine Rotor Blade," *ASME Journal of Engineering for Gas Turbines and Power*, Vol. 107, No. 4, pp. 1016-1021.

Camci, C., Arts, T., and Breugelmans, F. A. E., 1985, "Experimental Convective Heat Transfer Investigation Around a Film-Cooled High Pressure Turbine Blade," presented at 7th AIAA Symposium on Air Breathing Engines, Beijing, People's Republic of China.

Consigny, H., and Richards, B. E., 1982, "Short Duration Measurements of Heat Transfer Rate to a Gas Turbine Rotor Blade," *ASME Journal of Engineering for Power*, Vol. 104, No. 3, pp. 542-551.

Crawford, M. E., Kays, W. M., and Moffat, R. J., 1980, "Full Coverage Film Cooling, Part II: Heat Transfer Data and Numerical Simulation," *ASME Journal of Engineering for Power*, Vol. 102, pp. 1006-1012.

Dittus, F. W., and Boelter, L. M. K., 1930, *Univ. California (Berkeley) Pub. Eng.*, Vol. 2, p. 443.

Gillis, J. C., and Johnston, J. P., 1983, "Turbulent Boundary Layer Flow and Structure on a Convex Wall and its Redevelopment on a Flat Wall," *Journal of Fluid Mechanics*, Vol. 135, pp. 123-153.

Jones, T. V., Schultz, D. L., and Hendley, A. D., 1973, "On the Flow in an Isentropic Free Piston Tunnel," A.R.C. R & M 3731.

Ligrani, P. M., Camci, C., and Grady, M. S., 1982, "Thin Film Heat Transfer Gauge Construction and Measurement Details," Von Karman Institute Technical Memorandum No. 33.

Ligrani, P. M., and Camci, C., 1985, "Adiabatic Film Cooling Effectiveness From Heat Transfer Measurements in Compressible, Variable-Property Flow," *ASME Journal of Heat Transfer*, Vol. 107, No. 2, pp. 313-320.

Richards, B. E., 1980, "Heat Transfer Measurements Related to Hot Turbine Components in the Von Karman Institute Hot Cascade Tunnel," AGARD Conference Proceedings, No. 281, *Testing and Measurement Techniques in Heat Transfer and Combustion*, Brussels.

Schultz, D. L., and Jones, T. V., 1973, "Heat Transfer Measurements in Short Duration Hypersonic Facilities," AGARDograph No. 165.

Schultz, D. L., Jones, T. V., Oldfield, M. L. G., and Daniels, L. C., 1977, "A New Transient Facility for the Measurement of Heat Transfer Rates," in: *High Temperature Problems in Gas Turbine Engines*, AGARD CP 229, Paper 31.

Yavuzkurt, D. L., Moffat, R. J., and Kays, W. M., 1980, "Full-Coverage Film Cooling. Part I: Three Dimensional Measurements of Turbulence Structure," *Journal of Fluid Mechanics*, Vol. 101, pp. 120-158.

Zienkiewicz, O. C., 1971, *The Finite Element Method in Engineering Science*, McGraw-Hill, London.

P. M. Ligrani
Associate Professor.

A. Ortiz
Graduate Student.

S. L. Joseph
Graduate Student.

D. L. Evans
Graduate Student.

Department of Mechanical Engineering,
Naval Postgraduate School,
Monterey, CA 93943-5000

Effects of Embedded Vortices on Film-Cooled Turbulent Boundary Layers

Heat transfer effects of longitudinal vortices embedded within film-cooled turbulent boundary layers on a flat plate were examined for free-stream velocities of 10 m/s and 15 m/s. A single row of film-cooling holes was employed with blowing ratios ranging from 0.47 to 0.98. Moderate-strength vortices were used with circulating-to-free stream velocity ratios of -0.95 to -1.10 cm. Spatially resolved heat transfer measurements from a constant heat flux surface show that film coolant is greatly disturbed and that local Stanton numbers are altered significantly by embedded longitudinal vortices. Near the downwash side of the vortex, heat transfer is augmented, vortex effects dominate flow behavior, and the protection from film cooling is minimized. Near the upwash side of the vortex, coolant is pushed to the side of the vortex, locally increasing the protection provided by film cooling. In addition, local heat transfer distributions change significantly as the spanwise location of the vortex is changed relative to film-cooling hole locations.

Introduction

In order to design efficient schemes to protect surfaces using film cooling, an understanding of the interaction between film cooling jets and the nearby flow is necessary. This is particularly important in regard to turbine blade passages, where, even without film cooling, flows may be extremely complex, containing numerous vortices, secondary flows, and three-dimensional separation.

As the inlet boundary layer approaches the turbine blade row, one portion flows into the blade passage and then from the pressure side of one blade to the suction side of an adjacent blade. Another portion approaches the blade, where just in front, a horseshoe vortex forms. At the saddle point, the horseshoe splits into a vortex on the suction side and a vortex on the pressure side. The pressure side vortex becomes the passage vortex, moving from the leading edge of the blade toward the low-pressure side of the adjacent blade. Such vortices are often embedded in the wall boundary layer, with cross-stream length scales at least equal to the local boundary layer thickness. Consequently, they are capable of significant perturbations to local heat transfer rates. Eibeck and Eaton (1987) showed how such vortices caused Stanton number increases as great as 24 percent and decreases of 14 percent in a study of turbulent boundary layer flow on a flat plate. Such variations were found to persist over 100 boundary layer thicknesses, indicating that longitudinal vortices maintain their coherence over large streamwise distances.

If the film cooling is present on the endwall or blade surface, then there is certain to be an interaction between vortices and cooling jets. One of the purposes of this paper is to show that

this interaction can lead to local hot spots. These, in turn, often lead to increased thermal stresses and reduced blade life.

Blair (1974) reported heat transfer measurements from an endwall film-cooled using a slot inclined at a 30 deg angle. On the endwall, large variations of heat transfer and film cooling effectiveness were measured, which were attributed to a large vortex located in the corner between the endwall and the suction surface of their cascade. Langston et al. (1977) described the passage vortex as one that increases in size through the turbine passage, entraining fluid from the mainstream and separated fluid from the endwall and suction surface boundary layers. Langston (1980) later found that the passage vortex had the features of a distorted Rankine vortex in a plane located about 2/3 of the way through the blade passage. Sieverding (1985) summarized the development and character of various vortices and secondary flows which exist in turbine passages. Goldstein and Chen (1985, 1987) performed an experimental study on the influence of the endwall on film cooling of gas turbine blades using one and two rows of injection holes, respectively. These authors concluded that on the convex side of the blade there is a triangular region where coolant is swept away from the surface by the passage vortex, while the concave side was not significantly affected by secondary flows originating near the endwall. Sato et al. (1987) studied distributions of heat transfer and film cooling effectiveness on the endwall and airfoil within an annular low aspect ratio cascade. Horseshoe vortices were found to promote heat transfer and decrease the film cooling effectiveness on the endwall near the blade leading edge. Secondary flows resulted in increased heat transfer coefficients on the blade suction surface near the endwall, with very little effect on blade pressure surfaces. Other studies of secondary flows in turbine cascades are reviewed by Eibeck and Eaton (1987). Westphal et al. (1987) provide a review of

Contributed by the International Gas Turbine Institute and presented at the 33rd International Gas Turbine and Aeroengine Congress and Exhibition, Amsterdam, The Netherlands, June 5-9, 1988. Manuscript received by the International Gas Turbine Institute June 5-9, 1988. Paper No 88-GT-170.

the extensive amount of work that has been done on vortices in boundary layers.

Studies of the interaction between film cooling injection and embedded vortices are scarce (Blair, 1974; Goldstein and Chen, 1985, 1987). This lack of data and the difficulty in modeling the complicated three-dimensional aspects of the flow field motivated the present experimental study. Its principal objective was to investigate the effect of a single embedded vortex on heat transfer in film-cooled turbulent boundary layers.

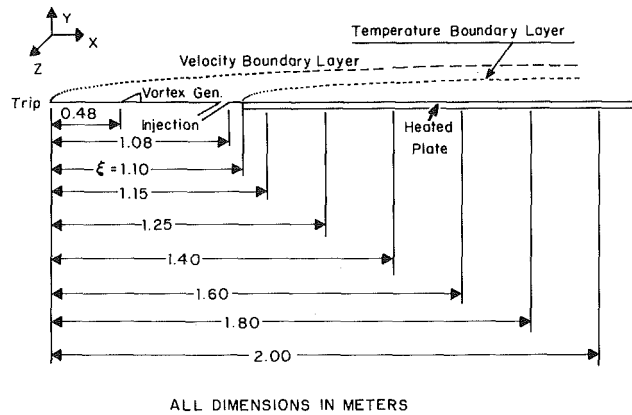
The study was undertaken in two parts. In the first, three mean velocity components were measured in a plane normal to the nominal flow direction using a five-hole pressure probe. In the second, wall heat transfer measurements were conducted along with surveys of the mean temperature field from film cooling. A systematic approach to the heat transfer measurements was employed to provide sufficient qualification of the facilities and procedures used. First, measurements were made beneath a turbulent boundary layer only. Second, the boundary layer with single embedded vortex was studied. Third, measurements were made of the boundary layer with film cooling from a single row of injection holes. Finally, measurements were made of the boundary layer with both film cooling and embedded vortex. Here, attention was focused on overall vortex effects, and the effect of spanwise vortex position.

Experimental Approach

The influence of a single embedded vortex on local convective heat transfer was determined by mapping Stanton number distributions in a flat plate turbulent boundary layer downstream of a single row of film cooling holes. A constant heat flux surface instrumented with thermocouples was used to measure Stanton number variations. The three mean velocity components were measured using a five-hole pressure probe.

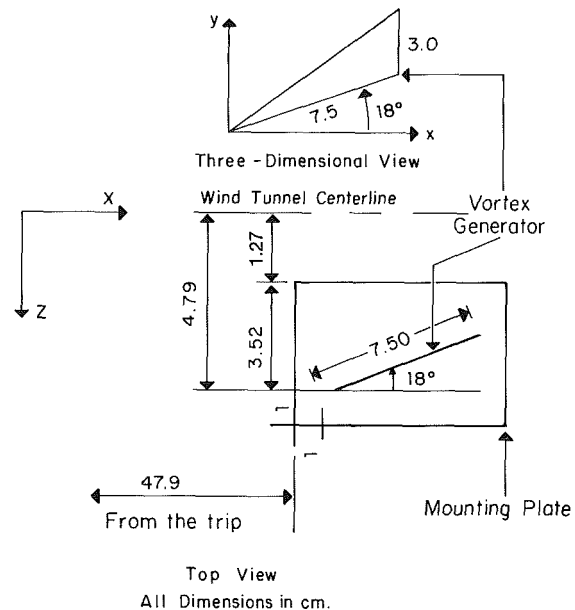
The experiments were conducted in an open-circuit, subsonic wind tunnel located in the laboratories of the Department of Mechanical Engineering of the Naval Postgraduate School. The wind tunnel consisted of a centrifugal blower, a diffuser with filters, a header box with a honeycomb and three screens, a nozzle, and a test section. The test section was a rectangular duct 3.05 m long and 0.61 m wide, with adjustable top wall height. For the present study, a zero pressure gradient was maintained without vortex or film cooling to within 0.018 cm of water differential pressure along the test plate. The air speed through the test section can be adjusted from 5 to 40 m/s. The free-stream turbulence intensity was about 0.1 percent based on a free-stream velocity of 30 m/s.

The coordinate system is shown in Fig. 1. With the heat transfer surface at elevated temperature, an unheated starting length of 1.10 m existed. Free-stream air was maintained at ambient temperature, and thus, the direction of heat transfer was from the wall to gas. Also labeled in Fig. 1 are the locations of thermocouple rows along the test surface. At $x = 1.86$ m, boundary layer thickness, boundary layer displacement thickness, and boundary layer momentum thickness were 29.7 mm,



ALL DIMENSIONS IN METERS

Fig. 1 Coordinate system



All Dimensions in cm.

Fig. 2 Schematic of vortex generator and its position for vortex position B

5.09 mm, and 3.59 mm, respectively. At a free-stream velocity of 21.0 m/s, the momentum thickness Reynolds number was 4780 and the friction velocity was 0.8 m/s.

A schematic of the vortex generator is shown in Fig. 2. It consisted of a half-delta wing attached to the wind tunnel floor at an angle of 18 deg with respect to the tunnel centerline. The generator design was similar to ones employed by Westphal

Nomenclature

d = injection hole diameter
 h = heat transfer coefficient = $\dot{q}_w'' / (T_{rc} - T_w)$
 m = blowing ratio = $\rho_c U_c / \rho_\infty U_\infty$
 q'' = heat flux
 St = Stanton number
 St_0 = baseline Stanton number, no film cooling, no vortex
 St_f = Stanton number with film cooling only
 T = static temperature
 U = mean velocity

x = downstream distance as measured from the leading edge of the boundary layer trip or from the downstream edges of injection holes when used as x/d
 y = vertical distance from the test surface upward
 z = spanwise distance from the test section center line
 δ_1 = boundary layer displacement thickness

θ = nondimensional coolant temperature = $(T_{rc} - T_{rc}) / (T_w - T_{rc})$
 ξ = unheated starting length
 ρ = density

Subscripts

c = coolant at exit of injection holes
 r = recovery condition
 w = wall
 ∞ = free stream

et al. (1985, 1987) and by Eibeck and Eaton (1987). Three different spanwise locations of the vortex generator were employed to give three different spanwise vortex positions. These were labeled A, B, and C. Figure 2 shows generator position B. The leading edge of the generator was 4.79 cm off the wind tunnel axis, and the vortex center was estimated to pass between two injection hole locations. The generator leading edge was 3.52 cm and 6.06 cm from the wind tunnel axis for positions A and C, respectively.

The injection system, which included a small heat exchanger, provided film coolant at temperatures above ambient. Thirteen injection holes were inclined at an angle of 30 deg. Their spanwise spacing was three diameters, with the middle tube located on the center line of the test surface. Diameters of the injection holes were 0.95 cm, scaled such that δ_1/d ranged from 0.37 to 0.40. The blowing ratio m was varied between 0.47 and 0.98. Nondimensional coolant temperature θ was maintained at approximately 1.6. For all test conditions, the injectant was turbulent. Values of the blowing ratio m , discharge coefficients, and other injection parameters were determined using methods described by Ortiz (1987) and Joseph (1986). Discharge coefficients ranged between 0.5 and 0.73, and increased with Reynolds number in agreement with results given by Ligrani and Camci (1985).

Copper-constantan thermocouples were used to measure plate and gas temperatures. One calibration was used for all thermocouples of similar manufacture, since their outputs were the same within one or two microvolts at any given temperature. Surveys of $(T - T_\infty)$ were performed with a thermocouple mounted on a two-component automated traversing device constructed in the Department of Mechanical Engineering shop. The device was driven by two electric motors manufactured by the Superior Electric Company. These motors were controlled by a microprocessor. Each survey consisted of 800 probe locations, covering an area 12 cm \times 22 cm.

The heat transfer surface was designed and developed to provide a constant heat flux over its area. The plate was constructed so that its upward-facing part was adjacent to the wind tunnel air stream, with minimal heat loss by conduction from the sides and beneath the test surface. Magnitudes of conduction loss were determined by an energy balance. Radiation losses from the top were estimated analytically. The design was based on ones used at the University of Minnesota (Wang, 1984; Wang et al., 1985). It consisted of a thin stainless steel foil, 1.3 m \times 0.467 m \times 0.20 mm, painted flat black with seven layers of liquid crystals. Attached to the underside of the foil were six rows of thermocouples. Twenty-one thermocouples were located in each row, where spacing within each row was 1.27 cm. The contact resistance between the thermocouples and the foil top was estimated based on temperatures from the thermocouples and calibrated liquid crystals. The contact resistance was then correlated as a function of heat flux through the foil. Beneath the thermocouples was a thin foil heater, a Lexan sheet, foam insulation, styrofoam, and balsa wood. The level of surface temperature was controlled by adjusting the input voltage to the heater using a variac power supply. Additional details on the heat transfer surface, including qualification procedures used, are given by Joseph (1986) and Ortiz (1987).

The uncertainty of the heat transfer coefficient h , based on a 95 percent confidence level, was estimated to be ± 4.5 percent or ± 1.03 W/m²°C based on an h value of 24.2 W/m²°C. The uncertainty of Stanton numbers was estimated to be ± 4.4 percent. The uncertainty of St/St_0 was estimated at ± 5.5 percent or ± 0.058 based on $St/St_0 = 1.05$. (Kline and McClintock, 1953).

The three mean velocity components were measured using a United Sensor five-hole pressure probe. The probe was calibrated for yaw angles from -40 to $+40$ deg and for pitch

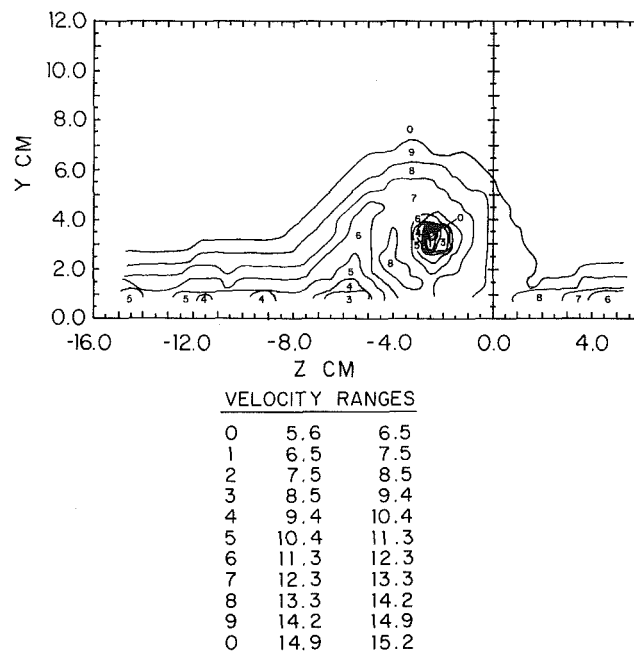


Fig. 3 Streamwise velocity contours in boundary layer with embedded vortex, 0.50 blowing ratio, and 15 m/s free-stream velocity

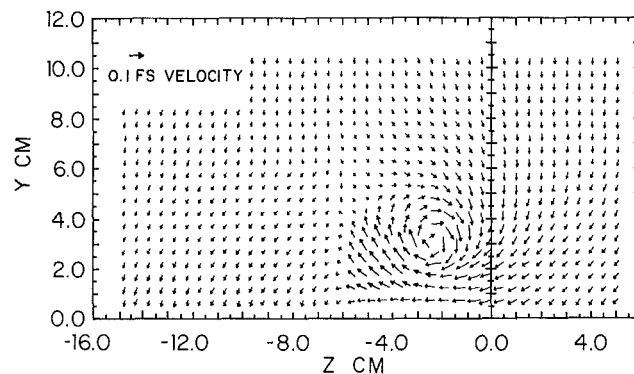


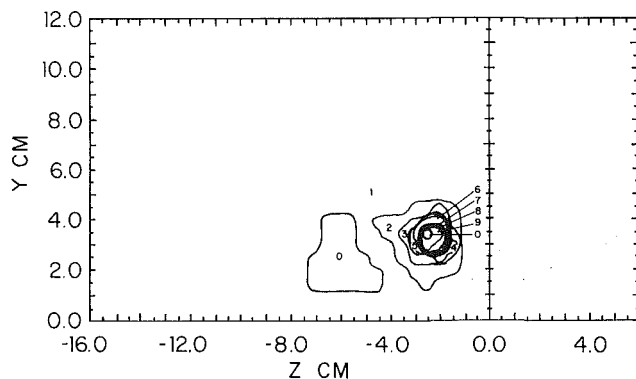
Fig. 4 Secondary flow vectors in boundary layer with embedded vortex, 0.50 blowing ratio, and 15 m/s free-stream velocity

angles from -15 to $+15$ deg. The five-hole probe was connected to five Celesco LCVR pressure transducers. Each of these was connected to a Celesco Carrier Demodulator to convert transducer output to a d-c voltage. The pressure probe was positioned using the same automated traversing device as was used for the $(T - T_\infty)$ surveys. Voltages from thermocouples and the Carrier Demodulators were read by a Hewlett-Packard 3497A Data Acquisition/Control Unit with a 3498A Extender. These units were controlled by a Hewlett-Packard Series 300, Model 9836S computer. Additional details are given by Ortiz (1987) and Evans (1987).

Fluid Mechanics Results

Mean velocities for the boundary layer with embedded vortex and film cooling at $x/d = 41.9$ are presented in Figs. 3 and 4. These data were obtained at a free-stream speed of approximately 15 m/s with a blowing ratio m of 0.50. The vortex was located at position B.

The tremendous perturbation caused by the vortex is evident. Longitudinal velocity contours are altered over z ranging from -10 cm to 5 cm. Outside of this region, the film-cooled boundary layer extends 2.5–3.0 cm from the wall, and is relatively undisturbed by the vortex. This is shown by longitudinal velocity contours in Fig. 3, which are spanwise uniform slightly



VORTICITY RANGES *.01

0	-1.0	-.3
1	-.3	.5
2	.5	1.3
3	1.3	2.0
4	2.0	2.8
5	2.8	3.6
6	3.6	4.3
7	4.3	5.1
8	5.1	5.9
9	5.9	6.4
0	6.4	6.6

Fig. 5 Streamwise vorticity contours in boundary layer with embedded vortex, 0.50 blowing ratio, and 15 m/s free-stream velocity

away from the wall. Near the wall, velocity deficits from film cooling are present spaced about 3 cm apart for $z \leq -6.0$ cm.

Because of the vortex, low-speed fluid is lifted away from the wall near the vortex upwash side ($-8 \text{ cm} < z < -3 \text{ cm}$). Here, the local boundary layer thickness may be as much as three times its undisturbed value. Of particular interest here is the velocity deficit from film cooling at $z = -6 \text{ cm}$, which seems to be increased in size by the vortex upwash. The extent and magnitude of the vortex upwash is evident from secondary flow vectors in Fig. 4.

Near the downwash side of the vortex ($-2 \text{ cm} < z < 3 \text{ cm}$), Fig. 3 shows that high-speed fluid is convected close to the wall and the local boundary layer thickness is less than its undisturbed value. In Fig. 4, the locations of the downwash region are indicated by secondary flow vectors. These additionally indicate significant crossflow velocities below the vortex center located at $z = -2.5 \text{ cm}$, $y = 3.5 \text{ cm}$. Within these regions ($z > -4.0 \text{ cm}$), there is no evidence of near-wall velocity deficits from film cooling. Here, coolant appears to have been swept away or decimated by the secondary flows of the vortex.

Axial vorticity contours for the same flow, estimated from the y and z velocity components, are presented in Fig. 5. The peak of vorticity locates the vortex center. This center is surrounded by a core of roughly circular vortical fluid, which, in turn, is surrounded by nonvortical fluid. These two regions together show similarity to a Rankine vortex (Eibeck and Eaton, 1987). Near the upwash side of the vortex, there is also a region of negative vorticity, which would not be included in the Rankine model. The circulation of the vortex Γ was determined by integrating the vorticity in the plane of the secondary flow vectors. To provide some noise immunity in performing this integration, procedures of Westphal et al. (1985) were followed wherein vorticity levels less than 20 percent of the peak vorticity were taken as zero vorticity. With this approach, Γ/U_∞ was estimated to be -0.95 cm with film cooling and -1.10 cm without film cooling. Streamwise vorticity contours are similar for the two cases, except that the vortex center is located at slightly smaller y and z without film cooling.

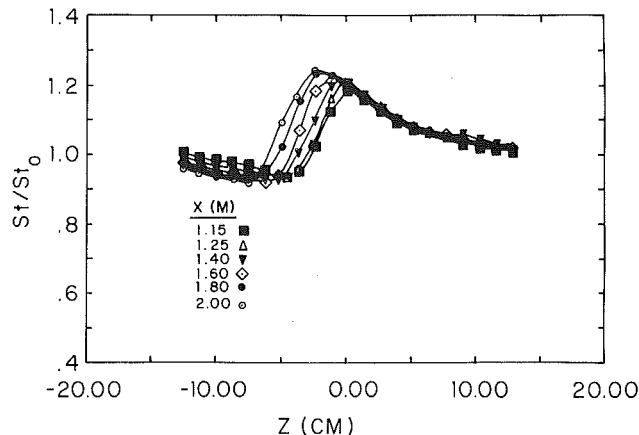


Fig. 6 Local Stanton number ratios in boundary layer with embedded vortex; 15 m/s free-stream velocity

Heat Transfer Results

Boundary Layer Only. Measurements were made at free-stream velocities of 10 m/s and 15 m/s, without vortex and without film cooling in order to validate and qualify the heat transfer plate and measurements procedures used. Spanwise-averaged Stanton number data showed agreement with the empirical equation from Kays and Crawford (1980) for turbulent boundary layers on a flat plate at constant free-stream velocity, constant heat flux, and unheated starting length of 1.10 m. Local measurements showed good spanwise uniformity, particularly away from the leading edge of the heat transfer plate.

Boundary Layer With Single Vortex. Measurements were made at free-stream velocities of 10 m/s and 15 m/s with an embedded longitudinal vortex and no film cooling to test further the capability of the heat transfer surface for spatially resolved measurements. Spanwise variations of local St/St_0 for 15 m/s are presented in Fig. 6.

The influence of the vortex is evident at locations where St/St_0 values are not equal to 1. Maximum values of St/St_0 are about 1.25 at locations that correspond to the downwash side of the vortex. For $-5.0 < z < 0.0 \text{ cm}$ a large gradient of heat transfer exists at each downstream location. This gradient moves to smaller z with downstream distance. For even smaller z , Stanton number ratios reach minima of about 0.90 at locations that correspond to the upwash sides of vortices. Similar behavior is observed at 10 m/s, except maxima and minima are slightly different. These results show qualitative agreement with the measurements of Eibeck and Eaton (1987), where small quantitative differences are a result of different vortex generator geometries, and different magnitudes of vortex circulation.

Boundary Layer With Film Cooling. To qualify further the heat transfer surface and the film cooling injection system, measurements were made with film cooling but without an embedded vortex. Stanton numbers were obtained at 10 m/s with blowing ratios from 0.68 to 1.26, and at 15 m/s with blowing ratios from 0.47 to 0.86. Nondimensional coolant temperature was maintained at about 1.6. These results showed trends consistent with the film cooling effectiveness data of Goldstein and Yoshida (1982) for turbulent injection from a single row of holes into turbulent boundary layers. In that study, spanwise-averaged effectiveness decreased significantly as blowing ratio increased from 0.5 to 1.0. In the present study, the lowest spanwise-averaged St_f/St_0 were observed for $m = 0.68$ at 10 m/s and for $m = 0.47$ at 15 m/s. As the blowing ratio increased from these values to near one, St_f/St_0 then also increased.

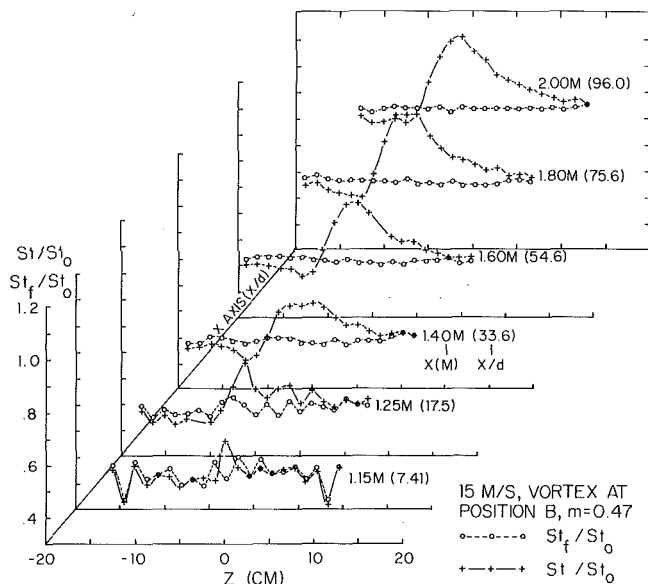


Fig. 7 Local Stanton number ratios; boundary layers with film cooling, with and without an embedded vortex

Boundary Layers With Film Cooling and Vortex

General Observations. Overall effects of embedded vortices on film-cooled turbulent boundary layers are now discussed referring to data in Fig. 7. These results were obtained at the same experimental conditions as the fluid mechanics data in Figs. 3, 4, and 5. The vortex was located at position B with a free-stream velocity of 15 m/s and a blowing ratio of 0.47. The general features of the Stanton number distributions remained similar for other free-stream velocities, blowing ratios, and vortex positions tested.

In Fig. 7, spanwise distributions of Stanton number ratios St/St_0 and St_f/St_0 are shown at different downstream locations. $St/St_0 = 1$ indicates an undisturbed two-dimensional thermal boundary layer. The St/St_0 and St_f/St_0 data are presented together so that the effects of the embedded vortex on the film-cooled boundary layers are readily apparent.

From Fig. 7, it is evident that embedded vortices cause significant changes in the surface heat transfer in film-cooled turbulent boundary layers. From an overall qualitative point of view, these changes show some similarity to those observed in the present study (Fig. 6) and by Eibeck and Eaton (1987) without film cooling. In both cases, many of the overall spanwise variations of heat transfer can be related to the mean velocity field of the vortex. Near the downwash side of the vortex ($z > -2$ cm to -5 cm), the boundary layer is locally thinner, and heat transfer is augmented. Here, the protection provided by film cooling is minimized. The embedded vortex produces a thicker boundary layer near the upwash side ($z < -2$ cm to -5 cm), reducing the heat transfer and increasing the protection provided by film cooling.

Also evident from Fig. 7 is a very steep heat transfer gradient, which extends along the length of the test surface. The vortex center approximately follows this same path, starting near $z = -1.5$ cm at the upstream end of the test plate. The path of the vortex axis is skewed at an angle of several degrees from the plate centerline. At large z locations, high heat transfer regions exist near the vortex downwash, which in this case also extend along the entire length of the test surface. This shows the strong persistence of the vortices in regard to surface heat transfer.

Further comparison of Figs. 7 and 6 reveals important qualitative differences between boundary layers with vortices only, and boundary layers with vortices and film cooling. For the former case, a St/St_0 maximum exists near the downwash side of the vortex. If film cooling is present, this maximum will

again be present, but a second peak may also exist in the downwash region for $x/d \geq 17.5$. The second peak seems to result from an interaction between the vortex and film cooling jets. At $x/d = 17.5$, it is located near $z = 4$ cm. The magnitude and downstream persistence of the secondary peak are dependent upon the blowing ratio and relative location between the vortex center and cooling jets. With downstream development, the two St/St_0 peaks may merge together to form one large broad peak, such as the one at $x/d = 33.6$ in Fig. 7, and the one at $x/d = 54.6$ in Fig. 9. This large peak increases in magnitude relative to the film-cooled boundary layer, and continues to grow as the layer develops to the end of the test plate.

At $x/d = 7.4$ in Fig. 7, the vortex seems to have only a very small effect on the spanwise variation of St/St_0 . Similar behavior was observed by Eibeck and Eaton (1987) near the leading edge of their heat transfer surface. They attributed this behavior to a thermal boundary layer so thin that it could not be significantly perturbed by the vortex. In the present experiment, spanwise averaged Stanton numbers at $x/d = 7.4$ with film cooling only are 53 percent of their flat plate values. Here, the coolant, rather than the vortex, is responsible for most of the spanwise variations of St/St_0 . The boundary layer is thickened by coolant, which may also cause the vortex to be lifted slightly above the surface near the injection locations.

Without film cooling, the perturbations to heat transfer caused by the vortex appear to be more localized than when film cooling is present. These differences are the result of interactions between film cooling jets and the vortices, especially near the upwash side. A comparison of Figs. 6 and 7 shows that, without cooling, St/St_0 less than 1 occur for $z < -2$ to -5 cm due to the upwash effect. However, as z becomes less than -12 cm, St/St_0 in Fig. 6 approach the unperturbed value of 1.0. In contrast, measurements from the film-cooled boundary layer in Fig. 7 show St/St_0 lowered from vortex effects that extend to the left edge of the test plate. Here, the vortex seems locally to increase the protection provided by the coolant since $St/St_0 < St_f/St_0$.

Goldstein and Chen (1985, 1987) also observed drastic alterations to film-cooled boundary layers by embedded vortices. In their study, a region totally void of coolant resulted on the convex surfaces of gas turbine blades near the endwalls, where coolant jets were swept away from the surface by passage vortices. As in the present study, the coolant was maintained on the upwash sides of the vortices.

Effects of Spanwise Vortex Position. To study the effect of the spanwise location of the vortex relative to injection holes, the vortex position was changed to three different locations by moving the vortex generator. The spanwise spacing of adjacent injection holes was 2.86 cm. To obtain vortex positions A, B, and C, the leading edge of the generator delta wing was positioned at z locations of 3.52 cm, 4.79 cm, and 6.06 cm, respectively. The generator location for position B is shown in Fig. 2. With vortex positions A and C, the vortex core passed near injection holes, whereas with position B the vortex core was located between two injection holes.

Stanton number data for vortex positions A, B, and C at a free-stream velocity of 10 m/s and a blowing ratio m of 0.98 are presented in Figs. 8, 9, and 10, respectively. To produce a blowing ratio of 0.47 for data in Fig. 7, 13 injection holes were employed and the coolant spanned the entire width of the test surface. However, this was not the case for the $m = 0.98$ data, where 9 injection holes were employed to achieve the blowing ratio used for film cooling. As a result, injectant covered only the midspan of the test plate where -12 cm $< z < 12$ cm. Consequently, Stanton numbers are larger outside of this range of spanwise locations.

Comparison of Figs. 8, 9, and 10 shows that for low x/d values up to 17.5, a double peak in the St/St_0 distributions is

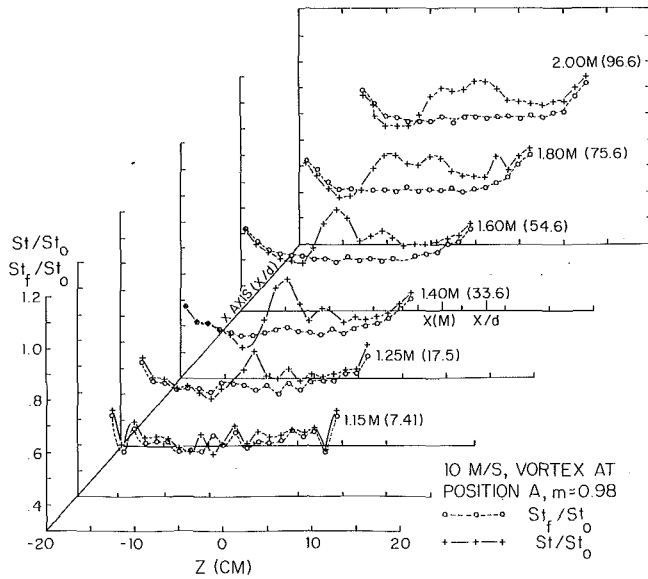


Fig. 8 Local Stanton number ratios; boundary layers with film cooling, with and without an embedded vortex

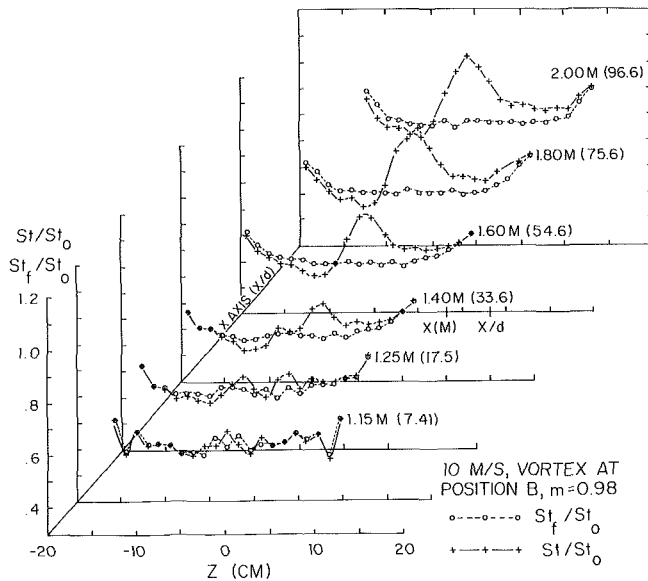


Fig. 9 Local Stanton number ratios; boundary layers with film cooling, with and without an embedded vortex

present for all three vortex positions. At locations farther downstream, the shape and size of the high heat transfer region vary, depending on the spanwise vortex position. Results for vortex positions A and C show much quantitative similarity, which is sensible since the vortices were positioned at almost the same locations with respect to injection locations. At $x/d \geq 17.5$ for vortex positions A and C, the double peak in St/St_0 distributions starts to grow, and the portion of the plate covered by high St/St_0 becomes enlarged in the spanwise direction. In addition, St/St_0 peaks for vortex positions A and C are not as high as for vortex positions B. St/St_0 regions on the upwash side of the vortex were lowest for vortex position B. In addition, the heat transfer gradient aligned along the vortex center is steeper for vortex position B, especially for $x/d > 54$.

A comparison may also be made between boundary layers with different blowing ratios but the same vortex position B. This is accomplished by examining Figs. 7 and 9 for $m = 0.47$ and $m = 0.98$, respectively. When compared at a particular downstream location, St/St_0 maxima are higher and St/St_0 minima are lower for $m = 0.47$. In addition, St/St_0 maxima increase more rapidly with downstream distance at this blowing

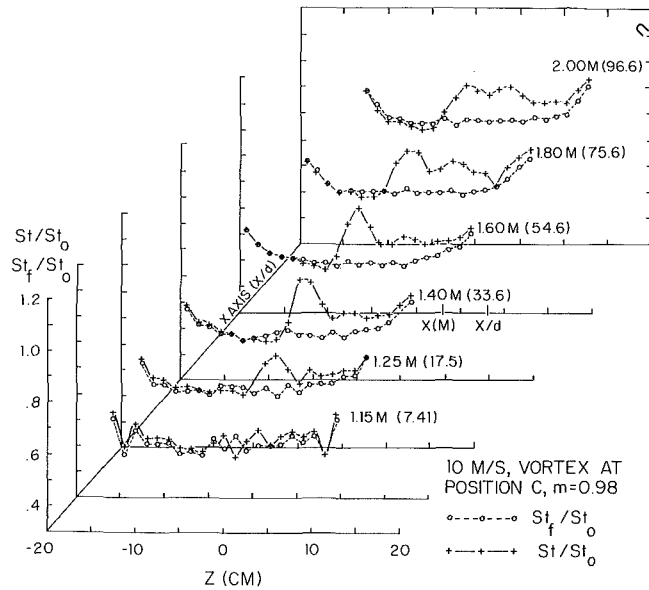


Fig. 10 Local Stanton number ratios; boundary layers with film cooling, with and without an embedded vortex

ratio. The rapid downstream growth of these maxima becomes more apparent when one considers that Stanton numbers in the film-cooled boundary layers are lower at $m = 0.47$ than at $m = 0.98$. This is particularly true for $x/d = 7.4, 17.5,$ and 33.6 because of more effective film cooling at the lower blowing ratio.

Figure 11 shows the $(T - T_\infty)$ temperature field in $^\circ\text{C}$ at $x/d = 41.9$ for vortex positions A, B, and C. For these tests, the free-stream velocity was 10 m/s and the blowing ratio m was 0.98, as for results in Figs. 8–10. In addition, film-cooling jets were heated to 51°C without providing any heat to the test plate. Thus, the temperature field shows how fluid from the film cooling holes is convected and distorted by the vortex, where higher temperatures generally indicate greater amounts of injectant. The most dramatic effect occurs on the upwash side, where coolant is lifted away from the wall. At $x/d = 41.9$ injectant fluid affected by the vortex is 7.0 cm from the surface. Without the perturbation, the film-cooled thermal boundary layer is ordinarily about 4 cm thick.

Figures 8, 9, and 10 show that St/St_0 is lower than St_f/St_0 on the left side of the plate at locations that depend upon the downstream location and vortex position. Figure 11 shows that these low heat transfer regions correspond precisely with locations where injectant accumulates after being redistributed by the vortex. The vortex spreads injectant along the wall beneath the vortex center, convecting it in the direction of secondary flow vectors. Eventually, much of the injectant is relocated near the upwash side.

Qualitatively, $(T - T_\infty)$ results for vortex positions A and C are similar because the locations of vortex centers relative to injection holes are nearly the same. Near-wall secondary flows for positions A and C seem to sweep injectant in the spanwise direction to the upwash side more efficiently than for vortex position B. As a result, more injectant seems to be convected farther from the wall by the upwash than for vortex position B. The vortex downwash also perturbs the film injectant more dramatically for vortex positions A and C. This is evident from the high St/St_0 regions in Figs. 8 and 10, and the corresponding regions on the righthand side of Fig. 11, which show the near absence of injectant.

Also featured in Fig. 11 are spanwise temperature gradients. One is located beneath the vortex center for all three vortex positions. The gradient extends about 5 cm from the wall with a spanwise location which changes with vortex position. A second set of temperature gradients is located near $z = -12$

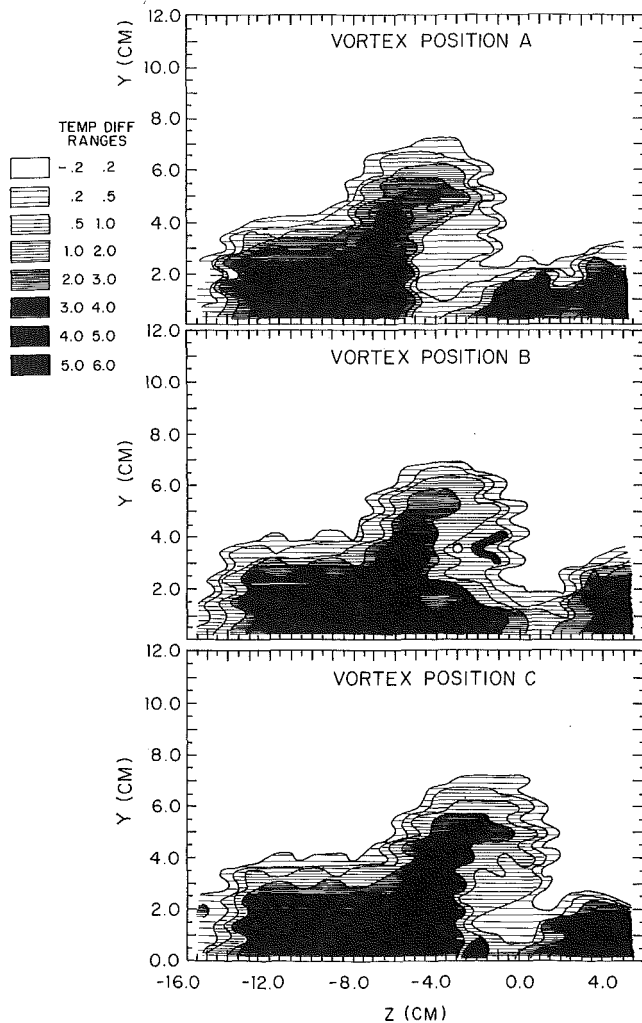


Fig. 11 $(T - T_\infty)$ temperature field for $x = 1.48$ m, $x/d = 41.9$ for a free-stream velocity of 10 m/s; results for vortex positions A, B, and C show the effect of spanwise vortex position on the film-cooled turbulent boundary layer

cm. These correspond to the spanwise edges of film-cooled regions.

Summary and Conclusions

Longitudinal vortices were found to cause significant changes to wall heat transfer distributions, mean temperatures, and mean velocities in film-cooled turbulent boundary layers. For all experimental conditions investigated, the film coolant was greatly disturbed by the vortex. In addition, the spanwise location of the vortex with respect to film-cooling holes was found to be very important. For this study, blowing ratios of 0.47 and 0.98 were employed from a single row of injection holes at free-stream velocities of 15 m/s and 10 m/s, respectively. The circulation to free-stream velocity ratio of the vortex was -0.95 cm with film cooling, compared to -1.10 cm without film cooling.

Some additional major conclusions are as follows:

1 The embedded vortex caused Stanton number augmentations as large as 30 percent, and reductions as much as 10 percent. Changes from the vortex were observed to persist as many as 23 boundary layer thicknesses or 96 film cooling hole diameters downstream of injection holes.

2 Near the downwash side of the vortex, Stanton numbers were augmented, vortex effects dominated flow behavior, and the protection from film cooling was minimized. Stanton num-

ber peaks from the downwash increased more rapidly with downstream distance for $m = 0.47$ than for $m = 0.98$.

3 Near the upwash side of the vortex, coolant was pushed along the wall to the side of the vortex, locally increasing the protection from film cooling.

4 Changing the position of the vortex with respect to the film cooling jets resulted in significant local quantitative changes in heat transfer even though the general qualitative trends were unchanged. When the vortex core passed film cooling holes above an injection location, injectant was swept in the spanwise direction to the upwash side more effectively than if the core passed between two injection locations. This resulted in a larger area of high heat transfer relative to the film-cooled boundary layer.

Acknowledgments

This study was supported by Wright Aeronautical Laboratories, Wright-Patterson Air Force Base, MIPR number FY 1455-86-N0616. Dr. Charles MacArthur was program monitor. Many of the facilities used in this study were purchased using funds from the Naval Postgraduate School Foundation Research Program.

References

- Blair, M. F., 1974, "An Experimental Study of Heat Transfer and Film Cooling on Large-Scale Turbine Endwalls," *ASME Journal of Heat Transfer*, Vol. 96, pp. 524-529.
- Eibeck, P. A., and Eaton, J. K., 1987, "Heat Transfer Effects of a Longitudinal Vortex Embedded in Turbulent Boundary Layer," *ASME Journal of Heat Transfer*, Vol. 109, pp. 16-23.
- Evans, D. L., 1987, "Study of Vortices Embedded in Boundary Layers With Film Cooling," M.S. Thesis, U.S. Naval Postgraduate School, Monterey, CA.
- Goldstein, R. J., and Chen, H. P., 1985, "Film Cooling on a Gas Turbine Blade Near the End Wall," *ASME Journal of Engineering for Gas Turbines and Power*, Vol. 107, pp. 117-122.
- Goldstein, R. J., and Chen, H. P., 1987, "Film Cooling of a Turbine Blade With Injection Through Two Rows of Holes in the Near-Endwall Region," *ASME JOURNAL OF TURBOMACHINERY*, Vol. 109, pp. 588-593.
- Goldstein, R. J., and Yoshida, T., 1982, "The Influence of a Laminar Boundary Layer and Laminar Injection on Film Cooling Performance," *ASME Journal of Heat Transfer*, Vol. 104, pp. 355-362.
- Joseph, S. L., 1986, "The Effects of an Embedded Vortex on a Film-Cooled Turbulent Boundary Layer," M.E. Thesis, U.S. Naval Postgraduate School, Monterey, CA.
- Kays, W. M., and Crawford, M. E., 1980, *Convective Heat and Mass Transfer*, 2nd ed., McGraw-Hill, New York.
- Kline, S. J., and McClintock, F. A., 1953, "Describing Uncertainties in Single-Sample Experiments," *Mechanical Engineering*, pp. 3-8.
- Langston, L.S., 1980, "Cross Flows in a Turbine Cascade Passage," *ASME Journal of Engineering for Power*, Vol. 102, No. 4, pp. 866-874.
- Ligrani, P. M., and Camci, C., 1985, "Adiabatic Film Cooling Effectiveness From Heat Transfer Measurements in Compressible Variable-Property Flow," *ASME Journal of Heat Transfer*, Vol. 107, pp. 313-320.
- Ortiz, A., 1987, "The Thermal Behavior of Film Cooled Turbulent Boundary Layers as Affected by Longitudinal Vortices," M.E. Thesis, U.S. Naval Postgraduate School, Monterey, CA.
- Sato, T., Aoki, S., Takeishi, K., and Matsuura, M., 1987, "Effect of Three-Dimensional Flow Field on Heat Transfer Problem of a Low Aspect Ratio Turbine Nozzle," Takasago Research and Development Center, Mitsubishi Heavy Industries, Ltd.
- Sieverding, C. H., 1985, "Recent Progress in the Understanding of Basic Aspects of Secondary Flows in Turbine Blade Passages," *ASME Journal of Engineering for Gas Turbines and Power*, Vol. 107, pp. 248-257.
- Wang, T., 1984, "An Investigation of Curvature and Free Stream Turbulent Effects on Heat Transfer and Fluid Mechanics in Transitional Boundary Layer Flows," Ph.D. Thesis, Mechanical Engineering Department, University of Minnesota, Minneapolis, MN.
- Wang, T., Simon, T. W., and Buddhavarapu, J., 1985, "Heat Transfer and Fluid Mechanics Measurements in Transitional Boundary Layer Flows," *ASME Journal of Engineering for Gas Turbines and Power*, Vol. 107, pp. 1007-1015.
- Westphal, R. V., Pauley, W. R., and Eaton, J. K., 1987, "Interaction Between a Vortex and a Turbulent Boundary Layer, Part I: Mean Flow Evolution and Turbulence Properties," NASA Technical Memorandum 88361.
- Westphal, R. V., Eaton, J. K., and Pauley, W. R., 1985, "Interaction Between a Vortex and a Turbulent Boundary Layer in a Streamwise Pressure Gradient," Fifth Symposium on Turbulent Shear Flows, Cornell University, Ithaca, NY.

Free-Stream Turbulence From a Circular Wall Jet on a Flat Plate Heat Transfer and Boundary Layer Flow

R. MacMullin

W. Elrod

Air Force Institute of Technology,
Wright-Patterson AFB, OH 45433

R. Rivir

Aero Propulsion Laboratory,
Wright-Patterson AFB, OH 45433

The effects of the longitudinal turbulence intensity parameter of free-stream turbulence (FST) on heat transfer were studied using the aggressive flow characteristics of a circular tangential wall jet over a constant heat flux surface. Profile measurements of velocity, temperature, integral length scale, and spectra were obtained at downstream locations (2 to 20 x/D) and turbulence intensities (7 to 18 percent). The results indicated that the Stanton number (St) and friction factor (C_f) increased with increasing turbulence intensity. The Reynolds analogy factor ($2St/C_f$) increased up to turbulence intensities of 12 percent, then became constant, and decreased after 15 percent. This factor was also found to be dependent on the Reynolds number (Re_x) and plate configuration. The influence of length scale, as found by previous researchers, was inconclusive at the conditions tested.

Introduction

The influence of elevated free-stream turbulence on fluid dynamics and convective heat transfer has recently been recognized as a major factor in turbine blade design. Early studies indicated that the only effect of free-stream turbulence (FST) was to advance the transition Reynolds number (Re_x) (White, 1974) and increase the friction factor with no apparent changes in heat transfer (Kestin, 1966; Junkhan and Serovy, 1977). These early studies used turbulence generating devices (trip wires) and were based on low Re_x where transitional effects may have been present (Simonich and Bradshaw, 1978). Studies by Simonich and Bradshaw (1978), Blair and Werle (1980), Blair (1983), and Hancock (1980) using wind tunnel flows with turbulence intensities (T_u) up to 7 percent clearly demonstrated the increase in heat transfer associated with the presence of free-stream turbulence. The Stanton number (St) and friction factor (C_f) increased with increasing free-stream turbulence intensity when the length scale was near the boundary layer thickness. The increased turbulence levels slightly depressed the wake regions of the velocity and temperature profiles, while the logarithmic portions of the profiles were unaffected (Blair and Werle, 1980; Blair, 1983).

The flow fields of free jets and wall jets have been used in the more recent research to simulate the high free-stream turbulence encountered in turbomachinery. In a study by Moffat and Maciejewski (1985) at 26 and 48 percent T_u , Stanton numbers in the margin of a free jet were as much as 350 percent above the standard zero free-stream turbulence correlation,

which is given by equation (1) from Kays and Crawford (1980)

$$St = 0.03 Re_x^{-0.2} Pr^{-0.4} \quad (1)$$

A blade wake loss calculation of T_u due to the blade or vane wake yields levels of 10 to 20 percent for this source in a turbine engine. For this investigation a circular wall jet was used to establish T_u values in this range and expand the range of parameters of previous investigations to a range applicable to the turbine engine.

Experimental Approach

The wall jet combines the characteristics of a boundary layer and a free jet; thus a uniform flow field was absent in the vertical (y) direction. The reference point for all boundary layer and heat transfer measurements was defined as the height above the plate (Y_{max}) where the velocity achieved a maximum (U_{max}). From previous studies of Launder and Rodi (1981), MacArthur (1986), Chandrasekhara and Bandyopadhyay (1975), and Schlichting (1979), it was noted that when the velocity and temperature profiles at a given downstream location were normalized by U_{max} , they collapsed into a single curve. Thus, given any U_{max} , T_a , and T_p , the friction coefficient and integral thickness parameters could be predicted from a velocity/temperature profile at a corresponding x/D . In this study a minimum of two independent profile sets at widely different jet velocities was used to determine the characteristic curve at each location.

The emphasis in this study was the determination of the Stanton number (St) as a function of the variables (T_u , L_e , and Re). The length scale was a linear function of distance downstream of the nozzle and was not intentionally varied during this study. Centerline T_u above the wall jet boundary

Contributed by the International Gas Turbine Institute and presented at the 33rd International Gas Turbine and Aeroengine Congress and Exhibition, Amsterdam, The Netherlands, June 5-9, 1988. Manuscript received by the International Gas Turbine Institute July 15, 1987. Paper No. 88-GT-183.

layer varied as a function of longitudinal distance down the plate and was largely independent of nozzle velocity. Accordingly, T_u and L_e were fixed by location on the plate. The Re_x was varied by adjusting the nozzle exit jet velocity. Measurements were taken over a range of Re_x for three different T_u values with and without a 1.5-m unheated starting length (USL).

Experimental Apparatus and Instrumentation

The experimental apparatus included an instrumented flat plate test section, a traversing system for precise sensor positioning, an ASME nozzle and air supply system, and data acquisition to sample and reduce temperature and velocity measurements. A circular wall jet was produced at the outlet of the ASME nozzle with a contraction ratio of 16:1. Air was supplied to the nozzle through a 1.5-m-long horizontal stilling chamber. The test section was located in a 12.2-m by 24.4-m area with a 7-m-high ceiling. The jet stagnation temperature was monitored with an iron-constantan thermocouple in the center of the chamber. The chamber stagnation pressure was adjusted to establish set velocity conditions at positions where data were obtained.

Two configurations of the flat plate test section were investigated. The first consisted of a 0.61-m-wide by 3-m-long constant heat flux surface as shown in Fig. 1. The second, shown schematically in Fig. 2, located this heated section behind a 0.61-m-wide by 1.5-m-long unheated starting length (USL). The constant heat flux was established by passing an alternating current through the 0.038 mm stainless steel foil that comprised the test surface. The foil was heated with an isolated a-c power supply. The energy dissipation was calculated using the root mean square voltage drop across the plate and the voltage across a shunt in series with the foil.

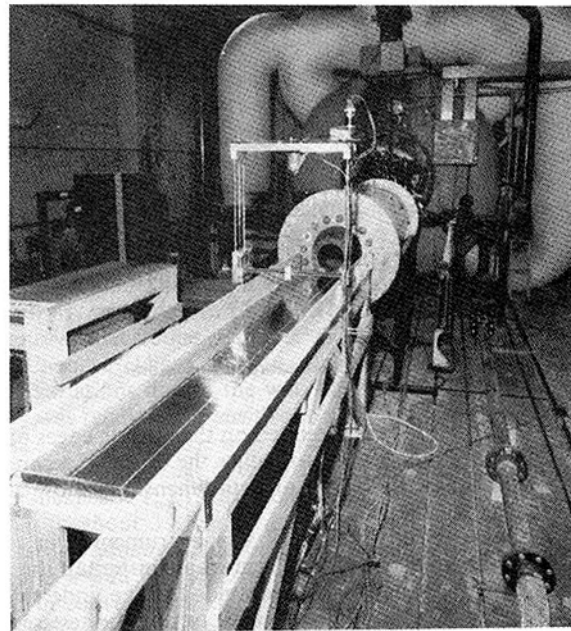


Fig. 1 Flat plate test section in the normal configuration

The stainless steel foil covered the full length of the 3-m table in three parallel 15.2-cm-wide strips, which were connected in series. A 7.6-cm strip of formica formed each edge of the plate. The heated section was backed with 0.3 cm of fiberglass laminate with 10.2 cm of urethane foam insulation. The 1.5-m USL was installed to extend the range of Reynolds numbers at the measuring stations. Two 14-cm-high by 4.6-

Nomenclature

A = area, m^2	St = Stanton number = $h / (U \rho C_p)$	Y_{max} = distance above plate where U is a maximum, cm
C_p = specific heat at constant pressure, $W \cdot s / kg \cdot ^\circ C$	t = time, s	z = lateral distance from wall jet centerline, cm
C_f = coefficient of friction = $2\tau_p / (\rho_m U_{max}^2)$	\bar{T} = mean temperature, $K, ^\circ C$	α = defined in Fig. 11
D = inside diameter of ASME nozzle, cm	T^+ = nondimensional temperature, defined by equation (3)	β = defined in Fig. 11
d = outside diameter or dimension, cm	T_u = longitudinal turbulence intensity = $(U'^2)^{0.5} / U_{max}$	Δ_2 = enthalpy thickness, cm
E = voltage, V	U = total velocity component in x direction, m/s	δ = conventional boundary layer thickness, cm
f = frequency, Hz	\bar{U} = mean velocity component in x direction, m/s	δ_1 = displacement thickness, cm
FST = free-stream turbulence	U' = instantaneous fluctuating component of velocity, m/s	θ = momentum thickness, cm
h = heat transfer coefficient, $W / m^2 \cdot ^\circ C$	U^+ = nondimensional velocity, defined by equation (2)	μ = dynamic viscosity, $kg / m \cdot s$
I = current, A	U_r = friction velocity = $(\tau_p / \rho)^{0.5}$	ν = kinematic viscosity, m^2 / s
J_u = integral time scale, s	USL = configuration of test section: unheated starting length attached between nozzle and heated section	ρ = density, kg / m^3
L_c = characteristic dimension, defined by equation (14)	U_{max} = maximum U along the y axis at a specified location on the plate	τ_p = shear stress at plate, N / m^2
L_e = integral length scale, cm	x = distance from nozzle, cm	τ = time increment, s
M = Mach number = U / U_{sound}	y = vertical distance from plate, cm	
Pr = Prandtl number = $\mu C_p / k$	Y^+ = nondimensional distance from plate, defined by equation (2)	
Pr_t = turbulent Prandtl number, ratio of momentum eddy diffusivity to thermal eddy diffusivity		
q = heat flux per unit area, W / m^2		
Re = Reynolds number = $\rho \bar{U} x / \mu$, $\rho \bar{U} \theta / \mu$, $\rho \bar{U} \Delta_2 / \mu$		
Ru = autocovariance, defined by equation (5)		

Subscripts

a = ambient condition outside of wall jet
m = evaluated at Y_{max}
noz = evaluated at the exit plane of the nozzle
o = evaluated at the zero FST turbulence level
p = evaluated at the plate
ref = reference datum for a calculation, usually at Y_{max}
wj = wall jet
x = evaluated at a distance from nozzle along x axis

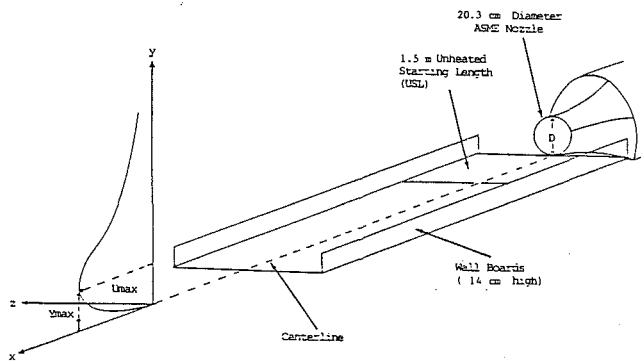


Fig. 2 Wall jet coordinate system

m-long wall boards were mounted on the outside edges of the top surface of both sections to reduce the effect of secondary flows and increase the width of two-dimensional flow along the centerline of the jet.

The center section of the foil was instrumented in seven locations with an array of 0.013-cm iron-constantan thermocouples. The thermocouples were welded to the underside of the metal foil with the wires brought out of the test section through small holes in the urethane insulation and supporting structure. Two 66° C iron-constantan reference junctions provided the thermocouple reference points. A schematic of the flat plate test section and thermocouple array is shown in Fig. 3.

The computer-controlled traverse mechanism shown mounted on the test section in Fig. 1 provided precise location of velocity and temperature sensors in the vertical direction (y), and across the plate (z) (± 0.013 cm). The entire apparatus could be easily moved along the plate (x) to fixed positions corresponding to thermocouple array locations.

The data acquisition hardware was commanded by a computer-controller. All thermocouple and anemometer voltages were output to an 80 channel data scanner unit and digital voltmeter. The anemometer output was also parallel with a correlator and spectrum display for autocorrelation length scale and power spectral density measurements.

Data Acquisition and Reduction

Heat Transfer Tests. Heat transfer tests were conducted both separately and in conjunction with profile tests. All measurements were acquired along the centerline of the jet and above the location of the thermocouple arrays in the foil to eliminate uncertainty in wall temperature. The wall jet coordinate system is defined in Fig. 2. Prior to performing heat transfer tests, a velocity profile was obtained at each x/D location to determine the height above the surface where \bar{U} was a maximum (Y_{\max}). The reference temperature (T_a) used for the heat transfer calculation was obtained at Y_{\max} . The Y_{\max} was chosen for two reasons. First, Y_{\max} was a definable, repeatable length at any x/D . Second, when the wall jet temperature was equal to the ambient temperature, the temperature profile became asymptotic at Y_{\max} . A temperature difference cannot be avoided in this type of test; therefore, to reduce errors associated with this anomaly, the jet/ambient temperature difference was maintained less than 1/2°C and the local plate temperature was maintained at least 17°C above the ambient temperature. The integral properties and wall shear stress inferred from the profiles were used to relate heat transfer results to the more recent correlations in the literature of Blair and Werle (1980) and Blair (1983). The local heat transfer coefficient was calculated by measured plate power, ignoring conduction losses (less than 1/2 percent), and subtracting power lost from thermal radiation. The radiation model used for this test was that of a small graybody surface enclosed in a large cavity (Siegel

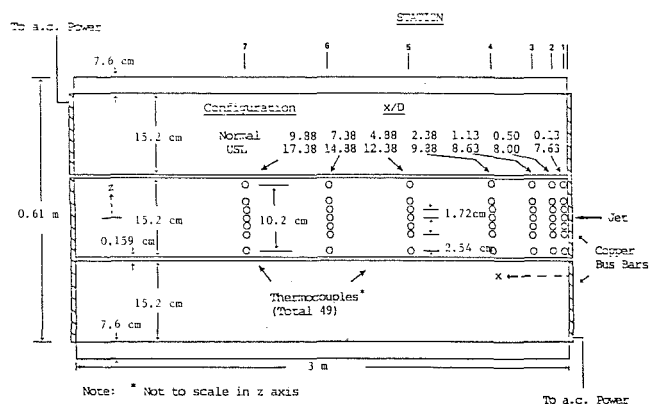


Fig. 3 Schematic of heated section depicting thermocouple locations

and Howell, 1981). Aside from small changes in resistance and thermal radiation differences along the plate, the foil was considered a good model of a constant heat flux surface. A heat transfer measurement was also performed at several data points in the vicinity of Y_{\max} . Length scale and longitudinal turbulent spectral data were obtained throughout the traverse for selected profiles. The analytical basis for the data reduction equations was obtained from the current theory of turbulent flow and convective heat transfer as found in White (1974), Kays and Crawford (1980), and Schlichting (1979) for law of the wall coordinates.

Law of the Wall Coordinates. The friction velocity (U_*) for each profile was determined by iteration of a least-squares line through the data to the constant property two-dimensional flat plate law of the wall at Y^+ of approximately 40 (Kays and Crawford, 1980)

$$U^+ = 2.44 \ln Y^+ + 5.0 \quad (2)$$

where $U^+ = U/U_*$ and $Y^+ = yU_*/\nu$.

Using this value of U_* , the velocity and temperature data were plotted in universal (wall) coordinates. The velocity data were compared with equation (2) and the temperature data with the temperature law of the wall (Kays and Crawford, 1980)

$$T^+ = 2.195 \ln Y^+ + 13.2 \text{Pr} - 5.66 \quad (3)$$

$$\text{where } T^+ = (T_p - \bar{T}) \rho C_p U_* / \dot{q}_w''$$

The shear stress at the wall was then estimated

$$C_f = 2 U_*^2 / U_{\max}^2 \quad (4)$$

Integral Quantities. The integral quantities were calculated on the boundary layer portion of the wall jet profiles (below Y_{\max}). This calculation was done in order to compare the heat transfer data obtained in this test with other conventional two-dimensional flat plate heat transfer data presented in integral format (Re_θ , $Re_{\Delta 2}$). The integral thickness for displacement, momentum, and enthalpy thickness were obtained by digitizing and then numerically integrating the velocity and temperature profiles. A thermal boundary layer probe with a 0.005-cm-dia bead was used for mean flow temperature profile measurements. During heat transfer tests, a miniature Kiel probe was used as a check on local velocity measurements. The velocity at Y_{\max} , determined by using the anemometer, was consistently within 1–2 percent of Kiel probe measurements.

To account for the lack of data between the plate surface and the lowest point in the y axis, linear velocity and temperature profiles were used to extrapolate the data through the laminar sublayer region to the wall. Since the nondimensionalized profile data generated a single unique velocity and temperature curve at each station, these integral thickness quantities could be calculated for any flow condition. The procedure

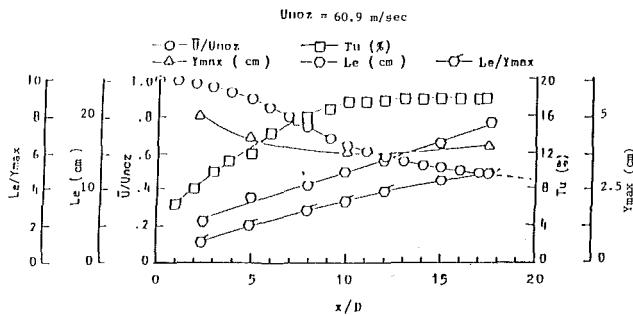


Fig. 4 Circular tangential wall jet performance as a function of x/D

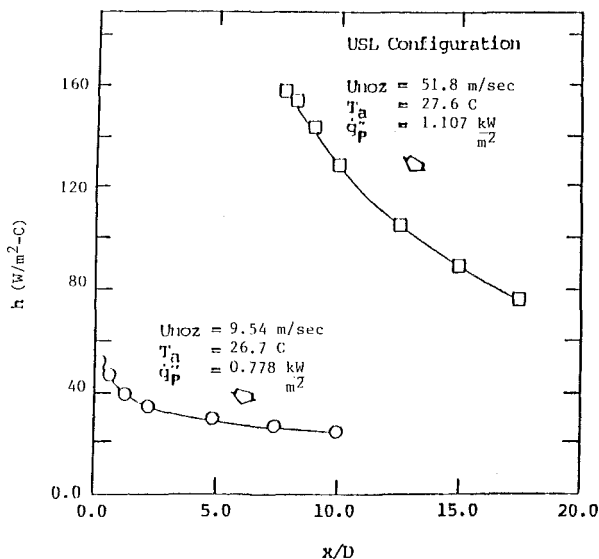


Fig. 5 Typical variation of heat transfer coefficients along the centerline as a function of x/D

required: measurement of U_{max} , T_p , and T_{ref} at a specified x/D location (obtained during heat transfer tests); converting the characteristic nondimensional profiles (obtained during profile tests for the corresponding x/D location) to dimensional profiles; and performing the integration.

Integral Length Scales. The correlator was used indirectly to calculate the integral length scale (autocorrelation length scale). The autocovariance was normalized by the turbulent variance and represented as

$$Ru(\tau) = U(t)U(t+\tau)/\overline{U^2} \quad (5)$$

This quantity is integrated over all time and then represents the integral time scale

$$J_u = \int_0^\infty U(t)U(t+\tau)/\overline{U^2} d\tau \quad (6)$$

In practice, a 30–60 s scale interval was used with the assumption that turbulent flow rapidly becomes uncorrelated with increasing time and distance. Using Taylor's hypothesis (Hinze, 1959), the integral length scale becomes

$$L_e = \bar{U} J_u \quad (7)$$

The correlation curves obtained in this study were digitized, normalized, and then numerically integrated to obtain the integral scale.

Spectral Distributions. The velocity fluctuations were documented to determine the power distribution as a function of frequency. The spectrum analyzer produced the Fourier transform of the autocorrelation curve to determine the energy level in selected frequency bands. The power spectral density distributions were obtained in dimensionless form with the dimensionless spectrum, $U_{max} E(f)/\overline{U^2} L_e$, as a function of the dimensionless wave number $L_e f/U_{max}$.

Results and Discussion

The level of turbulence intensity T_u and the Reynolds number Re_x were the major factors varied in the heat transfer tests. After examining the surface temperature distributions and general characteristics of the wall jet flow, heat transfer and profile data were obtained at four x/D locations in two flat plate configurations over a 12 percent change of turbulence intensity.

General Characteristics of the Wall Jet. The performance of various boundary layer parameters as a function of the plate geometry is presented in Fig. 4. The data compared well to previous wall jet studies (Lauder and Rodi, 1981; MacArthur, 1986; Chandrasekhara and Bandyopadhyay, 1975,) with some minor variations due to the wall boards. The turbulence intensity was relatively insensitive to velocity changes at a fixed distance from the nozzle with variations of only 1 to 2 percent over a wide speed range (5 to 60 m/s). The apparent boundary layer thickness (Y_{max}) was largest near the nozzle, then decreased to about 3.8 cm at an x/D of 10, beyond which it increased gradually. This behavior was typical of the core region in a wall jet (MacArthur, 1986) and opposite to that found in conventional flat plate boundary layers (Kays and Crawford, 1980; Schlichting, 1979).

Integral Length Scale. The integral length scale L_e varied linearly with distance down the plate, but L_e/Y_{max} was nonlinear due to the variance of Y_{max} down the plate. Between an x/D of 10 and the end of the plate was a region where T_u was relatively constant but L_e varied. In this region the L_e/Y_{max} ratio was much higher than one.

The integral length scale appeared to remain constant throughout the y axis except close to the plate. In the vicinity of Y_{max} there was considerable scatter (about 20 percent). Near the plate the integral length scale appeared to decrease at about the same rate as the velocity. This characteristic was expected as the size and nominal distance between turbulent eddies must decrease when close to a physical boundary.

The spectrum of the free-stream turbulence was measured at each heat transfer data point and at various locations during profile tests. The major portion of the energy was at low frequencies. The spectra for the fully developed wall jet followed a $-5/3$ power law decay at high frequencies (Hinze, 1959).

Heat Transfer Coefficient Distribution. The distribution of heat transfer coefficients on the heated surface is presented in Fig. 5. At stations #4 to 7, the variation of h in the z direction is minimal; however, it is more than 5 percent at the two stations closest to the nozzle. The large variations at the first two stations were due in part to their proximity to the edge of the plate, where the presence of insulation on the front side of the table caused uneven heating. In the normal configuration at station #1, the outer two thermocouple sensors were not in the flow region and results in higher temperatures compared to the rest of the plate. During this test, all heat transfer and profile data were obtained downstream of station #4.

Effects of Free-Stream Turbulence on Heat Transfer. The relationship between Stanton number and Reynolds number is presented in Figs. 6 and 7. The data presented are for T_u within 1 percent of the indicated value in each configuration. The effect of increasing the level of T_u was an increase in the heat transfer from the plate at constant Re_x . The increase in Stanton number from the zero free-stream turbulence (FST) flat plate correlation, equation (1), ranged from 17 to 78 percent, as a function of T_u and configuration. The Stanton numbers for the 7 percent T_u data set were 2 to 11 percent higher than the 6 percent T_u results of Blair and Werle (1980). Within the scope of this investigation, the transition region was completely eliminated at the low Reynolds numbers. There was no

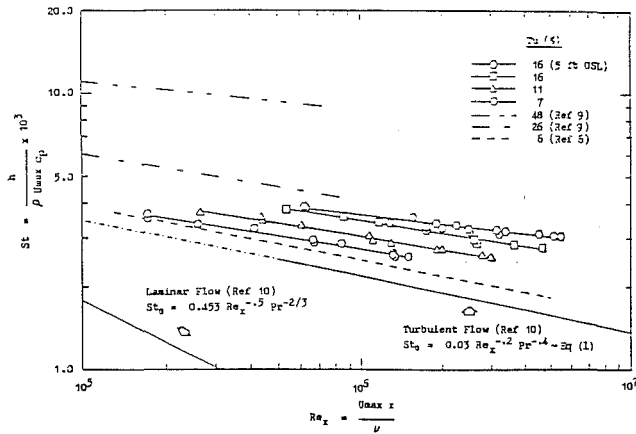


Fig. 6 The effects of high free-stream turbulence on heat transfer

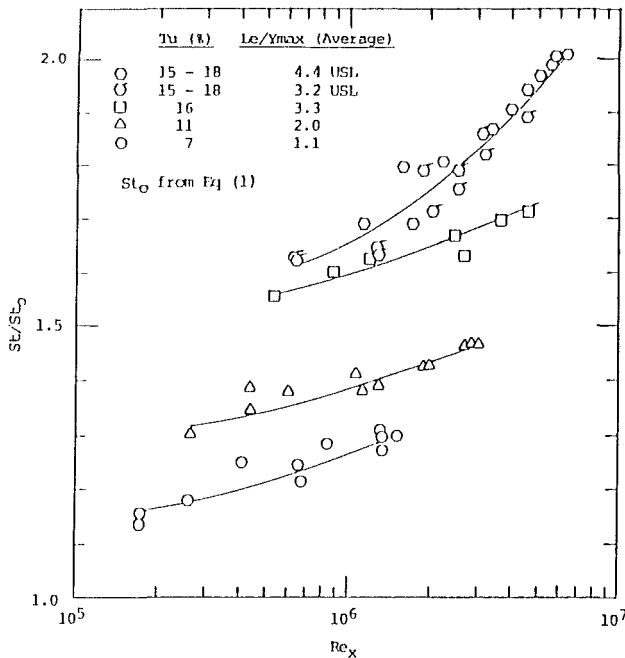


Fig. 7 The increase in heat transfer as a function of Tu and Re_x

indication of a decrease in Stanton number even with Re_x less than 1.5×10^5 . The data followed a different slope than the zero FST correlation and this might be caused by the decrease of velocity with distance down the plate. By combining the empirical correlations from each Tu level the data in the normal configuration can be represented within 5 percent as

$$St = 0.0141 \exp^{0.0379 Tu} Re_x^{-0.1413} \exp^{0.005892 Tu} Pr^{-0.4} \quad (8)$$

Unheated Starting Length Configuration. The unheated starting length was used to increase the range of Reynolds numbers at the highest turbulence intensity. Also, since the Tu was relatively constant beyond an x/D of 10, the effects of L_e changes on the heat transfer rate might be observed by comparing the results between the USL data at x/D positions of 9.813 and 17.438. However, the results require interpretation in that the effects of the unheated starting length alone will theoretically generate approximately 6 percent difference in Stanton number between these two positions. This was calculated based on the zero Tu intensity, constant free-stream velocity step heat flux integral solutions from Baxter and Reynolds (1958). Accounting for the geometry of the plate the zero turbulence intensity step heat flux solution for x/D of 9.813 (USL) is

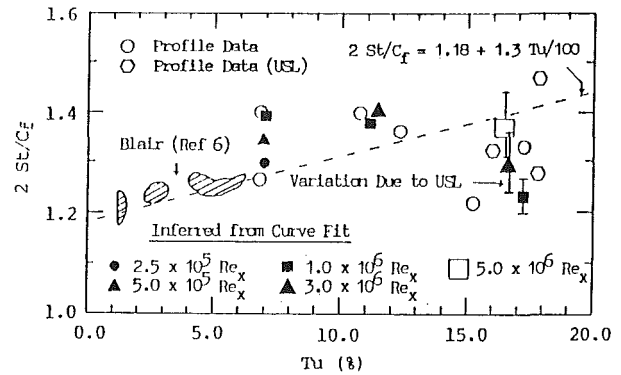


Fig. 8 Reynolds analogy factor

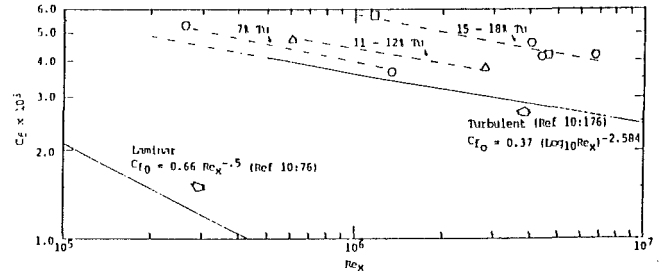


Fig. 9 The effects of high free-stream turbulence on friction coefficient

$$St_0 = 0.03346 Re_x^{-0.2} Pr^{-0.4} \quad (9)$$

This solution predicts Stanton numbers approximately 8 percent higher than the constant heat flux solution of equation (1). The zero Tu step heat flux solution for x/D of 17.438 (USL) is

$$St_0 = 0.03156 Re_x^{-0.2} Pr^{-0.4} \quad (10)$$

and predicts about 2 percent difference from equation (1). However, comparison of the results for the two positions indicated that the Stanton numbers were approximately the same magnitude at the same Reynolds number within the range of experimental error (Fig. 7). Comparison of the data indicated that the USL configuration caused a 10 percent increase in Stanton number at high Re_x compared to the normal configuration at the same turbulence intensity, but this reduced to only 1–2 percent at the lowest Re_x tested. The difference between the USL and normal configuration would appear to vanish at about an Re_x of 3×10^5 . These results were inconsistent with the trends predicted by Baxter and Reynolds (1958). The high turbulence combined with the variation of U_{max} down the plate apparently caused the unheated starting length to influence the rate of heat transfer differently as a function of Re_x . An empirical equation that describes the data in the USL configuration within 5 percent is

$$St = 0.0125 Re_x^{-0.1003} Pr^{-0.4} \quad (11)$$

Reynolds Analogy Factor. The Reynolds analogy factor ($2St/C_f$) is plotted in Fig. 8. The friction factor (C_f) was inferred from a force fit of the velocity profiles to the law of the wall and is presented in Fig. 9. The friction factor appeared to increase in a manner similar to the Stanton number in the presence of free-stream turbulence; however, more profile or measured data are required to confirm the trends. The scatter in the data in Fig. 8 appeared large when plotted in this format. However, upon closer examination, there was an Re_x effect. If turbulence intensity was held constant, the difference in slope between the St versus Re_x and C_f versus Re_x curves forced the Reynolds analogy factor to become larger at higher Reynolds numbers. In addition, the USL configuration resulted

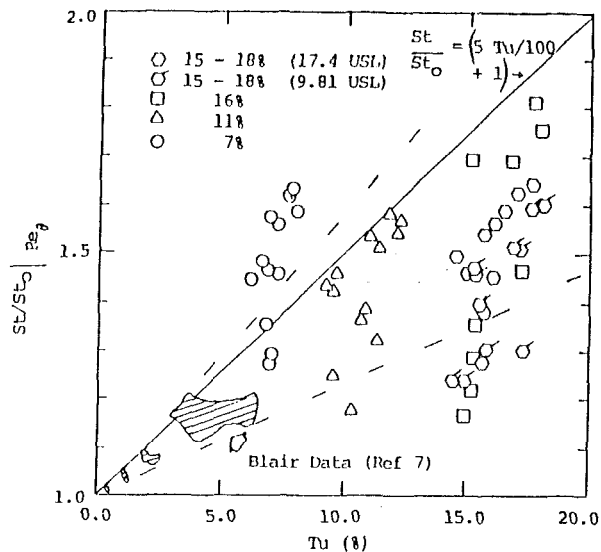


Fig. 10 Heat transfer data compared to Simonich correlation

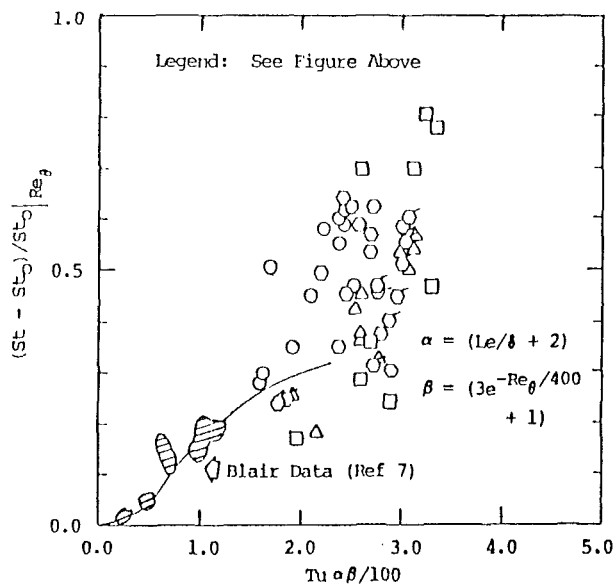


Fig. 11 Heat transfer data compared to Blair/Hancock correlation

in a higher factor compared to continuous heating at the same T_u . The Reynolds analogy factor was in the same range as obtained by Blair and Werle (1980) at low T_u and appeared to increase at a slope of 1.3 and parallel to the correlation up to about 12 percent T_u . Between 12 and 15 percent T_u the factor was constant and above 15 percent it appeared to decrease. The significance of the Reynolds analogy factor was that it provided an indication of the average turbulent Prandtl number in the wall jet boundary layer ($Pr_t^{-1} = 2St/C_f$). The data indicated that as T_u increased the turbulent Prandtl number (Pr_t) decreased further below one. Since Pr_t varies through the boundary layer (increasing near the wall) and is significant in understanding the physics of the heat transfer, Pr_t profile measurements should be obtained at numerous x/D and z/D locations. The Reynolds analogy results should be viewed with caution as the factor is based on approximate calculations of C_f in this study. Combined skin friction and heat transfer measurements should also be performed to corroborate the data.

Comparison With Previous Results. The data obtained in this study were compared to the lower turbulence results of Blair and Werle (1980), Blair (1983), and Simonich and Brad-

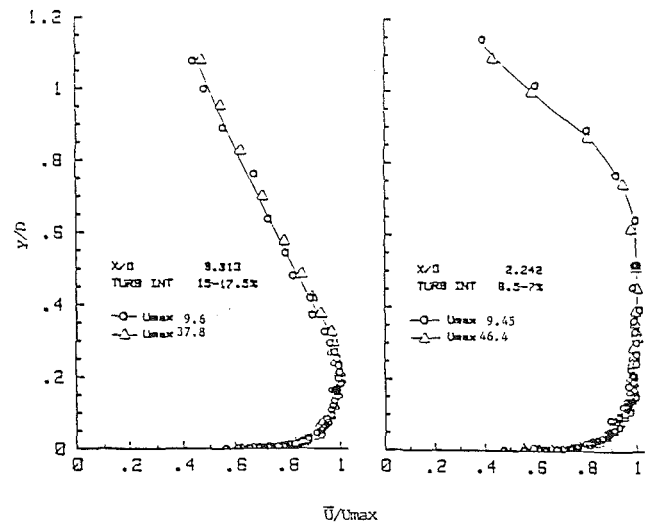


Fig. 12 Similarity of the velocity profiles at various x/D

shaw (1978). The one-parameter correlation of Simonich and Bradshaw (Fig. 10) resulted in considerable scatter. When plotted against the correlation of Blair (Fig. 11), which introduced an effect for momentum thickness Reynolds number, the scatter was only slightly reduced. The one and two-parameter correlations did little to aid in the prediction of heat transfer at the higher levels of free-stream turbulence. It must be noted, however, that the comparison with Blair's correlation was based on integral boundary layer parameters, which may not be totally applicable for the wall jet due to the absence of a constant velocity free-stream above the wall shear layer. In addition, the basis of St/St_0 in both figures was the zero free-stream turbulence correlation, equation (1), which does not account for velocity changes in the free stream. In essence the present known combinations of influencing parameters and correlations developed from conventional boundary layer flow are not robust descriptors in the presence of high free-stream turbulence generated by jets.

Effects of Free Stream Turbulence on Profile Characteristics. Mean velocity, temperature, and turbulence intensity profiles as a function of y/D were obtained at three locations in the standard plate configuration and at two locations with the 1.5-m unheated starting length attached.

Velocity Profiles. Dimensionless mean velocity profiles are presented in Fig. 12. The three different regions of wall jet development as depicted in Launder and Rodi (1981), MacArthur (1986), and Chandrasekhara and Bandyopdhyay (1975) were discernible during the test. The potential core region, indicated by a constant velocity region between the wake and boundary layer region, was clearly present at an x/D of 2.2 and appeared to have almost disappeared by an x/D of 5. the transition or changeover region where the jet starts to lose the structure of the nozzle flow was present at an x/D of 10. At an x/D of 17.4 the slope of the region above Y_{max} was not as sharp and Y_{max} was increasing with distance—an indication that the fully developed region had started. The region development was similar to that found in other wall jets (MacArthur, 1986), except that the transition to the changeover region occurred 1 to 2 jet diameters earlier. As shown in Fig. 12, the dimensionless velocity profiles for each different U_{max} collapsed into one characteristic curve, which was unique at each x/D location. Similarity (the same characteristic curves between x/D locations) was not achieved in the range of x/D tested. However, similarity does occur in the fully developed region (MacArthur, 1986).

The velocity profiles were converted to inner coordinates

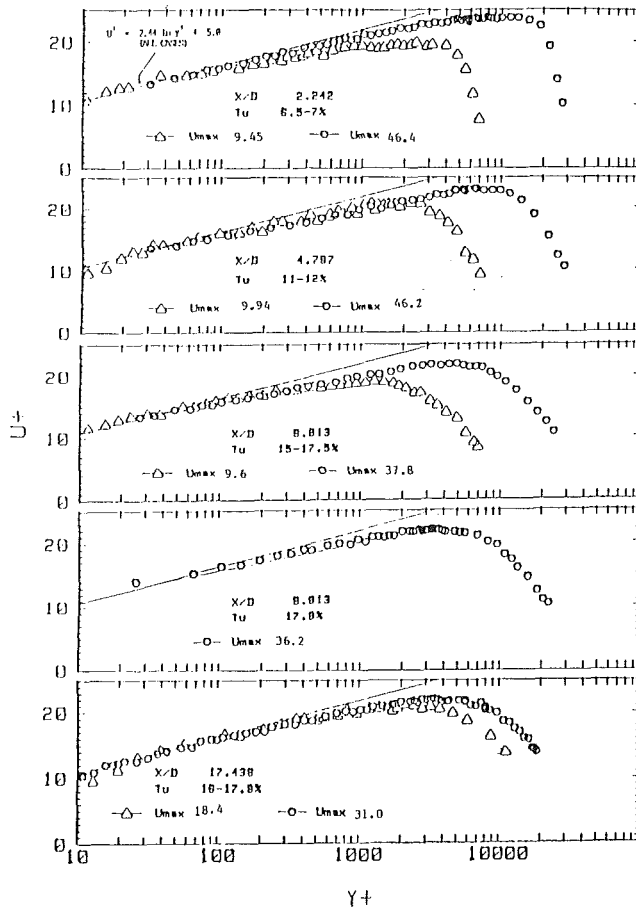


Fig. 13 Comparison of mean velocity profiles in law of the wall coordinates

(U^+ versus Y^+) and presented in Fig. 13. A force fit of the data to equation (4) was accomplished at approximately $Y^+ = 40$ to calculate skin friction coefficients. The wall jet boundary layer exhibited two characteristics that distinguished it from the flat plate boundary layer. The first, and most obvious, was the reversal in the wake region caused by the decrease of velocity above the boundary layer. The second was a tendency of the log-law region to decrease in slope with increasing turbulence intensity and distance down the plate. This also occurred with the data of Han (1985). The profiles at 7 percent turbulence intensity showed that they followed the law of the wall out to about $600 Y^+$. These results were similar to the data of Blair and Werle (1980) at 6.4 percent turbulence intensity. At an x/D of 4.8, and farther down the plate where the turbulence intensity was at least 10 percent, the log-law region was displaced below the law of the wall. This effect has not been observed in conventional flat plate boundary layers at low turbulence levels. The decrease in slope was not fully investigated during this study, and more data are needed to separate the influence of turbulence intensity and associated shear stress from the three-dimensional effects downstream of the core region.

Temperature Profiles. Dimensionless temperature profiles are presented in Fig. 14. The variation in T_u did not appear to affect the mean profile shape significantly. The major feature was the influence of the jet temperature. If the exit jet temperature was different from ambient, the profile above the boundary layer was displaced from the vertical.

$$\text{If } T_{wj} > T_a \text{ then } (T_p - \bar{T}) / (T_p - T_a) < 1.0 \quad (12)$$

$$\text{If } T_{wj} < T_a \text{ then } (T_p - \bar{T}) / (T_p - T_a) > 1.0 \quad (13)$$

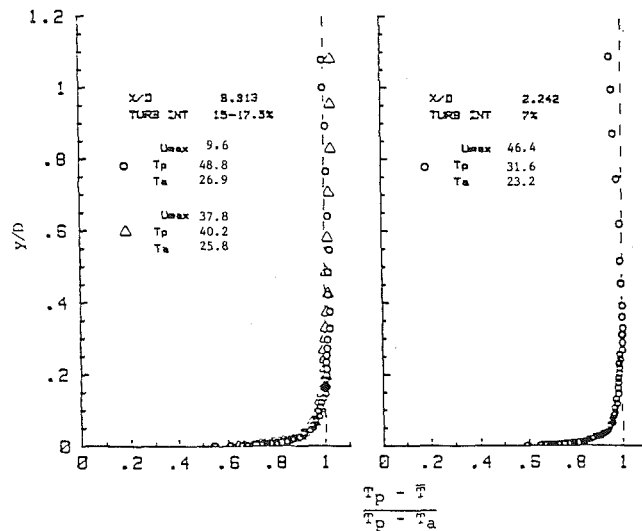


Fig. 14 Temperature profiles at various x/D

Temperature differences between the jet and ambient air were avoided to reduce heat transfer between different regions throughout the profile and minimize the variation of temperature at Y_{\max} with x distance. As in the velocity profiles, the dimensionless temperature profiles also collapsed, approximately, into one characteristic curve at each x/D location. The temperature profiles were not similar between x/D locations, but the difference in profile shape was not large.

The law of the wall coordinates were calculated for the temperature profiles by using the shear velocity generated from the corresponding velocity profile. The results are presented in Fig. 15 and compared to equation (5). Despite the large number of experimental quantities incorporated in Y^+ , the data generally intercepted and followed the law of the wall in the same region as the velocity profiles ($Y^+ = 20$ to 100), indicating self-consistency of the shear velocity and friction coefficient calculations. The temperature data and gradient fell below the law of the wall in a manner similar to the velocity profiles, and more profile data are needed to determine the influence of turbulence intensity, exit jet temperature, and three-dimensional effects.

Turbulence Intensity Profiles. The turbulence intensity profiles are plotted in Fig. 16. The profile shape was primarily a function of distance from the nozzle. Close to the nozzle ($x/D = 2.24$) the distribution was uniform at 6 to 7 percent turbulence intensity in the core flow. Below the core flow in the wall region, T_u increased and then sharply decreased close to the plate. In the region above the core T_u increased up to approximately one nozzle diameter. Above $y/D = 1$ the T_u reversed again and then began to decrease rapidly. In the boundary layer region the same effects are noted at each location. However, the core region behaved in a manner similar to that of the velocity profiles, so that by an x/D of 10, the distribution of constant turbulence intensity had completely disappeared. At an x/D of 17.4 the distribution of turbulence intensity was virtually constant throughout the y direction except close to the wall. The turbulence intensity profiles at each location appeared to be slightly affected by the nozzle velocity, varying about 2 percent. In the boundary layer region the distance from the wall (L_c) where sharp changes in T_u occurred was plotted for each profile (Fig. 17)

$$L_c = \frac{\partial[(\bar{U}^2)^{0.5}/U_{\max}]|_{y \rightarrow \infty}}{\partial y} \quad (14)$$

The characteristic distance L_c appeared to be a function of both position and velocity with L_c increasing with x/D and

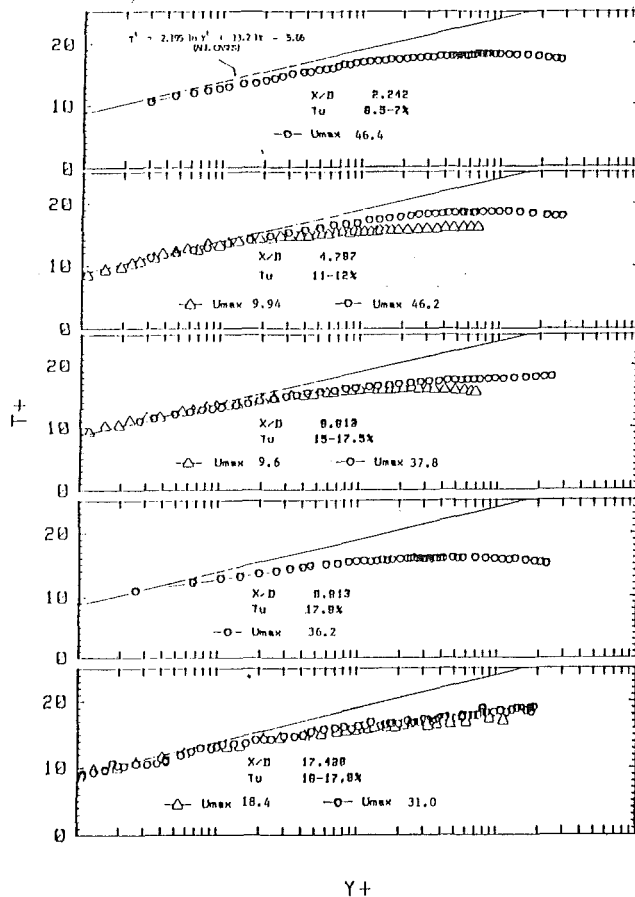


Fig. 15 Comparison of mean temperature profiles in law of the wall coordinates

U_{max} . The character of the wall jet turbulence intensity profiles compared well to those obtained by Han (1985). In the boundary layer the shape of the profile near the wall was similar to that of a conventional flat plate boundary layer except that the intensity was much higher near the wall in the presence of free-stream turbulence (White, 1974).

Conclusions

The wall jet is useful in generating turbulence levels of 5 to 20 percent. The wall jet heat transfer results were found to parallel those of wind tunnel grid-generated data even though there is a lack of complete simulation of the entire boundary layer. The near wall region demonstrates a log-law region that is below that of the flat plate for both velocity and temperature.

The high turbulence levels eliminated transition effectively for all conditions tested. Increasing the level of turbulence intensity T_u resulted in substantial increases in the Stanton number from the two-dimensional flat plate fully turbulent intensity correlation.

The addition of the unheated starting length caused an increase in Stanton number compared to the normal plate configuration, with the effect somewhat magnified at the higher Reynolds numbers and reduced at the lower Reynolds numbers tested. The 1.5 m unheated starting length data were required for a subsequent film cooling data base. The unheated length, for these tests, was marginal and it created an additional influencing variable on the heat transfer.

The Reynolds analogy factor ($2St/C_f$) increased with turbulence intensity up to a turbulence intensity of 12 percent. At higher intensity levels the factors leveled off and then decreased. The Reynolds analogy factor varied slightly with Reynolds number Re_x and plate configuration. The friction

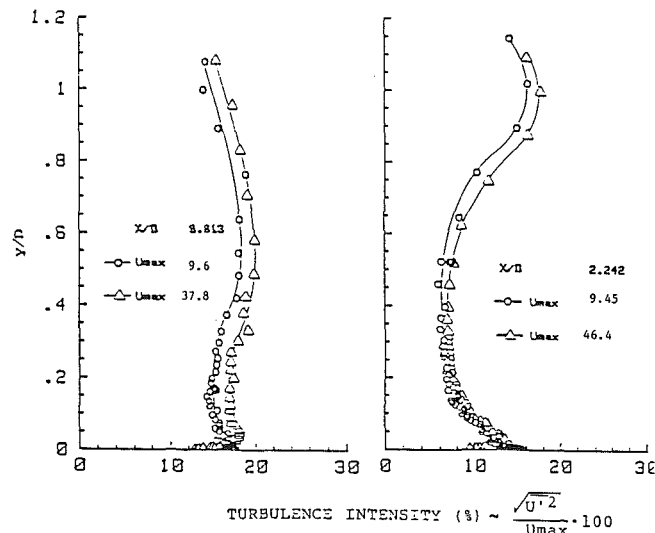


Fig. 16 Turbulence intensity profiles at various x/D

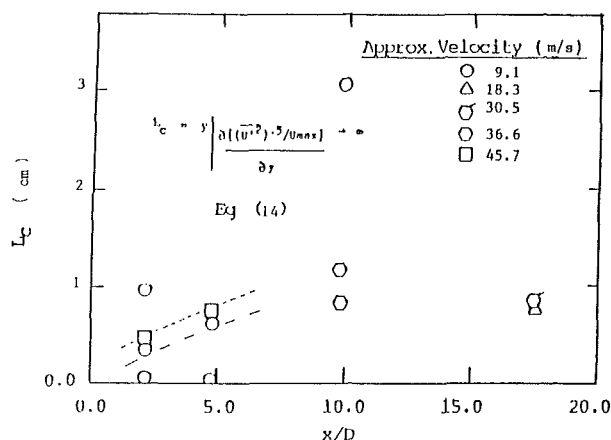


Fig. 17 Variation of L_c as a function of x/D and U_{max}

factor, inferred from log-law plots, increased in a similar manner to the Stanton number with increased turbulence intensity.

The effect of integral length scale could not be concluded from this study. The one and two-parameter correlations recommended from previous wind tunnel studies failed to predict the heat transfer rate for the wall jet adequately. A larger independent variation in length scale at the high turbulence conditions is required to ascertain its role.

References

- Baxter, D. C., and Reynolds, W. C., 1958, "Fundamental Solutions for Heat Transfer From Nonisothermal Flat Plates," *Journal of the Aeronautical Sciences*, Vol. 25, pp. 403-404.
- Blair, M.F., 1983, "Influence of Free-Stream Turbulence on Turbulent Boundary Layer Heat Transfer and Mean Profile Development, Parts I and II," *ASME Journal of Heat Transfer*, Vol. 105, pp. 33-47.
- Blair, M. F., and Werle, M. J., 1980, "The Influence of Free-Stream Turbulence on the Zero Pressure Gradient Fully Turbulent Boundary Layer," (R80-914388-12), Contract No. F49620-78-C-0064. UTCRC, East Hartford, CT.
- Chandrasekhara Swamy, N. V., and Bandyopadhyay, P., 1975, "Mean and Turbulence Characteristics of Three-Dimensional Wall Jets," *Journal of Fluid Mechanics*, Vol. 71, pp. 541-562.
- Han, J. C., 1985, "Effect of High Free-Stream Turbulence From a Free Jet on Flat Plate Turbulent Boundary Layer Flow and Heat Transfer," 1985 USAF-UES Summer Faculty Research Program, Contract No. F49620-85-C-0013.
- Hancock, P. D., 1980, "Effect of Free-Stream Turbulence in Turbulent Boundary Layers," Ph.D. Thesis, Imperial College, London University, London, United Kingdom.
- Hinze, J. O., 1959, *Turbulence*, McGraw-Hill, New York, pp. 41, 202.
- Junkhan, G. H., and Serovy, G. K., "Effects of Free-Stream Turbulence and Pressure Gradient on Flat-Plate Boundary-Layer Velocity Profiles and on Heat Transfer," *ASME Journal of Heat Transfer*, Vol. 89, pp. 169-176.

- Kays, W. M., and Crawford, M. E., 1980, *Convective Heat and Mass Transfer*, 2nd ed., McGraw-Hill, New York, pp. 76, 172, 176, 211-217.
- Kestin, J., 1966, "The Effect of Free Stream Turbulence on Heat Transfer Rates," *Advances in Heat Transfer*, Academic Press, New York, pp. 21-32.
- Launder, B. E., and Rodi, W., 1981, "The Turbulent Wall Jet," *Progress in Aerospace Sciences*, P. J. Finley, ed., Pergamon Press, New York, Vol. 19, pp. 81-128.
- MacArthur, C. D., 1986, "Fluid Dynamics and Heat Transfer of the Circular Tangential Wall Jet," Ph.D. Dissertation, University of Dayton, Dayton, OH.
- Moffat, R., and Maciejewski, P. K., 1985, "Heat Transfer With Very High Free-Stream Turbulence," NASA Grant NAG3-522, *Proceedings of the 1985 Turbine Engine Hot Section Technology Conference* (NASA Conference Publication 2405), pp. 203-215.
- Schlichting, H., 1979, *Boundary Layer Theory*, 7th ed., McGraw-Hill, New York, pp. 586-598, 638, 751.
- Siegel, R., and Howell, J.R., 1981, *Thermal Radiation Heat Transfer*, 2nd ed., McGraw-Hill, New York, p. 241.
- Simonich, J. C., and Bradshaw, P., 1978, "Effect of Free-Stream Turbulence on Heat Transfer Through a Turbulent Boundary Layer," *ASME Journal of Heat Transfer*, Vol. 100, pp. 671-677.
- White, F. M., 1974, *Viscous Fluid Flow*, McGraw-Hill, New York, pp. 493-500, 559-573.

The Effects of Turbulence and Stator/Rotor Interactions on Turbine Heat Transfer: Part I— Design Operating Conditions

M. F. Blair

Senior Research Engineer.
Mem. ASME

R. P. Dring

Manager, Gas Turbine Technology.
Mem. ASME

H. D. Joslyn

Research Engineer.

United Technologies Research Center,
East Hartford, CT 06108

A combined experimental and analytical program was conducted to examine the effects of inlet turbulence, stator-rotor axial spacing, and relative circumferential spacing of first and second stators on turbine airfoil heat transfer. The experimental portion of the study was conducted in a large-scale (approximately 5× engine), ambient temperature, stage-and-a-half rotating turbine model. The data indicate that while turbine inlet turbulence can have a very strong impact on the first stator heat transfer, its impact in downstream rows is minimal. The effects on heat transfer produced by relatively large changes in stator/rotor spacing or by changing the relative row-to-row circumferential positions of stators were very small. Analytical results consist of airfoil heat transfer distributions computed with a finite-difference boundary layer code. Data obtained in this same model for various Reynolds numbers and rotor incidence angles are presented in a companion paper (Part II).

Introduction

The accurate prediction of gas turbine airfoil convective heat load distributions is recognized throughout the industry to be an exceedingly difficult yet important problem. A wide variety of factors are known to contribute to the complexity of airfoil passage flows and heat transfer, e.g., high levels of turbulence and unsteadiness, extreme accelerations and decelerations in the boundary layers, velocities ranging from low subsonic to supersonic, strong secondary flows produced by the typically high-turning, low-aspect-ratio airfoils, nonuniform time-mean total pressure and temperature distributions, strong surface curvature, film coolant/boundary layer interactions, rotational effects, airfoil row interactions (rotor/stator and stator/stator), local flow separations, and shock-boundary layer interactions. The difficulties of incorporating this formidable list of effects into design systems have been compounded by an ever-widening gap between turbine inlet flow temperatures and allowable airfoil metal temperatures.

The gas turbine community has expended a great deal of effort to develop analytical tools for airfoil boundary layer computation, and in particular, for heat transfer predictions. In order of increasing mathematical complexity these tools include: (1) correlations corrected for design-specific velocity distributions, curvature, turbulence, etc., (2) finite-difference and integral boundary layer computation schemes using velocity distributions computed from airfoil row potential flow codes, and finally (3) three-dimensional Navier-Stokes flow

field solutions. A variety of empirically adjusted analytical turbulence and transition models have been incorporated into these computation schemes.

Instrumentation and testing techniques are not currently available for the direct documentation of either the surface heat transfer distributions or the unsteady velocity and temperature fields in the extremely hostile environment of operating gas turbines. For this reason the assessment of the relative merits of the predictive techniques has relied on comparisons with experimental data gathered in cascades and turbine-simulation models. Each of these experimental approaches has been designed to examine the isolated impact on the heat transfer of certain specific effects. Excellent reviews of the best available existing published data along with comparisons to the state-of-the-art predictive schemes are given by Han et al. (1982), Hylton et al. (1983), and Rae et al. (1986).

As might be expected for any collection of experiments covering such a large number of complex variables, there are numerous apparent discrepancies between the various data sets. Because different experimental techniques were employed by the various investigators and since the thoroughness of the flow field documentation varied widely, there presently exists considerable uncertainty as to the role and importance of some of the factors believed to affect turbine heat transfer. For example, the data of Lokay and Trushin (1970) indicate that rotation may strongly increase airfoil heat transfer levels raising a question as to the validity of using cascade data for the design of a rotating airfoil row. Other examples are the uncertainties regarding the roles of periodic unsteadiness (due to rotor and stator wake chopping and potential flow field interactions) and broad-band turbulence on airfoil heat transfer.

Contributed by the International Gas Turbine Institute and presented at the 33rd International Gas Turbine and Aeroengine Congress and Exhibition, Amsterdam, The Netherlands, June 5-9, 1988. Manuscript received by the International Gas Turbine Institute September 15, 1987. Paper No 88-GT-125.

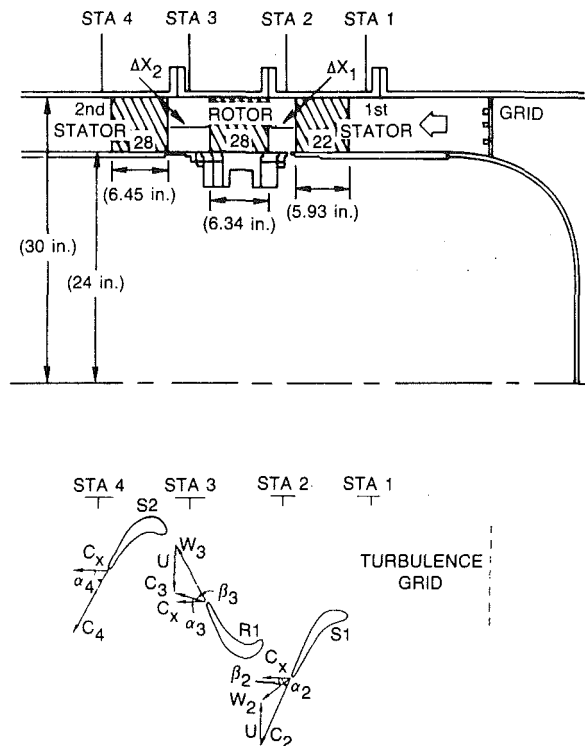


Fig. 1 Large-scale rotating rig geometry and velocity triangles

The present experiment was specifically designed to examine the combined effects of broad-band (grid generated) turbulence and airfoil interactions (periodic unsteadiness) on a rotating turbine model. These tests were conducted in a low-speed, large-scale turbine model making possible the accurate documentation of the mean and fluctuating flow fields at both the inlet of the turbine and downstream of each airfoil row. Data were obtained for three airfoil rows, a first stator, first rotor, and a second stator. The present paper (Part I) contains data obtained at the turbine model design rotor incidence for various combinations of low or high inlet turbulence intensity, first-stator/rotor axial spacing, and relative circumferential position of the first and second stators. Part II of the paper presents heat transfer data obtained for various combinations of Reynolds number and inlet turbulence and for a very wide range of rotor incidence.

A comprehensive report of the experiment is given by Dring et al. (1986a). This report contains detailed descriptions of the experimental apparatus, instrumentation, and techniques employed. In addition Dring et al. (1986b, 1986c, 1986d) present the tabulated heat transfer and aerodynamic data.

Experimental Apparatus

1 Turbine Model. All experimental work for this program

Nomenclature

B_x = airfoil axial chord
 C = absolute velocity
 CP = pressure coefficient
 C_x = axial flow velocity
 f = frequency, Hz
 L = fraction of a stator pitch
 P = static pressure
 PT = total pressure
 Re = Reynolds number based on axial chord and exit flow conditions

Re_o = Reynolds number based on momentum thickness
 S = surface arc length
 Tu = turbulence intensity
 U = rotor velocity at midspan
 U = mean streamwise velocity
 $U'^2(f)$ = velocity fluctuations (squared) per Hertz
 W = relative velocity
 X = axial distance from the stator 1 leading edge
 α = absolute yaw flow angle

β = relative yaw flow angle
 ΔX_1 = axial spacing between stator 1-rotor
 ΔX_2 = axial spacing between rotor-stator 2
 Λ_f = longitudinal integral length scale

Subscripts

1 = stator 1 inlet station
 2 = stator 1 exit station
 3 = rotor 2 exit station
 4 = stator 2 exit station

Table 1 Geometries tested

TEST	NOMINAL S1/R1 AXIAL GAP	ΔX_1		ΔX_2	
		(in.)	(m)	(in.)	(m)
SINGLE STAGE HEAT TRANSFER	15%	0.92	0.023		
SINGLE STAGE HEAT TRANSFER	65%	3.99	0.101		
1 1/2 STAGE HEAT TRANSFER	65%	3.99	0.101	3.36	0.085
1 1/2 STAGE AERODYNAMICS	50%	3.07	0.078	4.31	0.110

Table 2 Airfoil midspan geometry and nominal Reynolds numbers

AIRFOIL	STATOR 1	ROTOR	STATOR 2
PITCH/Bx	1.30	0.96	0.94
SPAN/Bx	1.01	0.95	0.93
CAMBER LINE ANGLES			
LEADING EDGE	90.0°	42.2°	45.7°
TRAILING EDGE	21.4°	26.0°	25.0°
$Re_{nom} \times 10^{-5}$	6.4	5.8	5.9

was conducted in the United Technologies Research Center Large-Scale Rotating Rig (LSRR). This test facility was designed for conducting detailed experimental investigations of the flow around turbine and compressor blading. For the present program the turbine test section (Fig. 1) was assembled in both single-stage (stator 1/rotor) and 1 1/2 stage (stator 1/rotor/stator 2) configurations with various axial spaces between adjacent rows. Table 1 lists the various geometric combinations for which data were obtained. The turbine model simulates a relatively heavily loaded machine with a hub/tip radius ratio of 0.8. The midspan geometry and nominal Reynolds numbers of the three airfoils are listed in Table 2. When operating at design conditions the turbine has a flow coefficient (C_x/U_m) of 0.78, a rotor relative inlet flow angle at midspan of 40 deg, a stage loading coefficient of 2.8, and 34 percent static pressure reaction. The axial spacing between the first stator and the rotor was varied from 15 to 65 percent B_x (typical engine spacing is 25 to 50 percent B_x). In the stage and a half configuration the axial spacing between the rotor and the second stator was 63 percent B_x . The rotor tip clearance was 0.090 in. or 1.5 percent span, which is typical of engine design.

2 Turbulence Generating Grid. For selected test cases, high levels of broad-band turbulence were generated upstream of the turbine inlet (Fig. 1). The turbulence generator, designed using the correlations of Baines and Peterson (1951), consisted of a nearly square array biplane lattice of three rings spaced uniformly in the radial direction with 80 evenly spaced radial bars. Both the rings and radial bars were of 1/2 in. square cross section. The mean spacing of the bar was 2.1 in. radially and 4.5 deg (2.1 in. at midannulus) circumferentially. The grid was located 15 in. upstream of the first stator leading edge.

3 Airfoil Heat Transfer Measurements. Heat transfer measurements were obtained in this study using extremely low

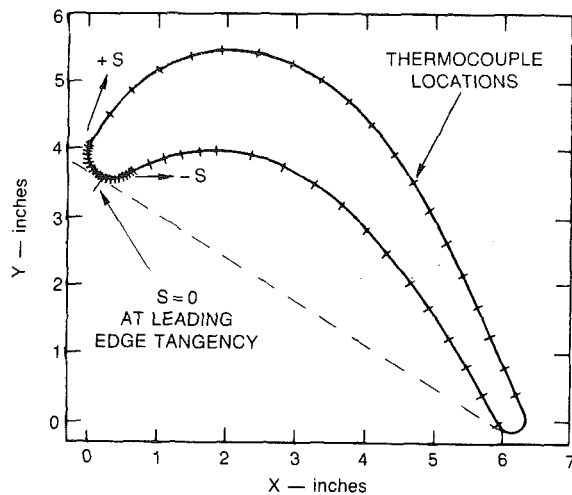


Fig. 2 Instrumentation diagram for the first-stage rotor

conductivity rigid urethane foam castings of the airfoils. A uniform heat flux was generated on the surface of each of the foam airfoils using an electrically heated 0.001-in.-thick stainless steel foil strip bonded to the airfoil surface. The foil heater strip on each airfoil was 3.5 in. wide and passed around the entire airfoil surface (see Dring et al., 1986a, for details). Local heat transfer coefficients around the airfoils were determined using miniature thermocouples to measure the temperature difference between the heated metal skin and the free stream. Slight corrections to the uniform-convective-heat-flux condition resulting from surface radiation, heat conduction through the foam, and local variations in strip resistance produced by local metal temperature differences were included in the data reduction procedures. Standard error analysis techniques (see Graziani et al., 1980) indicate that the final heat transfer coefficients were accurate to within ± 4 percent. The important advantage of using these construction materials and instrumentation techniques is that they permit extremely accurate heat transfer data to be obtained even in regions of strong spatial gradients (e.g., due to a separation bubble). Examples of other applications of these techniques can be found in Blair (1983, 1985).

The thermocouple heat transfer instrumentation on the test airfoils consisted primarily of midspan rows with limited numbers of off-midspan sites for measurement of spanwise gradients. Because of the thermocouple installation techniques it was practical to instrument one surface (suction or pressure) of a given test airfoil and the opposite surface of a "twin" airfoil. Both of the "twin" airfoils, however, were densely instrumented near their leading edges in order that the extreme variations in that region could be accurately documented. A sample airfoil instrumentation pattern is presented in Fig. 2. This figure shows a composite of the instrumentation installed in the two "twin" rotor airfoils and indicates the extreme density of the thermocouple arrays provided in the leading edge regions. There was an average of 96 thermocouple sites around each of the three airfoils.

The locations of all heat transfer data presented in this report are given in terms of a distance along the respective airfoil surface(s) as measured from a reference ($s = 0$) location. To achieve high experimental location accuracy the $s = 0$ location for each airfoil was determined using a geometric criterion instead of the location of the aerodynamic stagnation point. This geometric "zero" was defined as the point on the leading edge, at midspan, tangent to a straight line, which was also tangent to the trailing edge radius. This definition is illustrated for the rotor airfoil in Fig. 2.

The thermocouple instrumentation system used for this study

consisted of a low-noise, multiwiper Wendon slip ring, Kaye Instruments Uniform Temperature Reference Blocks, a Kaye Instruments Ice Point Reference, and a Hewlett-Packard 3497A/3498A data acquisition unit. Reduction of the data was accomplished using an LSI 11/03 minicomputer.

4 Flowpath Steady Aerodynamic Instrumentation. Airfoil midspan pressure distributions and hub and casing flow path static pressure distributions were obtained for all three airfoil rows with and without the turbulence generating grid installed. In addition, surveys of the inlet flow total pressure were obtained 23 percent B_x upstream of the first stator leading edge. These total pressure surveys, together with hub and outer casing flowpath static pressures measured upstream of the first stator leading edge plane, provided the mass flow for the turbine model and hence the turbine flow coefficient C_x/U_m .

Five-hole, yaw-nulled pneumatic probe traverse measurements were also obtained downstream of each of the three airfoil rows. These measurements include midspan circumferential traverses of the total and static pressures and the flow yaw and pitch angles. The axial gap separating the first-stator rotor and stator during this testing was 50 percent of the rotor axial chord. These measurements define the inlet and exit aerodynamic conditions for each airfoil row.

5 High-Response Aerodynamic Measurements. Turbulence intensity, length scale, and spectral distribution measurements of the streamwise component of the fluctuating velocity were obtained both at and just upstream of the first stator leading edge (Stator 1, Fig. 1). Data were obtained over a 4 pitchwise by 12 spanwise array 23 percent chord upstream of the turbine first stator leading edge and for a single spanwise survey at 50 percent pitch at the first stator leading edge plane. All of these measurements were obtained using a TSI Model 1210-20 cylindrical hot film probe, a TSI Model 1050 Constant Temperature Anemometer, and a TSI Model 1052 4th order polynomial linearizer. Autocorrelations of the linearized hot-film signals were generated using a Saicor Model SAI-42 Correlator and Probability Analyzer. Spectral distributions were determined using a Spectral Dynamics Model SD 340 MICRO FFT narrow band analyzer.

Interrow velocity traverse measurements were acquired at midspan downstream of each airfoil row. These traverses were obtained at Stator 2, 3, and 4 in Fig. 1 at the same axial locations at which the five-hole pneumatic probe traverse data were acquired. These measurements were made with a (TSI) Model 1211-20 radially oriented temperature compensated hot-film probe. The interrow data were acquired using a high-speed, phase-locked, multichannel analog/digital system. At each stationary frame circumferential traverse location (typically 60 per traverse), high response data were acquired at 300 rotor positions over three consecutive rotor pitches. One hundred sets of high response (instantaneous) data (300 per revolution for 100 revolutions) were acquired and digitized at each traverse location and recorded on magnetic tape for detailed off-line analysis.

Test Conditions

1 Steady Aerodynamics. The aerodynamic performance of this turbine model has been thoroughly documented in earlier publications (e.g., see Dring et al., 1982). Measurements obtained during the present tests indicated that all parameters were very close to the prior results. As an example the midspan pressure distributions for the first stator, rotor, and second stator are shown in Fig. 3. The measured data are represented by the symbols and the results of a two-dimensional potential flow calculation (Caspar et al., 1980) are given by the curves. The parameters required as input to the calculation and for defining the pressure coefficients (CP) for each airfoil row

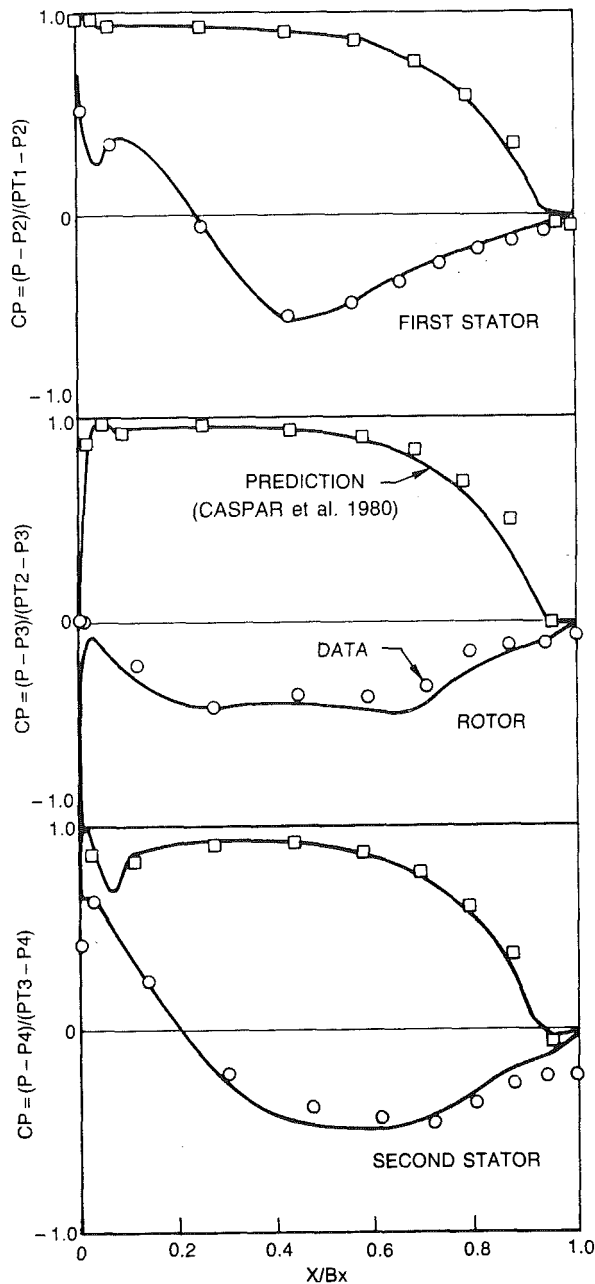


Fig. 3 Airfoil pressure distributions, $Cx/U_m = 0.78$

were: (1) the streamtube contraction and loss estimated from an axisymmetric throughflow calculation, (2) the airfoil inlet total pressure as deduced from the measured airfoil pressure surface static pressure, and (3) the airfoil exit static pressure calculated by assuming a free vortex distribution between the measured hub and casing static pressures. The airfoil inlet and exit flow angles were varied to obtain the best agreement of the calculation with the measured airfoil surface pressure distributions. As seen in Fig. 3, agreement between the two-dimensional potential flow calculation and the measured pressures at midspan is excellent. Surface velocity distributions computed with this potential flow analysis were used as input to the boundary layer calculations presented later in this report.

The flow at midspan on the first stator was well behaved. On the pressure surface, the flow accelerated smoothly from the leading edge to the trailing edge. On the suction surface, there was an overspeed near the leading edge followed by an acceleration to the throat. From the throat, the flow decelerated smoothly to the trailing edge without separating. Flow

Table 3 Airfoil inlet and exit flow angles (from tangential) from the five-hole probe traverse data (5 hp) and as inferred from the potential flow analysis (PFA)

AIRFOIL		STATOR #1	ROTOR	STATOR #2
INLET	PFA	90.0°	41.0°	62.0°
	5HP	—	40.6°	64.0°
EXIT	PFA	22.5°	25.25°	26.0°
	5HP	22.4°	31.7°	23.7°

visualization studies conducted previously on this airfoil showed the flow on both the suction and pressure surfaces to be nearly two-dimensional and free of any regions of local separation.

On the rotor there was a slight overspeed in the flow near the leading edge on both the pressure and suction surfaces. The absence of midspan boundary layer separation on both the pressure and suction surfaces has been demonstrated previously by extensive flow visualization (Dring et al., 1982).

Pressure distributions were obtained on the second stator with a first stator/rotor axial spacing of 50 percent. Overall, the match between the potential flow calculation and the measured results was good except in the region aft of the throat on the suction surface. On the pressure surface there was a very pronounced overspeed in the flow near the leading edge. The free-vortex static pressures calculated at midspan from the measured hub and casing static pressures agreed very well with circumferentially averaged five-hole pneumatic probe results downstream of each airfoil row.

Documentation of the time-mean velocity distributions at the inlet to the turbine model was accomplished using the previously described hot-film anemometer system. The resulting mean velocity distributions were spanwise uniform (over the central 80 percent of the span) for both the grid-out configuration and with the grid-in indicating that the grid blockage was very evenly distributed, radially. At this station ($X/B_x = -0.23$) both the measured data and a potential flow prediction indicate that a ± 10 percent pitchwise variation of the mean flow field was induced by the first stator row. The measured results were in excellent agreement with the potential flow prediction. The potential flow prediction also indicated that this upstream influence did not extend very far upstream of the stator leading edge station. For example, at $X/B_x = -0.8$ the pitchwise variation in mean velocity was predicted to be less than ± 1 percent.

A comparison of the inlet and exit angles determined from the five-hole probe traverse with those inferred from the potential flow calculations is shown in Table 3. Overall, the flow yaw angles deduced from the two-dimensional potential flow calculations are in good agreement with the circumferentially averaged traverse measurements. The exception occurs at the rotor exit, where the yaw angle obtained from the traverse is nearly 6 deg greater than that deduced from the potential flow calculation. This underturning indicated by the traverse data is due to the fact that the traverse was conducted nearly 36 percent of axial chord downstream of the rotor trailing edge plane where the two counterrotating rotor passage vortices do in fact result in an underturning of the flow (Joslyn and Dring, 1983). This three-dimensional flow mechanism appears to have only had a very weak impact on the rotor midspan pressure distribution since it is in such good agreement with the two-dimensional calculation.

2 Unsteady Velocity Measurements

Turbulence Measurements at the Turbine Model Inlet. Surveys of the turbine inlet turbulence intensity, scale, and spectral distributions were obtained at Stator 1 (Fig. 1), at $X/B_x = -0.23$ both with and without the turbulence-generating grid

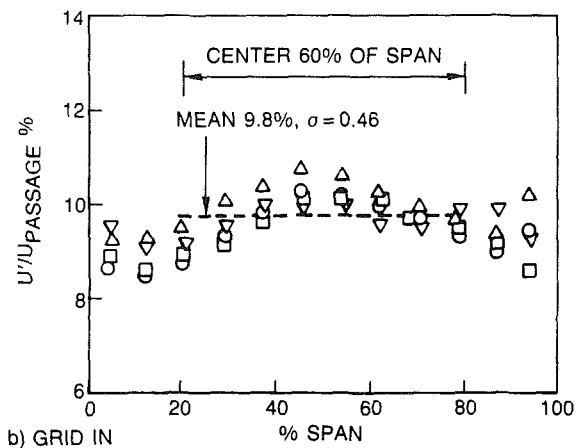
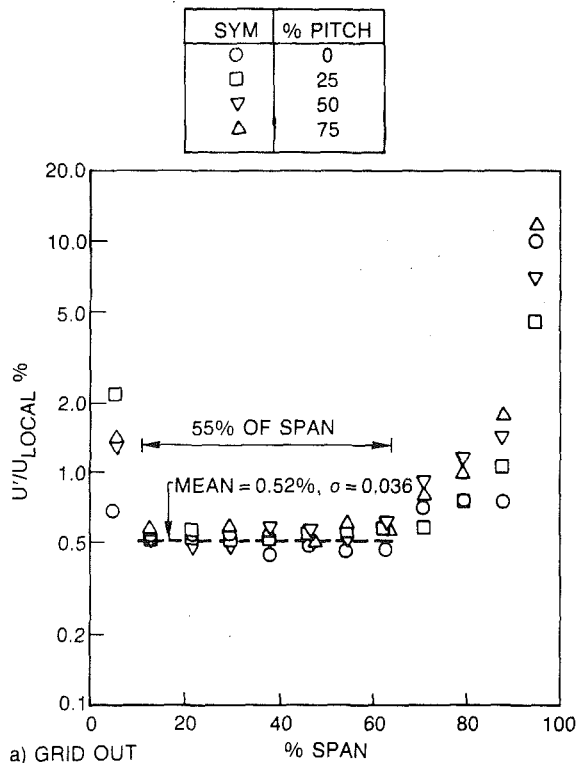


Fig. 4 The rms level of the streamwise component of turbulence at $X/B_x = 0.23$

installed. Spanwise distributions of the turbulence intensity are presented for the grid-out case in Fig. 4(a) and with the grid-in in Fig. 4(b). Note that the velocity fluctuations are normalized by local-mean (± 10 percent pitchwise variation) velocity in Fig. 4(a) and by the mean-passage velocity in Fig. 4(b), the respective denominators being chosen to collapse that group of data best. That the low-turbulence (grid-out) intensities agreed when nondimensionalized on local velocity while the high-turbulence (grid-in) intensities agreed when based on mean passage velocity is a consequence of the radically different wavenumber distributions for the two disturbance spectra. The grid-generated turbulence had practically all its energy in eddies close to the size of the grid bars while most of the energy for the grid-out natural turbulence was in the very low-wavenumber range. This very long-wavelength natural turbulence is an inherent consequence of the fact that the facility draws air from the outside with huge scale ($> 100'$) atmospheric fluctuations. The difference, then, between the grid-in and grid-out conditions is that while the grid-generated turbulent eddies are small relative to the stator pitch the important

ACOUSTIC AND VIBRATION CONTRIBUTIONS TO THE TOTAL UNSTEADY HOT-FILM SIGNAL

SYM	f - Hz	SOURCE	% TOTAL POWER SPECTRUM
A	4.6	FLOOR VIBRATION (HOT FILM VIBRATES)	26
B	29.8	MAIN BLOWER SHAFT FREQUENCY	$3\frac{1}{2}$
C	40.6	ACOUSTIC STANDING WAVE (REFLECTION BETWEEN INLET HONEYCOMB AND TURBINE MODEL NOSEPIECE)—FUNDAMENTAL FREQUENCY	$7\frac{1}{2}$
D	81.2	ACOUSTIC STANDING WAVE — FIRST HARMONIC OF C	$< 1\frac{1}{2}$
E	118	ACOUSTIC STANDING WAVE — FUNDAMENTAL FREQUENCY OF THE CROSS-DUCT MODE OF C (OR POSSIBLY THE SECOND HARMONIC OF C)	$< 1\frac{1}{10}$
F	190.7	TURBINE MODEL ROTOR PASSING FREQUENCY	18
G	328	MAIN BLOWER BLADE PASSING FREQUENCY	$< 1\frac{1}{10}$
H	381.4	FIRST HARMONIC OF F	$1\frac{1}{2}$
I	424	STROUHAL SHEDDING FROM DOWNSTREAM SPARS	$< 1\frac{1}{10}$

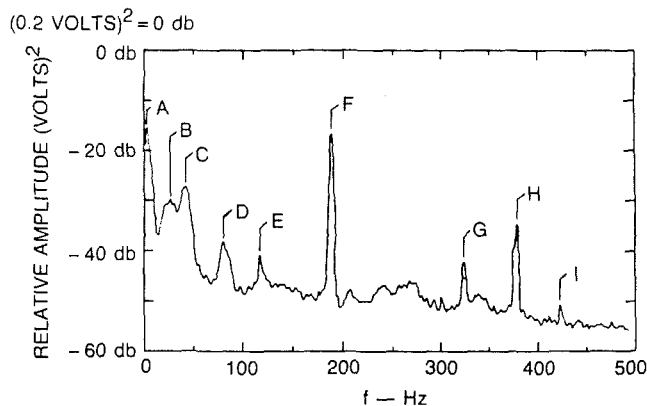


Fig. 5 Spectral distribution of the unfiltered hot-film signal at $X/B_x = -0.23$ for the no-grid configuration

eddy scale of the natural turbulence is immense compared to these same dimensions. The relatively uniform grid-generated velocity fluctuations translate to a uniform turbulence intensity based on a single mean passage velocity. The huge-scale portion of the natural turbulence, on the other hand, appears as an unsteady flow field to the entire stator row. The entire potential flow fluctuates with the unsteadiness and hence turbulence intensities based on local mean velocities collapse to a single distribution.

A comparison of the present grid-in turbulence results with the classic biplane grid study of Baines and Peterson (1951) indicated excellent agreement.

A sample unfiltered spectral distribution (0 to 500 Hz) of the turbulence measured for the low-turbulence (grid-out) case is presented in Fig. 5. This figure shows that the hot-film signal contained a number of narrow bands, labeled A through I, with very strong contributions to the total power spectrum. Identification of the probable sources of each of these narrow bands was accomplished by process of elimination. The turbine model was operated at a number of rotation speeds to determine which spikes were contributed by the model itself and which originated from other sources. All the remaining non-turbine-model bands were identified from known disturbance frequencies (e.g., the main blower blade passing frequency) or as predictable acoustic resonance lengths in the test facility. The specific frequency and probable source of each of the narrow bands is listed in Fig. 5. These "spikes" in the unfiltered signal almost certainly do not result from velocity fluctuations (turbulence) in the flow but are either the result of the probe shaking relative to the flow (A, Fig. 5) or acoustic waves in the flowpath. These acoustic contributions to the signal (approximately 30 percent of the total signal) must be subtracted to determine the turbulence level. It should be mentioned that the possibility was explored that band F was not an acoustic disturbance but was indeed a periodic velocity fluctuation induced upstream of the rotor. This possibility was discounted because a potential flowfield computation indicated that at the

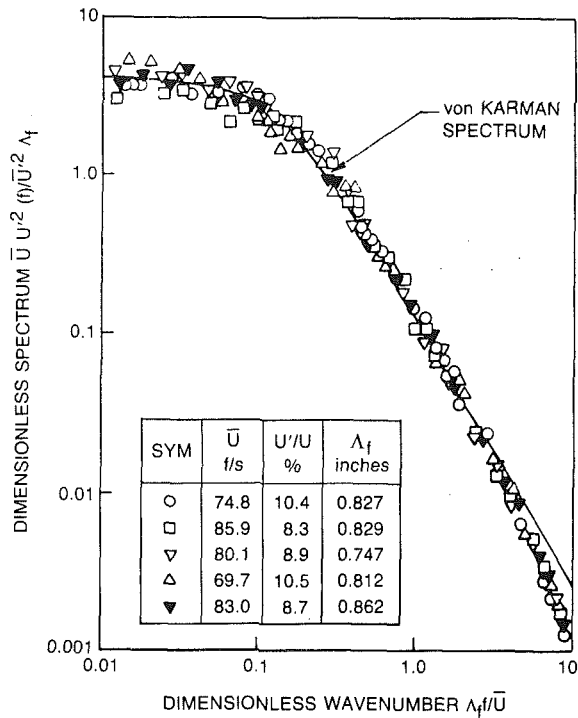


Fig. 6 Power spectral density distributions at various pitch, span, and axial locations with the turbulence grid in

hot-film sensor location the velocity fluctuations produced by the passing rotor blades would have been less than 1/10 percent of the mean velocity. The turbulence intensity data of Fig. 4(a) represent the streamwise component of the turbulence computed by subtracting bands A through I (Fig. 5) from the total local signal. As shown in Fig. 4, in the midspan region the turbulence intensity was slightly greater than 1/2 percent with much higher levels in the endwall boundary layers (as high as 10 percent near the case).

The power spectral density distributions measured at five locations near the first stator leading edge with the grid-in are presented in Fig. 6. Also given in Fig. 6 are the local values of the mean and turbulent velocities and the measured local integral scale. As can be seen from an examination of Fig. 6, the spectral distributions at all five locations were in excellent agreement with the von Karman theoretical spectrum for one-dimensional isotropic turbulence.

Measurements of the local integral scale were obtained at 20 locations. These results indicated that the streamwise integral scale was relatively uniform with a mean value of $\Lambda = 0.80$ in. and a standard deviation for the 20 samples of $\sigma = 0.09$ in.

The conclusions that have been reached from an examination of Figs. 4(b) and 6 are that in the midspan region: (1) The grid-generated turbulence was relatively uniform with a mean value of $U'/U = 9.8$ percent at Plane 1, $X/B_x = -0.23$, (2) the performance of the turbulence-generating grid was in excellent agreement with the performance of similar biplane grids, and (3) the spectral distribution of the grid-generated turbulence was in excellent agreement with the von Karman spectrum, a result typical of fully developed grid-generated turbulence.

Experimental Results

The distributions of heat transfer along the airfoil surfaces are presented as Stanton numbers based upon the exit velocity and density for each airfoil. The Stanton numbers are plotted as a function of surface distance from the reference location

(Fig. 2) nondimensionalized by the axial chord. On each figure the location of the airfoil trailing edge is indicated by TE.

Midspan heat transfer distributions for all three airfoil rows of the model are presented in Fig. 7(a, b, and c). For this case the stator 1/rotor and rotor/stator 2 spacings were 65 percent and 63 percent B_x , respectively. Data are presented for test cases with and without the upstream turbulence grid.

For each of the three figures the experimental data are compared to heat transfer distributions predicted by a two-dimensional finite difference boundary layer code (Carter et al., 1982; Edwards et al., 1981). For Figs. 7(a) and 7(b) predictions for both fully laminar (L) flow and fully turbulent (T) flow are included. The fully turbulent calculations employed the turbulence model of Cebeci-Smith (1979). Only the fully turbulent (T) prediction was presented for Fig. 7(c). Each of these finite-difference boundary layer computations employed the respective computed airfoil velocity distribution of Fig. 3 as input.

For the first stator (Fig. 7(a)) the two-dimensional prediction provided an excellent description of the heat transfer distribution measured with low inlet turbulence (grid-out). For nearly the entire pressure surface and for the upstream half of the suction surface the agreement between the heat transfer data and the laminar prediction was excellent. At $S/B_x \sim 1$ the data indicate that the suction surface boundary layer passed through transition downstream of which the heat transfer slightly exceeded the level predicted for fully turbulent flow. This local post-transition "overshoot" of the heat transfer level was probably a result of the low local boundary layer momentum thickness Reynolds number (Re_θ). The predicted growth rate of the laminar portion of the suction surface boundary layer was considerably lower than the predicted growth rate of the fully turbulent portion. At $S/B_x = 0.9$ the laminar boundary layer calculation predicted $Re_\theta = 490$ while the fully turbulent computation predicted $Re_\theta = 1510$. For this reason at $S/B_x \sim 1$, where the boundary layer actually passed through transition, the test boundary layer Re_θ was considerably smaller than that predicted for fully turbulent flow. The local measured heat transfer then locally exceeded the predicted fully turbulent value. Downstream of the "overshoot" the rapid growth rate of the post-transitional boundary layer brought the measured heat transfer into close agreement with the fully turbulent prediction.

The data of Fig. 7(a) indicate that the impact of the high inlet turbulence (grid-in) on the first stator distribution was dramatic, with significant increases of heat transfer on the leading edge and along both the suction and pressure surfaces. On the suction surface the increased turbulence moved the location of transition well upstream from $S/B_x \approx 1.0$ to $S/B_x \approx 0.3$. For this high level of turbulence, then, transition occurred in a region of accelerating flow instead of near the minimum pressure point. Another effect of the turbulence on the first stator suction surface distribution was to produce considerably (~ 15 to 20 percent) enhanced heat transfer in the fully turbulent portion of the flow. The observed percentage increase in heat transfer is in quite good agreement with the free-stream turbulence enhancement results of Blair (1983) assuming that the aft-region turbulence intensity was reduced in proportion to the increasing velocity ($U_{exit}/U_{inlet} = 2.73$, $Tu_{exit} \sim 3.5$ percent).

The effect of the higher turbulence level was also very evident along the first stator pressure surface. For the low turbulence case the heat transfer was essentially laminar while with high turbulence the measured heat transfer was as much as 60 percent greater than the two-dimensional fully turbulent prediction. The enhanced pressure surface heat transfer noted here was observed for a number of the Part I test cases. The phenomenon will be discussed more fully in Part II.

In contrast to the accuracy of the two-dimensional boundary layer predictions for the first stator, the comparisons between the predictions and the low inlet turbulence data for the rotor

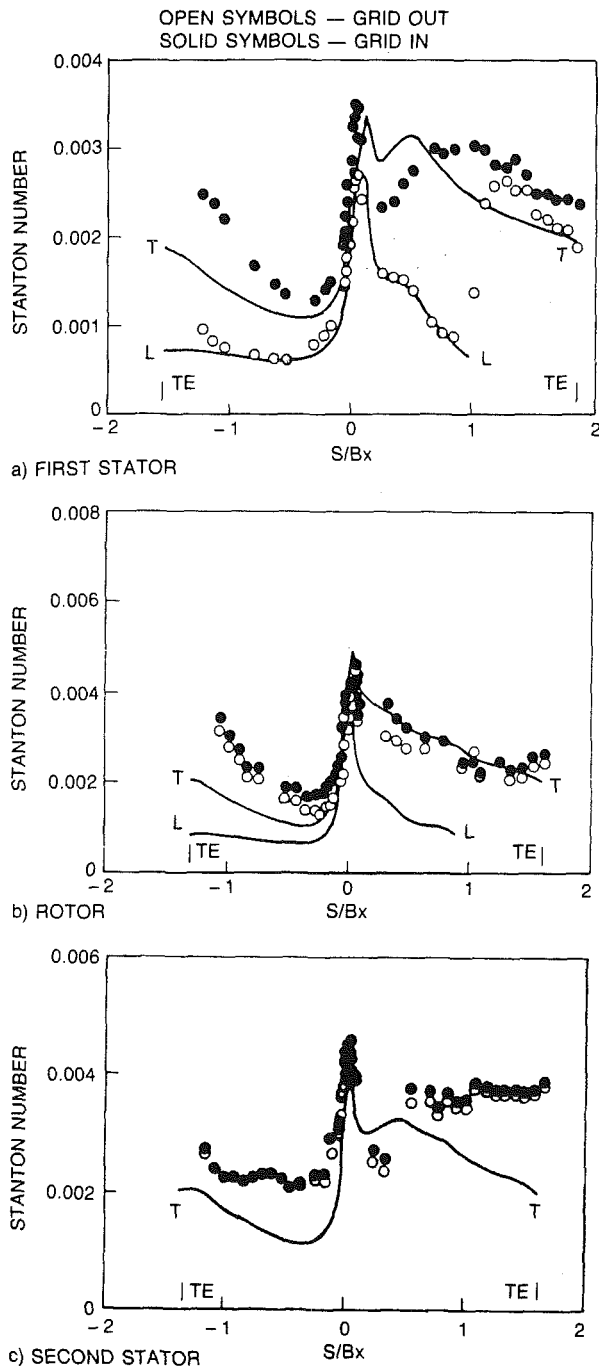


Fig. 7 Effect of the upstream grid on the airfoil midspan heat transfer distributions, design flow coefficient, 65 percent axial gap

(Fig. 7b) showed considerably greater disagreement. The rotor airfoils, of course, were exposed to a much more disturbed flow than the first stator, since they were passing through the wakes generated by the first stators (see Dring et al., 1982). As can be seen from an examination of Fig. 7(b), the measured low inlet turbulence (grid-out) heat transfer distribution indicates that the only region of laminar flow on the entire rotor was in the immediate vicinity of the stagnation region. On the suction surface there appears to be about 1/3 of a chord of transitional flow followed by fully turbulent two-dimensional heat transfer. On the pressure surface the measured heat transfer rates exceeded the two-dimensional fully turbulent level by as much as 50 percent.

On the rotor the effects produced by increasing the inlet turbulence (grid-in) were much less dramatic than for the first

stator. A much smaller change to the heat transfer resulted for the rotor because even with the low inlet turbulence (grid-out) the rotor flow is highly disturbed by the first stator wakes. The incremental change in the unsteadiness level produced by installing the grid was much less for the rotor than for the first stator. On the rotor suction surface, transition appears to have moved upstream to $S/B_x \sim 0.2$ with the grid-in.

Figure 7(c) indicates that for the second stator the two-dimensional analysis had little relationship to the measured results and that the impact of the inlet turbulence was negligible. This result was probably a consequence of the intense turbulence, unsteadiness, and secondary flows generated by the rotor. Note that for both the pressure and suction surfaces the measured heat transfer rates were well in excess of the predicted fully turbulent levels.

The important observation to be made from Fig. 7 is that there was a progressive and significant increase in the complexity of the flow as it proceeded through the turbine. At the first stator the measured heat transfer distribution was very well described by two-dimensional laminar (grid-out) or turbulent (grid-in) boundary layer predictions. These predictions worked reasonably well for the leading edge region and suction surface of the rotor but quite poorly for the rotor pressure surface and for both surfaces of the second stator. Secondary flows, unsteadiness, and turbulence generated at each successive airfoil row appear to have made the flow less and less well described by a two-dimensional boundary layer analysis.

Probably the most striking feature of the second stator heat transfer distributions, for both the grid-in and grid-out cases, is the very high values of Stanton number relative to the two-dimensional turbulent boundary layer prediction. On the pressure surface the heat transfer data are 50–100 percent above the prediction. This result is in general agreement with the first stator (grid-in) and rotor pressure surface measurements. On the suction surface, however, the second vane heat transfer is entirely different from the first stage results. Not only are the suction surface heat transfer data well in excess of the two-dimensional prediction, but the data and theory are diverging with increasing distance. It appears that by the second stator the flow field has become so contaminated by secondary flow that a two-dimensional prediction is inappropriate.

The effects on airfoil heat transfer produced by changing stator-rotor spacing were examined in the present study using two model configurations. The test configurations consisted of stator 1/rotor axial separations of 15 and 65 percent B_x . Heat transfer distributions were measured on both the first stator and the rotor for both spacings with and without the upstream grid. An examination of these results revealed that, at least for this turbine model, even this relatively large change in axial spacing did not significantly change either the stator or the rotor heat transfer distributions. This result is in conflict with data published by Dring et al. (1980), which were measured in an earlier study in this same facility. These earlier data indicated that changing the axial separation had produced a significant difference in the stator heat transfer. Since these earlier data were obtained using a considerably less accurate thermocouple monitoring system than used for the present experiment and since greater care was taken to insure inlet temperature uniformity, the present results are considered to be far more reliable. The conclusion drawn from this test, then, is that changes to the stator-rotor axial spacing with or without the turbulence generating grid produced negligible effects on the heat transfer distributions on either the stator or the rotor.

The flow field entering the second stator row fluctuates temporally at the rotor airfoil passing frequency. The wakes generated by the first stator remain sufficiently coherent while passing through the rotor, such that a circumferential variation with the pitch of the first stator is present in the second stator inlet flow field (Sharma et al., 1985). For this reason, the

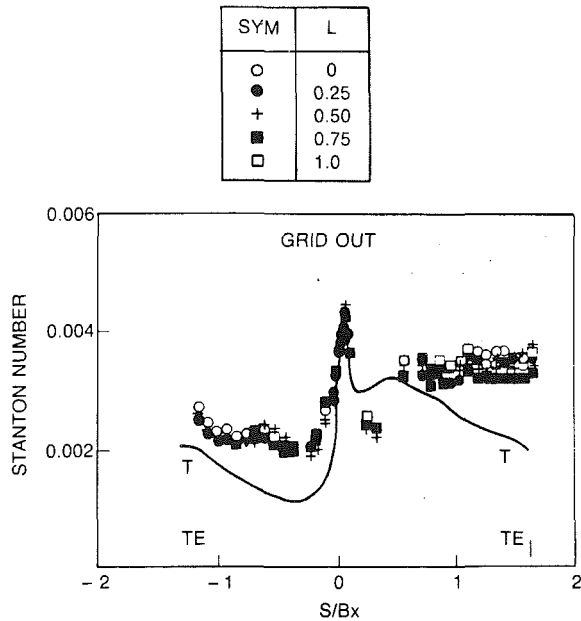
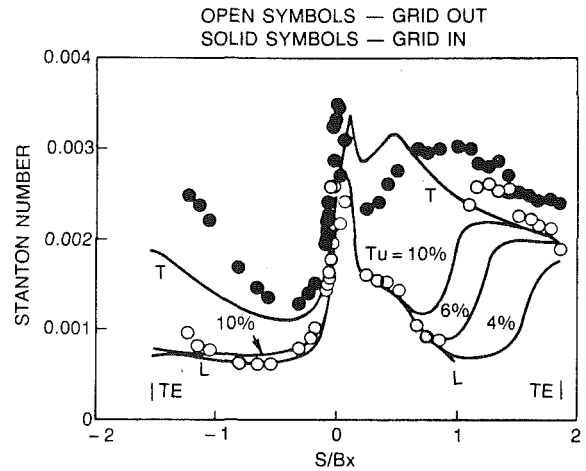


Fig. 8 Effects of relative circumferential positions of the first and second stators on the second stator heat transfer

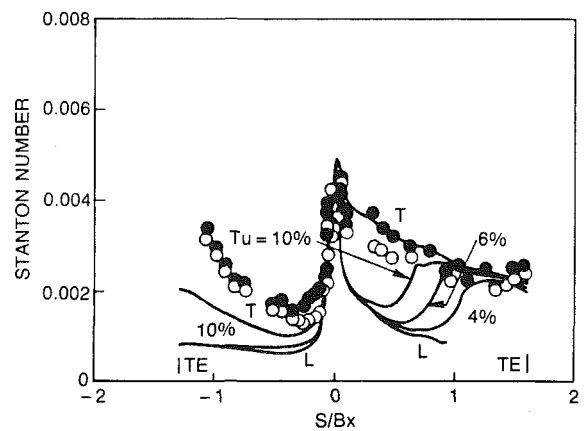
possibility that the second stator heat transfer was dependent upon its circumferential location relative to the first stator was examined as part of this program. The second stator heat transfer was determined with the first stator located at five circumferential positions. The first stator row was indexed in five increments of 25 percent pitch so that the first and last locations were geometrically similar. The heat transfer distributions measured for the five index locations with the inlet turbulence grid-out are given in Fig. 8. The value (L) given for each data set indicates the stator 1/stator 2 relative circumferential position in fractions of a pitch.

The effects associated with stator 1/stator 2 relative location were minor. The suction surface data obtained at $L = 0.0, 0.25, 0.50,$ and 1.0 were in good agreement, with only the data at $L = 0.75$ falling about 10 percent below the other four sets. On the pressure surface the data for all five index locations were virtually identical. These results indicate that the strong circumferential gradients from the first stator have spread across most of the channel by the second stator leading edge to the extent that their impact on heat transfer is minimal. Finally, data were also obtained at all five index locations with the turbulence grid in. The grid-in and grid-out results were very close, indicating that the influence of inlet turbulence was restricted to the first stage.

The boundary layer analysis chosen for the present assessment was the "ABLE" code of Carter et al. (1982). This is an efficient and versatile calculation for laminar, transitional, and turbulent flow. A number of options for the transition and turbulence models are incorporated in the code. In the present assessment two such models have been evaluated. The first was the algebraic turbulence model of Cebeci and Smith (1974), the second was that of McDonald et al. (1973, 1974). The McDonald analysis includes models for both transitional and turbulent flow, both of which are functions of the imposed free-stream turbulence. With this model the level of free-stream turbulence controls both the onset and the length of transition. The turbulent Prandtl number profile used in the present comparison was not that of McDonald and Kreskovsky (1974) but rather a profile based on the measurements of Blair (1982). The effect of this modified turbulent Prandtl number profile was to increase the predicted Stanton numbers slightly beginning in the transitional region and continuing through the turbulent zone. The increase was typically 6 percent in the turbulent region.



a) FIRST STATOR



b) ROTOR

Fig. 9 Analytical/experimental comparisons for the first-stage airfoils

The analytical/experimental comparisons for this assessment are shown in Fig. 9 for the first-stage stator and rotor. The comparisons are all for the data acquired in the 65 percent axial gap configuration both with and without the turbulence generating grid. Each of the figures includes a laminar prediction up to laminar separation indicated by "L," a fully turbulent prediction (using the Cebeci and Smith, 1974, model), indicated by "T," and a family of transitional predictions (using the model of McDonald and Kreskovsky, 1974, with the turbulent Prandtl number profile of Blair, 1982) indicated by the level of the free-stream turbulence used in each calculation. On the pressure surfaces the transitional predictions for free-stream turbulences up to 10 percent were generally very close to the laminar predictions. On the suction surfaces increasing the free-stream turbulence produced a monotonic upstream movement of transition.

On the pressure surfaces of the three airfoils reasonable agreement between the measured and the computed results was only obtained on the first stator with the grid-out. With the grid-in the measured data were far above even the fully turbulent prediction. Similarly the pressure surface data for the rotor and the second stator were far above the fully turbulent predictions both with and without the grid.

On the suction surfaces of the airfoils the agreement between the measured and computed results was generally unsatisfactory for both the cases with and without the grid. The best agreement was obtained on the rotor for the case with the grid-in. In this case after transition the data were in good agreement with the fully turbulent prediction. On the first stator the

transition predictions were in poor agreement with the data in spite of the relatively benign inflow condition, i.e., without an upstream airfoil row. On the rotor the predictions of transition were also poor. This may be related to the wakes of the upstream stator but this is unlikely since the rotor Stanton number distribution varied only slightly for large changes in the stator/rotor axial gap.

Conclusions

A combined experimental and analytical program has been conducted to examine the impact of the following variables on turbine airfoil midspan heat transfer.

- turbine inlet turbulence (0.5 and 10 percent)
- stator 1/rotor axial spacing (15 and 65 percent)
- relative stator 1/stator 2 circumferential position.

It was demonstrated that while turbine inlet turbulence can have a very strong impact on the first stator heat transfer, its impact in downstream rows is minimal. The effects on heat transfer produced by relatively large changes in stator/rotor spacing or by changing the relative row-to-row circumferential positions of stators were very small. Specific conclusions and observations are listed below.

1 Steady aerodynamic documentation measurements indicated that the turbine model airfoil midspan pressure distributions were in good agreement with two-dimensional potential flow and that they were essentially unaffected by either the turbulence generating grid or the axial gaps between the airfoil rows. It was also observed that the turbulence-generating grid had no significant impact on the circumferential distributions of flow speed downstream of each row of airfoils. The conclusion reached here was that the midspan aerodynamics in this experiment were well behaved and that the heat transfer results would be typical of those of a well-designed turbine.

2 Measurements of the streamwise fluctuating component of the turbine inlet velocity indicated that the turbulence intensity just upstream of the first stator leading edge was 0.5 percent without the turbulence-generating grid and 9.8 percent with the grid installed. At the rotor exit and at the second stator exit, however, the change in unsteadiness level due to the grid was insignificant. The performance of the present turbulence-generating grid was in excellent agreement with the performance of similar biplane grids and the spectral distribution of the grid generated turbulence was in excellent agreement with the von Karman spectrum, a result typical of fully developed grid-generated turbulence.

3 The heat transfer distributions measured on the first stator, rotor, and second stator for the design flow coefficient and with no turbulence grid indicate that there was a progressive and significant increase in the complexity of the flow as it proceeded through the turbine. At the first stator the measured heat transfer distribution was very well described by two-dimensional laminar and turbulent boundary layer predictions. These predictions worked reasonably well for the leading edge region and suction surface of the rotor but quite poorly for the rotor pressure surface and for both surfaces of the second stator. Secondary flows, unsteadiness, and turbulence generated by each successive airfoil row appear to have made the flow less and less well described by a two-dimensional boundary layer analysis.

4 The impact of high inlet turbulence on the first stator heat transfer distribution was dramatic with significant increases of heat transfer on the leading edge and along both the suction and pressure surfaces. On the suction surface the increased turbulence moved the location of transition well upstream from $S/B_x \approx 1.0$ to $S/B_x \approx 0.3$. For this high level of turbulence, then, transition occurred in a region of accelerating flow instead of near the minimum pressure. The effect of the higher turbulence level was also very evident along the first

stator pressure surface. For the low-turbulence case the heat transfer was essentially laminar while with high turbulence the measured heat transfer was as much as 60 percent greater than the two-dimensional fully turbulent prediction.

5 On the rotor the effects produced by increasing the inlet turbulence were much less dramatic than for the first stator. On the rotor suction surface, transition appears to have moved upstream to $S/B_x \approx 0.2$ with the increased turbulence level. Changes downstream of transition in the fully turbulent region were negligible. The only region of the rotor pressure surface that showed any effects from the increased turbulence was close to the leading edge ($-0.5 < S/B_x < 0$).

6 Changes to the stator-rotor axial spacing produced negligible effects on the heat transfer distributions on both the stator and the rotor. This same insensitivity to spacing resulted for both the grid-in and grid-out test conditions.

7 The effects associated with stator 1/stator 2 relative location appear to have been minor. The data for all five index locations were virtually identical, both with and without the turbulence grid installed. These results indicate that the strong circumferential gradients from the first stator had spread across most of the channel by the second stator leading edge to the extent that their impact on heat transfer was minimal.

8 The impact of changing the turbine inlet turbulence level on the stator 2 heat transfer was negligible. This was expected since the baseline second stator flow field was so highly disturbed even in the absence of the turbulence grid.

Acknowledgments

The research was sponsored by the National Aeronautics and Space Administration (NASA), Lewis Research Center, under Contract NAS3-23717. The United States Government is authorized to reproduce and distribute reprints for governmental purposes notwithstanding any copyright notation herein. The contract monitor for this project was Dr. Robert J. Simoneau, Chief, Heat Transfer Branch.

References

- Baines, W. D., and Peterson, E. G., 1951, "An Investigation of Flow Through Screens," *Trans. ASME*, Vol. 73, pp. 467-480.
- Blair, M. F., and Edwards, D. E., 1982, "The Effects of Free-Stream Turbulence on the Turbulence Structure and Heat Transfer in Zero Pressure Gradient Boundary Layers," Final Report for AFOSR Contract No. F49620-81-C-0053, AFOSR TR-83-0149, Gov't Acc. No. ADA 126465.
- Blair, M. F., 1983, "Influence of Free-Stream Turbulence on Turbulent Boundary Layer Heat Transfer and Mean Profile Development," *ASME Journal of Heat Transfer*, Vol. 105, pp. 33-47.
- Blair, M. F., 1985, "Heat Transfer in the Vicinity of a Large-Scale Obstruction in a Turbulent Boundary Layer," *AIAA Journal of Propulsion and Power*, Vol. 1, No. 8, pp. 158-160.
- Carter, J. E., Edwards, D. E., and Werle, M. J., 1982, "Coordinate Transformation for Laminar and Turbulent Boundary Layers," *AIAA Journal*, Vol. 20, No. 2, pp. 282-284.
- Caspar, J. R., Hobbs, D. E., and Davis, R. L., 1980, "Calculation of Two-Dimensional Potential Cascade Flow Using Finite Area Methods," *AIAA Journal*, Vol. 18, pp. 103-109.
- Cebeci, T., and Smith, A. M. O., 1974, *Analysis of Turbulent Boundary Layers*, Academic Press, New York.
- Dring, R. P., and Joslyn, H. D., 1981, "Measurements of Turbine Rotor Blade Flows," *ASME Journal of Engineering for Power*, Vol. 103, No. 2, pp. 400-405.
- Dring, R. P., Joslyn, H. D., Hardin, L. W., and Wagner, J. H., 1982, "Turbine Rotor-Stator Interaction," *ASME Journal of Engineering for Power*, Vol. 104, pp. 729-742.
- Dring, R. P., Blair, M. F., Joslyn, H. D., Power, G. D., and Verdon, J. M., 1986a, "The Effects of Inlet Turbulence and Rotor Stator Interactions on the Aerodynamics and Heat Transfer of a Large-Scale Rotating Turbine Model, Vol. I—Final Report," NASA CR 4079, UTRC-R86-956480-1.
- Dring, R. P., Blair, M. F., and Joslyn, H. D., 1986b, "The Effects of Inlet Turbulence and Rotor Stator Interactions on the Aerodynamics and Heat Transfer of a Large-Scale Rotating Turbine Model, Vol. II—Heat Transfer Data Tabulation, 15% Axial Spacing," NASA CR 179467, UTRC-R86-956480-2.
- Dring, R. P., Blair, M. F., and Joslyn, H. D., 1986c, "The Effects of Inlet Turbulence and Rotor Stator Interactions on the Aerodynamics and Heat Transfer of a Large-Scale Rotating Turbine Model, Vol. III—Heat Transfer Data Tabulation, 65% Axial Spacing," NASA CR 179468, UTRC-R86-956480-3.

Dring, R. P., Blair, M. F., and Joslyn, H. D., 1986d, "The Effects of Inlet Turbulence and Rotor Stator Interactions on the Aerodynamics and Heat Transfer of a Large-Scale Rotating Turbine Model, Vol. IV—Aerodynamic Data Tabulation," NASA CR 179469, UTRC-R86-956480-4.

Edwards, D. E., Carter, J. E., and Werle, M. J., 1981, "Analysis of the Boundary Layer Equations Including a Coordinate Transformation—The ABLE Code," UTRC81-30.

Graziani, R. A., Blair, M. F., Taylor, J. R., and Mayle, R. E., 1980, "An Experimental Study of Endwall and Airfoil Surface Heat Transfer in a Large Scale Turbine Blade Cascade," *ASME Journal of Engineering for Power*, Vol. 102, pp. 257-267.

Han, L. S., Chait, A., Boyce, W. F., and Rapp, J. R., 1982, "Heat Transfer on Three Turbine Airfoils," AFWAL-TR-82-2124, Aero Propulsion Laboratory, Air Force Wright Aeronautical Laboratories, Air Force Systems Command, Wright-Patterson Air Force Base, OH 45433.

Hylton, L. D., Mihelc, M. B., Turner, E. R., Nealy, D. A., and York, R. E., 1983, "Analytical and Experimental Evaluation of the Heat Transfer Distribution Over the Surfaces of Turbine Vanes," NASA CR 168015, Final Report for Contract No. NAS3-22761.

Joslyn, H. D., and Dring, R. P., 1988, "An Experimental and Analytical

Study of Turbine Temperature Profile Attenuation," AFOSR Contract No. F49620-86-C-0020, completion date: Aug. 1988.

Lokay, V. I., and Trushin, V. A., 1970, "Heat Transfer From the Gas and Flow-Passage Elements of a Rotating Gas Turbine." *Heat Transfer—Soviet Research*, Vol. 2, No. 4.

McDonald, H., and Fish, R. W., 1973, "Practical Calculation of Transitional Boundary Layer," *International Journal of Heat and Mass Transfer*, Vol. 16, No.9, pp. 1729-1744.

McDonald, H., and Kreskovsky, X. X., 1974, "Effect of Free-Stream Turbulence on the Turbulent Boundary Layer," *Int. J. Heat Mass Transfer*, Vol. 17.

Rae, W. J., Taulbee, D. B., Civinskas, K. C., and Dunn, M. G., 1986, "Turbine-Stage Heat Transfer: Comparison of Shock-Duration Measurements With State-of-the-Art Prediction," AIAA Paper No. AIAA-86-1465, submitted to the *AIAA Journal of Propulsion and Power*.

Sharma, O. P., Butler, T. L., Joslyn, H. D., and Dring, R. P., 1985, "Three-Dimensional Unsteady Flow in an Axial Flow Turbine," *AIAA Journal of Propulsion and Power*, Vol. 1, No. 1, pp. 29-38 (presented in expanded form as AIAA Paper No. AIAA-83-1170).

The Effects of Turbulence and Stator/Rotor Interactions on Turbine Heat Transfer: Part II—Effects of Reynolds Number and Incidence

M. F. Blair

Senior Research Engineer.
Mem. ASME

R. P. Dring

Manager, Gas Turbine Technology.
Mem. ASME

H. D. Joslyn

Research Engineer.

United Technologies Research Center,
East Hartford, CT 06108

Part I of this paper presents airfoil heat transfer data obtained in a rotating turbine model at its design rotor incidence. This portion of the paper presents heat transfer data obtained in the same model for various combinations of Reynolds number and inlet turbulence and for a very wide range of rotor incidence. On the suction surfaces of the first-stage airfoils the locations and lengths of transition were influenced by both the inlet turbulence level and the Reynolds number. In addition it was demonstrated that on the first-stage pressure surfaces combinations of high Reynolds number and high turbulence can produce heat transfer rates well in excess of two-dimensional turbulent flow. Rotor heat transfer distributions indicate that for relatively small deviations from the design incidence, local changes to the heat transfer distributions were produced on both pressure and suction sides near the stagnation region. For extremely large negative incidence the flow was completely separated from the rotor pressure surface, producing very high local heat transfer.

Introduction

The importance of accurate prediction of boundary layer development and heat transfer on gas turbine airfoils is recognized throughout the industry. Enormous efforts have been expended to develop both analytical and empirical tools to achieve this end. This present program was conducted to produce a set of thoroughly documented, accurate turbine airfoil heat transfer data that could be employed to develop and validate these predictive tools. The data of this present program were obtained in a large-scale, low-speed, rotating turbine model that realistically simulated the geometry, velocity triangles, velocity distributions, and Reynolds numbers of modern aircraft turbines. The data presented in Part I of this paper were all obtained for the turbine model operating at design rotor incidence and at a single throughflow velocity (Reynolds number). Included in Part I were descriptions of the inlet mean and fluctuating velocity fields.

As part of this study heat transfer distribution data were obtained over a range of airfoil Reynolds numbers for both high and low inlet turbulence intensity levels. A wide variety of factors affecting local boundary layer development were produced through these Reynolds number variations. Data were obtained for both rotating and nonrotating airfoils for

various combinations of distributions of local acceleration factor, surface curvature, momentum thickness Reynolds number, and mainstream turbulence level. It is anticipated that these data sets will prove useful for the development of boundary layer codes for turbine airfoil applications.

In addition to the multiple-Reynolds number data, heat transfer distributions were also measured for an extremely wide range of rotor flow incidence. These results reflect operation at severe-off-design conditions and were examined to determine the impact on heat transfer for such extreme excursions. These off-design incidence cases should be useful for evaluation of codes designed to compute massive airfoil boundary layer separation.

The final purpose of the test program was to isolate and explore the role of rotation on airfoil heat transfer. It is widely known in the industry that certain aircraft engine airfoils seem to experience local exterior heat loads far in excess of what would be predicted by a two-dimensional boundary layer computation. The data of Lokay and Trushin (1970) raised suspicions that some mechanism intrinsic to rotation could strongly increase heat transfer and account for at least some of the anomalous high heat loads. The effects of rotation could be isolated in this study because detailed cascade heat transfer distribution data already existed for the rotor airfoil (Graziani et al., 1980). The existing cascade data and these new rotating airfoil data thus presented an opportunity for a direct comparison between similar rotating and stationary distributions.

Contributed by the International Gas Turbine Institute and presented at the 33rd International Gas Turbine and Aeroengine Congress and Exhibition, Amsterdam, The Netherlands, June 5-9, 1988. Manuscript received by the International Gas Turbine Institute September 15, 1987. Paper No. 88-GT-5.

Table 1

Incidence $i^\circ = (\beta - \beta_{ref})$	Relative flow angle β°	Flow coefficient (C_x/U_m)	(U_m/U_{mref})	(C_x/C_{xref})
+5	35	0.96	0.81	1.00
0	40	0.78	1.00	1.00
-5	45	0.68	1.15	1.00
-15	55	0.56	1.39	1.00
-25	65	0.50	1.56	1.00
-35	75	0.45	1.73	1.00
-45	85	0.42	1.73	0.93

A comprehensive report of this experiment is given by Dring et al. (1986a). This report contains detailed descriptions of the experimental apparatus, instrumentation, and techniques employed. In addition, Dring et al. (1986b, 1986c, 1986d) present the tabulated heat transfer and aerodynamic data.

Test Conditions

All data presented in Part I of this paper were obtained near the maximum (rig limit) turbine model inlet velocity and at the design rotor incidence. The airfoil Reynolds numbers, based on axial chord and exit velocity and density, for these near maximum velocity cases will be referred to here as NOMINAL (Re_{NOM}). For typical rig inlet conditions the first-stage NOMINAL Reynolds numbers were: Stator 1— $Re_{NOM} = 6.45 \times 10^5$; and Rotor— $Re_{NOM} = 5.79 \times 10^5$. This portion of the paper (Part II) presents airfoil heat transfer data obtained for various combinations of Reynolds number, high or low inlet turbulence, and a wide range of rotor incidence.

The effects of Reynolds number variation on the heat transfer were investigated with the turbine model operating at its design incidence value. These tests were conducted with the turbine model configured as a single-stage machine with a 15 percent B_x stator 1/rotor axial gap. Reynolds number variation was achieved by reducing the inlet flow velocity and setting the rotor rotational speed proportionally. For the first stator, heat transfer data were obtained for three Reynolds numbers (63 percent to NOM) with the turbulence grid out and for seven Reynolds numbers (37 percent to NOM) with the grid in. On the rotor, heat transfer data were recorded for five Reynolds numbers (35 percent to NOM) both with and without the turbulence grid installed.

Testing was also conducted to determine the impact of rotor incidence variation on the first-stage airfoil heat transfer distributions. For this series of tests the turbine model was configured as a 1 1/2 stage machine with 65 percent B_x stator 1/rotor and 63 percent rotor/stator 2 axial gaps. Here incidence is defined as the change in the rotor relative inlet flow angle (β) from its value at the nominal design, or reference conditions ($\beta_{ref} = 40$ deg). It should be pointed out, however, that the design relative angle (β_{ref}) is slightly larger than the leading edge mean camber line relative angle ($\beta_{1,m} = 42.2$ deg). Incidence variation was produced by changing the rotor rotational speed for a fixed turbine inlet flow velocity. The single exception to this was for the most extreme negative incidence case (-45 deg), which would have required a rotor rotational speed in excess of the maximum safe rig limit. This extreme incidence case was produced by dropping the turbine inlet velocity with the rig rotation speed held at its maximum safe

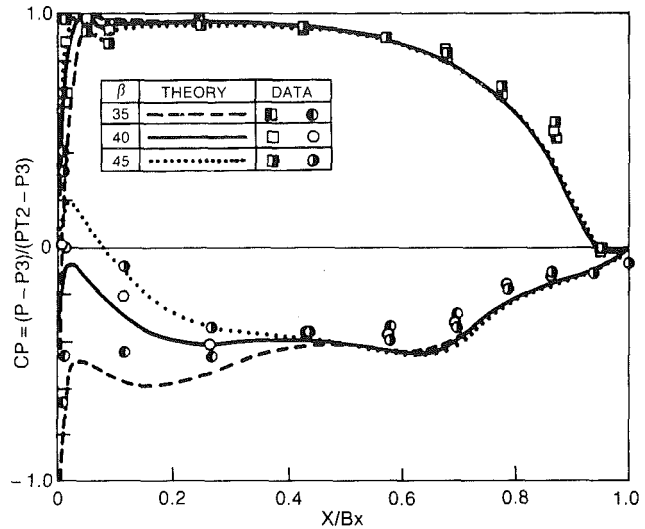


Fig. 1 Rotor pressure distributions for $\phi = 0.68, 0.78,$ and 0.96

value (700 rpm). Table 1 lists the various incidence values and relative rotational and throughflow velocities for which heat transfer data were obtained.

Extensive aerodynamic testing of this model (over the same range of off-design incidence values explored in this present study) was conducted in an earlier investigation (Joslyn and Dring, 1983). Although aerodynamic documentation was not repeated for all the present test cases, midspan airfoil pressure distributions obtained at three incidence values ($\beta = 35, 40,$ and 45 deg) were in excellent agreement with the equivalent earlier data sets. The rotor midspan distributions for these three incidences are presented in Fig. 1.

For $\beta = 35$ deg (Fig. 1), the flow on the rotor suction surface underwent a strong overspeed near the leading edge and decelerated to the trailing edge. The suction surface overspeed resulted from the inlet flow being at nearly 5 deg positive incidence relative to that at the nominal design point. At $\beta = 40$ and 45 deg there was a slight overspeed in the flow near the leading edge on both the pressure and suction surfaces. The pressure surface leading edge overspeed was more pronounced at $\beta = 45$ deg where the inlet flow was at 5 deg negative incidence relative to that at the nominal design point. Overall, the steady-state flow over the rotor was weakly dependent on axial spacing and inlet turbulence. There was, however, a strong dependence on the relative inlet flow angle.

Results

Effects of Reynolds Number. Heat transfer distributions obtained for the first stator with the turbulence grid out are presented in Fig. 2 for Re (based on axial chord and exit conditions) = 41 to 65×10^4 . Each of the measured data sets is shown compared to the predicted two-dimensional heat transfer distribution for that particular Reynolds number. On the pressure surface, agreement with the fully laminar prediction was excellent for all three Reynolds numbers. Evidence of possible boundary layer transition near the pressure surface

Nomenclature

- B_x = airfoil axial chord
- CP = pressure coefficient
- P = static pressure
- PT = total pressure
- Re = Reynolds number based on

- axial chord and exit flow conditions
- S = surface arc length
- X = axial distance from the stator 1 leading edge

- β = relative yaw flow angle
- Subscripts**
- 1 = stator 1 inlet station
 - 2 = stator 1 exit station
 - 3 = rotor exit stator

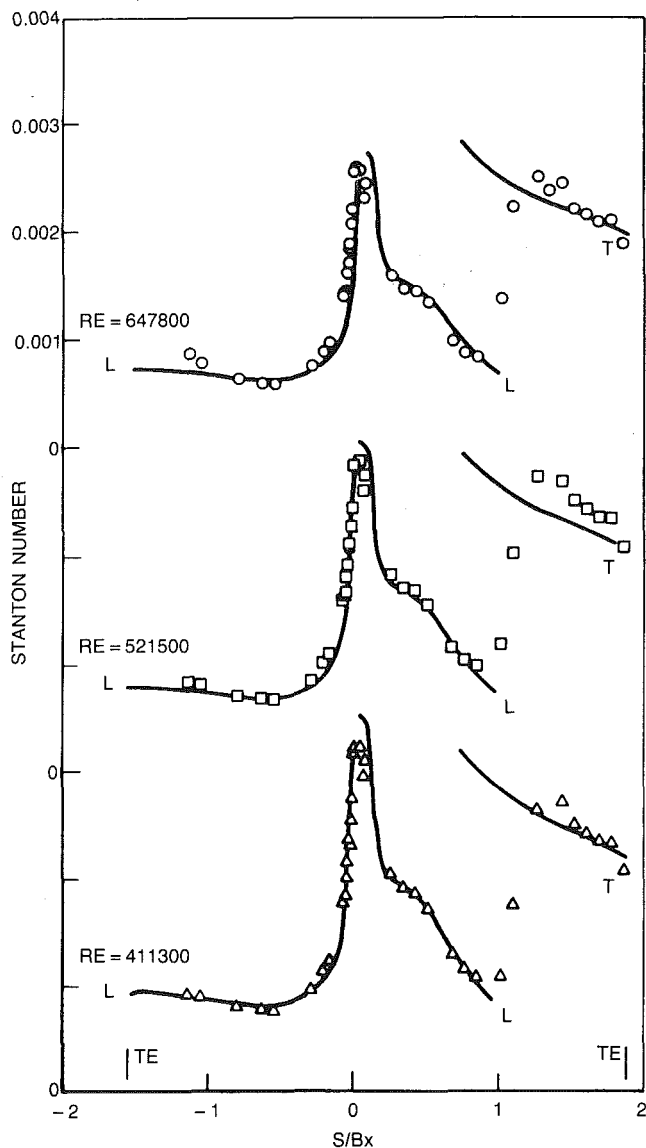


Fig. 2 Effect of Reynolds number on the first stator heat transfer, grid out

trailing edge progressively decreased with decreasing Reynolds number. On the suction surface the agreement between the laminar prediction and upstream half of the data was also excellent in all cases. A careful examination of the data near $S/B_x = 1$ indicates that transition moved progressively, albeit slightly, downstream as Re decreased. Finally for $S/B_x > 1$ both the highest and lowest Re data agreed very well with the two-dimensional fully turbulent prediction. For $Re = 52 \times 10^4$ an anomalous discrepancy of about 10 percent between theory and data is present for this region. One possible explanation for this difference is that an undetected shift in model heat flux occurred during the process of data acquisition. The results of Fig. 2 can be interpreted as a confirmation that the facility, turbine model, and instrumentation system all behaved as expected. As the Reynolds number changed for this relatively ideal (low turbulence) first stator flow the data and the theory remained in excellent agreement.

The rotor heat transfer distributions for the grid-out configuration are presented in Fig. 3 for $Re = 29-58 \times 10^4$. Each data set is again shown compared with the two-dimensional prediction for that particular Re . Note that the computed heat transfer distributions are for fully turbulent flow. Unlike the first stator (Fig. 2) there were no regions of laminar heat

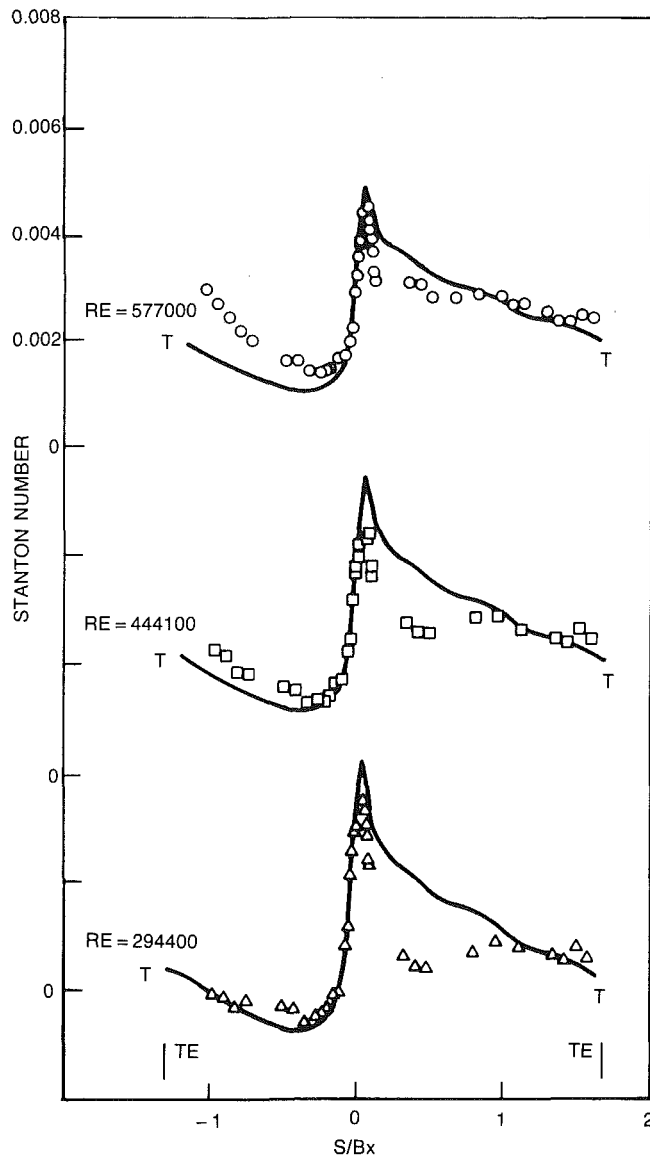


Fig. 3 Effect of Reynolds number on the rotor heat transfer, design flow coefficient, grid out

transfer on the rotor. On the suction surface there was an increasingly significant, both in size and heat transfer level, transitional region as the Reynolds number dropped. For all cases, however, the suction surface heat transfer data agreed reasonably well with the two-dimensional, fully turbulent boundary layer prediction in the trailing edge region.

The pressure surface heat transfer distributions shown in Fig. 3 reveal a strong dependence on the Reynolds number. At the largest Reynolds number the pressure surface heat transfer is significantly higher (by 50 to 80 percent) than the fully turbulent prediction. As the Reynolds number drops, the data approach the turbulent predictions. Discussion of this pressure-surface phenomenon will follow as more examples are presented.

The next figure (Fig. 4) displays the impact of Reynolds number on the first stator transfer distribution with high inlet turbulence. The first stator distributions with the turbulence grid in are given for four Reynolds numbers ranging from 2.4 to 6.4×10^5 . On the suction surface Fig. 4 shows an orderly, progressive downstream movement of the transition zone with decreasing Reynolds number. As the Reynolds number decreased the length of the near-laminar heat transfer zone increased and the length of the fully turbulent zone contracted.

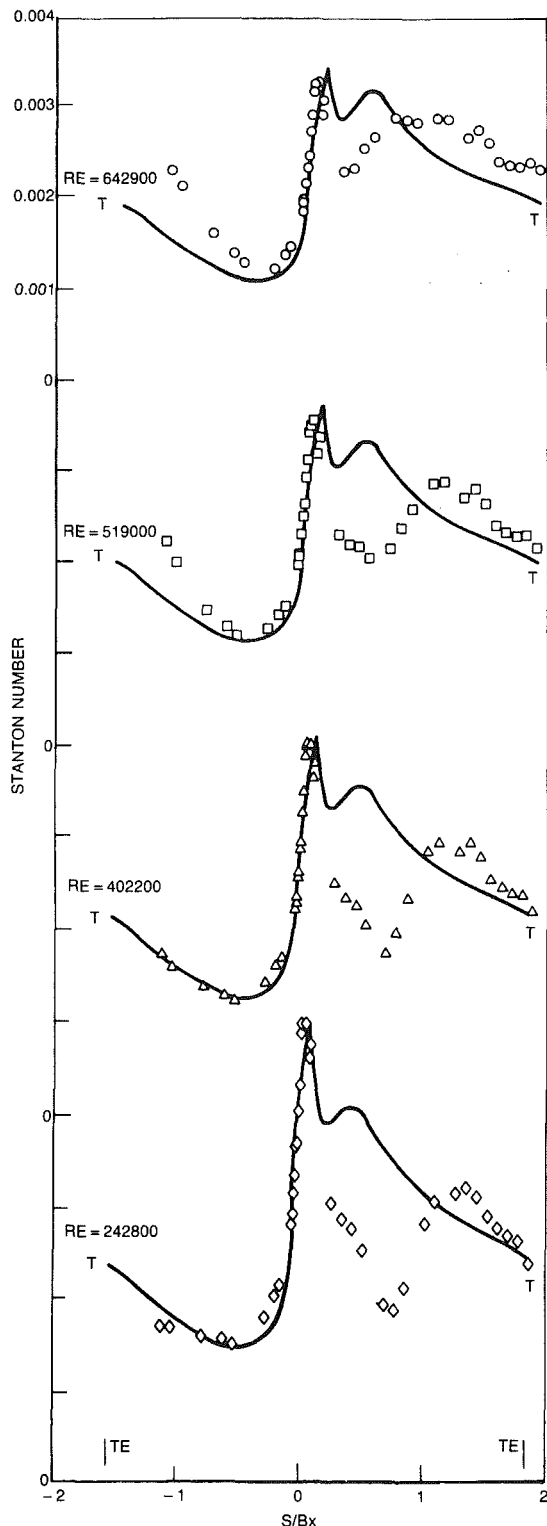


Fig. 4 Effect of Reynolds number on the stator heat transfer, grid in

On the pressure surface the data sets can be separated into two groups. For $Re > 4.0 \times 10^5$ the measured heat transfer exceeded each fully turbulent prediction, while for $Re \leq 4.0 \times 10^6$ there was near agreement between the data sets and the respective two-dimensional predictions.

For the rotor heat transfer distributions measured with the turbulence grid in, the results (not shown) were similar to those of the first stator. On the suction surface, for the highest Reynolds number, the data and fully turbulent prediction agreed for the entire chord. As Reynolds number decreased a

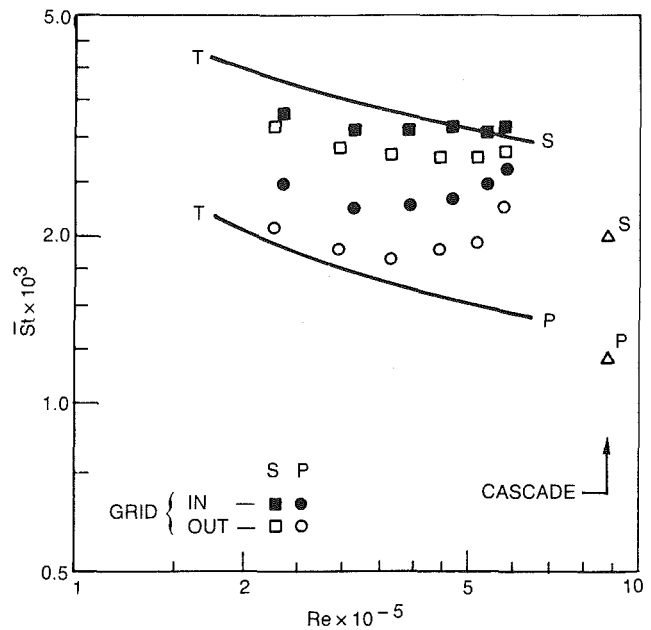
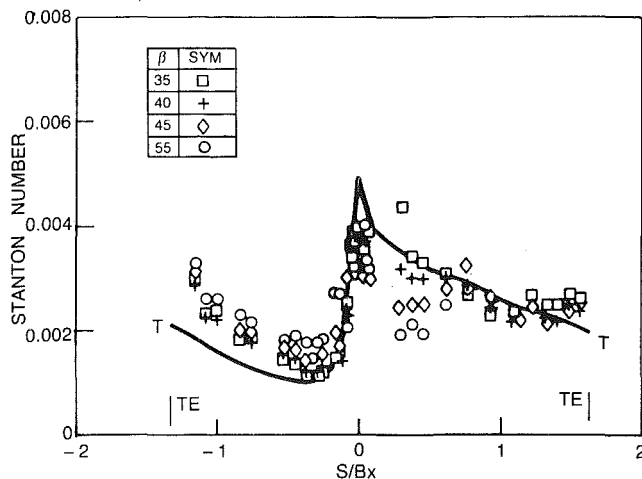


Fig. 5 Rotor-averaged suction (S) and pressure (P) surface heat transfer, $\phi = -0.78$, 15 percent gap

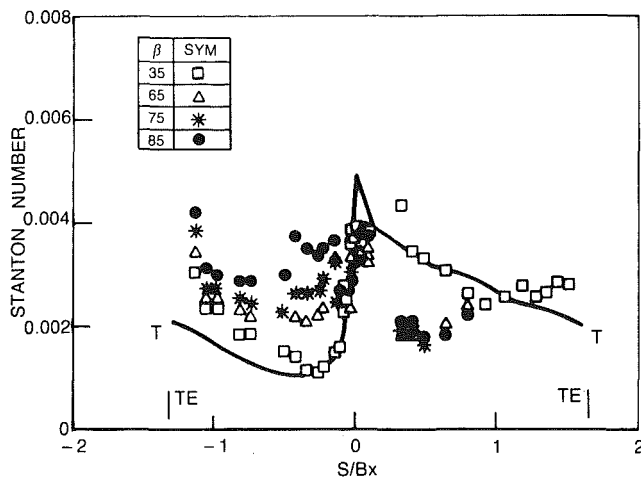
progressively growing zone of transitional flow developed and the region of fully turbulent heat transfer decreased. On the pressure surface the sharp rise in heat transfer near the trailing edge steadily decreased with the Reynolds number. Although the differences between the fully turbulent predictions and the respective pressure surface data decreased with falling Reynolds number there was no case that provided good agreement along the entire pressure surface. Specifically, the data in the region around $S/B_x = -0.4$ were always about 40 percent above the prediction.

Pressure Surface Heat Transfer. A large number of examples have been presented here in which pressure surface heat transfer rates significantly exceeded predicted two-dimensional, fully turbulent transport. For the first stator, heat transfer rates in excess of fully turbulent were demonstrated for high Reynolds numbers and high inlet turbulence (Fig. 4). For the rotor, very high-pressure surface heat transfer was documented for high Reynolds number-low inlet turbulence flow (Fig. 3) and for all Reynolds numbers with high inlet turbulence. These results indicate that there can be an interaction between the effects of concave surface curvature, Reynolds number, and the level of free-stream disturbance producing heat transfer far in excess of fully turbulent. Because the variation of the Reynolds number for these tests was produced by changing the velocity, the variations affected both the surface momentum thickness distributions and the local boundary layer acceleration parameter, $K = \nu/U^2 \partial U/\partial x$. For a fixed location on any particular airfoil, then, there was a reduction in Re_θ and an increase in K as the Reynolds number dropped. One possibility is that for certain critical combinations of concave surface curvature, Re_θ , K , and free-stream disturbance level, important Goertler vortex systems are produced in the boundary layer. Perhaps the development of these systems is suppressed for subcritical situations and two-dimensional, fully turbulent flow results. Whatever the physical cause of this phenomenon, similar effects have been observed by other investigators. Both Consigny and Richards (1982) and Daniels and Browne (1981) reported pressure surface heat transfer rates well in excess of fully turbulent values.

Enhanced pressure-surface heat transfer is illustrated in another format in Fig. 5 in which the rotor surface-average Stanton numbers are plotted as a function of chord Reynolds



a) $\beta = 35, 40, 45$ AND 55 deg



b) $\beta = 35, 65, 75$ AND 85 deg

Fig. 6 Effect on flow coefficient on the rotor heat transfer distribution, grid out

number. Suction (S) and pressure (P) surface data are shown as the symbols along with the fully turbulent (T) predictions. For the suction surface, both the absolute values and trends of the measured average Stanton numbers were in generally good agreement with the prediction. The pressure surface results, however, display a trend of increasing Stanton number with increasing Reynolds number both with and without the grid installed. At the highest Reynolds number with the grid installed the average pressure surface Stanton number is 80 percent greater than the fully turbulent prediction (and 50 percent higher with the grid out).

Effects of Rotor Incidence. The effects of rotor incidence on airfoil heat transfer were examined for a range of off-design conditions by holding the facility through-flow velocity (C_x) constant and adjusting the rotor speed (U) (see Table 1). Although the rotor inlet relative velocity was a function of incidence, the rotor exit relative velocity was essentially invariant. All of the Stanton number distributions presented here are based upon airfoil exit conditions so it is possible to make a comparison between heat transfer distributions obtained at different incidences. It had been observed in previous flow visualization tests with this rotor (Joslyn and Dring, 1983) that the airfoil had attached boundary layers over the incidence range from $\beta = 35$ deg down to 55 deg. At $\beta = 65$ deg and below a separation bubble appeared on the rotor pressure surface near the leading edge. This bubble grew with further

reductions in flow coefficient. At $\beta = 85$ deg the bubble had grown to about midchord.

Rotor heat transfer distributions obtained over a relatively small range of incidence are presented in Fig. 6(a) for the grid-out condition. Distributions for the more extreme values of incidence are presented in Fig. 6(b), again for low inlet turbulence. To avoid crowding only the design incidence theoretical heat transfer distribution is presented for each figure. Note that the data for $\beta = 35$ deg are given in both Figs. 6(a) and 6(b) for purposes of comparison.

Because of the symbol size and large quantity of data presented in Figs. 6(a, b), some of the incidence-related heat transfer effects are difficult to discern. Readers particularly interested in these incidence effects should consult Dring et al. (1986a, 1986b, 1986c).

The data of Fig. 6(a) indicate that: (1) the heat transfer rates near the trailing edge on both the pressure and suction surfaces were independent of incidence, (2), the peak stagnation region ($S/B_x = 0$) heat transfer depended on the incidence as a consequence of the changing relative inlet velocity, and (3) there were local effects on both the pressure and suction sides near the stagnation region that were dependent on the incident flow speed and angle. Note the effects on the rotor suction surface near $S/B_x = 0.3$. As β decreased a region of very high local Stanton number resulted at this location. The basic cause of this spike in heat transfer is the suction surface overspeed (Fig. 1a), the strength of which is a function of the incidence. At $\beta = 45$ deg there was only a slight overspeed followed by a favorable pressure gradient to midchord, while for $\beta = 35$ deg the suction surface overspeed location has by far the highest velocity on the airfoil and is followed by a strong adverse pressure gradient. For $\beta = 35$ deg the boundary layer is apparently unable to negotiate the adverse pressure gradient, separates, passes through a very short transition, and reattaches as a high-speed fully turbulent layer. For $\beta = 45$ deg the boundary layer experiences an extended transition length through the favorable pressure gradient to near midchord. A much subdued version of this same phenomenon can be seen on the pressure surface where the most severe overspeed ($S/B_x \sim 0.1$) occurs for $\beta = 45$ deg.

Rotor heat transfer distributions obtained for extremely large values of negative incidence are presented in Fig. 6(b). On the suction surface, for $S/B_x < 0.7$, the local Stanton numbers decreased with increasingly negative incidence until they approached laminar heat transfer rates.

On the pressure surface there was a continuous, systematic increase in Stanton numbers through the entire range of test incidences. The appearance of the distributions of Fig. 6(b) suggests that for $\beta > 65$ deg the flow was separated from the pressure surface. At these extreme negative incidence values the heat transfer was evidently dominated by a large, possibly unsteady, pressure surface separation bubble observed to start at $\beta = 65$ deg and to grow in chordal extent as β was increased.

Examination of first stator heat transfer data for these tests indicates that changing the incidence had no significant impact on the distributions. In addition it was observed on the rotor that for modest variations in incidence (± 5 deg) the addition of free-stream turbulence tended to reduce the relative importance of the incidence effects. With the high inlet turbulence, nearly the entire suction surface was fully turbulent, while the pressure surface distributions nearly collapsed to a single curve. No data were taken at extreme negative incidence with the turbulence grid installed.

Comparison of Rotor and Plane Cascade Data. Surface heat transfer distribution data were obtained in an earlier investigation in a cascade with the same rotor airfoil geometry used in this present program. The earlier data were obtained in a large-scale plane cascade and were published by Graziani et al. (1980). In brief, the cascade test airfoils had an axial

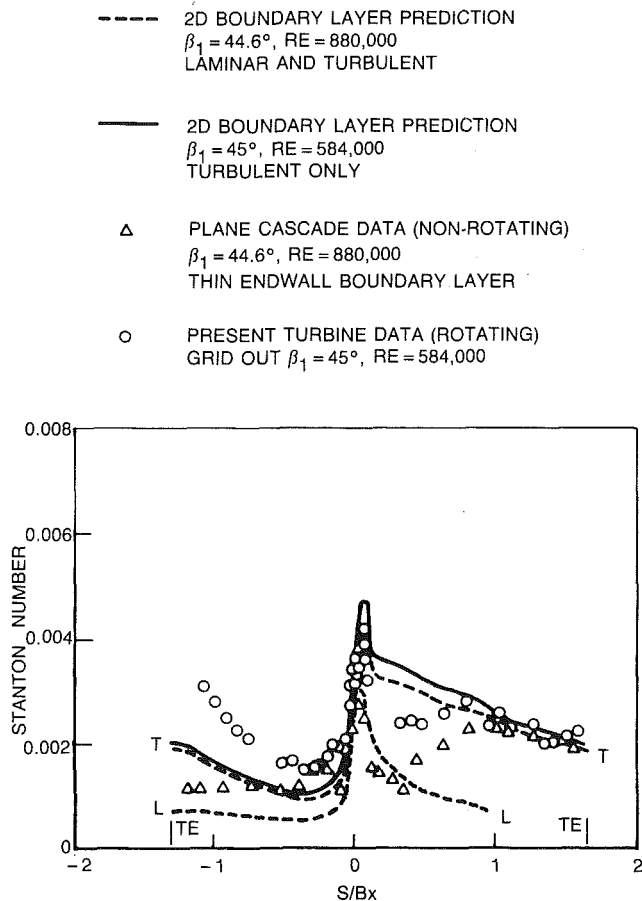


Fig. 7 Measured and predicted heat transfer distributions for the rotor and the same airfoil geometry installed in a plane cascade

chord of 11.08 in. and an aspect ratio and solidity near unity. The cascade inlet angle was 44.6 deg so the airfoil incidence was nearly identical to that for the cases in the present study with $\beta = 45$ deg. The cascade heat transfer data were obtained for an exit Reynolds number of 8.8×10^5 and for two values of endwall boundary layer thickness. The heat transfer data of the cascade study were measured using an electrically-heated-wall/thermocouple system similar in principle to that used for the present study. Only a very limited number of data points were obtained in the leading edge region of the cascade.

A comparison of the heat transfer distribution measured in the cascade with thin endwall boundary layers with the data obtained in the rotor of the present study is presented in Fig. 7. These two data sets were obtained at somewhat different Reynolds numbers so the predicted heat transfer distributions are given for both conditions. An examination of Fig. 7 indicates that, on the suction surface, transition was somewhat earlier for the rotating case than for the cascade. This result is not surprising as the disturbance level for the rotating blade was considerably higher than the 1 percent turbulence level at the entrance of the cascade. When allowance is made for the effect of Reynolds number, the post-transitional ($S/B_x > 0.8$) results for the rotating and cascade tests were practically identical. There was, however, a significant difference between the heat transfer distributions measured on the pressure surface with the cascade data falling well below the set from the rotating blade. This provides an additional piece of evidence, which indicates that strong enhancement of fully turbulent, concave surface heat transfer may only occur for high levels of free-stream disturbance. The surface (pressure and suction) average Stanton numbers for the cascade results are plotted in Fig. 5. The cascade results are seen to be consistent with

the rotating rig data when the difference in Reynolds number and inlet turbulence (unsteadiness) are accounted for. The major difference between the rotating and nonrotating airfoil midspan heat transfer distributions was the considerably higher levels on the pressure surface of the rotating airfoil. There is no evidence in the present results that this difference is directly related to the effects of rotation (e.g., Coriolis or centrifugal effects).

Conclusions

A combined experimental and analytical program has been conducted to examine the impact of the following variables on turbine airfoil midspan heat transfer:

- Reynolds number (flow speed)
- turbine inlet turbulence (0.5 and 10 percent)
- flow coefficient (airfoil incidence)
- rotation (rotor versus cascade)

It was observed that combinations of unsteadiness, high Reynolds number, and concave curvature can produce pressure surface heat transfer distributions well in excess of fully turbulent levels. It was also shown that large boundary layer separation bubbles produced by severe incidence angles could also cause large increases in heat transfer. There was no evidence that rotation effects, per se, effected airfoil heat transfer. The most important conclusion reached was that pressure surface heat transfer could be well in excess of design predictions due to both combustor- and turbine-generated unsteadiness. Specific conclusions are listed below.

1 Heat transfer distributions were measured on the first stator and rotor with no turbulence grid over a range of Reynolds numbers. These data indicate that on the suction surfaces on each airfoil there was an increasingly significant transitional region as the Reynolds number dropped. For all cases, however, the suction surface heat transfer data agreed reasonably well with two-dimensional, fully turbulent boundary layer predictions in the trailing edge region. Laminar heat transfer rates were measured for the entire stator 1 pressure surface for all test Reynolds numbers. On the rotor pressure surface the measured heat transfer exceeded predicted fully turbulent rates, the magnitude of the excess increasing with Reynolds numbers.

2 For the grid-in cases the suction surface data on both the stator and rotor indicate a progressively growing transitional zone as the Reynolds number dropped. On the pressure surfaces heat transfer rates well in excess of fully turbulent predictions were measured for all cases except for the first stator at the lowest test Reynolds number.

3 The first stator and rotor pressure surface heat transfer distributions indicate that for certain regimes of the test matrix there was an interaction between the effects of concave surface curvature, Reynolds number, and the level of free-stream disturbance that can produce heat transfer far in excess of fully turbulent. One possibility is that for certain critical combinations of concave surface curvature, Re_∞ , acceleration, and free-stream disturbance level, important Goertler vortex systems are produced in the boundary layer.

4 Rotor heat transfer distributions obtained over a relatively small (near design) range of rotor incidence indicate that: (1) the heat transfer rates near the trailing edge on both the pressure and suction surfaces were independent of incidence, (2) the peak stagnation region ($S/B_x = 0$) heat transfer depends on the incidence as a consequence of the changing relative inlet velocity, and (3) there were local effects on both the pressure and suction sides near the stagnation region that were dependent on the incidence.

5 Rotor heat transfer distributions obtained for extreme negative incidence indicated that for $\beta > 65$ deg the flow was

separated from the pressure surface. At these extreme negative incidence values the heat transfer was evidently dominated by a large, possibly unsteady, pressure surface separation bubble observed to start at $\beta = 65$ deg and to grow in chordal extent as β was increased.

6 The rotor heat transfer distributions obtained in the present program were compared with data obtained for the same airfoil section in a plane cascade. This comparison indicated that if the rotating and nonrotating tests had been conducted at the same Reynolds number and inlet turbulence levels the heat transfer distributions would have been nearly identical.

Acknowledgments

The research was sponsored by the National Aeronautics and Space Administration (NASA), Lewis Research Center, under Contract NAS3-23717. The United States Government is authorized to reproduce and distribute reprints for governmental purposes notwithstanding any copyright notation hereon. The contract monitor for this project was Dr. Robert J. Simoneau, Chief, Heat Transfer Branch.

References

Consigny, H., and Richards, B. E., 1982, "Shock Duration Measurements

of Heat Transfer Rate to a Gas Turbine Rotor Blade," *ASME Journal of Engineering for Power*, Vol. 104, No. 3, pp. 542-551.

Daniels, L. D., and Browne, W. B., 1981, "Calculation of Heat Transfer Rates to Gas Turbine Blades," *International Journal of Heat and Mass Transfer*, Vol. 24, No. 1, pp. 871-879.

Dring, R. P., Blair, M. F., Joslyn, H. D., Power, G. D., and Verdon, J. M., 1986a, "The Effects of Inlet Turbulence and Rotor Stator Interactions on the Aerodynamics and Heat Transfer of a Large-Scale Rotating Turbine Model, Vol. I - Final Report," NASA CR 4079, UTRC-R86-956480-1.

Dring, R. P., Blair, M. F., and Joslyn, H. D., 1986b, "The Effects of Inlet Turbulence and Rotor Stator Interaction on the Aerodynamics and Heat Transfer of a Large-Scale Rotating Turbine Model, Vol. II - Heat Transf. Data Tabulation, 15% Axial Spacing," NASA CR 179467, UTRC-R86-956480-2.

Dring, R. P., Blair, M. F., and Joslyn, H. D., 1986c, "The Effects of Inlet Turbulence and Rotor Stator Interactions on the Aerodynamics and Heat Transfer of a Large-Scale Rotating Turbine Model, Vol. III - Heat Transf. Data Tabulation, 65% Axial Spacing," NASA CR 179467, UTRC-R86-956480-2.

Dring, R. P., Blair, M. F., and Joslyn, H. D., 1986d, "The Effects of Inlet Turbulence and Rotor Stator Interactions on the Aerodynamics and Heat Transfer of a Large-Scale Rotating Turbine Model, Vol. IV - Aerodynamic Data Tabulation," NASA CR 179469, UTRC-R86-956480-4.

Graziani, R. A., Blair, M. F., Taylor, J. R., and Mayle, R. E., 1980, "An Experimental Study of Endwall and Airfoil Surface Heat Transfer in a Large Scale Turbine Blade Cascade," *ASME Journal of Engineering for Power*, Vol. 102, pp. 257-267.

Joslyn, H. D., and Dring, R. P., 1983, "Negative Incidence Flow Over a Turbine Rotor Blade," ASME Paper No. 83-GT-23 (based on USAF Report No. AFWAL-TR-81-2114).

Lokay, V. I., and Trushin, V. A., 1970, "Heat Transfer from the Gas and Flow-Passage Elements of a Rotating Gas Turbine," *Heat Transfer - Soviet Research*, Vol. 2, No. 4.